SEISMIC ANALYSIS OF HORIZONTAL AXIS WIND TURBINES

By

Otoniel Díaz-Nevárez

A dissertation submitted in partial fulfillment of the requirements for the degree of

DOCTOR OF PHILOSOPHY
in
CIVIL ENGINEERING

UNIVERSITY OF PUERTO RICO
MAYAGÜEZ CAMPUS

2010

Approved by:

_____	_____
Luis E. Suárez-Colche, Ph.D. President, Graduate Committee	Date
_____	_____
Ricardo R. López-Rodríguez, Ph.D. Member, Graduate Committee	Date
_____	_____
José A. Martínez-Cruzado, Ph.D. Member, Graduate Committee	Date
_____	_____
Miguel A. Pando-López, Ph.D. Member, Graduate Committee	Date
_____	_____
Mario A. Rivera-Borrero, Ph.D. Member, Graduate Committee	Date
_____	_____
Carlos U. Pabón-Ortiz, Ph.D. Representative of Graduate Studies Office	Date
_____	_____
Ismael Pagán-Trinidad, M.Sc. Chairperson of the Department of Civil Engineering and Surveying	Date

ABSTRACT

The wind energy industry has seen a substantial growth in several industrialized countries in recent years. Traditionally, territories in northern Europe, with a low level of seismicity, have been the leaders in the use of this technology, but nowadays its growth has extended to other regions susceptible to earthquakes, such as the US, China, and India. In order to improve the reliability of the system under these adverse conditions, there is a need to perform a detailed assessment of the seismic response of wind turbines. This dissertation presents the development of a new analytical model for the seismic response of a three-bladed horizontal axis wind turbine. The proposed model allows assessment of the likelihood of yielding or buckling failure of the structure. The proposed model involves a multi-body system with 16 degrees of freedom that account for flexibilities in the flap direction of the blades and the twisting and flexure motions of the tower. The equations of motion of the rotor were developed based on Lagrange equations. They were subsequently coupled with the equations of motion of the tower which was modeled with beam elements. The model considers aerodynamic and structural damping, as well as gyroscopic effects due to the rotational nature of the system. The proposed model was applied to a specific example involving the Vestas V82 wind turbine. This turbine was analyzed under several historical earthquake records using the three components of motion. The analysis of the results revealed that in seismic regions some aspects of the tower design, specifically at the tower top end section, may be controlled by the combination of earthquake loads and mean steady wind loads rather than by the extreme wind load conditions.

RESUMEN

Recientemente la industria de la energía eólica ha visto un crecimiento substancial en muchos países industrializados. Históricamente, territorios con poca actividad sísmica ubicados al norte de Europa han sido los líderes en el uso de esta tecnología, pero ahora el mercado está creciendo en países con mayor actividad sísmica como los Estados Unidos, China e India. Esta situación hace necesaria la evaluación de la respuesta sísmica de las turbinas eólicas con el fin de mejorar la confiabilidad de estos sistemas bajo estas condiciones adversas. Esta disertación presenta el desarrollo de un nuevo modelo analítico para una turbina eólica de tres aspas en un eje horizontal. El modelo propuesto permite la evaluación de su respuesta sísmica y la posibilidad de que sufra algún daño estructural por plasticidad o por pandeo local. El modelo propuesto consiste de un sistema compuesto de múltiples cuerpos con 16 grados de libertad que considera la flexibilidad de las aspas en la dirección frontal y el movimiento torsional y de flexión de la torre. Las ecuaciones de movimiento del rotor fueron derivadas mediante las ecuaciones de Lagrange y luego acopladas con las ecuaciones de movimiento de la torre modelada con tres elementos de vigas. El modelo consideró el amortiguamiento aerodinámico y estructural, así como los efectos giroscópicos debido a la naturaleza rotacional del sistema. El modelo fue evaluado en un ejemplo que incluye la turbina Vestas V82. Esta turbina fue analizada bajo varios registros históricos de terremotos usando las tres componentes de movimiento. Del análisis de resultados se desprende que, en lugares de alta sismicidad, algunos aspectos del diseño de la torre, específicamente el diseño de la sección superior de la torre, pueden estar controlados por la combinación de cargas de terremoto y de viento promedio constante en vez de por cargas de viento extremo.

To my wife Adamaris and our children
Sofía Marie, Gabriel and Marisol

ACKNOWLEDGMENTS

Firstly, I would like to especially thank Dr. Luis E. Suárez, advisor and president of my graduate committee, for his important contributions throughout the development of this dissertation, as well as his opportune suggestion of this subject of investigation. I also wish to thank Dr. Javier A. Quintana, Dean of the School of Engineering, and Prof. Juan F. Martínez, Chancellor, both from the Inter American University of Puerto Rico (IAUPR), for providing me with the release time and financial support necessary for the completion of this work. I am also indebted to Profs. Eduardo Lay and Amilcar Rincón, former and current Chairpersons of the Department of Mechanical Engineering at IAUPR, respectively, for providing the flexibility to arrange my academic duties in order to successfully complete this project. I also extend my thanks to Dr. José A. Martínez, Dr. Miguel A. Pando, Dr. Ricardo R. López, and Dr. Mario A. Rivera, members of my graduate committee, as well as to Dr. Carlos U. Pabón, representative of the Graduate Studies Office, for their valuable suggestions on how to improve this investigation and in their reviews of the manuscript. Finally, I would like to acknowledge the encouragement and support of my lovely wife, Adamaris, who made many sacrifices during these years and during the preparation of this dissertation.

CONTENTS

LIST OF TABLES

LIST OF FIGURES

LIST OF SYMBOLS

$\{a_b\}$	vector of accelerations at the ground surface
A_b	blade root cross-sectional area
A_{be}	tower base cross-sectional area
A_i	average cross-sectional area of tower section i
A_T	rotor swept area
A_{te}	tower top end cross-sectional area
$[A(t)]$	periodic first order state matrix
$[B(t)]$	periodic matrix
c	damping constant
c_T	thrust coefficient
$c_1 \ldots c_4$	aerodynamic damping constants
$[C]$	global damping matrix
$[C_d]$	modal damping matrix
$[C_s]$	structural damping matrix
d_h	distance between the hub and tower top end center
E	tower linear modulus of elasticity
E_b	linear modulus of elasticity for the blade
F_{bi}	resultant normal force in the blade
F_c	centrifugal force in blade
F_{gi}	normal component of the blade weight
$(F_R)_{te}$	resultant shear force at tower top end
$(F_x)_{be}$	base shear force at tower in x direction

$(F_x)_{te}$	shear force at tower top end in x direction
$(F_z)_{be}$	base shear force at tower in z direction
$(F_z)_{te}$	shear force at tower top end in z direction
$[F]$	Floquet transition matrix
g	acceleration of gravity
G	tower linear shear modulus
h_h	hub height
h_t	tower height
I	equivalent moment of inertia of area at the blade root
I_a	axial moment of inertia of the hub
I_b	transverse moment of inertia of the blade; moment of inertia of area at the blade root
I_i	moment of inertia of tower at section i
I_t	transverse moment of inertia of the hub
I_{te}	moment of inertia of the tower top end section
$[I]$	identity matrix
$[I_b]$	principal moment of inertia of the blades
$[I_h]$	principal moment of inertia matrix of the hub
i	subscript index
j	$\sqrt{-1}$
J	polar moment of inertia of tower section
J_{be}	polar moment of inertia at tower base
J_{te}	polar moment of inertia at tower top end
k	stiffness constant, integer multiple constant
k_b	blade torsion stiffness constant

k_t	tower torsion stiffness constant
$[k_e]$	beam element stiffness matrix
$[K]$	global stiffness matrix
$[K_G]$	tower global stiffness matrix
l_e	tower section length
L_b	blade length
m	mass
m_b	mass of a blade
m_n	nacelle mass
m_r	total mass of the rotor
m_t	tower mass
$[m_e]$	beam element mass matrix
M_{bi}	resultant bending moment at the blade root
$(M_{bi})_e$	bending moment at the blade root in the edgewise direction
$(M_{bi})_f$	bending moment at the blade root in the flapwise direction
M_{mbi}	moment produced by gravity force at the blade root
$(M_R)_{te}$	resultant bending moment at tower top end
$(M_x)_{be}$	base bending moment at tower about x axis
$(M_x)_{te}$	bending moment at tower top end about x axis
$(M_z)_{be}$	base bending moment at tower about z axis
$(M_z)_{te}$	bending moment at tower top end about z axis
$M_{\theta_{bi}}$	moment on blade root due to thrust force
$[M]$	global mass matrix
$[M_e]$	mass matrix associated to earthquake acceleration
$[M_G]$	tower global mass matrix

n	number of blades
p_C	circumferential force intensity
p_T	thrust intensity
P_i	horizontal projection of phasor i
$[P(t)]$	time periodic matrix
q_i	generalized coordinate
$\{q\}$	first order state vector
Q_i	generalized forces
r	rotor radial coordinate; radius
r_b	blade root radius; tower radius at base
r_{be}	tower base radius
r_h	hub radius
r_{te}	tower top end radius
$\{\dot{r}\}$	vector of relative velocities of the tower top end with respect to the tower base
$\{r_h'\}$	position vector of the rotor center with respect to tower top end
$\{r_x\}$	vector of influence coefficient associated to x direction
$\{r_y\}$	vector of influence coefficient associated to y direction
$\{r_z\}$	vector of influence coefficient associated to z direction
$[R]$	constant matrix in Floquet theory
s_i	characteristic exponent i
$[S]$	diagonal matrix of characteristic exponents
t	time; wall thickness
t_b	tower wall thickness at base
T	kinetic energy; total torque in the rotor; yaw torque in the tower; time period

T_r	kinetic energy associated to the rotational motion of the hub and blades about their centers of mass
T_t	kinetic energy associated to the motion of the centers of mass of the hub and blades
$\{u\}$	vector of generalized coordinates
v_∞	steady wind speed
$\{v_b\}$	vector of ground velocities
$\{v_{bi}\}$	relative velocity vector of the blade center of gravity with respect to the hub
$\{v_h\}$	absolute velocity vector of the rotor center
V	potential energy
V_{bi}	resultant shear force at the blade root
V_c	shear force at blade root in the edgewise direction
V_{ei}	total shear force at blade root in the edgewise direction
V_{mbi}	shear force at blade root due to weight component
V_r	rotor potential energy
$[V]$	matrix of eigenvectors
$\dot{W}$	generator output power
x_c	coordinate of center of pressure of the blade
x_i	tower lateral translational coordinates
$\{x\}$	first order state vector
X_b	base displacement in x direction
Y_b	base displacement in y direction
z_i	tower fore-aft translational coordinates
Z_b	base displacement in z direction
α	ratio between hub radius and blade length

α_B	stress reduction coefficient
β	ratio between upper and base radius; constant used in buckling of cylindrical shells
δ	blade pre-cone angle
Δp_{Ti}	increment in thrust intensity over blade *i*
ϕ	Euler angle
ϕ_i	eigenvector *i*
$[\Phi]$	matrix of eigenvectors normalized with respect to the mass matrix
$[\Phi(t)]$	fundamental matrix
η	overall efficiency of the turbine
λ_i	characteristic multiplier *i*
ν	Poisson ratio constant
θ	Euler angle; phasor phase angle
θ_{bi}	blade *i* flap angle
θ_{xi}	tower flexural angles about *x* axis
$\theta_{y'}$	tower twist angle
θ_{zi}	tower flexural angles about *z* axis
ρ_a	air density
ρ	tower density
σ_{ai}	normal axial stress at blade root
σ_{bi}	bending stress at the blade root
σ_{cr}	critical local buckling stress
σ'_{cr}	corrected critical local buckling stress
σ_u	ultimate strength

σ_y	yield strength
$(\sigma_b)_{te}$	maximum bending stress at tower base
$(\sigma_b)_{te}$	maximum bending stress at tower top end
$(\sigma_{be})_{max}$	maximum normal stress at tower base
$(\sigma_{te})_{max}$	maximum normal stress at tower top end
τ_{be}	maximum transverse shear stress at tower base
$\tau_{i_{\max}}$	maximum shear stress at the blade root
τ_{te}	maximum transverse shear stress at tower top end
τ_u	ultimate shear strength
τ_y	yield shear strength
$(\tau_{be})_{\max}$	maximum shear stress at tower base
$(\tau_{te})_{\max}$	maximum shear stress at tower top end
$(\tau_{be})_{\max}$	maximum shear stress at tower base
$(\tau_{te})_{\max}$	maximum shear stress at tower top end
ω_i	angular velocity component of body principal axis *i*; modal frequency *i*
$[\omega]$	angular velocity matrix of the nacelle relative to the translating frame of reference at tower base
$\{\omega_{bi}\}$	angular absolute velocity vector of the blade *i*
$\{\omega_h\}$	angular absolute velocity vector of the hub
Ω	rotor angular speed
ξ_i	real part of characteristic exponent; modal damping ratio
ψ	blade 1 azimuth angle; Euler angle

CHAPTER 1: INTRODUCTION

1.1 INTRODUCTION

As prices of oil have increased in the last decade, new and reliable renewable energy technologies are emerging and becoming more popular. Other factors such as the contribution to global warming of traditional fossil-fuel based plants add to the call for clean energy sources. One of the most promising and realistic solutions to this problem are the wind turbine generators. For instance, the US Department of Energy expects that the wind power generation will reach the 20% of the national power capacity by 2030 (see DOE, 2008). In this direction, continuous efforts have been made by the wind industry to develop bigger and higher wind turbines to reach more and faster winds. A modern wind turbine can measure more than 100 m of blade rotor diameter, and 90 m height at the hub, generating more than 3 MW of power (see Malcolm and Hansen, 2006). The feasibility of constructing wind turbines of this size (or larger) depends in part on how good the analytical models are able to predict the dynamic behavior of the system. Another important factor that has restricted the increase in size is the development of light materials with better strength to weight ratios for the construction of the blades. The unsatisfactory structural properties of the materials employed in the blades are one of the reasons why the rotor-blade system has encountered many problems through the years, including catastrophic failures due to fatigue, buckling, and skin abrasion (e.g., Sutherland, 1999, Hermann *et al*., 2005, and GE, 2005). There is abundant literature dealing with the structural behavior of the blades due to wind and cyclic loads (e.g., Eggers *et al*., 1996; Hermann *et al*., 2005; Malcolm and Laird, 2003; and Hansen, 1995). A less studied aspect, probably due to the more complex dynamics, is the structural response of the complete system, including the tower, nacelle, and

blades under variable loads. It is surprising that before 2003 little documented evidence was found in attention to the effects of strong ground motions on these structures. What is even more surprising is that the principal standards used for wind turbine design did not provide any guidelines for seismic analysis until recent years. This point was not adequately considered even when, due to the extreme rise of oil prices in the 70's, hundreds of medium size wind turbines were installed in the US, which by 1987 were generating a total power capacity of 1600 MW, most of them in California, the highest risk seismic zone in the continental US (see Gasch and Twele, 2004).

There are some reasons that could justify the apparent lack of interest in the seismic assessment of these structures. One explanation is that researchers and practitioners during several decades, trying to make the wind power generation more feasible, were mostly focused in the reliability of the blades under wind pressure and cyclic fatigue loads. For years, the blades have been the wind turbine component with the largest number of failures (see Sutherland, 1999). Another possible reason is that historically most of the development done by the wind industry has come from countries in northern Europe in regions where the earthquake risk is very low and thus seismic analysis is not usually considered (see Prowell *et al*., 2008a). This situation probably has led to the idea that wind loads and fatigue cyclic loads are always the driving design loads on wind turbines and hence, the seismic analysis can be neglected (Alcalde, 2004). But this unverified conception is in need of a rigorous study to support it. In the case of the blade design, this idea could be validated by the study of Hong (1984), which concluded that for constant rotor speed the response of a wind turbine blade was very stable under normal operating conditions and that the effect of wind turbulence on moment responses at the blade was greater than that of an earthquake. He also concluded that turbulence was likely the main cause of fatigue failure of wind turbine blades. However, the seismic assessment to other components of

the wind turbine, such as the tower sections, is still incomplete. Therefore, this dissertation intends to derive an analytical model of a full horizontal axis wind turbine subjected to an earthquake ground motion at its base and use it to provide an understanding of the magnitude of the forces induced in the entire structure by a strong seismic event.

1.2 COMPONENTS OF A WIND TURBINE

To understand how an earthquake can affect a wind turbine, it is important to have a basic knowledge of the principal components of this type of mechanical system and their functions. This section offers a brief description of a typical horizontal axis wind turbine (HAWT). For detailed information the reader is advised to consult the books by Burton *et al.* (2001) and Gasch and Twele (2004).

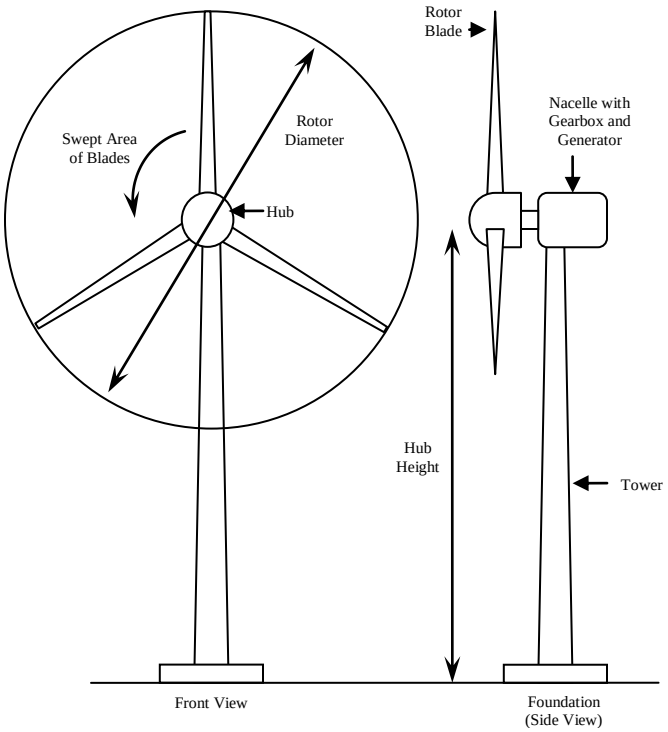

Fig. 1-1: Scheme of a typical wind turbine (from Energy Systeme Nord, n.d.)

The HAWT are complex systems composed of several mechanical, electrical, and structural parts. These can be grouped into four principal components: the blades, the rotor hub, the nacelle, and the tower, as illustrated in Fig. 1-1. The number of blades in large rotors varies from one to three, but nowadays three blades is the more common arrangement due to its symmetry and visual appearance. The blades are typically constructed with composite materials containing glass or carbon fibers. The ends or roots of the blades are attached to the rotor hub by means of steel studs and nuts.

There are several types of rotor hubs depending on the degrees of freedom that they provide to the blades. Figure 1-2 shows different hub designs and their respective relief of rotor shaft and blade roots. The fixed rotor hub configuration is shown in Fig. 1-2.A. This design does not allow any flapwise and pitch motion in the blade roots. Therefore, the blade roots must be able to resist the bending moments caused by the wind. The next type is known as active pitch control (Fig. 1-2.B) and it is one of the preferred rotor hub types (see Gasch and Twele, 2004). It permits the rotation of the blades around the radial blade axis, thus changing the angle of attack of the blade profile depending on the velocity of the wind. The pitch control helps to regulate the speed of the rotor in normal wind conditions. Also, for extreme wind velocities, as it may occur during storms, the blade can be stalled eliminating the potentially destructive effects of the larger wind forces. The flapping hinge rotor (Fig. 1-2.C) relieves each blade root of all bending moments in the flapwise or out-of-plane direction. Figure 1-2.D shows another type of rotor hub known as the teetered hub. It hinges the rotor hub and allows for small rotational motion of the blade system out of the plane of rotation. This configuration reduces the out-of-plane bending at the root of the blades during operation. Finally, there are hubs that combine pitching with teetering, thus gaining the benefits of both systems.

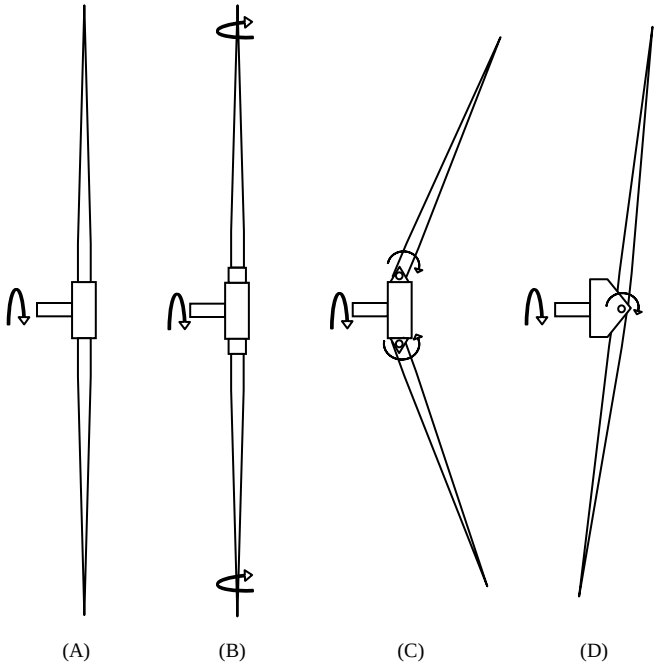

Fig. 1-2: Different hub designs: (A) fixed, (B) pitch and fixed, (C) flapped blades, and (D) teetered (from Gasch and Twele, 2004)

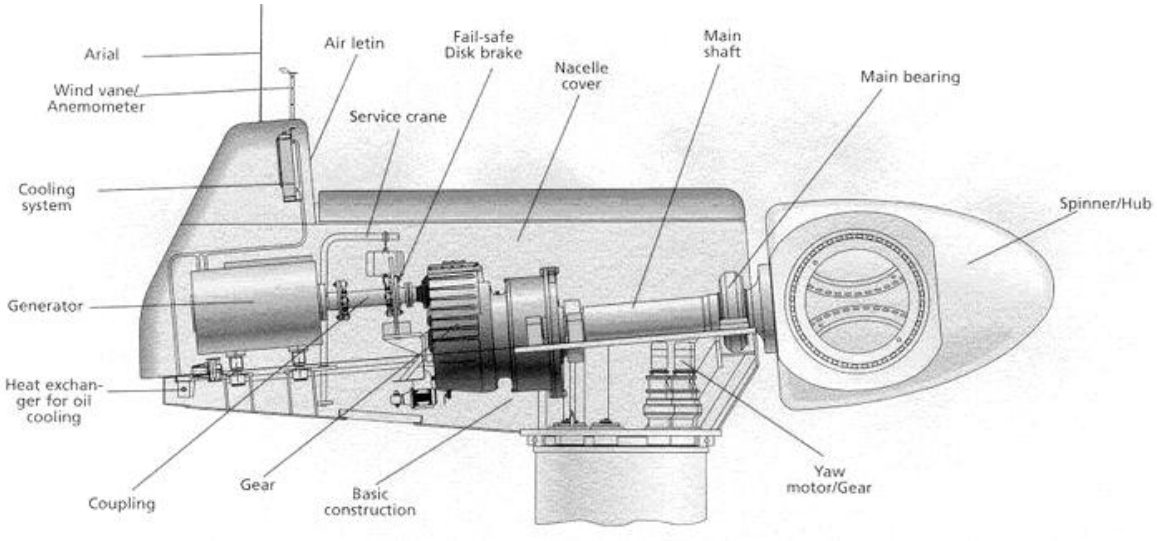

Fig. 1-3: Components inside the nacelle (from Fabricating & Metalworking Magazine, n.d.)

The nacelle is the machine room at the top of the tower that contains the gearbox system, the generator, and all the control systems of the turbine, as it can be observed in Fig. 1-3. The nacelle also contains the low speed shaft to which the rotor hub is connected. The low speed shaft transmits torque to the gearbox system and then to the generator. In general, there are two types of generators: the synchronous generator and the induction generator. The synchronous generator permits a variable speed in the rotor and a constant torque in the rotating components. On the other hand, the induction generator controls the rotor speed to an almost constant speed, but it produces a variable torque in the rotating parts. The nacelle is coupled to the tower by means of the yaw mechanism that permits directing the nacelle toward the wind. The yaw mechanism consists of an inner gear and several electric motors engaged with pinions. When the nacelle is directed toward the wind, the brake system is applied and the nacelle becomes completely fixed to the tower.

The tower is typically constructed of steel, although reinforced concrete towers have been used in special applications. The steel towers are erected by connecting two to four cylindrical sections with circular flanges until reaching the required height. A tapering conical design is commonly used for tubular towers. The length of each tower section ranges between 20 to 30 meters, and the wall thickness in the upper section is about 10 mm (see GE, 2005). The tower is anchored to the foundation system by means of a circular steel flange previously cased into the concrete foundation (GE, 2005). If the bearing capacity of the soil is adequate, the use of a raft foundation is the common alternative, whereas pile foundations are used when the soil near the surface has poor bearing capacity. Fig. 1-4 shows a picture of a first tower section being hoisted into position. Notice in this figure the circular flange at the bottom of the tower that will be bolted to the foundation system.

Fig. 1-4: The first tower section is hoisted into position (from Billings Gazette, n.d.)

1.3 LITERATURE REVIEW

Design Standards

There are several important standards that contain guidelines for the design of wind turbines. Among them, it is important to mention the contribution of the Germanischer Lloyd's (GL) first publication written in 1986, and last edited in 2003 with periodic revisions: *Guidelines for the Certification of Wind Turbines*. Other influential standards were published in The Netherlands (NEN 6096, Dutch Standard, 1988) and Denmark (DS 472, Danish Standard, 1992). Perhaps the

most widely used standard, adopted currently by several nations, is the *Wind Turbines - Part 1 Design Requirements*, with the number IEC 61400-1 from the International Electrotechnical Commission (2005). This standard was first published in 1988 and has been continuously revised and updated since then.

In general, the standards provide guidelines and procedures to determine the mean wind speed and gust speed and how they should be used in the structural design of the wind turbine components such as blades, tower, and foundations. They also specify design load combinations for ultimate load and fatigue load analyses. In addition, they discuss control and protection systems, electrical systems, and installation, operation, and maintenance. The sources of loading typically taken into account for ultimate and fatigue analyses are: aerodynamic loads, gravitational loads, inertia loads (including centrifugal and gyroscopic effects), and operational loads due to the actions in the control system such as braking, yawing, pitching, generator disconnection, among others. Although the standards in the past did not consider the effects of earthquakes in the turbines, recently, their latest revisions have incorporated simple processes for estimating seismic loading based on one degree of freedom models and site design response spectra. In addition to these standards, there are municipal or national permit regulations based on codes for engineered structures or machines (i.e., building codes, electrical or mechanical codes) that consider the earthquake loads, and thus design of wind turbines must comply with these other applicable permit regulation. However, the wind turbine designer should apply caution when using these permit regulation codes directly to wind turbines since normally they are based on seismic studies performed in buildings where inelastic behavior is regularly permitted in the engineered structures they regulate. It is a guideline that to ensure reliable

operation for the design life of the turbine, inelastic behavior for wind turbines is not allowed (see Germanisher Lloyd, 2003).

Technical Literature

Reports of failures of wind turbines during an earthquake are not found in the technical literature at the present day (see Prowell and Veers, 2009). Certainly this is a good indicator that these structures are likely able to withstand the seismic motions and loads without catastrophic failure. For years the seismic analysis in the design of large wind turbines has received little attention, probably due to the opinion (which could be realistic) that the wind load cases always drive the design parameters of the turbine (Alcalde, 2004). This speculative idea can be partially supported by a study of Hong (1984), who compared the effects of wind turbulence and earthquake loads based on fatigue failure criteria for a wind turbine blade model, and found that the effects of wind turbulence are more detrimental than earthquake loads. However, Hong based his study in the dynamics of just one blade and ignored the behavior of a multi-blade rotor as a whole unit and of the tower during an earthquake.

Because the wind turbines are becoming larger, heavier, and more expensive, it is necessary that any design uncertainty can be reduced. For this reason the idea of taking for granted that earthquake loads can be ignored in the design of wind turbines because the wind loads drive the design parameters needs of a rigorous supporting study. For instance, the gyroscopic loads at the tower top end could be amplified by the flexibility of the tower and its fore-aft and twisting motions during an earthquake. The consequences of these additional loads should be evaluated since there will be a demand increase in the supporting structure of any rotational part. Narayana

(1999) commented about the induced effects of gyroscopic moments on a small scale tilt-up wind turbine when it tries to tilt up due to winds exceeding the rated conditions. He states that in this situation, the dominant tilt-up rotation of the wind turbine in the vertical plane can cause a deviation in the horizontal plane due to gyroscopic effects. Due to this deviation, the wind turbine may come back to its previous position as a consequence of the change in the apparent wind speed or change of wind direction, thus producing a detrimental oscillatory motion. Bourke *et al.* (2004) recommended undertaking a thorough research about the noxious effect of the gyroscopic loads on the gearbox and bearings of a wind turbine during fast yaw motions. In their preliminary study, the equations to determine the reaction loads on these components were derived. Although it was not accomplished, they proposed to evaluate possible solutions for diminishing the magnitudes of the reaction loads by changing the position of the centers of mass of different components in the rotor shaft.

In spite of the lack of studies dealing with the dynamic behavior of an entire HAWT structure during seismic events, there are important contributions on the dynamic response of the turbines due to other loads such as wind fluctuations, ocean wave impacts in offshore wind farms, tower shadow excitation, or mass imbalance in the rotor. All of them are of particular interest because they make use of analytical or numerical techniques to obtain the dynamic parameters such as natural frequencies and modes of the full system. The most relevant contributions are summarized in the next paragraphs.

One of the first studies dealing with the dynamic response of a wind turbine was carried out by Carne *et al.* (1982). In their study, a finite element (FE) procedure was developed to model a Darrieus vertical axis wind turbine (VAWT) at the Sandia National Laboratories. The researchers obtained the equations of motion of the system by considering special phenomena

that occur on rotating bodies such as geometric stiffening and centrifugal and Coriolis effects. These phenomena affected the stiffness and damping matrices, respectively. The researchers neglected factors such as aeroelastic effects and structural damping because they considered them of less importance. The FE model used consisted of beam elements and concentrated masses to model the blades and the structure. The eigensystem obtained had a Hermetian form due to the skew-symmetry in the damping matrix coming from the Coriolis effect. Instead of developing new software for the eigensolution of the equations of motion, the authors used the NASTRAN code (see NEi, 2010) and modified the stiffness and damping matrices to include the rotational effects. The NASTRAN code condensed the matrices by applying techniques such as the Hessenberg and Guyan reductions to reduce the original model to sixty degrees of freedom. The model was compared with experimental results obtained at the Sandia 17-m research VAWT and excellent agreement was obtained between predicted and measured modal frequencies.

Lobitz (1984), one of the co-authors of the preceding study, continued the research and included the aeroelastic effects but now in a full dynamic model of a HAWT. The model took into account the flexibilities of the tower and blades in the flapwise and twisting directions. The turbulent nature of the wind was modeled by stochastic wind increments affecting the aerodynamic load computation. This author also used the NASTRAN computer code (NEi, 2010) to develop the mass, stiffness, and damping matrices. For the purpose of obtaining the matrices, a fixed coordinate system was used for the tower. A rotational coordinate system that moved at the operational speed of the turbine about an axis fixed in space was used for the rotor. The origins of both coordinate systems were fixed at the initial hub location. Rotational frame effects such as Coriolis and centrifugal forces were also included. The aerodynamic loads were computed using interference factors predicted by PROP-PC, a previously developed computer

code (Tangler, 1987). The final equations of motion were solved in the time domain using the implicit Newmark-Beta integrator. To validate the model, a two-bladed teetered-hub HAWT was modeled with 5 nodes per blade and 5 nodes in the tower. The model included lateral tower damping, yaw, and torsion springs and dampers to model the gearbox and generator. The results showed good agreement (errors of 5%) between the analytical natural frequencies and the experimental measured data. Somewhat larger discrepancies (errors about 10%) were found in the prediction of the frequencies of the symmetric flapwise bending mode and the symmetric edgewise mode. Although it was not pursued in the paper, the author suggested fine-tuning the model for a more accurate prediction. Of special interest was the fact that the frequency normalized by the rotor operational speed for the symmetric flapwise mode was very close to 4P (where P means *per rotor revolution*), which is an integer multiple of the rotor operational speed. Any periodic excitation originated by the revolving rotor, such as tower shadow effects, blade gravity loads or mass imbalance, for instance, could amplify the dynamic response of the blades. Two wind mean speeds of 20 and 27 mph in steady and turbulent conditions were analyzed in the model. For steady wind conditions the response of the tower was found to be predominately governed by gravity loads exciting the cyclic cantilever edgewise bending mode of the blades, but when the stochastic wind turbulence was incorporated, the flapwise bending mode was the dominant one.

Oscar and Paez (1988) used the model developed by Lobitz (1984) incorporating a finite element analysis to model an offshore support for a HAWT loaded by random waves. The wind industry is very interested in exploring this type of construction since it has the advantage of producing continuous wind energy at the ocean without the visual impact that wind farms cause on land. However, it has the disadvantage of being in a more hostile environment and it

demands a more complicated foundation system design. A wind turbine exposed to the ocean will be additionally loaded by marine currents and waves on the support structure. These loads could be considered somewhat similar to the seismic loads since both cause excitations in the tower base. In general terms, the derivation and solution of the equations of motion were almost similar to those employed by Lobitz (1984), with the exception of the inclusion of the new submerged structural platform and the ocean wave loads. The random wave loads were established as function of water particle velocities and accelerations acting perpendicular to the structural members and were correlated to the wind speed. The parallel components were neglected. These functions were incorporated into the Morison's equation that includes the effect of drag due to water particle velocities and an inertia term due to water particle accelerations. Point load time histories were integrated over the length of the submerged structural members and redistributed to the nodal points. It must be pointed out that the wind turbine platform used by the authors was very stiff and the wave induced response was very small. Therefore, no useful inferences could be done to predict the behavior of the turbine in the case of an earthquake.

Malcolm (2002), Stol *et al.* (2002), and Bir and Stol (1999) examined the modal behavior of a HAWT using transformation techniques for the periodic terms in the equations of motion of the system. Malcolm derived the equations for a 3-bladed wind turbine as a combination of the equations of motion of three subsystems: the tower, the hub, and the three blades. He considered aerodynamic loads but neglected the structural damping. The principal contribution of Malcolm was the use of the Coleman transformation to remove the periodic terms produced by the rotational motion of the blades. The Coleman transformation was first used in the analysis of helicopter rotors moving at constant angular velocity. This transformation changes the rotational

frame of reference of the blades in terms of a fixed one. The technique requires to solve the eigenvalue problem of the stationary system and the use of a FE code (the author used ADAMS) to extract the stiffness contribution of the centrifugal forces.

Bir and Stol (1999) and Stol *et al.* (2002) derived the equations of motion for a two-bladed HAWT. The full model contained 7 degrees of freedom that allowed tower motion, nacelle yaw, hub teeter, and blade flap. The authors considered the wind turbine as an assemblage of rigid bodies interconnected by springs, dampers, and pins. Although, the authors considered it as a simple model, it retained the essential physics of a HAWT. Due to the inertial asymmetry of a two-bladed rotor, time dependent terms appeared in the equations of motion, thus precluding the use of the Coleman transformation. The author used the Floquet theory to transform the periodic terms into time invariant terms. A complete explanation of the Floquet theory can be found in the book by Johnson (1994). The essence of the Floquet theory is to convert the second-order equations of motion to a first-order state-space form composed by a state transition matrix multiplied by a state vector. The state transition matrix, that contains periodic terms, is then decomposed into a periodic matrix and a matrix exponential of a constant matrix. The solution of the eigenvalue problem, often referred to as Floquet modes or Floquet exponents, comes from the analysis of the exponential matrix. The authors suggested that the computation of the state transition matrix will be overwhelming if the number of degrees of freedom exceeded about 50. In a previous paper, Stol and Balas (2001) used the same model to design a full-state feedback controller to control the blade pitch angle based on periodic control instead of constant gain.

The dynamic response of the previous models was calculated by means of time domain analysis which usually leads to large computational efforts. Although for some problems frequency domain analysis can be much faster than time domain simulations, due to the

nonlinearities caused by the rotation of the blades, the use of frequency domain methods is rigorously precluded. Nevertheless, some authors have successfully implemented frequency domain techniques in the response of certain types of wind turbines. Sorensen *et al.* (1995) developed a frequency domain model for a three or more bladed HAWT with flexible blades and tower, stiff hub (not teetering), fixed yaw motion, and constant rotor speed. The tower, low shaft, and blades were modeled as beam structures in terms of stiffness, damping, and inertia quantities whereas the generator was modeled as an induction generator described in terms of damping and inertia quantities. The equations of motion were solved using the modal decomposition technique in which several mode shape functions were assumed. The model considered three mode shapes for the tower (two backward and one sideway), one tower torsion mode, one shaft torsion mode, one generator mode, and two modes per blades (one flapwise mode and one edgewise mode). The structural azimuth-dependent variables contained in the equations of motion, i.e., masses, damping and stiffness, and the aerodynamic loads were decomposed into sums of harmonics in the constant angular frequency of the rotor. Thus, the nonlinear relations in the equations of motion were transformed into linear relations between the amplitudes of the harmonics of the variables. These equations were in turn transformed by means of the Fourier transform. Two HAWT were evaluated using the frequency domain method and the results were compared with a well tested time domain code using similar models. Both methods showed to be in very good agreement, but the frequency domain method was several hundred times faster than the time domain code.

Borg and Kirchhoff (1998) studied the effects of a mass imbalance in the rotor of a three-bladed HAWT. The authors considered that a perfectly balanced three or more bladed rotor can be modeled as a flat circular disk. Thus, the rotor was modeled as a rigid disk with mass. The

mass imbalance was considered by introducing a small eccentric lumped mass. The system consisted of 2 degrees of freedom measuring the rotation of the reference blade (azimuth) and the rotation of the nacelle (yaw). In spite of the simplicity of the model, a pair of coupled nonlinear differential equations was obtained. As expected, the equations contains the centrifugal and gyroscopic terms affecting the stiffness and damping matrices, respectively. For simplicity, the yaw motion was considered small. The authors also considered the aerodynamic effects due to the wind. The numerical solution of the equations was obtained by means of a perturbation technique and the Laplace transform. The solution of the perturbation technique was related to the number of terms used in the power series of the perturbed parameter. In their analysis the authors considered up to third order terms. As a result, the steady-state solution predicted that 1P, 2P and 3P frequencies are caused by the mass imbalance. The solution was applied to obtain the electrical power output from the turbine. Since it is relatively easy to measure the output power of a turbine generator, the authors proposed to use the response of the generator to diagnose an unbalanced turbine and determine the value of the unbalanced mass and its position. A practical solution to correct the mass imbalance (not explained here) was proposed in another paper by Borg and Kirchhoff (1997). The authors validated the model with data from tests on a HAWT from the National Renewable Energy Laboratory (NREL). They found that the contribution of the mass imbalance to the 1P component in the power fluctuation was the most influential. It is therefore hypothesized that the majority of the 2P and 3P contributions present in field data result from an aerodynamic effect rather than from a mass imbalance effect.

Although the study did not deal directly with wind turbines, Suárez *et al*. (1992) developed a FE based method to obtain the seismic response of rotating machines at grade level. The paper

provided the development of the equations of motion considering base excitations including three translational motions and three rotational motions. The developed equations of motion took into account the flexibility of the shaft. The shaft was modeled as a series of FE that considered flexural and shear deformations. The model could easily incorporate the use of a flexible pedestal in which the rotating machine is supported, thus resembling a HAWT. One limitation of the model was the use of rigid disks to model the rotating mass lumped to the shaft. The model works well for machines such as electric motors, generators or combustion turbines that have large core rigidities, which was the object of the authors' study. In the case of a HAWT, the flexibility of the blade rotor is significantly greater and therefore it is often considered in its dynamical analysis. Nevertheless, the paper gives an insight into the development of the equations of motion using a variational approach and their solution in the time domain.

In recent years, during the development and completion of this dissertation, a small number of studies related to wind turbine seismic analysis have appeared in the technical literature. Although not used at all in the development of the proposed model, they are relevant for future studies and deserve to be mentioned here. They were also summarized in the review report of Prowell and Veers (2009) on the existing literature in the subject and they will be presented in the next paragraphs. Additionally, the review report gives an introduction to seismic hazard as applied to wind turbine structures and describes the existing design methods. The report concludes that until extensive seismic studies will be performed on wind turbines, seismic loading should be routinely considered as part of the required load combinations in regions with high seismic risk. The authors recommended testing, both nondestructively and destructively,

wind turbines and documenting seismically induced damage to provide valuable data to validate and refine analytical modeling techniques.

Taking a more general and complex approach than the adopted in this dissertation, but without considering the earthquake loads, Zhao *et al*. (2006) developed a multi-body model for a wind turbine. They used cardanic joint beam elements to discretize the wind turbine rotor into a multi-rigid-body system consisting of rigid bodies, springs, and dampers. They also considered the flexibility of the tower, the flapping motion of the blades, as well as their lag bending and torsion motions. Aerodynamic damping was not introduced into the model and only the dynamics of the system in operation was examined. Later on, Zhao and Maisser (2006) improved the previous multi-body model to include wind loads and earthquake loads. Also, they considered the soil-structure interaction and evaluated the tower response, but assuming a rigid rotor (i.e., without flexible blades). The response of a 1.5 MW wind turbine subjected to a wind mean velocity of 10.16 m/s and an earthquake record with a PGA of 0.06g was obtained. It revealed that the induced earthquake loads and moments in the tower base were negligible. However, a complete understanding of the vulnerability of the structure under stronger earthquakes was not provided because the accelerogram they used contained a very low PGA.

One of the most commonly used modeling software programs in the wind industry is known as GH Bladed developed by Garrad Hassan and Partners, Ltd (GH Bladed, 2010). Recently, under demand for estimating the loading at seismically active sites, this software was upgraded with a seismic module containing two methods for simulating seismic loading (see, Witcher, 2005). One of the methods (similar to the one that was adopted in this dissertation) is based on the use of recorded acceleration time histories. The second method uses an iterative procedure to produce an artificial acceleration record based in a specified design response spectrum. Since

GH Bladed is a commercial software the author is more involved in presenting an overview of the capabilities of the program rather than giving a detailed derivation of the analytical model used. However, the author presents some preliminary results for loading of a 2 MW wind turbine with a rotor diameter of 80 m and a tower of 60 m simultaneously subjected to earthquake and wind loads. The author found that the base moment demand obtained by using analytic techniques in the time domain are in agreement (there are differences of 2.9%) with the results obtained by using the traditional simple design response spectrum method (frequency domain) for an operating turbine. Another case was considered in which the turbine rotor was stationary and the turbine was subjected to earthquake and wind loads. This scenario resulted in an increase of 79% in the moment demand for the time domain simulation than that from the frequency domain simulation. The authors believed that this variation came from the difference in damping between the operating and the stationary state, which was not captured by the frequency domain simulation. They also stated that by conducting the seismic analysis in the time domain, the correct aeroelastic interaction of the dynamic motion of the wind turbine with the wind loading acting on the blades can be modeled. However, their study did not allow the reader to obtain clear conclusions about the importance or necessity of considering seismic loads in the design of wind turbines.

In November 2005, researchers at the University of California, San Diego conducted a full-scale test on a 65 kW turbine with the objective to obtain the lateral damping ratio of the structure. The turbine was shaken perpendicular to the axis of the rotor (i.e., lateral tower motion only) with a seismic record containing a PGA of 0.15g. The results, published by Prowell *et al*. (2008b), showed that the earthquake record predominantly excited the first mode of the structure. They also found that the first lateral mode had a damping ratio of less than 1%, which was much

smaller than the typical values encountered in buildings and therefore, smaller than the criteria in which building codes are based upon. It is important to notice that the experiment was conducted with a stationary rotor and that aerodynamic damping was not evaluated. The authors recognized the importance of these preliminary results as an initial step of a series of experiments for developing a mature understanding of the impact of earthquakes on wind turbines; however, further work in this subject is still required.

1.4 SCOPE

This study examined the dynamic response of the main elements that comprise typical three-bladed HAWT when their foundations were subjected to earthquake-induced ground motions. The first step consisted to derive the equations of motion for three-bladed horizontal axis wind turbines with tubular steel towers subjected to multi-component ground motions. The dynamical system was simplified by considering constant rotor speed, deterministic mean wind conditions parallel to the rotor axis, and a fixed rotor hub. The model accounted for the flexibility of the tower in bending, as well as twisting. It was assumed that the tower was infinitely rigid in the axial direction. In addition, the flexibility of the blades was considered only in the flapwise direction. The main rotor shaft was considered rigid for bending and torsion deformations. The soil-structure interaction was not being accounted for in the present study.

The highly non-linear analytical model was analyzed in the time domain using a numerical method such as the Runge-Kutta integration scheme or any other available in the ordinary differential equations solvers of MATLAB.

The earthquake ground motion was represented by means of acceleration records from historical earthquakes. The three components of the ground motion were considered in the study. The accelerograms were selected among those historically used for seismic evaluation in Puerto Rico, such as El Centro and Taft records. As supplement, the Castaic and GIC records obtained during the earthquakes of Northridge in 1994 and San Salvador in 1986, respectively, were used since recent studies reveal that they can also be comparable to expected earthquakes affecting the southwestern region of Puerto Rico.

The study evaluated possible damages caused by the ground motions on the blade roots, tower section couplings, and tower base. No attempt was made to analyze whether the turbine could work properly during the earthquake event (this is a very complicated problem that calls for an experimental study). Moreover, the nonlinearities considered were limited to those that arose from the kinematic effects only. In other words, no inelastic behavior of the structural system was considered.

1.5 OBJECTIVES

The goal of the dissertation is to study the seismic response of a full horizontal axis wind turbine, a topic that has been little addressed in the published literature. More specific objectives are:

a. To derive the equations of motion of a full HAWT accounting for flexibilities in the blades and tower, and for aeroelastic and gyroscopic effects.

b. To determine the seismic response under different earthquake scenarios using time-domain numerical methods.
c. To evaluate the importance of considering non-linear terms in the equations of motion and see if they could be linearized without affecting the accuracy of the analysis.
d. To provide an assessment for the likelihood of yielding or buckling failure of the tower or damage of the blades.

1.6 METHODOLOGY

The methodology followed to accomplish the objectives of this research can be summarized in the following steps:

a. Develop the analytical model of an operating three bladed HAWT in terms of geometric and dynamic parameters. Due to the complex dynamics of the problem, it is convenient to start with a simple HAWT model with rigid blades and flexible tower and gradually increase the complexity by adding more degrees of freedom to represent the blade flexibility.
b. Obtain the drawings and specifications of at least one HAWT to get the required data and properties to build a realistic model.
c. Write a computer code in MATLAB to obtain the response of the HAWT system to the three translational components of acceleration time histories of several

earthquakes typically used for seismic evaluation of civil structures in Puerto Rico.

d. Assess the dynamic stability of the response of the operating, as well as the modal frequencies and mode shapes of a HAWT by evaluating the eigenvalue problem obtained from the Floquet theory.
e. Perform a study to evaluate the contribution of different terms in the equations of motion and eventually propose modifications to reduce the complexity of the equations.
f. Evaluate the stresses on different locations of the structure such as the tower base, blade root, and nacelle support to predict possible failures based on yield strength, ultimate strength or local buckling criteria.
g. Propose remedial solutions if the HAWT appears to be vulnerable or susceptible to damage due to typical design earthquake loading.

CHAPTER 2: EQUATIONS OF MOTION OF THE WIND TURBINE MODEL

2.1 INTRODUCTION

The proposed HAWT is modeled as a three-rigid-hinged blades and hub system rotating at constant angular velocity Ω in a rigid shaft of negligible mass attached to a flexible tower as shown in Fig. 2-1. The base of the tower has three translations (X_b, Y_b, and Z_b) referred to an inertial frame (X, Y, Z). A translating (x, y, z) system of axes is fixed to the base of the tower. In order to describe the translational motion of the center of mass of the rotor, a translating and rotating system of axes (x', y', z') is attached to the tower top end with the z'-axis along the longitudinal direction of the shaft. This set of axes moves with the rotor in the yawing and fore-aft rotations but does not spin with the shaft. Finally, other translating and rotating sets of axes (not shown in the figure) are fixed to the center of the hub and to the blade hinges to describe the rotational motion of the rotor and the flapping motion of each blade. These sets of body axes rotate at the same absolute angular velocity than the rotor and are directed towards the principal axes of each body.

Initially, the rotor axis is parallel to the base and the blades are placed in the vertical plane (i.e., no pre-cone angle is included). The blade number 1 is initially oriented in the positive (horizontal) x'-axis, so blades number 2 and 3 are 120^o and 240^o counterclockwise from

the *x'*-axis, respectively. All rotation angles, with the exception of the flapping angles of the blades, are considered positive following the right-hand rule. The wind turbine is analyzed considering a steady operating state in which all generalized coordinates have zero initial values. Thus, the forthcoming solutions correspond to motions about an operating pre-stressed state of its components.

To simplify the development of the model we will derive the equations of motion of the rotor and the tower in a separate fashion and finally bring them together. The equations of motion of the rotor will be obtained using a variational formulation such as the Lagrange equations. This formulation requires obtaining the kinetic and potential energy of the system and the virtual work of any non-conservative force.

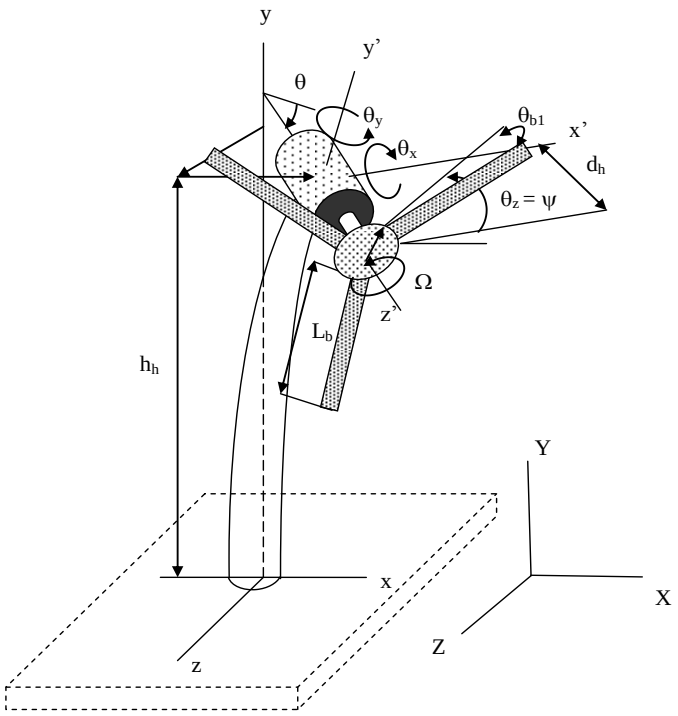

Fig. 2-1: Wind turbine analytical model

2.2 ROTOR KINETIC ENERGY

The wind turbine rotor is modeled as a multi-body system composed of four rigid bodies: the hub and the three blades. The hub has similar inertia properties than that of a thin circular disk and each blade is considered as a slender rod. From the analytical model shown in Fig. 2-1, the kinetic energy of the rotor can be written as the sum of the energy denoted by T_t associated to the motion of the center of mass of each body plus the energy associated to the angular rotations of the bodies denoted by T_r.

The first part of the kinetic energy T_t is made up of three components: one corresponding to the absolute translation of the complete rotor system, another associated to the product of the hub velocity and the linear momentum of the blades relative to the hub, and the last one corresponding to the motion of the centers of mass of the blades with respect to the center of the hub. It can be expressed in matrix form as

$$T_t = \tfrac{1}{2} m_r \{v_h\}^T \{v_h\} + \sum_{i=1}^{3} m_b \{v_h\}^T \{v_{bi}\} + \tfrac{1}{2} \sum_{i=1}^{3} m_b \{v_{bi}\}^T \{v_{bi}\} \tag{2-1}$$

where m_r is the total mass of the rotor (i.e., including the hub and the three blade masses) and m_b is the mass of a blade. The vector $\{v_h\}$ contains the absolute velocity components of the center of mass of the hub and can be defined as

$$\{v_h\} = \{v_b\} + \{\dot{r}\} + [\omega]\{r_h'\} \tag{2-2}$$

where the elements of the vectors $\{v_b\}$, $\{\dot{r}\}$, and $\{r_h'\}$ are defined, respectively, as

$$\{v_b\} = \begin{Bmatrix} \dot{X}_b \\ \dot{Y}_b \\ \dot{Z}_b \end{Bmatrix}; \quad \{\dot{r}\} = \begin{Bmatrix} \dot{x} \\ 0 \\ \dot{z} \end{Bmatrix}; \quad \{r_h'\} = \begin{Bmatrix} 0 \\ 0 \\ d_h \end{Bmatrix} \tag{2-3}$$

The distance d_h is measured from the hub center of gravity to the tower center axis. The skew-symmetric matrix $[\omega]$ corresponds to the angular velocity components of the rotating system (x', y', z') relative to the translating frame of reference (x, y, z) and is expressed as

$$[\omega] = \begin{bmatrix} 0 & -\dot{\theta}_{z'} & \dot{\theta}_{y'} \\ \dot{\theta}_{z'} & 0 & -\dot{\theta}_{x'} \\ -\dot{\theta}_{y'} & \dot{\theta}_{x'} & 0 \end{bmatrix} \tag{2-4}$$

The vectors $\{v_{bi}\}$, with i from 1 to 3, required for the second and third term in equation (2-1), contain the relative velocity components of the center of mass of each blade as viewed by a rotating observer fixed in the hub. They are defined as

$$\{v_{bi}\} = [\omega_{hi}]\{r_h\} + [\omega_{bi}]\{r_b\} \tag{2-5}$$

where the position vectors $\{r_h\}$ and $\{r_b\}$ are defined as

$$\{r_h\} = \begin{Bmatrix} r_h \\ 0 \\ 0 \end{Bmatrix}; \quad \{r_b\} = \begin{Bmatrix} \frac{L_b}{2} \\ 0 \\ 0 \end{Bmatrix} \tag{2-6}$$

where r_h is the hub radius and L_b is the length of the blades. The matrices $[\omega_{hi}]$ and $[\omega_{bi}]$ are also skew-symmetric matrices with forms similar to equation (2-4). They contain the absolute body angular velocities at the blade hinges and at the blade centers of mass, respectively.

Before proceeding with the definition of these angular velocities, it is necessary to mention an important characteristic of rotational motion in space. When large rotations are present and contrary to problems involving planar motion, body angular velocities in three-dimensional space cannot be defined as the time derivatives of rotations about any set of orthogonal axes since their integration does not correspond to the true orientation of a body in

space, (see Meirovitch, 1988). To describe the orientation of the rotor correctly it is necessary to use a different set of three independent rotations. One of the most used set consists of the Euler's angles θ, ϕ, and ψ as shown in Fig. 2-2. These rotations take place about a triad of axes that do not produce an orthogonal system of axes.

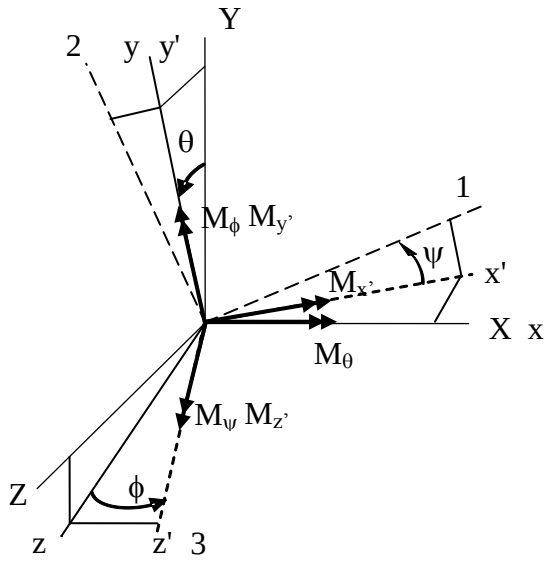

Fig 2-2: Coordinate system used to describe motion of the rotor

Fig. 2-2 shows that the rotation θ is measured about the *X*-axis, corresponding in Fig. 2-1 to the angle between the rotor shaft and the *x*-*z* plane. The rotation ϕ is measured about the *y*-axis, and ψ is the rotation of the system about the *z'*-axis. Thus, it can be shown that the time derivative vector $\dot{\phi}$ is perpendicular to $\dot{\psi}$ and $\dot{\theta}$; however, these last two vectors are not perpendicular to each other. If a set of absolute body angular velocities referred to the body

principal axes (*1*, *2*, *3*) is needed, we should sum the orthogonal projections of $\dot{\theta}, \dot{\phi}$, and $\dot{\psi}$ onto each of the axes of the (*1*, *2*, *3*) system. These expressions in terms of the Euler's angles are:

$$\begin{aligned} \omega_1 &= \dot{\theta}\cos\phi\cos\psi + \dot{\phi}\sin\psi \\ \omega_2 &= -\dot{\theta}\cos\phi\sin\psi + \dot{\phi}\cos\psi \\ \omega_3 &= \dot{\theta}\sin\phi + \dot{\psi} \end{aligned} \tag{2-7}$$

In the evaluation of the equation (2-5), the angular velocities at the blade hinges and at the blade centers of mass are referred to its own set of principal body axes, so a coordinate transformation is required to express the angular velocities of blade 2 and blade 3 in terms of the azimuth angle ψ of blade 1, measured from the positive *x'*-axis. This can be accomplished adding to the angle ψ the relative azimuth position of blades 2 and 3 with respect to blade 1. Also, it is necessary to include in $[\omega_{bi}]$ the flapwise angular velocity of each blade in the corresponding velocity component. The angular velocities expressions are defined as

$$\begin{aligned} \{\omega_{h1}\} &= \begin{Bmatrix} \dot{\theta}\cos\phi\cos\psi + \dot{\phi}\sin\psi \\ -\dot{\theta}\cos\phi\sin\psi + \dot{\phi}\cos\psi \\ \dot{\psi} + \dot{\theta}\sin\phi \end{Bmatrix} \\ \{\omega_{h2}\} &= \begin{Bmatrix} \dot{\theta}\cos\phi\cos\left(\psi + \frac{2\pi}{3}\right) + \dot{\phi}\sin\left(\psi + \frac{2\pi}{3}\right) \\ -\dot{\theta}\cos\phi\sin\left(\psi + \frac{2\pi}{3}\right) + \dot{\phi}\cos\left(\psi + \frac{2\pi}{3}\right) \\ \dot{\psi} + \dot{\theta}\sin\phi \end{Bmatrix} \\ \{\omega_{h3}\} &= \begin{Bmatrix} \dot{\theta}\cos\phi\cos\left(\psi + \frac{4\pi}{3}\right) + \dot{\phi}\sin\left(\psi + \frac{4\pi}{3}\right) \\ -\dot{\theta}\cos\phi\sin\left(\psi + \frac{4\pi}{3}\right) + \dot{\phi}\cos\left(\psi + \frac{4\pi}{3}\right) \\ \dot{\psi} + \dot{\theta}\sin\phi \end{Bmatrix} \end{aligned} \tag{2-8}$$

$$\{\omega_{b1}\} = \begin{Bmatrix} \dot{\theta}\cos\phi\cos\psi + \dot{\phi}\sin\psi \\ -\dot{\theta}_{b1} - \dot{\theta}\cos\phi\sin\psi + \dot{\phi}\cos\psi \\ \dot{\psi} + \dot{\theta}\sin\phi \end{Bmatrix}$$

$$\{\omega_{b2}\} = \begin{Bmatrix} \dot{\theta}\cos\phi\cos\left(\psi + \frac{2\pi}{3}\right) + \dot{\phi}\sin\left(\psi + \frac{2\pi}{3}\right) \\ -\dot{\theta}_{b2} - \dot{\theta}\cos\phi\sin\left(\psi + \frac{2\pi}{3}\right) + \dot{\phi}\cos\left(\psi + \frac{2\pi}{3}\right) \\ \dot{\psi} + \dot{\theta}\sin\phi \end{Bmatrix} \tag{2-9}$$

$$\{\omega_{b3}\} = \begin{Bmatrix} \dot{\theta}\cos\phi\cos\left(\psi + \frac{4\pi}{3}\right) + \dot{\phi}\sin\left(\psi + \frac{4\pi}{3}\right) \\ -\dot{\theta}_{b3} - \dot{\theta}\cos\phi\sin\left(\psi + \frac{4\pi}{3}\right) + \dot{\phi}\cos\left(\psi + \frac{4\pi}{3}\right) \\ \dot{\psi} + \dot{\theta}\sin\phi \end{Bmatrix}$$

where $\dot{\theta}_{b1}$, $\dot{\theta}_{b2}$, and $\dot{\theta}_{b3}$ are the flapping angular velocities of the blade number *1*, *2*, and *3*, respectively. Once equations (2-6), (2-8), and (2-9) are substituted into equation (2-5) we obtain the relative velocity vector at the center of mass of each blade.

$$\{v_{b1}\} = \begin{Bmatrix} 0 \\ \left(r_h + \frac{L_b}{2}\right)\left(\Omega + \dot{\theta}\sin\phi\right) \\ \left(r_h + \frac{L_b}{2}\right)\left(\dot{\theta}\cos\phi\sin\psi - \dot{\phi}\cos\psi\right) + \frac{L_b}{2}\dot{\theta}_{b1} \end{Bmatrix}$$

$$\{v_{b2}\} = \begin{Bmatrix} 0 \\ \left(r_h + \frac{L_b}{2}\right)\left(\Omega + \dot{\theta}\sin\phi\right) \\ \left(r_h + \frac{L_b}{2}\right)\left(\dot{\theta}\cos\phi\sin\left(\psi + \frac{2\pi}{3}\right) - \dot{\phi}\cos\left(\psi + \frac{2\pi}{3}\right)\right) + \frac{L_b}{2}\dot{\theta}_{b2} \end{Bmatrix} \tag{2-10}$$

$$\{v_{b3}\} = \begin{Bmatrix} 0 \\ \left(r_h + \frac{L_b}{2}\right)\left(\Omega + \dot{\theta}\sin\phi\right) \\ \left(r_h + \frac{L_b}{2}\right)\left(\dot{\theta}\cos\phi\sin\left(\psi + \frac{4\pi}{3}\right) - \dot{\phi}\cos\left(\psi + \frac{4\pi}{3}\right)\right) + \frac{L_b}{2}\dot{\theta}_{b3} \end{Bmatrix}$$

Finally, once we know all the velocity vectors required in equation (2-1), the first part of the kinetic energy for the rotor can be expressed as

$$
\begin{aligned}
T_t = {} & \frac{1}{2} m_r \left[\left(\dot{\theta}_{y'} d_h + \dot{X}_b + \dot{x} \right)^2 + \left(-\dot{\theta}_{x'} d_h + \dot{Y}_b \right)^2 + \left(\dot{Z}_b + \dot{z} \right)^2 \right] \\
& + 3 m_b \left(\dot{Y}_b - d_h \dot{\theta} \right) \left[\left(r_h + \tfrac{L_b}{2} \right) \left(\Omega + \dot{\theta} \sin\phi \right) \right] \\
& + m_b \left(\dot{Z}_b + \dot{z} \right) \left[\left(r_h + \tfrac{L_b}{2} \right) \left(\dot{\theta} \cos\phi \sin\psi - \dot{\phi} \cos\psi \right) + \tfrac{Lb}{2} \dot{\theta}_{b1} \right] \\
& + m_b \left(\dot{Z}_b + \dot{z} \right) \left[\left(r_h + \tfrac{L_b}{2} \right) \left(\dot{\theta} \cos\phi \sin\left(\psi + \tfrac{2\pi}{3}\right) - \dot{\phi} \cos\left(\psi + \tfrac{2\pi}{3}\right) \right) + \tfrac{Lb}{2} \dot{\theta}_{b2} \right] \\
& + m_b \left(\dot{Z}_b + \dot{z} \right) \left[\left(r_h + \tfrac{L_b}{2} \right) \left(\dot{\theta} \cos\phi \sin\left(\psi + \tfrac{4\pi}{3}\right) - \dot{\phi} \cos\left(\psi + \tfrac{4\pi}{3}\right) \right) + \tfrac{Lb}{2} \dot{\theta}_{b3} \right] \\
& + \frac{3}{2} m_b \left[\left(r_h + \tfrac{L}{2} \right)^2 \left(\Omega + \dot{\theta} \sin\phi \right)^2 \right] + \frac{1}{2} m_b \left[\left(r_h + \tfrac{L_b}{2} \right) \left(\dot{\theta} \cos\phi \sin\psi - \dot{\phi} \cos\psi \right) + \tfrac{Lb}{2} \dot{\theta}_{b1} \right]^2 \\
& + \frac{1}{2} m_b \left[\left(r_h + \tfrac{L_b}{2} \right) \left(\dot{\theta} \cos\phi \sin\left(\psi + \tfrac{2\pi}{3}\right) - \dot{\phi} \cos\left(\psi + \tfrac{2\pi}{3}\right) \right) + \tfrac{Lb}{2} \dot{\theta}_{b2} \right]^2 \\
& + \frac{1}{2} m_b \left[\left(r_h + \tfrac{L_b}{2} \right) \left(\dot{\theta} \cos\phi \sin\left(\psi + \tfrac{4\pi}{3}\right) - \dot{\phi} \cos\left(\psi + \tfrac{4\pi}{3}\right) \right) + \tfrac{Lb}{2} \dot{\theta}_{b3} \right]^2
\end{aligned}
\tag{2-11}
$$

Since the algebraic expressions are lengthy, the symbolic manipulations can be carried out using any computer software for mathematical manipulation such as Mathematica or Maple. We used here and henceforth the commercial software Maple.

The second part of the rotor kinetic energy T_r is made up of two parts that consider the contribution of the rotational energy of the hub and the rotational energy of the blades about their centers of mass. Written in matrix form, the rotational kinetic energy can be expressed as

$$
T_r = \frac{1}{2} \{\omega_h\}^T [I_h] \{\omega_h\} + \frac{1}{2} \sum_{i=1}^{3} \{\omega_{bi}\}^T [I_b] \{\omega_{bi}\} \tag{2-12}
$$

where $\{\omega_h\}$ and $\{\omega_{bi}\}$ are, respectively, vectors of absolute body angular velocities of the hub and the blades about their principal axes. The matrices $[I_h]$ and $[I_b]$ are the principal mass moment of inertia matrices for the hub and blades about their centers of mass, respectively. Since the hub is modeled as a thin circular disk and the blades are modeled as slender rods, the matrices take the following forms:

$$[I_h]=\begin{bmatrix} I_t & 0 & 0 \\ 0 & I_t & 0 \\ 0 & 0 & I_a \end{bmatrix};\quad [I_b]=\begin{bmatrix} 0 & 0 & 0 \\ 0 & I_b & 0 \\ 0 & 0 & I_b \end{bmatrix} \tag{2-13}$$

where the subscripts "*t*" and "*a*" stand for transverse and axial, respectively; and "*b*" for blade.

The body angular velocity vector $\{\omega_{bi}\}$ was previously defined in equation (2-9) and the vector $\{\omega_h\}$ is equal to $\{\omega_{h1}\}$, which was defined in the first equation (2-8). After substituting the first equation (2-8), and equations (2-9) and (2-13) into equation (2-12) the complete rotational part of the kinetic energy can be written in terms of the Euler's angles as

$$\begin{aligned} T_r = {} & \frac{1}{2} I_t \left(\dot{\theta}\cos\phi\cos\psi + \dot{\phi}\sin\psi\right)^2 + \frac{1}{2} I_t \left(\dot{\phi}\cos\psi - \dot{\theta}\cos\phi\sin\psi\right)^2 + \frac{1}{2} I_a \left(\dot{\psi} + \dot{\theta}\sin\phi\right)^2 \\ & + \frac{1}{2} I_b \left(-\dot{\theta}_{b1} + \dot{\phi}\cos\psi - \dot{\theta}\cos\phi\sin\psi\right)^2 + \frac{3}{2} I_b \left(\dot{\psi} + \dot{\theta}\sin\phi\right)^2 \\ & + \frac{1}{2} I_b \left[-\dot{\theta}_{b2} + \dot{\phi}\cos\left(\psi + \tfrac{2\pi}{3}\right) - \dot{\theta}\cos\phi\sin\left(\psi + \tfrac{2\pi}{3}\right)\right]^2 \\ & + \frac{1}{2} I_b \left[-\dot{\theta}_{b3} + \dot{\phi}\cos\left(\psi + \tfrac{4\pi}{3}\right) - \dot{\theta}\cos\phi\sin\left(\psi + \tfrac{4\pi}{3}\right)\right]^2 \end{aligned} \tag{2-14}$$

2.3 ROTOR POTENTIAL ENERGY

The potential energy of the rotor system required in the variational formulation stems from the flexibility of the blades and the torsional stiffness of the tower. The bending flexibility of the tower will be considered in a later section during the formulation of the equations of motion of the tower. The flexibility of the system in the proposed model is introduced by means of flap hinges with torsion springs at the root of each blade and a torsion spring at the top end of the tower that affects the yawing motion of the rotor. For the blades, the hinges allow the

flapwise motion of each blade independently. Assuming that the three blades have the same flexural rigidity, the rotor potential energy can be simply written as

$$V_r = \frac{1}{2}k_b\left(\theta_{b1}^2 + \theta_{b2}^2 + \theta_{b3}^2\right) + \frac{1}{2}k_t\left(\theta_{y'}^2\right) \tag{2-15}$$

where k_b and k_t are the stiffness constants for the blades and tower, respectively. If better data is not available, k_b can be estimated from the beam theory as

$$k_b = \frac{4E_bI}{L_b} \tag{2-16}$$

where E_b and I are the modulus of elasticity for the blades and the equivalent moment of inertia about the blade flap axis, respectively. This equation represents the required equivalent spring acting on one end of a rigid beam, such that the tip displaces the same amount than the free end of a cantilever beam when both are subjected to a same uniform load. In a similar fashion, the tower torsion constant k_t can be analytically obtained from the formula of the twisting angle. Due to the slight tapering conical design of the steel towers, the torsion stiffness can be obtained from the integral expression which results in

$$k_t = \left[\int_o^{h_t} \frac{dy}{GJ(y)}\right]^{-1} = \frac{6\pi G t_b r_b^3}{h_t}\frac{\beta^3}{\beta^2 + \beta + 1} \tag{2-17}$$

where G is the shear modulus, $J(y)$ is the polar moment of inertia as function of height; h_t, r_b, and t_b are the tower height, the base mean radius, and the tower thickness at the base, respectively. The constant β is the ratio between the upper and base radius. To model the variable wall thickness on actual steel towers used in wind turbines, it is assumed that the wall thickness changes with respect to height at the same rate as the mean radius does.

2.4 AERODYNAMIC FORCES AND DAMPING

To account for the forces induced by the wind on the rotor and include some sort of aerodynamic damping on the system, a simplified model using steady and homogenous wind parallel to the *z*-axis is now considered. The model uses the Betz theory (see Gasch and Tweele, 2004) to obtain the forces on the blades. The idealized model according to the Betz theory assumes that the rotor extracts the maximum possible kinetic energy of the wind neglecting frictional losses.

The wind forces on the rotor can be divided into a circumferential component and an axial or thrust component as shown in Fig. 2-3. The circumferential wind component gives to the rotor the torque and angular velocity necessary for the electric power generation. As stated previously, an operating state with a constant angular velocity Ω in the rotor was assumed, and since the blades are considered very stiff in their edgewise direction, there is no need to introduce the aerodynamic circumferential force in the equations of motion. On the other hand, the effects of the axial or thrust component of the wind should be studied since it can induce flapwise motion of the blades and its fluctuation can produce, as it will be shown shortly, aerodynamic damping on the system.

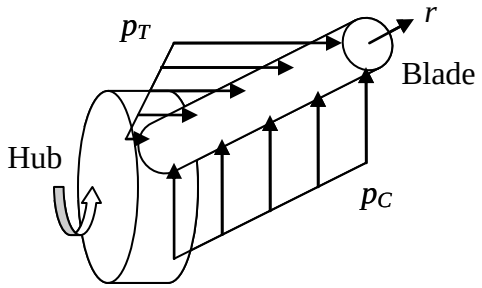

Fig. 2-3: Distribution of circumferential forces p_C and thrust forces p_T on the blade

A blade dimensioned according to Betz theory and operating at its design speed, has a thrust intensity p_T that is directly proportional to the rotor radius r and to the square of the wind velocity v_∞ (see Gasch and Twele, 2004). It can be shown that the thrust intensity over a blade can be expressed as

$$p_T = \frac{1}{n}\left(\frac{8}{9}\frac{\rho_a}{2}v_\infty^2\right)2\pi r \tag{2-18}$$

where n is the number of blades, and ρ_a is the air density. As it can be observed in Fig. 2-3, the force intensity p_T has a trapezoidal distribution over the blade. Its integration along the blade produces a concentrated force F_T equal to

$$F_T = \int_{r_h}^{r_h+L_b} p_T\,dr = \frac{1}{n}\left(\frac{8}{9}\frac{\rho_a}{2}v_\infty^2\right)\pi\left(2r_hL_b + L_b^2\right) \tag{2-19}$$

This force should be applied at the centroid x_c of the force distribution (the trapezoid) which is measured from the blade hinge and it can be calculated as

$$x_c = \frac{1}{3}\left(\frac{3\alpha+2}{2\alpha+1}\right)L_b \tag{2-20}$$

where α is the ratio between the hub radius r_h and the blade length L_b. The moment caused on each blade hinge due to the thrust can be obtained as

$$M_{\theta_{bi}} = F_T x_c = \frac{1}{n}\left(\frac{8}{9}\frac{\rho_a}{2}v_\infty^2\right)\frac{\pi}{3}(3\alpha+2)L_b^2 \tag{2-21}$$

Obviously, the moment in each blade is constant as the wind velocity stays constant; therefore they also will be ignored in the equations of motion provided the blade displacements are measured from a position of steady operational equilibrium. However, these moments should be considered if a stress evaluation of the blades is performed.

At this point we are interested in obtaining an expression for small variations of the apparent wind velocity when the tower and blades move back and forward during a strong ground motion. If the blades operate at a high angle of attack, which is our assumption, the change in thrust intensity mainly results from the change in the apparent wind velocity (see Gasch and Twele, 2004). Ignoring second order terms and the slight effect of the base motion of the tower, the increment in the thrust intensity due to the change in the relative wind velocity over each blade can be approximated to

$$\Delta p_{Ti} = \frac{1}{n}\frac{8}{9}\frac{\rho_a}{2} 2\pi v_\infty \left(2\dot{z} + 2\dot{\theta}_{bi} r\right) r \tag{2-22}$$

The total force increment on the blade hinge can be obtained by integrating over the blade length, i.e., by solving the integral in equation (2-19) changing p_T by Δp_{Ti}. Consequently, the total moment increment about the blade hinge can be obtained by multiplying the force increment by the arm x_c given by equation (2-20). The simplified equations can be expressed as

$$\Delta F_{Ti} = c_1 \dot{\theta}_{bi} + c_2 \dot{z} \tag{2-23}$$

$$\Delta M_{\theta_{bi}} = c_3 \dot{\theta}_{bi} + c_4 \dot{z} \tag{2-24}$$

where c_1, c_2, c_3, and c_4 are found to be aerodynamic damping constants and are defined as

$$c_1 = \frac{16\pi}{27n}(3\alpha + 1) L_b^3 \rho_a v_\infty \tag{2-25}$$

$$c_2 = \frac{8\pi}{9n}(2\alpha + 1) L_b^2 \rho_a v_\infty \tag{2-26}$$

$$c_3 = \frac{16\pi}{81n}\left(\frac{9\alpha + 2}{2\alpha + 1}\right) L_b^4 \rho_a v_\infty \tag{2-27}$$

$$c_4 = \frac{8\pi}{27n}(3\alpha + 2) L_b^3 \rho_a v_\infty \tag{2-28}$$

These aerodynamic damping forces and moments must be included appropriately into the equations of motion associated with the blade flapping rotations and with the wind turbine fore-aft motion.

2.5 LAGRANGE EQUATIONS

As stated before, the equations of motion for the rotor will be derived using a Lagrangian approach. The Lagrange equation has the general form

$$\frac{d}{dt}\left(\frac{\partial T}{\partial \dot{q}_i}\right) - \frac{\partial T}{\partial q_i} + \frac{\partial V}{\partial q_i} = Q_i \tag{2-29}$$

where T is the kinetic energy, V is the potential energy, Q_i is the generalized force components, and q_i are the generalized coordinates.

For the first part of the kinetic energy in equation (2-11), T_t must be differentiated with respect to the generalized coordinates x, z, the Euler's angles θ, ϕ, ψ, the blade angles θ_{b1}, θ_{b2}, θ_{b3}, and with respect to their respective velocity components. Notice that by considering small rotations and assuming that the main shaft rotates at constant velocity, it is possible to relate the Euler's angles to the cartesian rotations $\theta_{x'}$, $\theta_{y'}$, and the main shaft velocity Ω as

$$\theta = \theta_{x'}; \quad \phi = \theta_{y'} \; ; \quad \psi = \Omega t$$

By considering that the angles of the blade flapwise rotation are small, the resulting expressions can be further simplified. This assumption is consistent with the actual flexibility allowed in the blades design because if their backward motion exceeds a certain limit (usually a small angle), the blade tips may impact the tower. Performing the derivatives results in the following expressions:

$$\frac{d}{dt}\left(\frac{\partial T_t}{\partial \dot{x}}\right) = m_r \ddot{x} + m_r \ddot{X}_b + m_r d_h \ddot{\theta}_{y'} \tag{2-30}$$

$$\frac{d}{dt}\left(\frac{\partial T_t}{\partial \dot{z}}\right) = m_r \ddot{z} + m_r \ddot{Z}_b + \frac{1}{2} m_b L_b \ddot{\theta}_{b1} + \frac{1}{2} m_b L_b \ddot{\theta}_{b2} + \frac{1}{2} m_b L_b \ddot{\theta}_{b3} \tag{2-31}$$

$$\begin{aligned}\frac{d}{dt}\left(\frac{\partial T_t}{\partial \dot{\theta}}\right) &= m_r d_h^2 \ddot{\theta}_{x'} - m_r d_h \ddot{Y}_b + \frac{3}{2} m_b \left(r_h + \tfrac{L_b}{2}\right)^2 \ddot{\theta}_{x'} + \left[\frac{1}{2} m_b \left(r_h + \tfrac{L_b}{2}\right) L_b \sin \Omega t\right] \ddot{\theta}_{b1} \\ &+ \left[\frac{1}{2} m_b \left(r_h + \tfrac{L_b}{2}\right) L_b \sin\left(\Omega t + \tfrac{2\pi}{3}\right)\right] \ddot{\theta}_{b2} + \left[\frac{1}{2} m_b \left(r_h + \tfrac{L_b}{2}\right) L_b \sin\left(\Omega t + \tfrac{4\pi}{3}\right)\right] \ddot{\theta}_{b3} + 3 m_b \left(r_h + \tfrac{L_b}{2}\right)^2 \Omega \dot{\theta}_{y'} \\ &+ \left[\frac{1}{2} m_b \left(r_h + \tfrac{L_b}{2}\right) L_b \cos \Omega t\right] \Omega \dot{\theta}_{b1} + \left[\frac{1}{2} m_b \left(r_h + \tfrac{L_b}{2}\right) L_b \cos\left(\Omega t + \tfrac{2\pi}{3}\right)\right] \Omega \dot{\theta}_{b2} \\ &+ \left[\frac{1}{2} m_b \left(r_h + \tfrac{L_b}{2}\right) L_b \cos\left(\Omega t + \tfrac{4\pi}{3}\right)\right] \Omega \dot{\theta}_{b3} - \left[\frac{1}{2}\left(r_h + \tfrac{L_b}{2}\right) L_b \sin \Omega t\right] \dot{\theta}_{y'} \dot{\theta}_{b1} \theta_{y'} \\ &- \left[\frac{1}{2}\left(r_h + \tfrac{L_b}{2}\right) L_b \sin\left(\Omega t + \tfrac{2\pi}{3}\right)\right] \dot{\theta}_{y'} \dot{\theta}_{b2} \theta_{y'} - \left[\frac{1}{2}\left(r_h + \tfrac{L_b}{2}\right) L_b \sin\left(\Omega t + \tfrac{4\pi}{3}\right)\right] \dot{\theta}_{y'} \dot{\theta}_{b3} \theta_{y'} \\ &+ 3 m_b \left(r_h + \tfrac{L_b}{2}\right)^2 \dot{\theta}_{x'} \dot{\theta}_{y'} \theta_{y'} + 3 m_b \left(r_h + \tfrac{L_b}{2}\right) \ddot{Y}_b \theta_{y'} - 6 m_b \left(r_h + \tfrac{L_b}{2}\right) d_h \ddot{\theta}_{x'} \theta_{y'} - 6 m_b \left(r_h + \tfrac{L_b}{2}\right) d_h \dot{\theta}_{x'} \dot{\theta}_{y'} \\ &+ 3 m_b \left(r_h + \tfrac{L_b}{2}\right)^2 \ddot{\theta}_{x'} \theta_{y'}^2\end{aligned} \tag{2-32}$$

$$\begin{aligned}\frac{d}{dt}\left(\frac{\partial T_t}{\partial \dot{\phi}}\right) &= m_r d_h^2 \ddot{\theta}_{y'} + m_r d_h \ddot{x} + m_r d_h \ddot{X}_b + \frac{3}{2} m_b \left(r_h + \tfrac{L_b}{2}\right)^2 \ddot{\theta}_{y'} - \left[\frac{1}{2} m_b \left(r_h + \tfrac{L_b}{2}\right) L_b \cos \Omega t\right] \ddot{\theta}_{b1} \\ &- \left[\frac{1}{2} m_b \left(r_h + \tfrac{L_b}{2}\right) L_b \cos\left(\Omega t + \tfrac{2\pi}{3}\right)\right] \ddot{\theta}_{b2} - \left[\frac{1}{2} m_b \left(r_h + \tfrac{L_b}{2}\right) L_b \cos\left(\Omega t + \tfrac{4\pi}{3}\right)\right] \ddot{\theta}_{b3} \\ &+ \left[\frac{1}{2} m_b \left(r_h + \tfrac{L_b}{2}\right) L_b \sin \Omega t\right] \Omega \dot{\theta}_{b1} + \left[\frac{1}{2} m_b \left(r_h + \tfrac{L_b}{2}\right) L_b \sin\left(\Omega t + \tfrac{2\pi}{3}\right)\right] \Omega \dot{\theta}_{b2} \\ &+ \left[\frac{1}{2} m_b \left(r_h + \tfrac{L_b}{2}\right) L_b \sin\left(\Omega t + \tfrac{4\pi}{3}\right)\right] \Omega \dot{\theta}_{b3}\end{aligned} \tag{2-33}$$

$$\frac{d}{dt}\left(\frac{\partial T_t}{\partial \dot{\psi}}\right) = 3 m_b \left(r_h + \tfrac{L_b}{2}\right)^2 \ddot{\theta}_{x'} \theta_{y'} + 3 m_b \left(r_h + \tfrac{L_b}{2}\right) \ddot{Y}_b - 3 m_b \left(r_h + \tfrac{L_b}{2}\right) d_h \ddot{\theta}_{x'} + 3 m_b \left(r_h + \tfrac{L_b}{2}\right)^2 \dot{\theta}_{x'} \dot{\theta}_{y'} \tag{2-34}$$

$$\frac{d}{dt}\left(\frac{\partial T_t}{\partial \dot{\theta}_{b1}}\right)=\frac{1}{4}m_b L_b^2\ddot{\theta}_{b1}+\frac{1}{2}m_b L_b\ddot{z}+\frac{1}{2}m_b L_b\ddot{Z}_b+\left[\frac{1}{2}m_b\left(r_h+\tfrac{L_b}{2}\right)L_b\sin\Omega t\right]\ddot{\theta}_{x'}$$
$$-\left[\frac{1}{2}m_b\left(r_h+\tfrac{L_b}{2}\right)L_b\cos\Omega t\right]\ddot{\theta}_{y'}+\left[\frac{1}{2}m_b\left(r_h+\tfrac{L_b}{2}\right)L_b\cos\Omega t\right]\Omega\dot{\theta}_{x'} \quad (2\text{-}35)$$
$$+\left[\frac{1}{2}m_b\left(r_h+\tfrac{L_b}{2}\right)L_b\sin\Omega t\right]\Omega\dot{\theta}_{y'}-\left[\frac{1}{2}m_b\left(r_h+\tfrac{L_b}{2}\right)L_b\sin\Omega t\right]\dot{\theta}_{x'}\dot{\theta}_{y'}\theta_{y'}$$

$$\frac{d}{dt}\left(\frac{\partial T_t}{\partial \dot{\theta}_{b2}}\right)=\frac{1}{4}m_b L_b^2\ddot{\theta}_{b2}+\frac{1}{2}m_b L_b\ddot{z}+\frac{1}{2}m_b L_b\ddot{Z}_b+\left[\frac{1}{2}m_b\left(r_h+\tfrac{L_b}{2}\right)L_b\sin\left(\Omega t+\tfrac{2\pi}{3}\right)\right]\ddot{\theta}_x$$
$$-\left[\frac{1}{2}m_b\left(r_h+\tfrac{L_b}{2}\right)L_b\cos\left(\Omega t+\tfrac{2\pi}{3}\right)\right]\ddot{\theta}_y+\left[\frac{1}{2}m_b\left(r_h+\tfrac{L_b}{2}\right)L_b\cos\left(\Omega t+\tfrac{2\pi}{3}\right)\right]\Omega\dot{\theta}_x \quad (2\text{-}36)$$
$$+\left[\frac{1}{2}m_b\left(r_h+\tfrac{L_b}{2}\right)L_b\sin\left(\Omega t+\tfrac{2\pi}{3}\right)\right]\Omega\dot{\theta}_y-\left[\frac{1}{2}m_b\left(r_h+\tfrac{L_b}{2}\right)L_b\sin\left(\Omega t+\tfrac{2\pi}{3}\right)\right]\dot{\theta}_{x'}\dot{\theta}_{y'}\theta_{y'}$$

$$\frac{d}{dt}\left(\frac{\partial T_t}{\partial \dot{\theta}_{b3}}\right)=\frac{1}{4}m_b L_b^2\ddot{\theta}_{b3}+\frac{1}{2}m_b L_b\ddot{z}+\frac{1}{2}m_b L_b\ddot{Z}_b\left[\frac{1}{2}m_b\left(r_h+\tfrac{L_b}{2}\right)L_b\sin\left(\Omega t+\tfrac{4\pi}{3}\right)\right]\ddot{\theta}_x$$
$$-\left[\frac{1}{2}m_b\left(r_h+\tfrac{L_b}{2}\right)L_b\cos\left(\Omega t+\tfrac{4\pi}{3}\right)\right]\ddot{\theta}_y+\left[\frac{1}{2}m_b\left(r_h+\tfrac{L_b}{2}\right)L_b\cos\left(\Omega t+\tfrac{4\pi}{3}\right)\right]\Omega\dot{\theta}_x \quad (2\text{-}37)$$
$$+\left[\frac{1}{2}m_b\left(r_h+\tfrac{L_b}{2}\right)L_b\sin\left(\Omega t+\tfrac{4\pi}{3}\right)\right]\Omega\dot{\theta}_y-\left[\frac{1}{2}m_b\left(r_h+\tfrac{L_b}{2}\right)L_b\sin\left(\Omega t+\tfrac{4\pi}{3}\right)\right]\dot{\theta}_{x'}\dot{\theta}_{y'}\theta_{y'}$$

$$\frac{\partial T_t}{\partial \phi}=3m_b\left(r_h+\tfrac{L_b}{2}\right)^2\Omega\dot{\theta}_x-3m_b\left(r_h+\tfrac{L_b}{2}\right)d_h\dot{\theta}_{x'}^2+\frac{3}{2}m_b\left(r_h+\tfrac{L_b}{2}\right)^2\dot{\theta}_{x'}^2\theta_{y'}$$
$$-\left[\frac{1}{2}m_b\left(r_h+\tfrac{L_b}{2}\right)L_b\sin\Omega t\right]\dot{\theta}_{x'}\dot{\theta}_{b1}-\left[\frac{1}{2}m_b\left(r_h+\tfrac{L_b}{2}\right)L_b\sin\left(\Omega t+\tfrac{2\pi}{3}\right)\right]\dot{\theta}_{x'}\dot{\theta}_{b2} \quad (2\text{-}38)$$
$$-\left[\frac{1}{2}m_b\left(r_h+\tfrac{L_b}{2}\right)L_b\sin\left(\Omega t+\tfrac{4\pi}{3}\right)\right]\dot{\theta}_{x'}\dot{\theta}_{b3}$$

$$\frac{\partial T_t}{\partial \psi}=-\left[\frac{1}{2}m_b\left(r_h+\tfrac{L_b}{2}\right)L_b\sin\Omega t\right]\dot{\theta}_{y'}\dot{\theta}_{b1}-\left[\frac{1}{2}m_b\left(r_h+\tfrac{L_b}{2}\right)L_b\sin\left(\Omega t+\tfrac{2\pi}{3}\right)\right]\dot{\theta}_{y'}\dot{\theta}_{b2}$$
$$-\left[\frac{1}{2}m_b\left(r_h+\tfrac{L_b}{2}\right)L_b\sin\left(\Omega t+\tfrac{4\pi}{3}\right)\right]\dot{\theta}_{y'}\dot{\theta}_{b3} \quad (2\text{-}39)$$

$$\frac{\partial T_t}{\partial x}=\frac{\partial T_t}{\partial z}=\frac{\partial T_t}{\partial \theta}=\frac{\partial T_t}{\partial \theta_{b1}}=\frac{\partial T_t}{\partial \theta_{b2}}=\frac{\partial T_t}{\partial \theta_{b3}}=0 \quad (2\text{-}40)$$

In the case of the rotational kinetic energy in equation (2-14), T_r must be differentiated with respect to each one of the Euler's angles θ, ϕ, ψ, each blade rotation θ_{b1}, θ_{b2}, θ_{b3}, and with respect to their time derivatives. The derivatives of T_r required in the Lagrange equations for the rotor are

$$\begin{aligned}\frac{d}{dt}\left(\frac{\partial T_r}{\partial \dot{\theta}}\right) &= \left(I_t + \frac{3}{2}I_b\right)\ddot{\theta}_{x'} + \left(2I_a - 2I_t + 3I_b\right)\dot{\theta}_{x'}\dot{\theta}_{y'}\theta_{y'} + \left(I_a + 3I_b\right)\Omega\dot{\theta}_{y'} \\ &+ \left(I_b \sin\Omega t\right)\ddot{\theta}_{b1} + \left[I_b \sin\left(\Omega t + \tfrac{2\pi}{3}\right)\right]\ddot{\theta}_{b2} + \left[I_b \sin\left(\Omega t + \tfrac{4\pi}{3}\right)\right]\ddot{\theta}_{b3} \\ &- \left(I_b \sin\Omega t\right)\dot{\theta}_{y'}\dot{\theta}_{b1}\theta_{y'} - \left[I_b \sin\left(\Omega t + \tfrac{2\pi}{3}\right)\right]\dot{\theta}_{y'}\dot{\theta}_{b2}\theta_{y'} - \left[I_b \sin\left(\Omega t + \tfrac{4\pi}{3}\right)\right]\dot{\theta}_{y'}\dot{\theta}_{b3}\theta_{y'} \\ &+ \left(I_b \cos\Omega t\right)\Omega\dot{\theta}_{b1} + \left[I_b \cos\left(\Omega t + \tfrac{2\pi}{3}\right)\right]\Omega\dot{\theta}_{b2} + \left[I_b \cos\left(\Omega t + \tfrac{4\pi}{3}\right)\right]\Omega\dot{\theta}_{b3}\end{aligned} \tag{2-41}$$

$$\begin{aligned}\frac{d}{dt}\left(\frac{\partial T_r}{\partial \dot{\phi}}\right) &= \left(I_t + \frac{3}{2}I_b\right)\ddot{\theta}_{y'} - \left(I_b \cos\Omega t\right)\ddot{\theta}_{b1} - \left[I_b \cos\left(\Omega t + \tfrac{2\pi}{3}\right)\right]\ddot{\theta}_{b2} \\ &- \left[I_b \cos\left(\Omega t + \tfrac{4\pi}{3}\right)\right]\ddot{\theta}_{b3} + \left(I_b \sin\Omega t\right)\Omega\dot{\theta}_{b1} + \left[I_b \sin\left(\Omega t + \tfrac{2\pi}{3}\right)\right]\Omega\dot{\theta}_{b2} \\ &+ \left[I_b \sin\left(\Omega t + \tfrac{4\pi}{3}\right)\right]\Omega\dot{\theta}_{b3}\end{aligned} \tag{2-42}$$

$$\frac{d}{dt}\left(\frac{\partial T_r}{\partial \dot{\psi}}\right) = \left(I_a + 3I_b\right)\ddot{\theta}_{x'}\theta_{y'} + \left(I_a + 3I_b\right)\dot{\theta}_{x'}\dot{\theta}_{y'} \tag{2-43}$$

$$\begin{aligned}\frac{d}{dt}\left(\frac{\partial T_r}{\partial \dot{\theta}_{b1}}\right) &= I_b\ddot{\theta}_{b1} + \left(I_b \sin\Omega t\right)\ddot{\theta}_{x'} - \left(I_b \cos\Omega t\right)\ddot{\theta}_{y'} + \left(I_b \cos\Omega t\right)\Omega\dot{\theta}_{x'} \\ &+ \left(I_b \sin\Omega t\right)\Omega\dot{\theta}_{y'} - \left(I_b \sin\Omega t\right)\dot{\theta}_{x'}\dot{\theta}_{y'}\theta_{y'}\end{aligned} \tag{2-44}$$

$$\begin{aligned}\frac{d}{dt}\left(\frac{\partial T_r}{\partial \dot{\theta}_{b2}}\right) &= I_b\ddot{\theta}_{b2} + \left[I_b \sin\left(\Omega t + \tfrac{2\pi}{3}\right)\right]\ddot{\theta}_{x'} - \left[I_b \cos\left(\Omega t + \tfrac{2\pi}{3}\right)\right]\ddot{\theta}_{y'} \\ &+ \left[I_b \cos\left(\Omega t + \tfrac{2\pi}{3}\right)\right]\Omega\dot{\theta}_{x'} + \left[I_b \sin\left(\Omega t + \tfrac{2\pi}{3}\right)\right]\Omega\dot{\theta}_{y'} - \left[I_b \sin\left(\Omega t + \tfrac{2\pi}{3}\right)\right]\dot{\theta}_{x'}\dot{\theta}_{y'}\theta_{y'}\end{aligned} \tag{2-45}$$

$$\begin{aligned}\frac{d}{dt}\left(\frac{\partial T_r}{\partial \dot{\theta}_{b3}}\right) &= I_b\ddot{\theta}_{b3} + \left[I_b \sin\left(\Omega t + \tfrac{4\pi}{3}\right)\right]\ddot{\theta}_{x'} - \left[I_b \cos\left(\Omega t + \tfrac{4\pi}{3}\right)\right]\ddot{\theta}_{y'} \\ &+ \left[I_b \cos\left(\Omega t + \tfrac{4\pi}{3}\right)\right]\Omega\dot{\theta}_{x'} + \left[I_b \sin\left(\Omega t + \tfrac{4\pi}{3}\right)\right]\Omega\dot{\theta}_{y'} - \left[I_b \sin\left(\Omega t + \tfrac{4\pi}{3}\right)\right]\dot{\theta}_{x'}\dot{\theta}_{y'}\theta_{y'}\end{aligned} \tag{2-46}$$

$$\frac{\partial T_r}{\partial \phi} = \frac{1}{2}\left(2I_a - 2I_t + 3I_b\right)\dot{\theta}_{x'}^2\theta_{y'} + \left(I_a + 3I_b\right)\Omega\dot{\theta}_{x'} - \left(I_b \sin\Omega t\right)\dot{\theta}_{x'}\dot{\theta}_{b1}\theta_{y'} - \left[I_b \sin\left(\Omega t + \tfrac{2\pi}{3}\right)\right]\dot{\theta}_{x'}\dot{\theta}_{b2}\theta_{y'} - \left[I_b \sin\left(\Omega t + \tfrac{4\pi}{3}\right)\right]\dot{\theta}_{x'}\dot{\theta}_{b3}\theta_{y'} \tag{2-47}$$

$$\frac{\partial T_r}{\partial \psi} = \left(I_b \cos\Omega t\right)\dot{\theta}_{x'}\dot{\theta}_{b1} + \left[I_b \cos\left(\Omega t + \tfrac{2\pi}{3}\right)\right]\dot{\theta}_{x'}\dot{\theta}_{b2} + \left[I_b \cos\left(\Omega t + \tfrac{4\pi}{3}\right)\right]\dot{\theta}_{x'}\dot{\theta}_{b3} + \left(I_b \sin\Omega t\right)\dot{\theta}_{y'}\dot{\theta}_{b1} + \left[I_b \sin\left(\Omega t + \tfrac{2\pi}{3}\right)\right]\dot{\theta}_{y'}\dot{\theta}_{b2} + \left[I_b \sin\left(\Omega t + \tfrac{4\pi}{3}\right)\right]\dot{\theta}_{y'}\dot{\theta}_{b3} \tag{2-48}$$

$$\frac{\partial T_r}{\partial \theta} = \frac{\partial T_r}{\partial \theta_{b1}} = \frac{\partial T_r}{\partial \theta_{b2}} = \frac{\partial T_r}{\partial \theta_{b3}} = 0 \tag{2-49}$$

The derivatives of the potential energy in equation (2-15) are very simple because they only apply for the blade rotations and the tower twisting angle. They can be expressed as

$$\frac{\partial V_r}{\partial \theta_{b1}} = k_b\theta_{b1} \tag{2-50}$$

$$\frac{\partial V_r}{\partial \theta_{b2}} = k_b\theta_{b2} \tag{2-51}$$

$$\frac{\partial V_r}{\partial \theta_{b3}} = k_b\theta_{b3} \tag{2-52}$$

$$\frac{\partial V_r}{\partial \theta_{y'}} = k_t\theta_{y'} \tag{2-53}$$

Notice that the generalized force components Q_i from the Lagrange equations that were obtained from differentiation with respect to the Euler's angles, represent in each case generalized moments M_θ, M_ϕ, and M_ψ about the non-orthogonal set of axes. These generalized moments must include any non-conservative moment due to loads such as damping forces or any external load not considered yet that are acting in the rotor. In our case, we will ignore the structural damping for now, which means that we only need to consider the reaction moments at

the support between the nacelle and the tower. However, these reaction moments will disappear when we couple the equations of the rotor with those of the tower. Nevertheless, since the equations of motion of the rotor are based in non-orthogonal Euler's angles and the equations of motion of the tower will be based in orthogonal coordinates, it is necessary to transform the moments about the Euler's axes in terms of orthogonal axes. The transformation is performed by noticing from Fig. 2-2 that the generalized moments M_θ, M_ϕ, and M_ψ represent the sum of the projections of the moments $M_{x'}$, $M_{y'}$, and $M_{z'}$ in the non-orthogonal set of axes (X, y, z'), (see Greenwood, 1988). The specific transformation required can be obtained from the following equations:

$$\begin{aligned} M_\theta &= M_{z'} \sin\phi + M_{x'} \cos\phi \\ M_\phi &= M_{y'} \\ M_\psi &= M_{z'} \end{aligned} \tag{2-54}$$

2.6 EQUATIONS OF MOTION OF THE TOWER

Until now, the kinetic and potential energy obtained correspond to those associated with the rotor. However, part of the kinetic and elastic energy contribution of the wind turbine also comes from the nacelle and the tower. Instead of using a variational approach to model the tower, for convenience, we will use Newton's Law and we will model the tower with elastic beam elements. This component of the wind turbine resembles a conventional civil engineering structure and thus the form of the equations of motion is very well known (provided the system behaves in a linear elastic fashion). This leads straightforward to their mass and stiffness matrices.

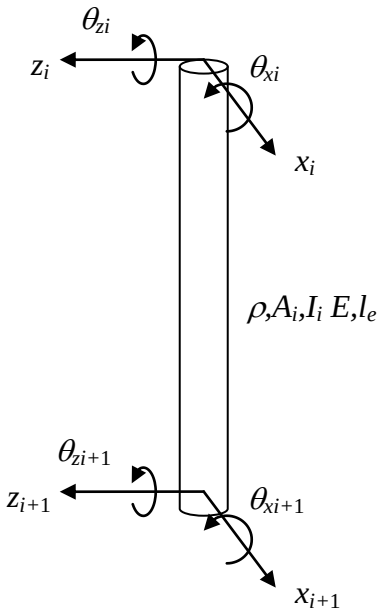

Fig. 2-4: Degrees of freedom for a tower beam element

Fig. 2-4 shows a typical beam element which consists of two nodes, each one with 4 degrees of freedom (two translations and two rotations). The vertical (axial) displacements of the tower nodes are neglected since the stiffness in the axial direction is much higher than the lateral directions and the base is fixed. The element stiffness matrix is well known (see Chandrupatla and Belegundu, 1997) and thus its derivation is omitted here. It has the form

$$[k_e] = \frac{EI_i}{l_e^3}\begin{bmatrix} 12 & 6l_e & -12 & 6l_e & 0 & 0 & 0 & 0 \\ 6l_e & 4l_e^2 & -6l_e & 2l_e^2 & 0 & 0 & 0 & 0 \\ -12 & -6l_e & 12 & -6l_e & 0 & 0 & 0 & 0 \\ 6l_e & 2l_e^2 & -6l_e & 4l_e^2 & 0 & 0 & 0 & 0 \\ 0 & 0 & 0 & 0 & 12 & 6l_e & -12 & 6l_e \\ 0 & 0 & 0 & 0 & 6l_e & 4l_e^2 & -6l_e & 2l_e^2 \\ 0 & 0 & 0 & 0 & -12 & -6l_e & 12 & -6l_e \\ 0 & 0 & 0 & 0 & 6l_e & 2l_e^2 & -6l_e & 4l_e^2 \end{bmatrix} \tag{2-55}$$

where E, I_i and l_e are the modulus of elasticity, moment of inertia and length of the element, respectively. The vector of nodal displacement associated with the stiffness matrix $[k_e]$ defined before is arranged as follows:

$$\{q_i\} = \begin{Bmatrix} x_i & \theta_{z_i} & x_{i+1} & \theta_{z_{i+1}} & z_i & \theta_{x_i} & z_{i+1} & \theta_{x_{i+1}} \end{Bmatrix}^T \tag{2-56}$$

The element lumped mass matrix has the form

$$[m_e] = \frac{\rho A_i l_e}{2} \begin{bmatrix} 1 & 0 & 0 & 0 & 0 & 0 & 0 & 0 \\ 0 & \frac{l_e^2}{12} & 0 & 0 & 0 & 0 & 0 & 0 \\ 0 & 0 & 1 & 0 & 0 & 0 & 0 & 0 \\ 0 & 0 & 0 & \frac{l_e^2}{12} & 0 & 0 & 0 & 0 \\ 0 & 0 & 0 & 0 & 1 & 0 & 0 & 0 \\ 0 & 0 & 0 & 0 & 0 & \frac{l_e^2}{12} & 0 & 0 \\ 0 & 0 & 0 & 0 & 0 & 0 & 1 & 0 \\ 0 & 0 & 0 & 0 & 0 & 0 & 0 & \frac{l_e^2}{12} \end{bmatrix} \tag{2-57}$$

where ρ and A_i are, respectively, the density and cross-sectional area of the beam element. Notice that the inertial effect associated to the rotational degrees of freedom is included as the mass moment of inertia of half of the beam segment about each end. By defining a rotational inertia in this way one can avoid the cumbersome static condensation process required when null values of moment of inertia are used in correspondence with rotational degrees of freedom. In our model, three beam elements of equal lengths are used to describe the tower.

After applying the boundary conditions in the base of the tower, the model of the tower has 12 degrees of freedom and the reduced global stiffness matrix can be expressed as

$$[K_G]=\begin{bmatrix}
k_{11}^{(1)} & k_{12}^{(1)} & 0 & 0 & k_{13}^{(1)} & k_{14}^{(1)} & 0 & 0 & 0 & 0 & 0 & 0 \\
 & k_{22}^{(1)} & 0 & 0 & k_{23}^{(1)} & k_{24}^{(1)} & 0 & 0 & 0 & 0 & 0 & 0 \\
 & & k_{55}^{(1)} & k_{56}^{(1)} & 0 & 0 & k_{57}^{(1)} & k_{58}^{(1)} & 0 & 0 & 0 & 0 \\
 & & & k_{66}^{(1)} & 0 & 0 & k_{67}^{(1)} & k_{68}^{(1)} & 0 & 0 & 0 & 0 \\
 & & & & k_{33}^{(1)}+k_{11}^{(2)} & k_{34}^{(1)}+k_{12}^{(2)} & 0 & 0 & k_{13}^{(2)} & k_{14}^{(2)} & 0 & 0 \\
 & & & & & k_{44}^{(1)}+k_{22}^{(2)} & 0 & 0 & k_{23}^{(2)} & k_{24}^{(2)} & 0 & 0 \\
 & & & & & & k_{77}^{(1)}+k_{55}^{(2)} & k_{78}^{(1)}+k_{56}^{(2)} & 0 & 0 & k_{57}^{(2)} & k_{58}^{(2)} \\
 & & -SYMMETRIC & & & & & k_{88}^{(1)}+k_{66}^{(2)} & 0 & 0 & k_{67}^{(2)} & k_{68}^{(2)} \\
 & & & & & & & & k_{33}^{(2)}+k_{11}^{(3)} & k_{34}^{(2)}+k_{12}^{(3)} & 0 & 0 \\
 & & & & & & & & & k_{44}^{(2)}+k_{22}^{(3)} & 0 & 0 \\
 & & & & & & & & & & k_{77}^{(2)}+k_{55}^{(3)} & k_{78}^{(2)}+k_{56}^{(3)} \\
 & & & & & & & & & & & k_{88}^{(2)}+k_{66}^{(3)}
\end{bmatrix} \tag{2-58}$$

where the subscripts indicate the position (i.e., row and column number) of the stiffness constant in the element stiffness matrix shown in equation (2-55) and the superscripts within parentheses indicate the beam element considered starting from the top of the tower. The vector of nodal displacements is arranged as

$$\{q\}=\{x_1 \quad \theta_{z1} \quad z_1 \quad \theta_{x1} \quad x_2 \quad \theta_{z2} \quad z_2 \quad \theta_{x2} \quad x_3 \quad \theta_{z3} \quad z_3 \quad \theta_{x3}\}^T \tag{2-59}$$

The diagonal global mass matrix has the form:

$$[M_G]=\begin{bmatrix}
m_n+\frac{\rho A_1 l_e}{2} & 0 & 0 & 0 & 0 & 0 & 0 & 0 & 0 & 0 & 0 & 0 \\
 & \frac{\rho A_1 l_e^3}{24} & 0 & 0 & 0 & 0 & 0 & 0 & 0 & 0 & 0 & 0 \\
 & & m_n+\frac{\rho A_1 l_e}{2} & 0 & 0 & 0 & 0 & 0 & 0 & 0 & 0 & 0 \\
 & & & \frac{\rho A_1 l_e^3}{24} & 0 & 0 & 0 & 0 & 0 & 0 & 0 & 0 \\
 & & & & \frac{\rho l_e}{2}(A_1+A_2) & 0 & 0 & 0 & 0 & 0 & 0 & 0 \\
 & & & & & \frac{\rho l_e^3}{24}(A_1+A_2) & 0 & 0 & 0 & 0 & 0 & 0 \\
 & & & & & & \frac{\rho l_e}{2}(A_1+A_2) & 0 & 0 & 0 & 0 & 0 \\
 & & SYMMETRIC & & & & & \frac{\rho l_e^3}{24}(A_1+A_2) & 0 & 0 & 0 & 0 \\
 & & & & & & & & \frac{\rho l_e}{2}(A_2+A_3) & 0 & 0 & 0 \\
 & & & & & & & & & \frac{\rho l_e^3}{24}(A_2+A_3) & 0 & 0 \\
 & & & & & & & & & & \frac{\rho l_e}{2}(A_2+A_3) & 0 \\
 & & & & & & & & & & & \frac{\rho l_e^3}{24}(A_2+A_3)
\end{bmatrix} \tag{2-60}$$

where m_n is the mass of the nacelle that must be added to the tower lumped mass only in the first node. Finally, the undamped equations of motion for the tower still uncoupled with the rotor can be expressed in matrix form in the usual way as

$$[M_G]\{\ddot{q}\}+[K_G]\{q\}=-[M_G]\{a_b\} \tag{2-61}$$

where the vector of ground accelerations $\{a_b\}$ is defined as

$$\{a_b\}=\left\{\ddot{X}_b\ \ 0\ \ \ddot{Z}_b\ \ 0\ \ \ddot{X}_b\ \ 0\ \ \ddot{Z}_b\ \ 0\ \ \ddot{X}_b\ \ 0\ \ \ddot{Z}_b\ \ 0\right\}^T \tag{2-62}$$

To couple the tower with the rotor it is necessary to combine the mass and stiffness terms of the equations of motion for the tower and the rotor associated to the generalized coordinates that both systems have in common. The common generalized coordinates are located at the top of the tower and they are related as follows:

$$x=x_1;\quad z=z_1;\quad \theta_{x'}=\theta_{x1} \tag{2-63}$$

2.7 MAXIMUM STRESSES IN THE WIND TURBINE

Once the solutions of the equations of motion for the wind turbine system are obtained, the maximum displacements and rotations for different components of the system can be evaluated over the duration of the base excitation. These displacements and rotations can be used to calculate the maximum internal loads and the maximum stresses at important locations in the wind turbine such as the blade roots, nacelle bedplate, tower base, and foundation (although this last component will not be covered here).

In our wind turbine model the dynamic response is obtained from a steady operating state in which the initial values of the degrees of freedom before the ground motion starts are set to

zero. It is important to notice that at the time of the stress evaluation, there are additional forces not present in the dynamic model that must be taken into account. These forces were omitted in the dynamic model as consequence of the selection of the degrees of freedom or the assumption of high rigidity of several structural parts. In our model, such forces are the wind thrust component, the wind circumferential component, and the gravity and centrifugal loads.

2.7.1 Blades: Loads and Stresses

The roots of the blades are expected to be the most critical part because the moments and shear forces are greater there. Initially, when the rotor is at rest, the blades have a small pre-cone angle δ, usually ranging from 5^o to 7^o, (see Gasch and Twele, 2004) against the wind direction. This angle is diminished when the centrifugal loads in the blades and the wind thrust act over the operating rotor. As it was mentioned before, in our model this angle was reduced to zero at the steady operating state. Therefore, the actual bending moment in the flapping axis can be calculated by using the resultant rotation of the pre-cone angle and the blade rotation θ_{bi}. The bending moment can be obtained as

$$\left(M_{bi}\right)_f = k_b\left(\delta - \theta_{bi}\right) \tag{2-64}$$

Notice that the minus sign of θ_{bi} arises from the selection of the forward rotation of the blades as the positive direction.

The circumferential component of the wind (parallel to the flapping axis) produces the torque required to generate electricity. This torque can be evaluated from an aerodynamic analysis of the wind forces induced in the blades, but it can also be easily estimated from the output power $\dot{W}$ of the generator as

$$T = \frac{\dot{W}}{\Omega \eta} \tag{2-65}$$

where T is the total torque in the rotor and η is the overall efficiency of the turbine. To obtain the edgewise bending moment on each blade, this torque must be divided by the number of blades in the rotor; three in our case. Also the hub radius must be taken into account to transfer the bending moment to the blade root instead to the hub center. Besides this moment, the vertical component of the blade weight also contributes to the bending moment along this axis. Assuming a prismatic blade, the weight can be concentrated at the middle of the blade length. Fig. 2-5 shows that the moment produced by the gravity force is cyclic and varies with the azimuth position of the blades. This moment can be computed for the blades number 1 to 3 as

$$\begin{aligned} M_{mb1} &= \frac{m_b g L_b}{2} \cos(\Omega t) \\ M_{mb2} &= \frac{m_b g L_b}{2} \cos\left(\Omega t + \tfrac{2\pi}{3}\right) \\ M_{mb3} &= \frac{m_b g L_b}{2} \cos\left(\Omega t + \tfrac{4\pi}{3}\right) \end{aligned} \tag{2-66}$$

Thus, the total bending moment for each blade in the edgewise axis can be obtained from the equation

$$\left(M_{bi}\right)_e = M_{mbi} - \frac{T}{3\left(\dfrac{2r_h}{L_b} + 1\right)} \tag{2-67}$$

Again, the minus sign in the second term comes from the assumption that the weight component of blade number 1, measured from the positive *x*-axis, produces a bending moment in the opposite direction than the blade bending due to the wind circumferential component.

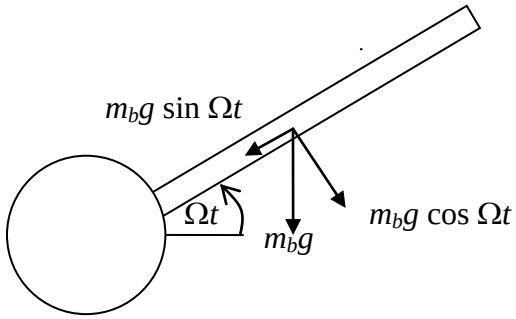

Fig. 2-5: Cyclic load on the blade due to weight

The resultant moment M_{bi} at the blade root can be evaluated as the vector addition of the flapping bending moment $(M_{bi})_f$ and the edgewise bending moment $(M_{bi})_e$, resulting on

$$M_{bi} = \sqrt{(M_{bi})_f^2 + (M_{bi})_e^2} \tag{2-68}$$

If r_b is the distance between the centroid of the blade cross-section to the upper surface of the blade, the bending stress can be expressed as

$$\sigma_{bi} = \frac{M_{bi} r_b}{I_b} \tag{2-69}$$

Normally the blade root section is tubular in shape so the values of r_b and I_b are very easy to compute.

In addition to the bending stress, the blades are subjected to normal stresses produced by the axial forces due to centrifugal forces and the cyclic normal component of the blade weight. The centrifugal force in each blade can be computed as

$$F_c = m_b \left(r_h + \frac{L_b}{2} \right) \Omega^2 \tag{2-70}$$

while the normal component of the weight for each blade can be expressed as

$$\begin{aligned} F_{g1} &= m_b g \sin(\Omega t) \\ F_{g2} &= m_b g \sin\left(\Omega t + \tfrac{2\pi}{3}\right) \\ F_{g3} &= m_b g \sin\left(\Omega t + \tfrac{4\pi}{3}\right) \end{aligned} \tag{2-71}$$

Since the centrifugal force always produce tension in the blade and the normal component of the weight is fully reversed as the blade rotates, the resultant normal force in the blade F_{bi} can be computed for i = 1 to 3 as

$$F_{bi} = F_c - F_{gi} \tag{2-72}$$

If the cross sectional area of the blade root A_b is known, the normal axial stress σ_{ai} can be easily obtained from

$$\sigma_{ai} = \frac{F_{bi}}{A_b} \tag{2-73}$$

To conclude the internal forces analysis in the roots of the blades, the transversal shear forces due to the wind components in the edgewise and flapwise direction, as well as the blade weight transversal component must be calculated. The flapwise shear component is identical to the thrust wind force F_T evaluated by equation (2-19) if the blade was designed according to Betz. In the case the Betz theory is not applied and the existing thrust coefficient c_T of the blade is known, the thrust in each blade can be obtained from the following equation:

$$F_T = \frac{1}{2}\frac{\rho_a}{n} c_T A_T v_\infty^2 \tag{2-74}$$

The new variable A_T is the swept area of the rotor and the remaining variables were previously defined elsewhere.

In the same manner, the circumferential wind component also produces shear in the blade root but this time in the edgewise direction of the blade. This force can be analyzed by an aerodynamic study of the blade profile, but it can also be estimated from the actual power generated by the turbine. Assuming a uniform distribution of the circumferential wind force

component over the entire blade, which is a consequence of designing the blade according to the Betz theory, the center of pressure of this force should be located at the middle of the blade length. Therefore, this shear force can be evaluated as

$$V_c = \frac{T}{3\left(r_h + \frac{L_b}{2}\right)} \tag{2-75}$$

where the torque T can be obtained from equation (2-65).

Also in the blade edgewise direction, the weight of the blades produces shear at their roots. The transversal component of the blade weight, shown in Fig. 2-5, must be subtracted from the shear V_c due to the wind. The transversal component can be obtained from the following equations:

$$\begin{aligned} V_{mb1} &= m_b g \cos(\Omega t) \\ V_{mb2} &= m_b g \cos\left(\Omega t + \tfrac{2\pi}{3}\right) \\ V_{mb3} &= m_b g \cos\left(\Omega t + \tfrac{4\pi}{3}\right) \end{aligned} \tag{2-76}$$

The total shear force V_{ei} in the edgewise direction can then be defined as

$$V_{ei} = V_c - V_{mbi} \quad ; \quad i = 1, 2, 3 \tag{2-77}$$

The resultant shear force V_{bi} on each blade root, obtained from the vector addition of the wind load F_T from equation (2-19) or (2-74), plus the reaction force in the blade due its flapping motion and V_{ei}, can be used to evaluate the maximum shear stresses in the blades. For a hollow shaft (see Hibbeler, 2004), the maximum shear stress can be approximated to

$$\tau_{i\max} = \frac{2V_{bi}}{A_b} \tag{2-78}$$

It is important to mention that the specific location and magnitude of the maximum normal stress and maximum shear stress depends on the rotor azimuth position and that, for the worse case situation, even the maximum normal stress and maximum shear stress certainly shall

occur at different places of the same cross-sectional area. Obviously, there exists a location in the cross-sectional area where the combined state of stresses is critical. In this particular place, the maximum principal stresses can be obtained and then evaluated by using a failure criterion in accordance with the composite materials used in the blades. Nevertheless, finding the particular location by analytical methods can be very complicated, especially for tubular sections. In this case, to solve this problem, it is recommended the use of finite element techniques; this topic, however, is beyond the scope of this dissertation. Since long beams design are usually controlled by bending stresses rather than shear, for simplification, we will assume as the critical location the place where the maximum normal stress is present.

2.7.2 Tower: Loads and Stresses

When it comes to the evaluation of the different stresses in the tower during an earthquake, we can see in advance at least two critical locations that might be susceptible to damage. They are the joint between the top of the tower and the nacelle bedplate, and the joint between the base of the tower and its foundation.

The joint at the top of the tower receives the forces and moments that arise from two sources: one coming from the relative displacements and rotations between the nacelle and tower and the other from the thrust loads and moments induced by the wind in the *z*-direction of the rotor. The first loads can be calculated by multiplying the global stiffness matrix in equation (2-58) by the particular degrees of freedom contributing to the development of the loads. The second set of loads can be obtained from the thrust load expressed in equation (2-19) or (2-74). Combining both calculations the following equations are obtained:

$$\begin{aligned}
\left(F_x\right)_{te} &= k_{11}^{(1)}x_1 + k_{12}^{(1)}\theta_{z1} + k_{13}^{(1)}x_2 + k_{14}^{(1)}\theta_{z2} \\
\left(M_z\right)_{te} &= k_{21}^{(1)}x_1 + k_{22}^{(1)}\theta_{z1} + k_{23}^{(1)}x_2 + k_{24}^{(1)}\theta_{z2} \\
\left(F_z\right)_{te} &= k_{55}^{(1)}z_1 + k_{56}^{(1)}\theta_{x1} + k_{57}^{(1)}z_2 + k_{58}^{(1)}\theta_{x2} - 3F_T \\
\left(M_x\right)_{te} &= k_{65}^{(1)}z_1 + k_{66}^{(1)}\theta_{x1} + k_{67}^{(1)}z_2 + k_{68}^{(1)}\theta_{x2} - 3F_T\left(h_h - h_t\right)
\end{aligned} \tag{2-79}$$

The stiffness constants *k*'s were previously defined in equation (2-55). The subscript "*te*" in each load stands for the tower "top end".

These forces and moments produce shear and bending stresses at the tower section. To obtain the maximum shear stress, it is necessary to calculate the resultant shear force as

$$\left(F_R\right)_{te} = \sqrt{\left(F_x\right)_{te}^2 + \left(F_z\right)_{te}^2} \tag{2-80}$$

and since the tower cross-section geometry is similar to that of a blade root, the use of equation (2-78) is also valid to obtain the maximum shear stress using the appropriate properties. It follows that

$$\tau_{te} = \frac{2\left(F_R\right)_{te}}{A_{te}} \tag{2-81}$$

where A_{te} is the cross-sectional area of the tower top end element. The maximum shear $(\tau_{te})_{\max}$ can be obtained adding to this shear the contribution coming from the torsion in the tower. It can be expressed as

$$\left(\tau_{te}\right)_{\max} = \tau_{te} + \frac{Tr_{te}}{J_{te}} = \frac{2\left(F_R\right)_{te}}{A_{te}} + \frac{k_t\theta_{y'}r_{te}}{J_{te}} \tag{2-82}$$

The torsion stiffness k_t was previously defined in equation (2-17), r_{te} is the radius of the tower, and J_{te} is the polar moment of inertia of the tower top end section.

To find the maximum normal stresses in the tower it is important to determine the maximum resultant moment. This moment can be obtained from the vector addition of the components in the *x'* and *z'* axes. For the *x'* component it is necessary to include the $(M_x)_{te}$ term

and the moment caused by the weight of the rotor due to the eccentricity between the center of gravity of the rotor and the longitudinal axis of the tower. Therefore, the resultant moment $(M_R)_{te}$ can be obtained from the equation

$$\left(M_R\right)_{te} = \sqrt{\left[\left(M_x\right)_{te} + m_r g d_h\right]^2 + \left(M_z\right)_{te}^2} \tag{2-83}$$

The maximum normal bending stress $(\sigma_b)_{te}$ is then obtained by

$$\left(\sigma_b\right)_{te} = \frac{\left(M_R\right)_{te} r_{te}}{I_{te}} \tag{2-84}$$

where I_{te} is the moment of inertia of the tower top end section. In addition to this stress, there is another normal stress in this area due to the gravity load caused by the mass of the rotor m_r and the mass of the nacelle m_n. Thus, the total normal stress which causes the maximum compression in the tower top end section can be computed as

$$\left(\sigma_{te}\right)_{\max} = \left(\sigma_b\right)_{te} + \frac{\left(m_r + m_n\right)g}{A_{te}} \tag{2-85}$$

Another important location that requires the evaluation of stresses is the base of the tower. The forces and moments in this area can be obtained as

$$\begin{aligned}
\left(F_x\right)_{be} &= k_{13}^{(3)} x_3 + k_{23}^{(3)} \theta_{z3} \\
\left(M_z\right)_{be} &= k_{14}^{(3)} x_3 + k_{24}^{(3)} \theta_{z3} \\
\left(F_z\right)_{be} &= k_{57}^{(3)} z_3 + k_{67}^{(3)} \theta_{x3} - 3F_T \\
\left(M_x\right)_{be} &= k_{58}^{(3)} z_3 + k_{68}^{(3)} \theta_{x3} - 3F_T h_h
\end{aligned} \tag{2-86}$$

In this case the subscript "*be*" stands for the tower "bottom end". Using a similar approach to that followed for the stresses at the top of the tower, the maximum shear stress can be computed by equation (2-82) by changing the subscripts "*te*" for "*be*".

$$\left(\tau_{be}\right)_{\max} = \tau_{be} + \frac{T r_{be}}{J_{be}} = \frac{2\left(F_R\right)_{be}}{A_{be}} + \frac{k_t \theta_y r_{be}}{J_{be}} \tag{2-87}$$

In the same manner, the maximum axial stress can be obtained by an expression similar to equation (2-85) but this time the mass of the tower m_t must be included in the second term.

$$(\sigma_{be})_{\max} = (\sigma_b)_{be} + \frac{(m_r + m_n + m_t)g}{A_{be}} \tag{2-88}$$

In the previous equation the bending stresses produced by P-Δ effects can be included; however they were ignored because their contribution was negligible.

2.7.3 Tower: Local Buckling

A possible type of failure in the wind turbine is local buckling in the tower, especially if the ratio between the radius of the tower and the wall thickness is high. This situation is more likely to occur at the base of the tower since the bending moments are larger there, but certainly can occur in any part of the tower especially if there are imperfections.

The study of local buckling of perfectly cylindrical shells almost did not change since the investigations of Brazier (1927) and Donnell (1934) at the first half of the twentieth century. Given an ideal geometry, the critical strength of a cylinder shell in axial and bending loads can be obtained as

$$\sigma_{cr} = \beta \frac{E}{\sqrt{3(1-\nu^2)}} \frac{t}{r} \tag{2-89}$$

where E is the modulus of elasticity of the material, ν is its the Poisson ratio, and t and r are the thickness and radius of the cylinder, respectively. The constant β is a correction factor to adjust the equation to different scenarios (e.g., $\beta = 1$ for the pure axial case and increases as the bending moment increases). Experiments on similar specimens tested in combined axial compression and bending indicate that using $\beta = 1.4$ gives results on the conservative side.

Using the values of Young's modulus E = 200 GPa for mild steel, β = 1.4, and ν = 0.3 the previous equation reduces to

$$\sigma_{cr} = 1.695 \times 10^{11} \frac{t}{r} \quad , \quad \text{in } [\text{Pa}] \tag{2-90}$$

Fig. 2-6 shows the variation of the maximum stress to prevent local buckling as a function of the ratio between the cylinder radius and the wall thickness for a steel cylinder.

As it can be noticed from the figure, for steel with a yield strength of 355 MPa, failure by yielding occurs prior than buckling for *r/t* less than 477. Although this value seems relatively high for the typical ratios adopted in wind turbine towers (which are around 100), the presence of imperfections, mainly those introduced by welding, reduces considerably the buckling capacity of the tower.

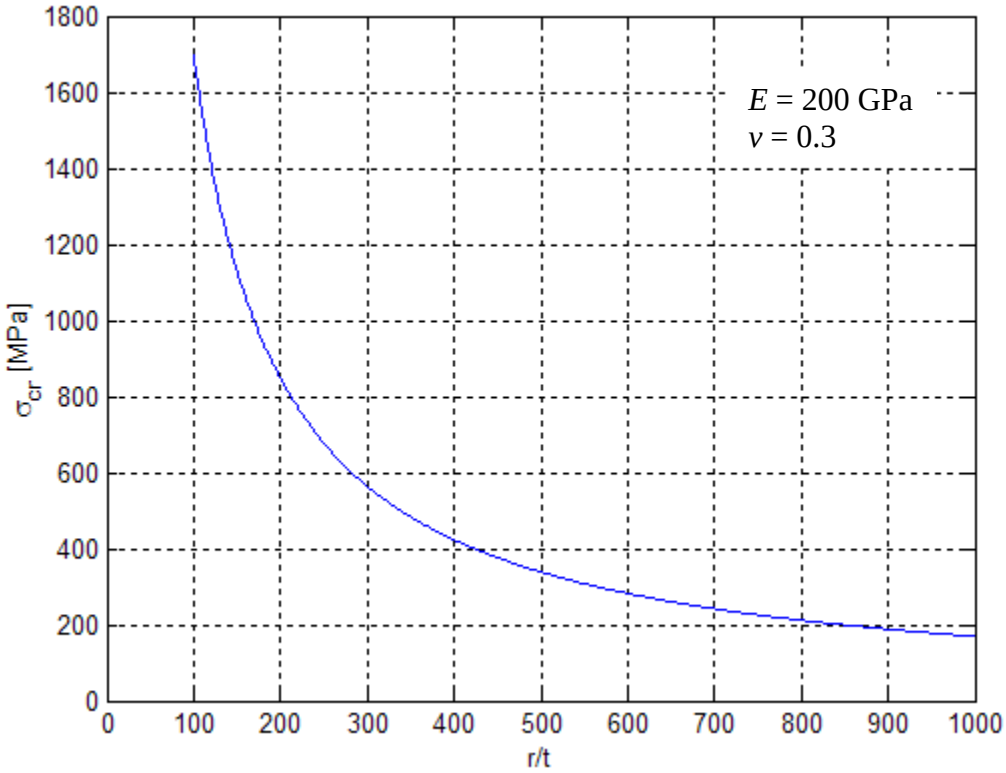

Fig.2-6: Maximum stress to prevent local buckling vs. ratio between tower radius and wall thickness

To consider the detrimental effects of imperfections, some design codes recommend the use of formulas based on empirical results. One of them, used by the European Convention for Constructional Steelwork (ECCS), (see Burton *et al*., 2001), proposes to apply a stress reduction coefficient α_B which is a function of *r/t*. The coefficient can be computed for *r/t* < 212 as

$$\alpha_B = 0.1887 + \frac{0.6734}{\sqrt{1 + 0.01 r/t}} \tag{2-91}$$

and for *r/t* > 212 as

$$\alpha_B = 0.1887 + \frac{0.5679}{\sqrt{1 + 0.01 r/t}} \tag{2-92}$$

The buckling strength σ'_{cr} is then given in terms of the yield strength σ_y and the elastic critical buckling stress σ_{cr} obtained from equation (2-89) with $\beta = 1$, as follows:

$$\begin{aligned} \sigma'_{cr} &= \sigma_y \left[1 - 0.4123 \left(\frac{\sigma_y}{\alpha_B \sigma_{cr}} \right)^{0.6} \right] \quad \text{for} \quad \alpha_B \sigma_{cr} > \frac{\sigma_y}{2} \\ \sigma'_{cr} &= 0.75 \alpha_B \sigma_{cr} \quad \text{for} \quad \alpha_B \sigma_{cr} < \frac{\sigma_y}{2} \end{aligned} \tag{2-93}$$

A plot of equation (2-93) as function of *r/t* is shown in Fig. 2-7. It was generated for a steel tower with a yield strength value of 355 MPa. Notice in this case that due to the imperfections in the tower construction, failure by local buckling always occurs prior than yielding. The discontinuity shown in the figure at *r/t* = 212 is the result of changing the coefficient α_B at this value.

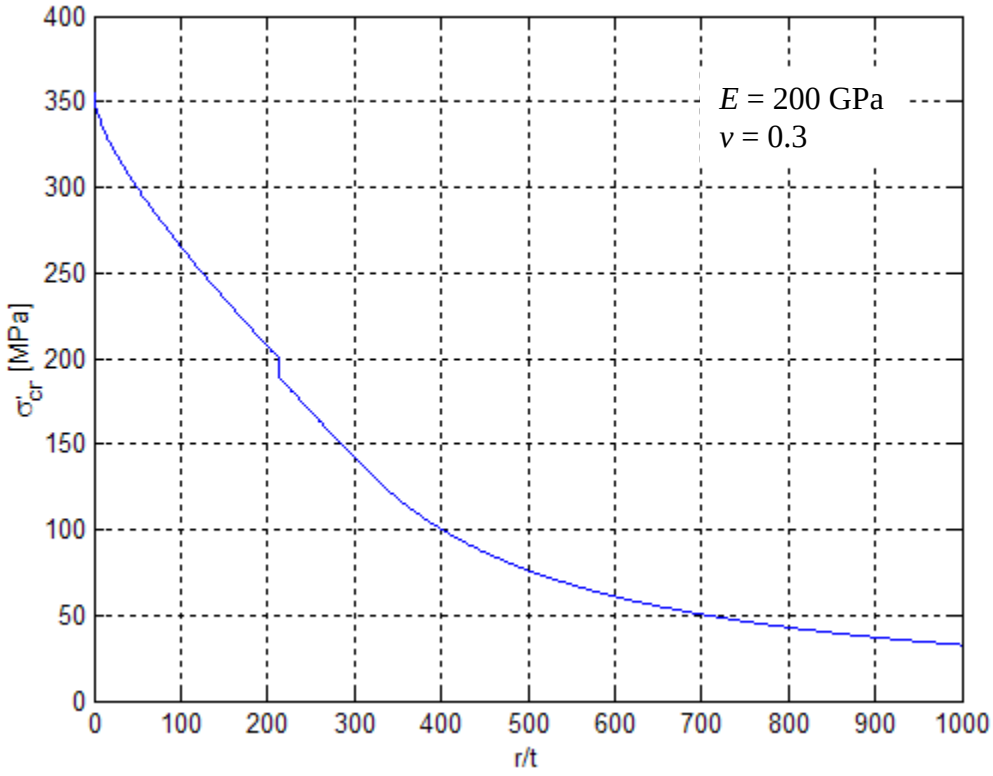

Fig.2-7: Buckling strength in bending for thin-walled steel tower based on ECCS rules

2.8 LINEARIZATION OF THE EQUATIONS OF MOTION

From equations (2-30) to (2-49) it can be observed that the set of equations of motion for the wind turbine contains non-linear terms that arise especially from the presence of gyroscopic moments due to the rotational nature of the system and terms containing time-dependent coefficients that arise from the need to trace the position of each blade in space. A dynamical

system having this last characteristic is called a non-autonomous system and the mathematical treatment is much more complicated than the analysis of an autonomous system. In order to obtain a set of equations of motion that could be studied analytically and find the natural frequencies and modal shapes of the system, some authors (see Stol *et al*., 2002 and Malcolm, 2002) linearized the system by excluding some gyroscopic terms that cross-couple the angular degrees of freedom. The implications of neglecting those terms have not been documented by the previous authors and will be the subject of study in this dissertation when the complete non-linear equations will be solved by a numerical method. Meanwhile, the approximate linearized equations can be analyzed as a linear system of differential equations with periodic coefficients. The theoretical analysis of such type of systems has been widely studied in Analytical Dynamics and applied to the study of rotorcrafts. It is frequently referred to as Floquet theory and its discussion and implementation will be presented in the next chapter.

Let us now consider the linearized equations of motion for free vibrations for the 16-degrees-of-freedom turbine model. They have the following form

$$[M(t)]\{\ddot{u}\}+[C(t)]\{\dot{u}\}+[K]\{u\}=\{0\} \tag{2-94}$$

where the vector of displacements and rotations $\{u\}$ is defined as

$$\{u\}=\{\theta_{b1} \quad \theta_{b2} \quad \theta_{b3} \quad \theta_{y'} \quad x_1 \quad \theta_{z1} \quad z_1 \quad \theta_{x1} \quad x_2 \quad \theta_{z2} \quad z_2 \quad \theta_{x2} \quad x_3 \quad \theta_{z3} \quad z_3 \quad \theta_{x3}\}^T \tag{2-95}$$

The symmetrical mass matrix and its entries are defined as

$$[M(t)]=\begin{bmatrix}
m_{aa} & 0 & 0 & m_{ad} & 0 & 0 & m_{ag} & m_{ah} & 0 & 0 & 0 & 0 & 0 & 0 & 0 & 0\\
0 & m_{bb} & 0 & m_{bd} & 0 & 0 & m_{bg} & m_{bh} & 0 & 0 & 0 & 0 & 0 & 0 & 0 & 0\\
0 & 0 & m_{cc} & m_{cd} & 0 & 0 & m_{cg} & m_{ch} & 0 & 0 & 0 & 0 & 0 & 0 & 0 & 0\\
m_{ad} & m_{bd} & m_{cd} & m_{dd} & m_{de} & 0 & 0 & 0 & 0 & 0 & 0 & 0 & 0 & 0 & 0 & 0\\
0 & 0 & 0 & m_{de} & m_{ee} & 0 & 0 & 0 & 0 & 0 & 0 & 0 & 0 & 0 & 0 & 0\\
0 & 0 & 0 & 0 & 0 & m_{ff} & 0 & 0 & 0 & 0 & 0 & 0 & 0 & 0 & 0 & 0\\
m_{ag} & m_{bg} & m_{cg} & 0 & 0 & 0 & m_{gg} & 0 & 0 & 0 & 0 & 0 & 0 & 0 & 0 & 0\\
m_{ah} & m_{bh} & m_{ch} & 0 & 0 & 0 & 0 & m_{hh} & 0 & 0 & 0 & 0 & 0 & 0 & 0 & 0\\
0 & 0 & 0 & 0 & 0 & 0 & 0 & 0 & m_{ii} & 0 & 0 & 0 & 0 & 0 & 0 & 0\\
0 & 0 & 0 & 0 & 0 & 0 & 0 & 0 & 0 & m_{jj} & 0 & 0 & 0 & 0 & 0 & 0\\
0 & 0 & 0 & 0 & 0 & 0 & 0 & 0 & 0 & 0 & m_{kk} & 0 & 0 & 0 & 0 & 0\\
0 & 0 & 0 & 0 & 0 & 0 & 0 & 0 & 0 & 0 & 0 & m_{ll} & 0 & 0 & 0 & 0\\
0 & 0 & 0 & 0 & 0 & 0 & 0 & 0 & 0 & 0 & 0 & 0 & m_{mm} & 0 & 0 & 0\\
0 & 0 & 0 & 0 & 0 & 0 & 0 & 0 & 0 & 0 & 0 & 0 & 0 & m_{nn} & 0 & 0\\
0 & 0 & 0 & 0 & 0 & 0 & 0 & 0 & 0 & 0 & 0 & 0 & 0 & 0 & m_{oo} & 0\\
0 & 0 & 0 & 0 & 0 & 0 & 0 & 0 & 0 & 0 & 0 & 0 & 0 & 0 & 0 & m_{pp}
\end{bmatrix} \tag{2-96}$$

$$m_{aa} = m_{bb} = m_{cc} = \tfrac{1}{4} m_b L_b^2 + I_b$$
$$m_{ad} = -\left[\tfrac{1}{2} m_b \left(r_h + \tfrac{L_b}{2}\right) L_b + I_b\right] \cos \Omega t$$
$$m_{ag} = m_{bg} = m_{cg} = \tfrac{1}{2} m_b L_b$$
$$m_{ah} = \left[\tfrac{1}{2} m_b \left(r_h + \tfrac{L_b}{2}\right) L_b + I_b\right] \sin \Omega t$$
$$m_{bd} = -\left[\tfrac{1}{2} m_b \left(r_h + \tfrac{L_b}{2}\right) L_b + I_b\right] \cos\left(\Omega t + \tfrac{2\pi}{3}\right)$$
$$m_{bh} = \left[\tfrac{1}{2} m_b \left(r_h + \tfrac{L_b}{2}\right) L_b + I_b\right] \sin\left(\Omega t + \tfrac{2\pi}{3}\right)$$
$$m_{cd} = -\left[\tfrac{1}{2} m_b \left(r_h + \tfrac{L_b}{2}\right) L_b + I_b\right] \cos\left(\Omega t + \tfrac{4\pi}{3}\right)$$
$$m_{ch} = \left[\tfrac{1}{2} m_b \left(r_h + \tfrac{L_b}{2}\right) L_b + I_b\right] \sin\left(\Omega t + \tfrac{4\pi}{3}\right)$$
$$m_{dd} = m_r d_h^2 + \tfrac{3}{2} m_b \left(r_h + \tfrac{L_b}{2}\right)^2 + I_t + \tfrac{3}{2} I_b$$
$$m_{de} = m_r d_h$$
$$m_{ee} = m_{gg} = m_r + m_n + \tfrac{1}{2} \rho A_1 l_e$$
$$m_{ff} = \tfrac{1}{24} \rho A_1 l_e^3$$
$$m_{hh} = m_r d_h^2 + \tfrac{3}{2} m_b \left(r_h + \tfrac{L_b}{2}\right)^2 + I_t + \tfrac{3}{2} I_b + \tfrac{1}{24} \rho A_1 l_e^3$$
$$m_{ii} = m_{kk} = \tfrac{1}{2} \rho \left(A_1 + A_2\right) l_e$$
$$m_{jj} = m_{ll} = \tfrac{1}{24} \rho \left(A_1 + A_2\right) l_e^3$$
$$m_{mm} = m_{oo} = \tfrac{1}{2} \rho \left(A_2 + A_3\right) l_e$$
$$m_{nn} = m_{pp} = \tfrac{1}{24} \rho \left(A_2 + A_3\right) l_e^3$$

As previously stated, the mass matrix contains inertia terms that are periodic in time. The non-symmetrical damping matrix and its entries are defined as

$$[C(t)]=\begin{bmatrix}
c_{aa} & 0 & 0 & c_{ad} & 0 & 0 & c_{ag} & c_{ah} & 0 & 0 & 0 & 0 & 0 & 0 & 0 & 0 \\
0 & c_{bb} & 0 & c_{bd} & 0 & 0 & c_{bg} & c_{bh} & 0 & 0 & 0 & 0 & 0 & 0 & 0 & 0 \\
0 & 0 & c_{cc} & c_{cd} & 0 & 0 & c_{cg} & c_{ch} & 0 & 0 & 0 & 0 & 0 & 0 & 0 & 0 \\
c_{ad} & c_{bd} & c_{cd} & 0 & 0 & 0 & 0 & c_{dh} & 0 & 0 & 0 & 0 & 0 & 0 & 0 & 0 \\
0 & 0 & 0 & 0 & 0 & 0 & 0 & 0 & 0 & 0 & 0 & 0 & 0 & 0 & 0 & 0 \\
0 & 0 & 0 & 0 & 0 & 0 & 0 & 0 & 0 & 0 & 0 & 0 & 0 & 0 & 0 & 0 \\
c_{ga} & c_{gb} & c_{gc} & 0 & 0 & 0 & c_{gg} & 0 & 0 & 0 & 0 & 0 & 0 & 0 & 0 & 0 \\
c_{ah} & c_{bh} & c_{ch} & -c_{dh} & 0 & 0 & 0 & 0 & 0 & 0 & 0 & 0 & 0 & 0 & 0 & 0 \\
0 & 0 & 0 & 0 & 0 & 0 & 0 & 0 & 0 & 0 & 0 & 0 & 0 & 0 & 0 & 0 \\
0 & 0 & 0 & 0 & 0 & 0 & 0 & 0 & 0 & 0 & 0 & 0 & 0 & 0 & 0 & 0 \\
0 & 0 & 0 & 0 & 0 & 0 & 0 & 0 & 0 & 0 & 0 & 0 & 0 & 0 & 0 & 0 \\
0 & 0 & 0 & 0 & 0 & 0 & 0 & 0 & 0 & 0 & 0 & 0 & 0 & 0 & 0 & 0 \\
0 & 0 & 0 & 0 & 0 & 0 & 0 & 0 & 0 & 0 & 0 & 0 & 0 & 0 & 0 & 0 \\
0 & 0 & 0 & 0 & 0 & 0 & 0 & 0 & 0 & 0 & 0 & 0 & 0 & 0 & 0 & 0 \\
0 & 0 & 0 & 0 & 0 & 0 & 0 & 0 & 0 & 0 & 0 & 0 & 0 & 0 & 0 & 0 \\
0 & 0 & 0 & 0 & 0 & 0 & 0 & 0 & 0 & 0 & 0 & 0 & 0 & 0 & 0 & 0
\end{bmatrix} \tag{2-97}$$

$$\begin{aligned}
c_{aa} &= c_{bb} = c_{cc} = c_3 \\
c_{ad} &= \left[\tfrac{1}{2} m_b \left(r_h + \tfrac{L_b}{2}\right) L_b + I_b\right] \Omega \sin \Omega t \\
c_{ag} &= c_{bg} = c_{cg} = c_4 \\
c_{ah} &= \left[\tfrac{1}{2} m_b \left(r_h + \tfrac{L_b}{2}\right) L_b + I_b\right] \Omega \cos \Omega t \\
c_{bd} &= \left[\tfrac{1}{2} m_b \left(r_h + \tfrac{L_b}{2}\right) L_b + I_b\right] \Omega \sin\left(\Omega t + \tfrac{2\pi}{3}\right) \\
c_{bh} &= \left[\tfrac{1}{2} m_b \left(r_h + \tfrac{L_b}{2}\right) L_b + I_b\right] \Omega \cos\left(\Omega t + \tfrac{2\pi}{3}\right) \\
c_{cd} &= \left[\tfrac{1}{2} m_b \left(r_h + \tfrac{L_b}{2}\right) L_b + I_b\right] \Omega \sin\left(\Omega t + \tfrac{4\pi}{3}\right) \\
c_{ch} &= \left[\tfrac{1}{2} m_b \left(r_h + \tfrac{L_b}{2}\right) L_b + I_b\right] \Omega \cos\left(\Omega t + \tfrac{2\pi}{3}\right) \\
c_{dh} &= -\left[3 m_b \left(r_h + \tfrac{L_b}{2}\right)^2 + I_a + 3 I_b\right] \Omega \\
c_{ga} &= c_{gb} = c_{gc} = c_1 \\
c_{gg} &= 3 c_2
\end{aligned}$$

Notice that the matrix [$C(t)$] contains some gyroscopic terms which arise from the nature of the three dimensional motion of the rotor. As it can be seen, they are time-dependent and also are proportional to the rotor speed Ω. Additionally, they cross-couple angular degrees of freedom thus meaning that a rotation of the system in one degree of freedom induces a moment in another angular degree of freedom.

The symmetrical stiffness matrix is constant and its entries are defined as

$$[K]=\begin{bmatrix}
k_{aa} & 0 & 0 & 0 & 0 & 0 & 0 & 0 & 0 & 0 & 0 & 0 & 0 & 0 & 0 & 0 \\
0 & k_{bb} & 0 & 0 & 0 & 0 & 0 & 0 & 0 & 0 & 0 & 0 & 0 & 0 & 0 & 0 \\
0 & 0 & k_{cc} & 0 & 0 & 0 & 0 & 0 & 0 & 0 & 0 & 0 & 0 & 0 & 0 & 0 \\
0 & 0 & 0 & k_{dd} & 0 & 0 & 0 & 0 & 0 & 0 & 0 & 0 & 0 & 0 & 0 & 0 \\
0 & 0 & 0 & 0 & k_{ee} & k_{ef} & 0 & 0 & k_{ei} & k_{ej} & 0 & 0 & 0 & 0 & 0 & 0 \\
0 & 0 & 0 & 0 & k_{ef} & k_{ff} & 0 & 0 & k_{fi} & k_{fj} & 0 & 0 & 0 & 0 & 0 & 0 \\
0 & 0 & 0 & 0 & 0 & 0 & k_{gg} & k_{gh} & 0 & 0 & k_{gk} & k_{gl} & 0 & 0 & 0 & 0 \\
0 & 0 & 0 & 0 & 0 & 0 & k_{gh} & k_{hh} & 0 & 0 & k_{hk} & k_{hl} & 0 & 0 & 0 & 0 \\
0 & 0 & 0 & 0 & k_{ei} & k_{fi} & 0 & 0 & k_{ii} & k_{ij} & 0 & 0 & k_{im} & k_{in} & 0 & 0 \\
0 & 0 & 0 & 0 & k_{ej} & k_{fj} & 0 & 0 & k_{ij} & k_{jj} & 0 & 0 & k_{jm} & k_{jn} & 0 & 0 \\
0 & 0 & 0 & 0 & 0 & 0 & k_{gk} & k_{hk} & 0 & 0 & k_{kk} & k_{kl} & 0 & 0 & k_{ko} & k_{kp} \\
0 & 0 & 0 & 0 & 0 & 0 & k_{gl} & k_{hl} & 0 & 0 & k_{kl} & k_{ll} & 0 & 0 & k_{lo} & k_{lp} \\
0 & 0 & 0 & 0 & 0 & 0 & 0 & 0 & k_{im} & k_{jm} & 0 & 0 & k_{mm} & k_{mn} & 0 & 0 \\
0 & 0 & 0 & 0 & 0 & 0 & 0 & 0 & k_{in} & k_{jn} & 0 & 0 & k_{mn} & k_{nn} & 0 & 0 \\
0 & 0 & 0 & 0 & 0 & 0 & 0 & 0 & 0 & 0 & k_{ko} & k_{lo} & 0 & 0 & k_{oo} & k_{op} \\
0 & 0 & 0 & 0 & 0 & 0 & 0 & 0 & 0 & 0 & k_{kp} & k_{lp} & 0 & 0 & k_{op} & k_{pp}
\end{bmatrix} \tag{2-98}$$

$$k_{aa} = k_{bb} = k_{cc} = k_b$$
$$k_{dd} = k_t$$

To avoid repetition, the entries that follow the same arrangement than the tower global stiffness matrix presented in equation (2-58) were omitted.

CHAPTER 3: STABILITY ANALYSIS OF THE LINEAR WIND TURBINE MODEL

3.1 INTRODUCTION

As previously discussed in Section 2.8, some researchers linearized the highly non-linear equations of motion by neglecting some gyroscopic terms that cross-couple the yawing velocity $\dot{\theta}_{y'}$ of the rotor with the fore-aft angular velocity $\dot{\theta}_{x'}$ of the rotor or with the flapping angular velocity of the blades (see for instance, Stol et al., 2002 and Malcom, 2002). In this way only the gyroscopic terms that cross-couple the constant azimuth velocity Ω of the blades remain. The importance of the omitted gyroscopic terms was not examined by the previous authors and this will be studied in this dissertation. Nevertheless, the resulting linearized and homogeneous equations of motion can be used to obtain an approximation of the natural frequencies of the system and verify its stability under different rotor speeds.

The linearized equations of motion for the steady operating state contain time-dependent periodic terms that stem from the cyclic position of the blades during their rotation. Because of those terms the system is governed by a set of ordinary differential equations with periodic coefficients. For this type of systems the conventional eigenvalue analysis is not applicable. The most significant tool for the analysis of the stability and response of this type of system is

known as the Floquet theory, named after the French mathematician Gaston Floquet (1847-1920). For the interested reader, Jordan and Smith (1983), Meirovitch (1988), and Johnson (1994), give excellent descriptions of the classical development of the Floquet theory. For the sake of completeness and since this is a specialized topic, the next section summarizes the fundamental concepts of the theory. Also for a better appreciation of the application of the Floquet theory, a few simple examples will be considered and finally applied to the specific wind turbine model used here.

3.2 FLOQUET THEORY

The first step in the application of the Floquet theory is to transform the system of differential equations with periodic coefficients into a first-order system known as the state form:

$$\{\dot{x}\} = [A(t)]\{x\} \tag{3-1}$$

where $\{x\}$ is a state vector composed of $2n$ elements and $[A(t)]$ is a time-periodic matrix with period T such that

$$[A(t)] = [A(t+T)] \tag{3-2}$$

Let us now assume that we know a closed form solution of equation (3-1) and that it can be arranged in terms of a fundamental matrix $[\Phi(t)]$ such that

$$\{x(t)\} = [\Phi(t)]\{x(0)\} \tag{3-3}$$

Based on the Floquet theorem (see Jordan and Smith, 1983), this fundamental matrix must satisfy two conditions: a) it can be resolved into a time periodic matrix and a matrix exponential

of a constant matrix and, b) the fundamental matrix is equal to the identity matrix for $t = 0$. Both conditions can be expressed as

$$[\Phi(t)] = [P(t)]e^{t[R]} \tag{3-4}$$

$$[\Phi(0)] = [I] \tag{3-5}$$

where $[P(t)] = [P(t+T)]$. Since each column of the fundamental matrix $[\Phi(t)]$, by definition, contains a linearly independent solution of equation (3-1), therefore, the fundamental matrix also satisfies the matrix equation

$$[\dot{\Phi}(t)] = [A(t)][\Phi(t)] \tag{3-6}$$

In view of equations (3-2) and (3-6) we can write

$$[\dot{\Phi}(t+T)] = [A(t+T)][\Phi(t+T)] = [A(t)][\Phi(t+T)] \tag{3-7}$$

from which we realize that $[\Phi(t+T)]$ is also a fundamental matrix of equation (3-1). Given that both $[\Phi(t)]$ and $[\Phi(t+T)]$ represent fundamental solutions of the system, there must exist a constant matrix $[F]$, sometimes called Floquet transition matrix or monodromy matrix, such that

$$[\Phi(t+T)] = [\Phi(t)][F] \tag{3-8}$$

Let us now evaluate equation (3-4) for $t = 0$ and for $t = T$. The results obtained are

$$[\Phi(0)] = [P(0)] = [I] \tag{3-9}$$

$$[\Phi(T)] = [P(T)]e^{T[R]} \tag{3-10}$$

Since $[P(t)]$ is periodic, it follows that

$$[P(0)] = [P(T)] = [I] \tag{3-11}$$

and setting $t = 0$ in equation (3-8), using the fact that $[\Phi(0)] = [I]$, and using the equation (3-10) with $[P(T)] = [I]$ one obtains

$$[F] = [\Phi(T)] = e^{T[R]} \tag{3-12}$$

and from this expression one can obtain that the matrix [*R*] is

$$[R] = \frac{1}{T}\ln[\Phi(T)] \tag{3-13}$$

From equations (3-3) and (3-4) we can write $\{x(t)\} = [P(t)]e^{t[R]}\{x(0)\}$ which permit us to conclude that, because [*P*(*t*)] is bounded, the stability of $\{x(t)\}$ is then governed by the eigenvalues of [*R*]. The eigenvalues of [*R*], denoted as s_i (for i = 1 to 2n), are called the *characteristic exponents* associated with the periodic matrix [*A*(*t*)] and are obtained from the solution of the eigenvalue problem

$$[R][V] = [V][S] \tag{3-14}$$

where [*S*] is a diagonal matrix containing the characteristic exponents s_i and [*V*] is a matrix of eigenvectors that describes the mode shapes for the system. In terms of the eigenvalues and eigenvectors, the matrix [*R*] can be expressed as

$$[R] = [V][S][V]^{-1} \tag{3-15}$$

Likewise, the eigenvalues of [*F*] or equivalently [Φ(*T*)] are called the *characteristic multipliers* associated with the periodic matrix [*A*(*t*)] and are denoted as λ_i. They are obtained from the eigenvalue problem

$$[\Phi(T)][V] = [V][\Lambda] \tag{3-16}$$

which can also be written as:

$$[\Phi(T)] = [V][\Lambda][V]^{-1} \tag{3-17}$$

The matrix [Λ] is a diagonal matrix that contains the characteristic multipliers λ_i. Note that the transition matrix [*F*] shares with [*R*] the same eigenvector matrix [*V*]. This can be shown by

using a property of exponential matrices (see Horn and Johnson, 1991), which states that if $[R] = [V]\,[S]\,[V]^{-1}$ and $[S]$ is diagonal, then

$$e^{T[R]} = [V] e^{T[S]} [V]^{-1} \tag{3-18}$$

Substituting equation (3-18) into equation (3-12) leads to

$$[\Phi(T)] = [V] e^{T[S]} [V]^{-1} \tag{3-19}$$

Comparing this equation with equation (3-17) it is evident that the characteristic multipliers can be related to the characteristic exponents by

$$\lambda_i = e^{s_i T} \tag{3-20}$$

This provides a convenient way to obtain the characteristic exponents s_i without requiring the prior evaluation of the matrix $[R]$. Since the characteristic multipliers λ_i are, in general, complex numbers, the characteristic exponent s_i can be obtained from the expression (see Moretti, 1964)

$$s_i = \frac{1}{T}\left[\ln|\lambda_i| + j\left(\tan^{-1}\left(\frac{\mathrm{Im}(\lambda_i)}{\mathrm{Re}(\lambda_i)}\right) + 2\pi k\right)\right] = \xi_i + j\omega_i \tag{3-21}$$

where $j = \sqrt{-1}$. The real part ξ_i represents a quantity directly associated to the amount of damping in the system. Although some authors call it *modal damping coefficient* or *damping rate* (e.g., Stol *et al*., 2002 and Bauchau and Nikishkov, 2001), it should not be confused with the usual modal damping ratio since the real part ξ_i is not dimentionless (it has units of $[s^{-1}]$). On the other hand, the imaginary part of the characteristic exponent is associated to the modal frequency ω_i. The indefinite integer k appears because there are unlimited branches in the logarithm of a complex number. The integer multiple can be determined, as shown later on, by frequency identification of the time response of the system.

Hence, the system is exponentially stable if all the characteristic exponents s_i have negative real parts ($\xi_i < 0$), and exponentially unstable if at least one of the characteristic exponents has a positive real part ($\xi_i > 0$). If the real part of a characteristic exponent is identical to zero, then the system has a purely periodic solution. If a characteristic exponent contains only a negative real part, the system does not oscillate and it is said to be overdamped.

In the case of the wind turbine system, the identification of the dominant motion of the system can be figured out from the matrix of eigenvectors [*V*]. This matrix contains the actual mode shapes of the system for $t = T$ (with $T = 2\pi/\Omega$) which coincide with the initial blade configuration of the wind turbine, i.e., when the blade number 1 is directed along the positive *x'*-axis (see Fig. 2-1).

In view of equation (3-12) and despite of the fact that it is usually impossible to obtain closed form expressions of [$\Phi(t)$], significant knowledge regarding the stability of the system can be obtained by evaluating the transition matrix [*F*] at the end of one period. This is the reason why the most important step in the application of the Floquet theory reduces to the calculation of the transition matrix [*F*]. As a result, several techniques have been developed to obtain the transition matrix. The classical approach is to calculate the transition matrix by solving equation (3-1) numerically (for instance, with a Runge-Kutta scheme) in sequence, using each time a specific set of initial conditions. The sets of initial conditions correspond to the columns of the identity matrix [*I*] to satisfy the criteria in equation (3-5). Subsequently, each set of equations, corresponding to the columns of the transition matrix, are evaluated for $t = T$. That technique can be easily implemented in systems with few degrees of freedom, but the computational cost becomes overwhelming for systems with a large quantity of degrees of freedom. For instance, Stol *et al*. (2002) recommend not to exceed 50 degrees of freedom. Since the wind turbine

model used herein contains at the most 16 degrees of freedom, we will use for simplicity the classical approach to obtain the transition matrix.

Nevertheless, to deal with systems with large number of degrees of freedom some researchers have proposed novel extensions to the Floquet theory. For instance, Sinha (2005), worked out a computational procedure to obtain the transition matrix in terms of Chevysheb polynomials which are suitable for algebraic manipulation. This procedure yields simpler forms of equations which in many cases can be integrated in closed form. Other authors (e.g., Bauchau and Nikishkov, 2001) proposed an implicit Floquet analysis in which the stability of the system is obtained without the explicit computation of [*F*]. The method relies on the properties of the Arnoldi algorithm (Saad, 1981) which permits to extract the dominant eigenvalues of the system without computing the complete transition matrix during one period. This results in significant computational savings.

3.3 EXAMPLES OF THE FLOQUET THEORY

Example 3-1

Let us now examine a particular case of a simple system of differential equations for which a closed form solution of a fundamental matrix is already known. For instance

$$\begin{aligned} &\dot{x}_1 - x_1 = x_2 \\ &\left(2 + \sin t - \cos t\right)\dot{x}_2 - \left(\cos t + \sin t\right)x_2 = 0 \end{aligned} \tag{3-22}$$

Obviously, the system contains periodic coefficients with a period of $T = 2\pi$. Written in first-order state form, the system can be expressed as

$$\begin{Bmatrix} \dot{x}_1 \\ \dot{x}_2 \end{Bmatrix} = [A(t)] \begin{Bmatrix} x_1 \\ x_2 \end{Bmatrix} = \begin{bmatrix} 1 & \dfrac{1}{(\cos t + \sin t)} \\ 0 & \dfrac{}{(2 + \sin t - \cos t)} \end{bmatrix} \begin{Bmatrix} x_1 \\ x_2 \end{Bmatrix} \tag{3-23}$$

It can be shown (see Jordan and Smith, 1983) that the explicit solutions of equation (3-15) are

$$\begin{aligned} x_1 &= a_1 e^t - a_2 (2 + \sin t) \\ x_2 &= a_2 (2 + \sin t - \cos t) \end{aligned} \tag{3-24}$$

where a_1 and a_2 are unknown constants that can be obtained from the initial conditions. Examining matrix $[A(t)]$ in equation (3-23) it is evident that the period T is 2π.

The specific fundamental matrix $[\Phi(t)]$ for the system that satisfy the criterion $[\Phi(0)] = [I]$ can be constructed finding two sets of constants a_1 and a_2. By equating the equations (3-24) to the columns of $[I]$ the sets of constants are found to be $a_1 = 1$, $a_2 = 0$ and $a_1 = 2$, $a_2 = 1$, respectively. Substitution of these sets of constants in equation (3-24) leads to:

$$[\Phi(t)] = \begin{bmatrix} e^t & 2e^t - (2 + \sin t) \\ 0 & 2 + \sin t - \cos t \end{bmatrix} \tag{3-25}$$

Therefore, recalling equation (3-12), the Floquet transition matrix can be obtained by evaluation of the fundamental matrix for $t = T = 2\pi$, which is

$$[\Phi(T)] = \begin{bmatrix} e^{2\pi} & 2e^{2\pi} - 2 \\ 0 & 1 \end{bmatrix} \tag{3-26}$$

The characteristic multipliers λ_i are obtained from the eigenvalue problem defined in equation (3-16): $[\Phi(T)]\{V_i\} = \lambda_i \{V_i\}$ where $\{V_i\}$ is the i^{th} eigenvector. The eigenvalues λ_i that form the diagonal matrix $[\Lambda]$ can be obtained from the characteristic determinant of $[\Phi(T)]$ set equal to zero:

$$\det \begin{bmatrix} e^{2\pi} - \lambda & 2e^{2\pi} - 2 \\ 0 & 1 - \lambda \end{bmatrix} = 0 \tag{3-27}$$

After expansion, the characteristic equation becomes

$$\lambda^2 - \left(e^{2\pi} + 1\right)\lambda + e^{2\pi} = 0 \tag{3-28}$$

with real solutions $\lambda_1 = 1$ and $\lambda_2 = e^{2\pi}$. The matrix $[\Lambda]$ is then arranged as

$$[\Lambda] = \begin{bmatrix} 1 & 0 \\ 0 & e^{2\pi} \end{bmatrix} \tag{3-29}$$

The characteristic exponents s_1 and s_2 are obtained from equation (3-21) resulting in: $s_1 = T^{-1}\ln(1) = 0$ and $s_2 = T^{-1}\ln\left(e^{2\pi}\right) = 1$. In this case the calculation is simple because λ_1 and λ_2 are real numbers. Since the first characteristic exponent s_1 is equal to zero, this indicates that exists a purely periodic solution for the system, in this case with period $T = 2\pi$. Notice from inspection of equation (3-24) that this actually occurs when $a_1 = 0$. The other characteristic exponent is an asymptotically unstable solution because it has a positive real part.

Example 3-2

The following example consists in a single pendulum with a harmonic motion of its support as shown in Fig. 3-1.

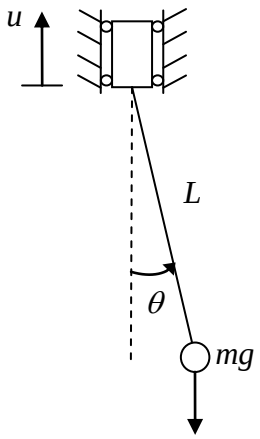

Fig.3-1: Pendulum with oscillatory motion in the support

Considering small rotations, it can be shown that the equation of motion for the pendulum whose support will be assumed to have a harmonic motion of the form $u = A \cos \Omega t$ is

$$\ddot{\theta} + \left(\frac{g}{L} - \frac{A\Omega^2}{L} \cos \Omega t \right) \theta = 0 \tag{3-30}$$

As it can be observed, this equation contains a periodic coefficient acting as a sort of stiffness coefficient with period $T = 2\pi/\Omega$. The equation of motion can be written in a first-order state form as

$$\begin{Bmatrix} \dot{x}_1 \\ \dot{x}_2 \end{Bmatrix} = [A(t)] \begin{Bmatrix} x_1 \\ x_2 \end{Bmatrix} \tag{3-31}$$

where $x_1 = \theta$ and $x_2 = \dot{\theta}$. In the notation of equation (3-1) matrix $[A(t)]$ is

$$[A(t)] = \begin{bmatrix} 0 & 1 \\ -\frac{g}{L} + \frac{A\Omega^2}{L} \cos \Omega t & 0 \end{bmatrix} \tag{3-32}$$

It is not the intention of this example to verify if explicit solutions exist for the Floquet transition matrix for this or other more complex systems; as it was mentioned before, in general, they do not exist. So we will directly use a numerical integration technique to evaluate equation (3-31) using the required sets of initial conditions. To accomplish this, the computer software MATLAB will be used. MATLAB includes a computational package that solves ordinary differential equations named *ode45* that is based on a one-step Runge-Kutta solver of order 4 or 5. In case that *ode45* fails or is too inefficient (as it usually happens with the so called stiff problems) we can use the higher order solver *ode15s*. A specific description of this solver is presented in the next section. In this example we will use the following values: A = 0.153 m, L = 0.305 m, $\Omega = 2\pi$ rad/s, and g = 9.81 m/s^2. The first column of the transition matrix is obtained from the numerical integration of equation (3-31) for $0 \le t \le T$ with initial conditions

$x_1(0) = 1$ and $x_2(0) = 0$. The second column is obtained in a similar fashion but now using the set of initial conditions $x_1(0) = 0$ and $x_2(0) = 1$. In both cases the solution must be evaluated at time $t = T$. The complete transition matrix is then given by

$$[F] = [\Phi(T)] = \begin{bmatrix} 0.7252 & -0.1350 \\ 3.5112 & 0.7252 \end{bmatrix} \tag{3-33}$$

The characteristic multipliers are obtained from the determinant of equation (3-33) set equal to zero, hence:

$$\begin{aligned} \lambda_1 &= 0.7252 + j0.6885 \\ \lambda_2 &= 0.7252 - j0.6885 \end{aligned} \tag{3-34}$$

The characteristic exponents are obtained from equation (3-21)

$$\begin{aligned} s_1 &= 0 + j0.7594 \\ s_2 &= 0 - j0.7594 \end{aligned} \tag{3-35}$$

The zero real part in the exponents implies that all modes are undamped. The imaginary part indicates one of the possible modal frequencies. It should be kept in mind that by adding integer multiples of $2\pi/T$ to the value 0.7594 rad/s one could obtain the true frequency. If the support of the pendulum is stationary, the natural frequency is $\sqrt{g/L}$ = 5.671 rad/s.

Example 3-3

Let us now consider a system with two degrees of freedom in order to examine its stability and mode shapes. The system, shown in Fig. 3-2, consists of two sprung masses in which one of them is attached to a viscous damper. Also, the mass of this car is harmonically changing in time with a frequency Ω.

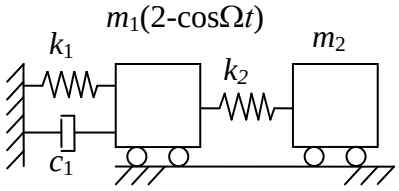

Fig.3-2: Two degrees of freedom system with periodic mass used in example 3-3

Considering the free vibration of the system, the equations of motion are

$$\begin{bmatrix} m_1(2-\cos\Omega t) & 0 \\ 0 & m_2 \end{bmatrix}\begin{Bmatrix} \ddot{u}_1 \\ \ddot{u}_2 \end{Bmatrix}+\begin{bmatrix} c_1 & 0 \\ 0 & 0 \end{bmatrix}\begin{Bmatrix} \dot{u}_1 \\ \dot{u}_2 \end{Bmatrix}+\begin{bmatrix} k_1+k_2 & -k_2 \\ -k_2 & k_2 \end{bmatrix}\begin{Bmatrix} u_1 \\ u_2 \end{Bmatrix}=\begin{Bmatrix} 0 \\ 0 \end{Bmatrix} \tag{3-36}$$

Note that the system is periodic and non-classically damped. The equations written in first-order state form are

$$\begin{Bmatrix} \dot{x}_1 \\ \dot{x}_2 \\ \dot{x}_3 \\ \dot{x}_4 \end{Bmatrix}=[A(t)]\begin{Bmatrix} x_1 \\ x_2 \\ x_3 \\ x_4 \end{Bmatrix} \tag{3-37}$$

where $x_1 = u_1$, $x_2 = u_2$, $x_3 = \dot{u}_1$, and $x_4 = \dot{u}_2$. The periodic matrix $[A(t)]$ is then defined as

$$[A(t)]=\begin{bmatrix} 0 & 0 & 1 & 0 \\ 0 & 0 & 0 & 1 \\ -\dfrac{k_1+k_2}{m_1(2-\cos\Omega t)} & \dfrac{k_2}{m_1(2-\cos\Omega t)} & -\dfrac{c_1}{m_1(2-\cos\Omega t)} & 0 \\ \dfrac{k_2}{m_2} & -\dfrac{k_2}{m_2} & 0 & 0 \end{bmatrix} \tag{3-38}$$

With the objective to study the effect of changing the amount of damping present in the system, let us examine several scenarios. The first one ignores the damping (i.e., $c_1 = 0$). Following the same steps to construct the Floquet matrix than in the previous example and using

the following values for the properties of the system: m_1 = 50 kg, m_2 = 50 kg, Ω = 6.0 rad/s, k_1 = 1000 N/m and k_2 = 1000 N/m, the two pairs of characteristic exponents are obtained:

$$s_1, s_2 = \{0 \pm j2.515\}; \quad s_3, s_4 = \{0 \pm j0.0307\} \tag{3-39}$$

As expected, the zero real parts indicate that the system is undamped. The following vectors (and their complex conjugates, not shown) represent the corresponding mode shapes. Note that the velocity components of the state-vector (the last two rows) were removed.

$$\begin{Bmatrix} 0.2706\angle 90^0 \\ 0.4006\angle 90^0 \end{Bmatrix}, \quad \begin{Bmatrix} 0.0186\angle 90^0 \\ 0.2023\angle -90^0 \end{Bmatrix} \tag{3-40}$$

The components in each vector represent the amplitude and phase angle contribution from each generalized coordinate. As it can be noticed from the first eigenvector, this mode describes a phased motion since both angles are the same. On the other hand, the second mode is an out-of-phase motion since the phase angles are 180^o apart.

As a second case, let us assume that a small damping is present by assigning a damper coefficient c_2 = 40 N-s/m. The following complex conjugate pairs represent the new characteristic exponents:

$$s_1, s_2 = \{-0.1101 \pm j2.5146\}; \quad s_3, s_4 = \{-0.1207 \pm j0.0373\} \tag{3-41}$$

Notice that the real part ξ of the characteristic exponent, which is related to a modal damping ratio, has a negative value meaning the system is stable. The corresponding eigenvectors, complemented by their complex conjugates (c.c.) are:

$$\begin{Bmatrix} 0.2708\angle 93.93^0 \\ 0.4008\angle 92.41^0 \end{Bmatrix}, \begin{Bmatrix} 0.0188\angle 95.30^0 \\ 0.2030\angle -91.24^0 \end{Bmatrix}, + \text{c.c.} \tag{3-42}$$

Comparing this case with the undamped one, we can see that the small amount of damping mostly affects the phase of the eigenvectors while the amplitude remains almost the same. As it will be further discussed on Section 3.5, the addition of damping makes the system less synchronized.

To conclude this example, let us now examine the same system but now considering a larger damping coefficient of c_2 = 400 N-s/m. The Floquet analysis now leads to the following characteristic exponents:

$$s_1, s_2 = \{-1.3653 \pm j2.4888\}; \quad s_3, s_4 \{-0.9434 \pm j0.6990\} \tag{3-43}$$

with the following eigenvectors:

$$\begin{Bmatrix} 0.2968\angle 91.91^0 \\ 0.4292\angle 79.29^0 \end{Bmatrix}, \begin{Bmatrix} 0.0427\angle 61.57^0 \\ 0.1972\angle -68.48^0 \end{Bmatrix}, + \text{c.c} \tag{3-44}$$

As it can be observed, there is now a change in the amplitude and phase of both eigenvectors associated to the high value of the damping. Let us take a look to the first eigenvalue for which the value of the real part is ξ < -1. The first impression coming from an erroneous comparison with a single degree-of-freedom problem is to assume that this mode is overdamped. Certainly this is not the situation here for two reasons; firstly, because the characteristic exponent contains an imaginary part with a probable frequency of 2.4888 rad/s. In addition, it is recalled that here $\xi_i = \text{Re}(s_i)$ is not an equivalent modal damping ratio but rather a quantity that is a measure of the amount of damping. A further examination of the free vibration response of the system indicates that the two car masses have an oscillatory motion with a highly decaying rate indicating the system is still underdamped.

3.4 SOLVING ORDINARY DIFFERENTIAL EQUATIONS USING MATLAB

The MATLAB software can solve ordinary differential equations with initial values by means of a series of files called *ode* suite solvers. MATLAB has several solvers but the most frequently employed are the *ode23* and *ode45* functions based on the Runge-Kutta algorithm. These solvers are suitable for problems that exhibit a small or a mild degree of stiffness. If the problem is stiff, it is recommended to use other solvers such as the *ode23s* or *ode15s* that are based on more sophisticated numerical algorithms.

Before using any *ode* solver, MATLAB requires to transform the differential equations into a first order system. This system of equations must be coded in a type of subprogram that must be invoked from the principal or main M-file program. This type of subprogram is known as a *function* M-file and can be created following the structure `function ydot = filename (t,y)`. The *function* file will accept as input a time `t` and a solution `y` and return as output the values for the derivatives `ydot`. The variable `t` is a scalar time input whereas `y` and `ydot` are column vectors.

As stated before, to solve the equations of motion, it is necessary to call the *function* file from the main program written in another M-file. The command structure required for the *ode45* (and any other *ode* solver) is the following:

```
[t,y] = ode45('filename', tspan, yo, options)
```

The `filename` must be the same used in the *function* file and must be enclosed in apostrophes (`''`) or preceded by the `@` symbol. The `tspan` is a time vector that can be constructed in two ways: the first one, giving the initial and end time values, or giving additionally a constant time

increment. In the first one, the solver can change the time increment discretionally in each iteration to produce an optimum solution in terms of computational effort. In the second way, the solution can be obtained in specific time increments. The vector `yo` contains the initial conditions of the system. The input argument `options` is an optional structure that can be used to set several solver features such as the relative and absolute error tolerance of the solution. For the interested reader, these and many other features of the argument are described in detail by typing `helpwin odefile` in the MATLAB command window.

3.5 WIND TURBINE SPECIFICATIONS AND STABILITY ANALYSIS

In order to present an example of a seismic analysis of a wind turbine, the model identified as Vestas V82 MK-II is considered. This particular wind turbine was selected mainly because this model will be used in the first wind farm planned to be erected in Puerto Rico and some of its plans and drawings are available to the public domain from the local Environmental Protection Board known as *Junta de Calidad Ambiental* (DIA-F WindMar, 2007), as well as from the General Specifications from the Vestas Wind Systems A/S (2004). The Vestas V82 MK-II is a large pitch-regulated upwind turbine with active yaw and a three-blade rotor. The model number 82 comes from the diameter of the rotor in meters. Its generator is rated at 1.65 MW at a rotor speed of 14.4 rpm. The blades are attached to a spherical hub and are constructed of fiberglass reinforced epoxy and carbon fibers following the geometry of the wing profiles series FFA-W3 and NACA 63.4. The tower is formed by three bolted sections constructed of welded S355 steel plates and it can reach heights of 70 to 80 m. The physical and mechanical

properties of this wind turbine used for the seismic analysis are given in the Table 3-1. It is important to mention that some of the properties such as the moments of inertia and stiffness coefficients are roughly estimated from the available data. For instance, the actual blades used in the wind turbine are constructed using the NACA 63.4 series with variable cord between the blade tip to its center and the FFA-W3 series from the blade root to its center. In addition, the blade is gradually twisted starting at the tip at 0^o and ending at 20^o in the root. Due to this complex geometry, the blade stiffness constant k_b is approximated by equation (2-16) by assuming a blade with a constant profile and not twisted. Although this was not attempted here, a more accurate value of the blade stiffness can be obtained by a 3-D finite element analysis of the actual blade. The sectional moment of inertia required was obtained by using the cross-section of the airfoil FFA-W3-301, shown in Fig. 3-3, rotated at 20^o from the rotor plane. An average cord value of 1.71 m and a wall thickness of 0.12 m were used. To model the tower, three elements of equal length were used. The average cross-sectional areas and moments of inertia were computed at the middle section of each element. The torsion stiffness constant k_t was evaluated according to equation (2-17).

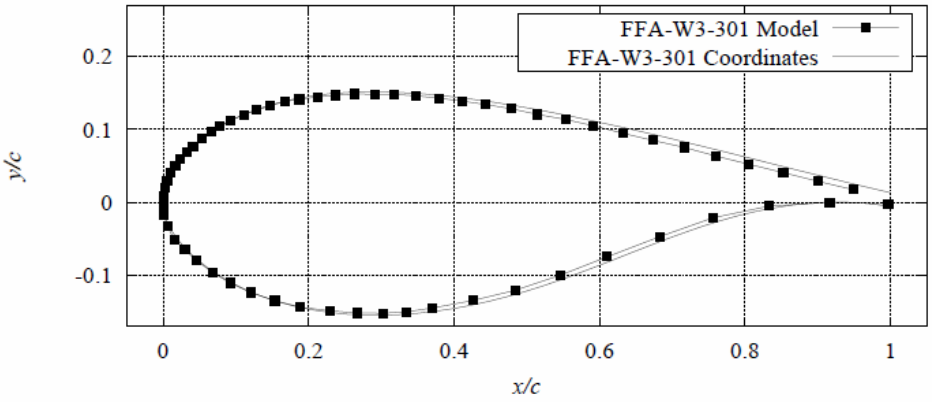

Fig. 3-3: FFA-W3-301 profile coordinates (from Fuglsang *et al.*, 1998)

Table 3-1: Physical and mechanical properties used in the wind turbine model

Rotor mass, m_r	= 43000 kg
Blade mass, m_b	= 8600 kg
Nacelle mass, m_n	= 52000 kg
Tower to hub distance, d_h	= 3.45 m
Blade length, L_b	= 40 m
Hub radius, r_h	= 1 m
Blade root radius, r_b	= 0.96 m
Blade root wall thickness, t_b	= 0.12 m
Blade moment of inertia, I_b	= 1.15 x 10^6 kg·m^2
Hub transverse moment of inertia, I_t	= 4300 kg·m^2
Hub axial moment of inertia, I_a	= 8600 kg·m^2
Blade sectional moment of inertia, I	= 5.96 x 10^{-3} m^4
Blade modulus of elasticity, E_b	= 4.4 x 10^{10} N/m^2
Tower height, h_t	= 76 m
Tower base mean radius, r_{be}	= 1.99 m
Tower base wall thickness, t_{be}	= 2.5 x 10^{-2} m
Tower top end mean radius, r_{te}	= 1.15 m
Tower top end thickness, t_{te}	= 1.1 x 10^{-2} m
Steel density, ρ	= 8900 kg/m^3
Steel modulus of elasticity, E	= 2.07 x 10^{11} N/m^2
Steel shear modulus, G	= 7.9 x 10^{10} N/m^2
Steel Poisson's ratio, v	= 0.3
Air density, ρ_a	= 1.225 kg/m^3
Average wind speed, v_∞	= 13 m/s
Maximum wind speed, $(v_\infty)_{max}$	= 42.5 m/s
Hub height, h_h	= 77 m
Thrust coefficient at average wind speed, c_T	= 0.438
Thrust coefficient at maximum wind speed, c_T	= 0.158
Generator output power, $\dot{W}$	= 1.65 x 10^6 W
Overall efficiency, η	= 0.92
Blade coning angle, δ	= 4^o
Steel yield strength, σ_y	= 3.55 x 10^6 N/m^2
Number of blades, n	= 3 pieces
Rotor operating angular velocity, Ω	= 14.4 rpm
Blade stiffness coefficient, k_b	= 2.62 x 10^7 N·m/rad
Tower torsion stiffness coefficient, k_t	= 3.90 x 10^8 N·m/rad
Aerodynamics damping constant, c_1	= 6.80 x 10^5 N·s/rad
c_2	= 2.49 x 10^4 N·s/m
c_3	= 1.79 x 10^7 N·m·s/rad
c_4	= 6.56 x 10^5 N·m·s/m
Tower element length, l_e	= 25.33 m

Table 3-1: (Cont.) Physical and mechanical properties used in the wind turbine model

Tower element areas,	A_1	= 0.108 m^2
	A_2	= 0.178 m^2
	A_3	= 0.264 m^2
Tower sectional moment of inertia,	I_1	= 8.83 x 10^{-2} m^4
	I_2	= 0.215 m^4
	I_3	= 0.443 m^4

The wind turbine analysis requires transforming the linearized matrix equations of motion into a first-order state form in a similar fashion as in the examples of the Floquet theory shown previously. The state equation is

$$\{\dot{q}\} = [A(t)]\{q\} \tag{3-45}$$

The state vector is $\{q\} = \left[\{u\}^T \ \{\dot{u}\}^T\right]^T$ with $\{u\}$ defined as in equation (2-95). Since the system originally has 16 degrees of freedom, the time periodic matrix [A(t)] becomes a 32 by 32 matrix defined as

$$[A(t)] = \begin{bmatrix} 0 & I \\ -M^{-1}K & -M^{-1}C \end{bmatrix} \tag{3-46}$$

The mass, damping and stiffness matrices were defined in equations (2-96) to (2-98).

The Floquet analysis yielded fifteen pairs of complex conjugates and two real characteristic exponents as shown in Table 3-2. The absence of a positive real part in each one of the characteristic exponents implies that this wind turbine is stable at the operating speed of 14.4 rpm. All modes, excluding the corresponding to s_2, are noticeably damped. An interesting situation occurs with the exponent s_2 that shows an almost zero real part (-0.0001), meaning that the damping associated to this mode is very small. This happens because, as it can be shown, this mode is predominantly a lateral tower mode without yaw motion. Recall that the model developed in the previous chapter lacks (up to now) any sort of structural damping, and that the

only damping present comes from the aerodynamic effect on the blades. The aerodynamic damping acts in the system only if a fore-aft movement exists in the rotor or in the blades, which is actually missing in this lateral mode. Also, since there is not yaw motion of the rotor in this mode, the gyroscopic effects cannot induce frontal motion in the tower.

Table 3-2: Characteristic exponents of the wind turbine model

s_1	=	-0.0188 ± j0.6782
s_2	=	-0.0001 ± j0.4453
s_3	=	-0.0056 ± j0.4519
s_4	=	-0.1866 ± j0.6650
s_5	=	-0.0100 ± j0.0544
s_6	=	-0.0283 ± j0.0606
s_7	=	-0.1228 ± j0.1539
s_8	=	-0.1577 ± j0.3849
s_9	=	-0.5896 ± j0.3120
s_{10}	=	-1.7812 ± j0.3806
s_{11}	=	-1.8490 ± j0.2440
s_{12}	=	-2.0641 ± j0.2166
s_{13}	=	-2.2406 ± j0.4851
s_{14}	=	-4.8970
s_{15}	=	-5.1442 ± j0.5319
s_{16}	=	-5.7737 ± j0.2814
s_{17}	=	-5.3323

As it can be observed, there are two characteristic exponents that do not contain imaginary parts (they are s_{14} and s_{17}). This means that these modes are actually overdamped modes precluding any oscillation and hence a modal frequency. These two “modes” are predominantly combined modes associated to large displacements of the blades in combination with large twisting motion of the tower in which aerodynamic damping and gyroscopic moments play a principal role.

The rest of the characteristic exponents are complex numbers. As previously mentioned, the imaginary part of each characteristic exponent indicates just one branch of a possible modal frequency but the true frequency must be found by adding to this value an integer multiple of $2\pi/T$. To determine the specific modal frequency, a time response of the turbine should be obtained by applying initial conditions associated to that frequency and later on analyzing the response time history with the Fourier transform. The information required for the initial conditions is obtained from the eigenvectors.

It is important to mention that, in general, a damped system does not have a specific mode shape since its motion is asynchronous. Synchronous motion occurs only if the system is undamped or if the damping is classical or proportional. In these cases, the phases between the components of the eigenvector are aligned (i.e., they are each other entirely in-phase or out-of-phase by 180^{o}). In asynchronous systems, such as the one examined in Example 3-3, the phases of the eigenvector components deviate more or less from this condition depending on the proportion of the damping present in the system.

When one attemp to define the mode shapes of the system from complex eigenvectors, it is incorrect to use only the real part or only the module of the components of the eigenvector associated to the displacement vector and ignore the velocity vector (recall that the eigenvector is a $2n$-dimensional state-vector). Since the general dynamical system was solved in the state space, the mode shapes demand a plot in the state space rather than in the configuration space. Bhaskar (1999) suggests two graphical ways of representing the mode shapes from complex eigenvectors. The first alternative is to plot a diagram that includes the real part of both the displacements and velocities of the generalized coordinates. In this method the displacements are represented in the traditional way by drawing nodes resembling the deformed shape, whereas

the velocity are represented by arrows located in the nodes, whose sizes are proportional to the magnitude of the velocities. Although this method is mathematically correct, it is not frequently used because the graphical visualization of displacements and velocities in the same plot does not reveal much about the deformed shape of the system.

The second alternative suggested by Bhaskar is an attempt to improve the drawbacks of the previous method and make it comparable to the conventional way of visualization of the mode shapes. The method consists in scaling only the half part of the eigenvector associated to the displacements such that the sum of the squares of the real parts will be maximal. This method is known as the *optimum mode shape* since it generates the best approximation to a synchronous mode shape. The first step consists in finding the phase angle θ in where the modules of the generalized coordinates of the eigenvector would be projected. This is accomplished by solving θ from the following expression:

$$\tan(2\theta) = \frac{\sum_{i=1}^{n} |V_i|^2 \sin(2\theta_i)}{\sum_{i=1}^{n} |V_i|^2 \cos(2\theta_i)} \tag{3-47}$$

where $|V_i|$ is the module of each of the elements of the eigenvector and θ_i is the actual phase angle of each element. Equation (3-47) contains four solutions in the range of $0 \le \theta \le 2\pi$. It can be shown that two of the solutions correspond to the line in which the maximum level of synchronicity is achieved and the other two solutions correspond to the least level of synchronicity. These lines are separated by a phase angle of 90^o. By inspection of the phasors (i.e., the complex elements of the eigenvectors expressed as a magnitude and a phase angle) one can easily identify the optimum angle but mathematically it must satisfy the following condition:

$$\sum_{i=1}^{n} |V_i|^2 \cos 2(\theta_i - \theta) > 0 \tag{3-48}$$

Otherwise, the angle will be a minimum. Hence, the maximum angle will be found adding or subtracting 90^o to it. The last step consists in projecting each phasor to the line at angle θ by

$$P_i = |V_i| \cos(\theta_i - \theta) \tag{3-49}$$

where P_i is the projection of each phasor. These projections can be normalized (for instance, such that the maximum entry will be 1) and subsequently they can be used as initial conditions to excite the corresponding mode shape of the system. The identification of the true modal frequency, which remains undefined in the Floquet analysis, can be obtained by analyzing the response of the system to these initial conditions. Also, the normalized projections will help in the graphical visualization of the different mode shapes of the system.

Returning to the wind turbine analysis, the mode shapes associated to the corresponding characteristic exponents can be identified from the eigenvectors V_i shown in Table 3-3. The first column associated to each characteristic exponent s_i represents the original eigenvector in phasor form (for sake of compactness, again the velocity components of the state vector were removed, as well as the complex conjugates eigenvectors). The vector at the right of each ($\Rightarrow$) symbol represents the optimum mode shape after applying equations (3-47) to (3-49) and then normalizing it as explained before. An approximated graphical representation of each optimum mode in ascending order is presented in Fig. 3-4.

For instance, the mode shape corresponding to s_2 is one of several lateral modes of the tower (after the frequency identification was completed, this proved to be the first tower lateral mode). The entries of this optimum eigenvector, which are represented by V_2 in Table 3-3, show that the amplitudes significantly correspond to tower displacements along x-direction. At the

same time the rotor maintains its original vertical configuration. After plotting the time response of one of the degrees of freedom of interest, let say x_1, and applying the Fourier transform of this response time history, we were able to easily identify the modal frequency for this eigenvector. In this case the modal frequency was found to be ω = 1.96 rad/s, which implied that the integer in equation (3-21) was k = 1.

We will examine now the eigenvector corresponding to s_4 by applying the same methodology. Notice from Table 3-3 that the optimum eigenvector contains amplitudes affecting the tower motion in the fore-aft z-direction and a symmetric rotor flap motion out of phase with respect to the tower motion. After performing the frequency identification, the modal frequency resulted to be ω = 2.18 rad/s, making the eigenvector associated with s_4 the first tower fore-aft mode of the system.

As it can be noticed in both previous examples, the modal frequencies were very similar. This occurred because the tower has equivalent properties in both x and z directions. The small discrepancy between them derived from the fact that the flapping of the blades in the fore-aft motion increased the system stiffness whereas the lateral motion did not. Table 3-4 provides a short description of the other mode shapes of the operating turbine.

Notice from Table 3-2 that there are several modes heavily damped, specifically those associated with the characteristic exponents s_{10} to s_{17}. Some of them are underdamped modes since their characteristic exponents have imaginary parts; the exceptions are the modes corresponding to s_{14} and s_{17}, which are overdamped modes. By plotting the optimum mode shape we can observe that these heavily damped modes contain considerably larger flap rotations of the blades or larger twisting rotations of the tower in comparison with the other modes. Although these modes require the flexural motion of the tower in a lesser scale, they can be

described as rotor/blades modes or tower twisting modes or a combination of both. The higher values of the damping are basically product of the aerodynamic effects influencing the blades and the rotor. In view of this fact we can anticipate that it is very unlikely that there could be resonance problems with these modes during a strong and long seismic motion.

It was mentioned earlier that heavily damped modes are very asynchronous in nature and the optimum mode shapes are less representative of the actual motion. As a consequence some difficulties come up while trying to establish their modal frequencies. The entries of the optimal mode shapes, which are used as initial conditions, were inaccurate and originated the excitation of multiple modes instead of a single mode. Moreover, the Fourier transform of a heavily damped response did not show a well defined peak which made the frequency identification harder. To solve the first problem, the use of the real part of the complete eigenvector (i.e., including displacements and velocities) as initial conditions for the free vibration response was required. Nevertheless, the second problem remained and the Fourier analysis was not the appropriate tool to identify the modal frequency. In this case, when the frequency was obtained by the Fourier spectrum, it was not possible to associate this value with any integer multiple of k as required by the Floquet theory in equation (3-21). Since by definition k must be an integer, when this situation occurred all frequencies were finally adjusted to the corresponding nearest integer. This situation which arises in heavily damped systems should be a matter of future investigation.

As expected, due to the gyroscopic effects and since the mass center of the system does not coincide with the stiffness center as observed from a top view, the modes that produce larger yaw or twisting rotations of the rotor about the vertical axis were strongly coupled with the tower motion in the z-direction and the x-direction. These combined mode situations can be found on

several ocassions in Fig. 3-4 (for instance, in the modes with the characteristic exponents s_9, s_{11}, s_{14}, s_{15}, and s_{17}). In these cases, the oscillatory motion of the tower never occurs purely in a vertical plane; rather if it could be observed from a top view of the turbine, its motion will resemble more an elliptical shape.

Table 3-3: Eigenvectors of the wind turbine model

	V_1		V_2		V_3	
θ_{b1}	$0.0004\angle 46.31^0$	0	$0.0000\angle -82.03^0$	0	$0.0001\angle -165.42^0$	0
θ_{b2}	$0.0001\angle -34.06^0$	0	$0.0002\angle 123.89^0$	0	$0.0000\angle 95.54^0$	0
θ_{b3}	$0.0005\angle -150.95^0$	0	$0.0004\angle -167.84^0$	0	$0.0001\angle -5.13^0$	0
$\theta_{y'}$	$0.0004\angle 23.69^0$	0	$0.0007\angle -92.58^0$	0	$0.0001\angle -173.49^0$	0
x_1	$0.0092\angle 93.25^0$	−0.15	$0.4146\angle -90.00^0$	1	$0.0010\angle -80.12^0$	0.04
θ_{z1}	$0.0044\angle -89.70^0$	0.07	$0.0102\angle 90.00^0$	−0.02	$0.0032\angle 90.23^0$	−0.13
z_1	$0.0007\angle 10.81^0$	0	$0.0038\angle -47.33^0$	0.01	$0.0000\angle 154.89^0$	0
θ_{x1}	$0.0003\angle -169.48^0$	0	$0.0001\angle 137.62^0$	0	$0.0001\angle -25.36^0$	0
x_2	$0.0614\angle -90.08^0$	1	$0.1824\angle -90.00^0$	0.44	$0.0153\angle 89.98^0$	−0.65
θ_{z2}	$0.0000\angle 62.35^0$	0	$0.0072\angle 90.00^0$	−0.02	$0.0026\angle -90.04^0$	0.11
z_2	$0.0040\angle -169.38^0$	0.01	$0.0015\angle -50.53^0$	0	$0.0004\angle -25.28^0$	0.01
θ_{x2}	$0.0000\angle -139.07^0$	0	$0.0001\angle 131.21^0$	0	$0.0001\angle 154.68^0$	0
x_3	$0.0314\angle -89.95^0$	0.51	$0.0444\angle -90.00^0$	0.11	$0.0235\angle -90.01^0$	1
θ_{z3}	$0.0019\angle 90.02^0$	−0.03	$0.0033\angle 90.00^0$	−0.01	$0.0007\angle 89.97^0$	−0.03
z_3	$0.0020\angle -169.31^0$	0.01	$0.0003\angle -52.23^0$	0	$0.0006\angle 154.67^0$	−0.01
θ_{x3}	$0.0001\angle 10.67^0$	0	$0.0000\angle 128.33^0$	0	$0.0000\angle -25.34^0$	0

	V_4		V_5		V_6	
θ_{b1}	$0.0168\angle -131.77^0$	−0.03	$0.0002\angle -27.58^0$	−0.01	$0.0002\angle 108.84^0$	0.02
θ_{b2}	$0.0154\angle -104.78^0$	−0.04	$0.0001\angle -163.80^0$	0	$0.0004\angle -109.29^0$	−0.04
θ_{b3}	$0.0176\angle -120.22^0$	−0.04	$0.0001\angle 128.76^0$	0.01	$0.0002\angle 38.94^0$	0.01
$\theta_{y'}$	$0.0011\angle -156.39^0$	0	$0.0002\angle -29.53^0$	−0.01	$0.0002\angle 107.70^0$	0.02
x_1	$0.0043\angle 42.17^0$	0.01	$0.0007\angle 110.32^0$	0.07	$0.0002\angle -68.98^0$	−0.02
θ_{z1}	$0.0001\angle -137.59^0$	0	$0.0009\angle 91.26^0$	0.10	$0.0001\angle 88.95^0$	0.01
z_1	$0.3546\angle 94.53^0$	1	$0.0001\angle 87.36^0$	0.01	$0.0005\angle 85.14^0$	0.05
θ_{x1}	$0.0090\angle -84.59^0$	−0.03	$0.0001\angle 89.56^0$	0.01	$0.0003\angle 61.66^0$	0.03
x_2	$0.0019\angle 41.97^0$	0	$0.0088\angle 89.98^0$	1	$0.0008\angle 93.63^0$	0.09
θ_{z2}	$0.0001\angle -137.85^0$	0	$0.0029\angle 90.27^0$	0.32	$0.0002\angle 92.78^0$	0.03
z_2	$0.1543\angle 93.99^0$	0.44	$0.0008\angle 86.01^0$	0.09	$0.0090\angle 90.00^0$	1
θ_{x2}	$0.0061\angle -85.66^0$	−0.02	$0.0003\angle 86.38^0$	0.03	$0.0027\angle 88.93^0$	0.30
x_3	$0.0005\angle 41.79^0$	0	$0.0010\angle 89.52^0$	0.11	$0.0001\angle 94.74^0$	0.01
θ_{z3}	$0.0000\angle -138.15^0$	0	$0.0042\angle 90.08^0$	0.47	$0.0004\angle 93.33^0$	0.04
z_3	$0.0375\angle 93.66^0$	0.11	$0.0001\angle 85.60^0$	0.01	$0.0011\angle 91.00^0$	0.12
θ_{x3}	$0.0028\angle -86.24^0$	−0.01	$0.0004\angle 86.17^0$	0.04	$0.0041\angle 89.55^0$	0.45

Table 3-3: (Cont.) Eigenvectors of the wind turbine model

$$\begin{Bmatrix} \theta_{b1} \\ \theta_{b2} \\ \theta_{b3} \\ \theta_{y'} \\ x_1 \\ \theta_{z1} \\ z_1 \\ \theta_{x1} \\ x_2 \\ \theta_{z2} \\ z_2 \\ \theta_{x2} \\ x_3 \\ \theta_{z3} \\ z_3 \\ \theta_{x3} \end{Bmatrix} \quad V_7 = \begin{Bmatrix} 0.0004\angle 10.45^0 \\ 0.0002\angle 133.59^0 \\ 0.0003\angle -146.14^0 \\ 0.0004\angle 13.84^0 \\ 0.0017\angle -107.90^0 \\ 0.0044\angle -89.35^0 \\ 0.0001\angle -115.53^0 \\ 0.0002\angle -116.10^0 \\ 0.0110\angle 90.10^0 \\ 0.0012\angle 88.56^0 \\ 0.0005\angle 64.02^0 \\ 0.0001\angle 62.74^0 \\ 0.0084\angle -90.47^0 \\ 0.0005\angle -91.05^0 \\ 0.0004\angle -116.40^0 \\ 0.0000\angle -116.97^0 \end{Bmatrix} \Rightarrow \begin{Bmatrix} 0.01 \\ 0.01 \\ -0.02 \\ 0.01 \\ -0.15 \\ -0.40 \\ -0.01 \\ -0.02 \\ 1 \\ 0.11 \\ 0.04 \\ 0 \\ -0.77 \\ -0.05 \\ -0.03 \\ 0 \end{Bmatrix}, \quad V_8 = \begin{Bmatrix} 0.0007\angle 162.87^0 \\ 0.0003\angle 33.36^0 \\ 0.0006\angle -40.94^0 \\ 0.0007\angle 160.24^0 \\ 0.0026\angle -69.08^0 \\ 0.0046\angle -88.66^0 \\ 0.0002\angle -76.20^0 \\ 0.0003\angle -74.98^0 \\ 0.0020\angle 96.26^0 \\ 0.0037\angle -89.77^0 \\ 0.0001\angle 109.62^0 \\ 0.0002\angle -77.43^0 \\ 0.0102\angle 89.88^0 \\ 0.0018\angle 90.68^0 \\ 0.0007\angle 102.17^0 \\ 0.0001\angle 102.94^0 \end{Bmatrix} \Rightarrow \begin{Bmatrix} 0.02 \\ 0.02 \\ -0.04 \\ 0.02 \\ -0.24 \\ -0.45 \\ -0.02 \\ -0.03 \\ 0.20 \\ -0.36 \\ 0.01 \\ -0.02 \\ 1 \\ 0.18 \\ 0.06 \\ 0.01 \end{Bmatrix}, \quad V_9 = \begin{Bmatrix} 0.0006\angle 99.84^0 \\ 0.0013\angle -53.16^0 \\ 0.0007\angle 159.08^0 \\ 0.0007\angle 98.45^0 \\ 0.0008\angle -83.15^0 \\ 0.0002\angle 116.95^0 \\ 0.0014\angle 101.52^0 \\ 0.0010\angle 134.32^0 \\ 0.0002\angle 86.50^0 \\ 0.0002\angle 107.53^0 \\ 0.0033\angle 72.69^0 \\ 0.0036\angle 91.52^0 \\ 0.0007\angle -74.27^0 \\ 0.0001\angle -71.49^0 \\ 0.0116\angle -90.44^0 \\ 0.0016\angle -87.73^0 \end{Bmatrix} \Rightarrow \begin{Bmatrix} -0.05 \\ 0.09 \\ -0.02 \\ -0.06 \\ 0.07 \\ -0.01 \\ -0.12 \\ -0.06 \\ -0.01 \\ -0.02 \\ -0.27 \\ -0.31 \\ 0.06 \\ 0.01 \\ 1 \\ 0.16 \end{Bmatrix}$$

$$\begin{Bmatrix} \theta_{b1} \\ \theta_{b2} \\ \theta_{b3} \\ \theta_{y'} \\ x_1 \\ \theta_{z1} \\ z_1 \\ \theta_{x1} \\ x_2 \\ \theta_{z2} \\ z_2 \\ \theta_{x2} \\ x_3 \\ \theta_{z3} \\ z_3 \\ \theta_{x3} \end{Bmatrix} \quad V_{10} = \begin{Bmatrix} 0.0927\angle 171.28^0 \\ 0.0904\angle -176.80^0 \\ 0.0844\angle -170.74^0 \\ 0.0020\angle 170.00^0 \\ 0.0016\angle 19.73^0 \\ 0.0000\angle -159.34^0 \\ 0.3660\angle 147.62^0 \\ 0.0094\angle -33.06^0 \\ 0.0007\angle 18.82^0 \\ 0.0000\angle -160.40^0 \\ 0.1554\angle 147.50^0 \\ 0.0063\angle -32.14^0 \\ 0.0002\angle 17.99^0 \\ 0.0000\angle -161.74^0 \\ 0.0368\angle 147.04^0 \\ 0.0027\angle -32.79^0 \end{Bmatrix} \Rightarrow \begin{Bmatrix} 0.24 \\ 0.21 \\ 0.18 \\ 0.01 \\ 0 \\ 0 \\ 1 \\ -0.03 \\ 0 \\ 0 \\ 0.42 \\ -0.02 \\ 0 \\ 0 \\ 0.10 \\ -0.01 \end{Bmatrix}, \quad V_{11} = \begin{Bmatrix} 0.1473\angle -23.39^0 \\ 0.1220\angle -145.69^0 \\ 0.1544\angle 98.01^0 \\ 0.0282\angle -124.03^0 \\ 0.0407\angle 40.60^0 \\ 0.0010\angle -142.51^0 \\ 0.1568\angle -119.53^0 \\ 0.0076\angle 2.55^0 \\ 0.0181\angle 43.48^0 \\ 0.0007\angle -138.97^0 \\ 0.0871\angle -79.39^0 \\ 0.0029\angle 80.87^0 \\ 0.0045\angle 45.97^0 \\ 0.0003\angle -134.86^0 \\ 0.0256\angle -67.23^0 \\ 0.0018\angle 109.43^0 \end{Bmatrix} \Rightarrow \begin{Bmatrix} 0.16 \\ 0.60 \\ -0.95 \\ 0.18 \\ -0.22 \\ 0.01 \\ 1 \\ -0.01 \\ -0.10 \\ 0 \\ 0.52 \\ -0.02 \\ -0.03 \\ 0 \\ 0.14 \\ -0.01 \end{Bmatrix}, \quad V_{12} = \begin{Bmatrix} 0.1762\angle -112.40^0 \\ 0.1971\angle 137.32^0 \\ 0.1607\angle 7.62^0 \\ 0.0151\angle -82.43^0 \\ 0.0103\angle 91.92^0 \\ 0.0003\angle -88.24^0 \\ 0.2427\angle -174.01^0 \\ 0.0110\angle 2.22^0 \\ 0.0044\angle 92.12^0 \\ 0.0002\angle -88.03^0 \\ 0.0639\angle -168.53^0 \\ 0.0034\angle 7.94^0 \\ 0.0010\angle 92.30^0 \\ 0.0001\angle -87.76^0 \\ 0.0108\angle -162.58^0 \\ 0.0009\angle 15.11^0 \end{Bmatrix} \Rightarrow \begin{Bmatrix} 0.30 \\ 0.58 \\ -0.66 \\ -0.01 \\ 0 \\ 0 \\ 1 \\ -0.05 \\ 0 \\ 0 \\ 0.26 \\ -0.01 \\ 0 \\ 0 \\ 0.04 \\ 0 \end{Bmatrix}$$

Table 3-3: (Cont.) Eigenvectors of the wind turbine model

$$\begin{Bmatrix} \theta_{b1} \\ \theta_{b2} \\ \theta_{b3} \\ \theta_{y'} \\ x_1 \\ \theta_{z1} \\ z_1 \\ \theta_{x1} \\ x_2 \\ \theta_{z2} \\ z_2 \\ \theta_{x2} \\ x_3 \\ \theta_{z3} \\ z_3 \\ \theta_{x3} \end{Bmatrix} \quad V_{13} = \begin{Bmatrix} 0.0044\angle 52.77^0 \\ 0.0062\angle -102.44^0 \\ 0.0040\angle 103.41^0 \\ 0.0041\angle 59.55^0 \\ 0.0053\angle -112.82^0 \\ 0.0003\angle 137.45^0 \\ 0.0120\angle -107.71^0 \\ 0.0056\angle 107.74^0 \\ 0.055\angle -172.16^0 \\ 0.0001\angle 58.16^0 \\ 0.0656\angle 99.70^0 \\ 0.0005\angle -24.08^0 \\ 0.0024\angle 175.00^0 \\ 0.0001\angle -1.830^0 \\ 0.0312\angle 92.85^0 \\ 0.0019\angle -85.27^0 \end{Bmatrix} \Rightarrow \begin{Bmatrix} 0.05 \\ -0.09 \\ 0.06 \\ 0.05 \\ -0.07 \\ 0 \\ -0.16 \\ 0.08 \\ 0 \\ 0 \\ 1 \\ 0 \\ 0.01 \\ 0 \\ 0.47 \\ -0.03 \end{Bmatrix}, \quad V_{14} = \begin{Bmatrix} 0.0096\angle 0^0 \\ 0.0109\angle 180^0 \\ 0.0011\angle 0^0 \\ 0.0085\angle 0^0 \\ 0.0113\angle 180^0 \\ 0.0006\angle 0^0 \\ 0.0021\angle 0^0 \\ 0.0061\angle 0^0 \\ 0.0015\angle 180^0 \\ 0.0002\angle 0^0 \\ 0.0109\angle 180^0 \\ 0.0001\angle 0^0 \\ 0.0001\angle 0^0 \\ 0.0000\angle 180^0 \\ 0.0029\angle 0^0 \\ 0.0001\angle 0^0 \end{Bmatrix} \Rightarrow \begin{Bmatrix} -0.85 \\ 0.96 \\ -0.09 \\ -0.75 \\ 1 \\ -0.05 \\ -0.19 \\ -0.54 \\ 0.13 \\ -0.02 \\ 0.96 \\ -0.01 \\ -0.01 \\ 0 \\ -0.25 \\ -0.01 \end{Bmatrix}, \quad V_{15} = \begin{Bmatrix} 0.0059\angle 72.80^0 \\ 0.0115\angle -137.99^0 \\ 0.0064\angle 16.67^0 \\ 0.0053\angle 63.14^0 \\ 0.0070\angle -117.81^0 \\ 0.0009\angle 35.09^0 \\ 0.0063\angle 19.41^0 \\ 0.0097\angle 29.80^0 \\ 0.0014\angle -103.16^0 \\ 0.0002\angle 46.06^0 \\ 0.0218\angle -141.57^0 \\ 0.0009\angle 158.27^0 \\ 0.0010\angle -12.17^0 \\ 0.0000\angle 170.69^0 \\ 0.0070\angle 75.50^0 \\ 0.0005\angle 5.49^0 \end{Bmatrix} \Rightarrow \begin{Bmatrix} -0.23 \\ 0.53 \\ -0.27 \\ -0.23 \\ 0.30 \\ -0.04 \\ -0.27 \\ -0.44 \\ 0.05 \\ -0.01 \\ 1 \\ 0.02 \\ -0.03 \\ 0 \\ -0.27 \\ -0.02 \end{Bmatrix}$$

$$\begin{Bmatrix} \theta_{b1} \\ \theta_{b2} \\ \theta_{b3} \\ \theta_{y'} \\ x_1 \\ \theta_{z1} \\ z_1 \\ \theta_{x1} \\ x_2 \\ \theta_{z2} \\ z_2 \\ \theta_{x2} \\ x_3 \\ \theta_{z3} \\ z_3 \\ \theta_{x3} \end{Bmatrix} \quad V_{16} = \begin{Bmatrix} 0.0570\angle 2.47^0 \\ 0.0339\angle 176.28^0 \\ 0.0171\angle -171.48^0 \\ 0.0404\angle 0.67^0 \\ 0.0520\angle -179.21^0 \\ 0.0017\angle -44.39^0 \\ 0.0590\angle -161.23^0 \\ 0.0045\angle -130.30^0 \\ 0.0169\angle 179.88^0 \\ 0.0008\angle 9.54^0 \\ 0.1716\angle 50.93^0 \\ 0.0142\angle -79.85^0 \\ 0.0039\angle 170.85^0 \\ 0.0003\angle -6.75^0 \\ 0.1703\angle -71.08^0 \\ 0.0051\angle 138.86^0 \end{Bmatrix} \Rightarrow \begin{Bmatrix} 0.13 \\ -0.06 \\ -0.05 \\ 0.08 \\ -0.11 \\ 0 \\ -0.22 \\ -0.03 \\ -0.03 \\ 0 \\ 1 \\ -0.08 \\ 0 \\ 0 \\ -0.83 \\ 0.01 \end{Bmatrix}, \quad V_{17} = \begin{Bmatrix} 0.0004\angle 0^0 \\ 0.0008\angle 0^0 \\ 0.0007\angle 180^0 \\ 0.0007\angle 180^0 \\ 0.0011\angle 0^0 \\ 0.0003\angle 180^0 \\ 0.0048\angle 180^0 \\ 0.0016\angle 180^0 \\ 0.0009\angle 180^0 \\ 0.0001\angle 0^0 \\ 0.0191\angle 0^0 \\ 0.0012\angle 180^0 \\ 0.0003\angle 180^0 \\ 0.0000\angle 0^0 \\ 0.0173\angle 180^0 \\ 0.0002\angle 0^0 \end{Bmatrix} \Rightarrow \begin{Bmatrix} 0.02 \\ 0.04 \\ -0.04 \\ -0.04 \\ 0.06 \\ -0.02 \\ -0.25 \\ -0.08 \\ -0.05 \\ 0 \\ 1 \\ -0.06 \\ -0.02 \\ 0 \\ -0.91 \\ 0.01 \end{Bmatrix}$$

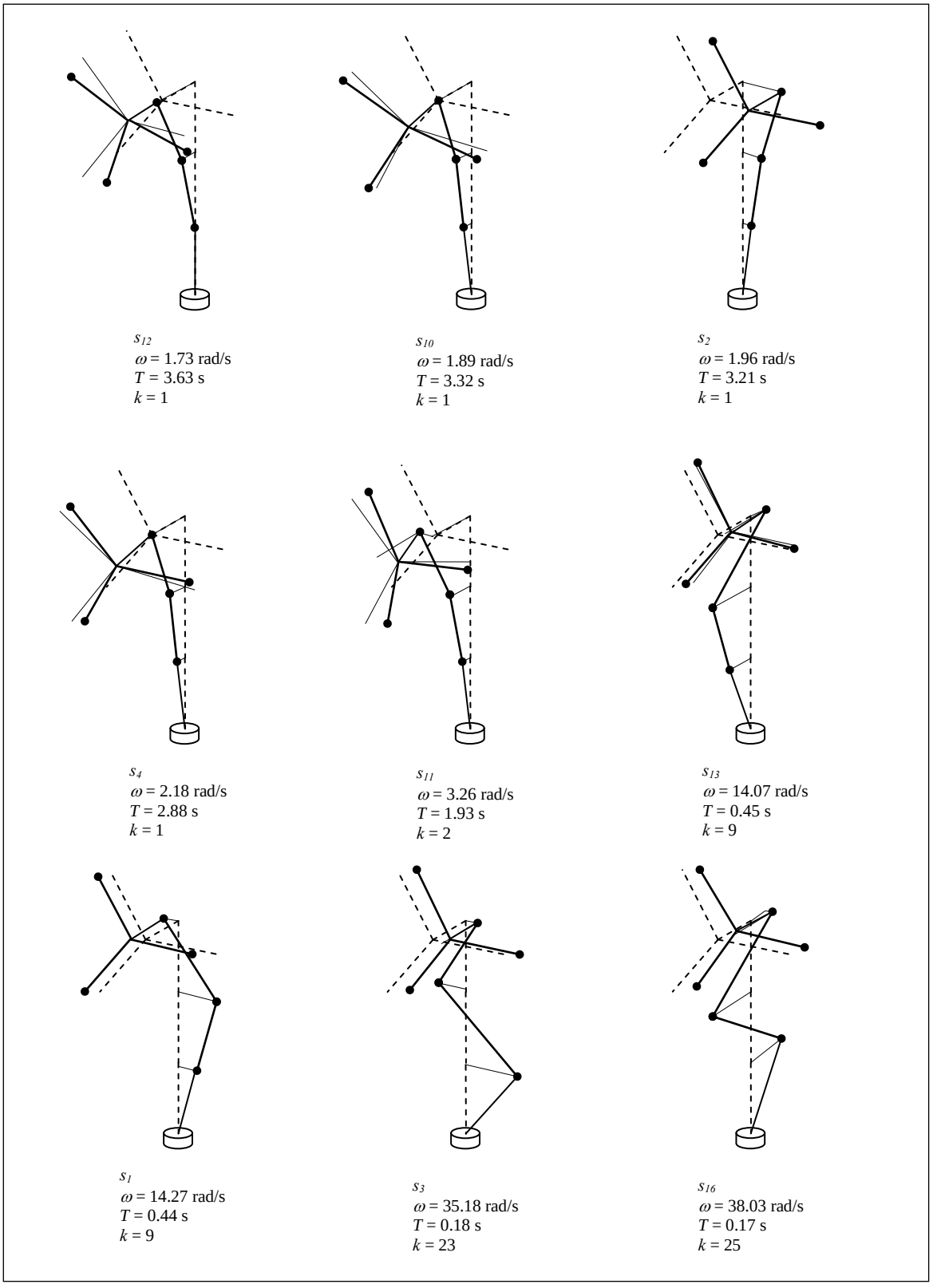

Fig. 3-4: Optimum mode shapes in ascending order

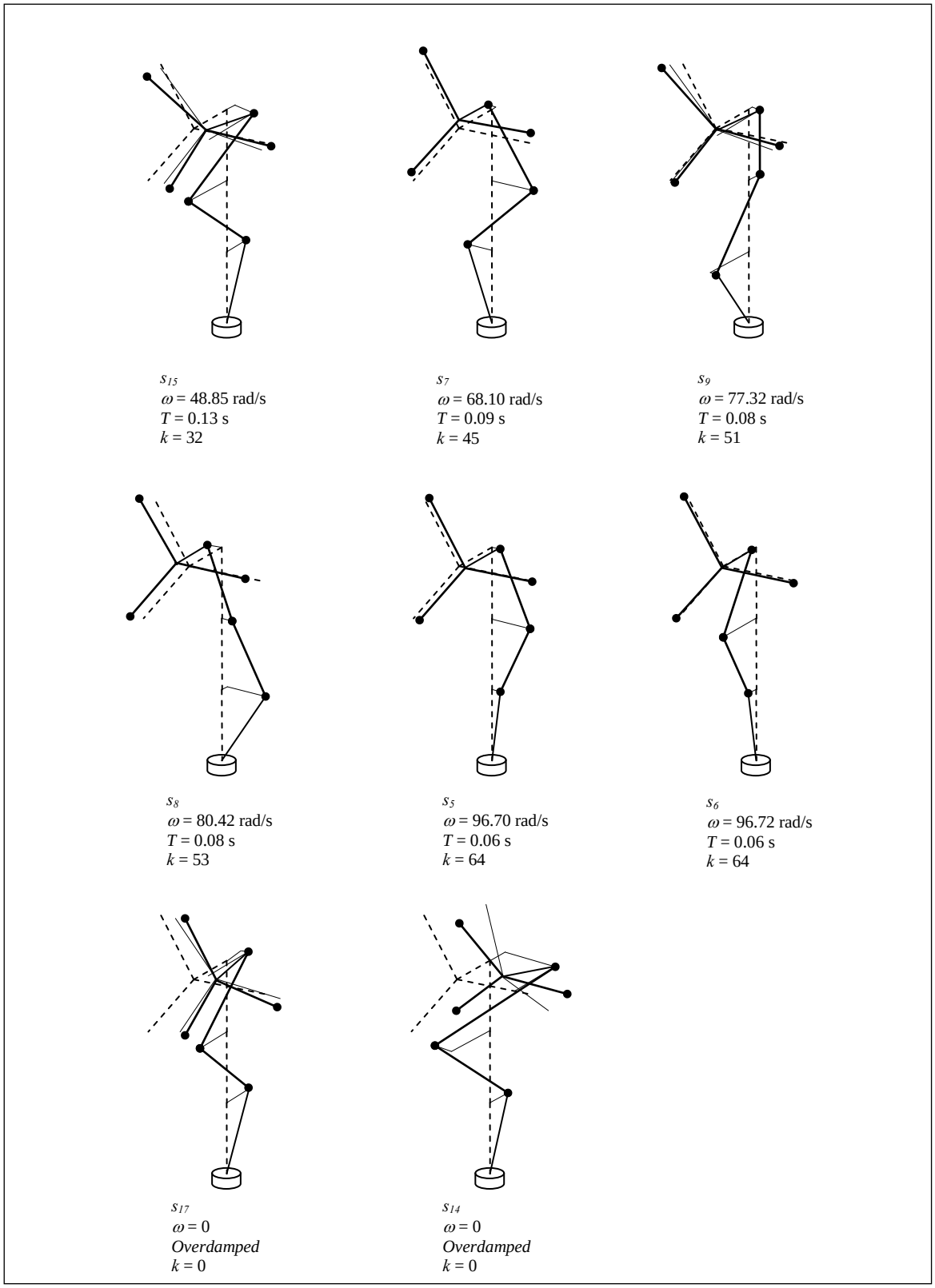

Fig. 3-4: (Cont.) Optimum mode shapes in ascending order

Table 3-4: Frequency identification and mode shapes description

Characteristic exponent	***k***	**Frequency ω (rad/s)**	**Period *T* (s)**	**Mode Shape Description**
s_1	9	14.27	0.44	*Tower lateral*
s_2	1	1.96	3.21	*Tower lateral*
s_3	23	35.18	0.18	*Tower lateral*
s_4	1	2.18	2.88	*Tower fore-aft*
s_5	64	96.70	0.06	*Tower lateral*
s_6	64	96.70	0.06	*Tower fore-aft*
s_7	45	68.10	0.09	*Tower lateral*
s_8	53	80.42	0.08	*Tower lateral*
s_9	51	77.32	0.08	*Tower fore-aft*
s_{10}	1	1.89	3.32	*Tower fore-aft coupled with symmetric rotor flap*
s_{11}	2	3.26	1.93	*Combined with asymmetric rotor flap*
s_{12}	1	1.73	3.63	*Tower fore-aft with asymmetric rotor flap*
s_{13}	9	14.07	0.45	*Tower fore-aft*
s_{14}	0	0	--	*Tower twisting with asymmetric rotor flap*
s_{15}	32	48.85	0.13	*Combined with asymmetric rotor flap*
s_{16}	25	38.03	0.17	*Combined with asymmetric rotor flap*
s_{17}	0	0	--	*Tower fore-aft*

CHAPTER 4: SEISMIC ANALYSIS OF THE WIND TURBINE MODEL

4.1 INTRODUCTION

In the present chapter the behavior of the Vestas V82 wind turbine is studied under the effects of several strong motions acting at the base of the structure. Since this type of turbine could be erected in the southern region of Puerto Rico and there is a lack of recorded data of strong earthquakes occurred in the island, the use of earthquakes traditionally recommended for Puerto Rico such as the El Centro record of 1940 or Kern County record of 1952 has been selected to perform the seismic analysis. As a supplementary study to investigate near-fault effects in the turbine two records obtained from the Northridge earthquake in 1994 and the San Salvador earthquake in 1986 will be also considered. All ground motion accelerograms used here are the latest corrected records obtained from the PEER Strong Motion Database (from The Pacific Earthquake Engineering Research Center, at the University of California at Berkeley).

Initially, the linearized equations of motion used in Chapter 3 are considered. Subsequently, the original non-linearized set of equations is taken into account. This gives us the opportunity to evaluate the contribution of the non-linear gyroscopic terms, frequently neglected for mathematical convenience. The goal is to determine whether these terms can be ignored from the equations without affecting the accuracy of the calculated response.

4.2 SELECTED EARTHQUAKES

The first ground motion record to be used in the evaluation of the turbine is that from the Kent County earthquake that occurred in California on July 21, 1952 with a moment magnitude of 7.4. Housner conducted a study in 1980 (see Martínez *et al*., 2001), in which he compared the size and distance of the active faults in Puerto Rico with others around the world. He recommended the S69E horizontal component of the earthquake recorded at the Taft Lincoln School station because it contained the expected characteristics of an earthquake that could hit the island. This recommendation was officially implemented in the Puerto Rico Building Code of 1987 and the use of the record was mandatory to evaluate the seismic performance of structures until the main revision of the code in 1999. The accelerograms of the three components of the Taft record is displayed in Fig. 4-1 and the Fourier (amplitude) spectrum of the S69E component is shown in the upper plot of Fig. 4-2. The second plot shown in Fig. 4-2 corresponds to the Fourier spectrum of the last part of the N21E record (it will be required later in Section 4.4). From these figures one can observe that its peak ground acceleration is 0.178g and its first three dominant frequencies are 11.37 rad/s, 14.26 rad/s, and 18.66 rad/s. On the other hand, the N21E horizontal component has a peak ground acceleration of 0.156g and the peak ground acceleration of the vertical component is of 0.109g. The total duration of the event was of 54 seconds.

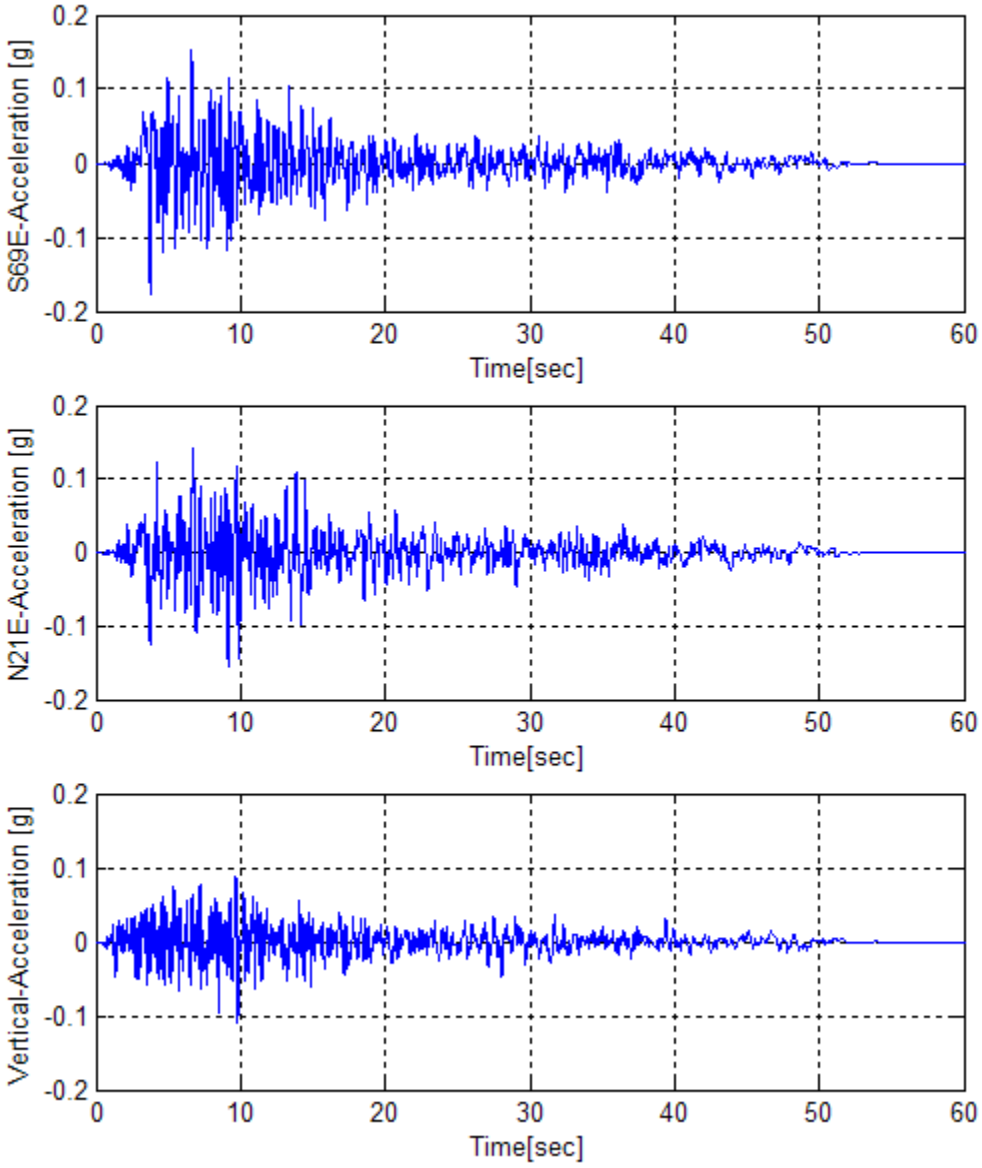

Fig. 4-1: Kern County earthquake acceleration time histories

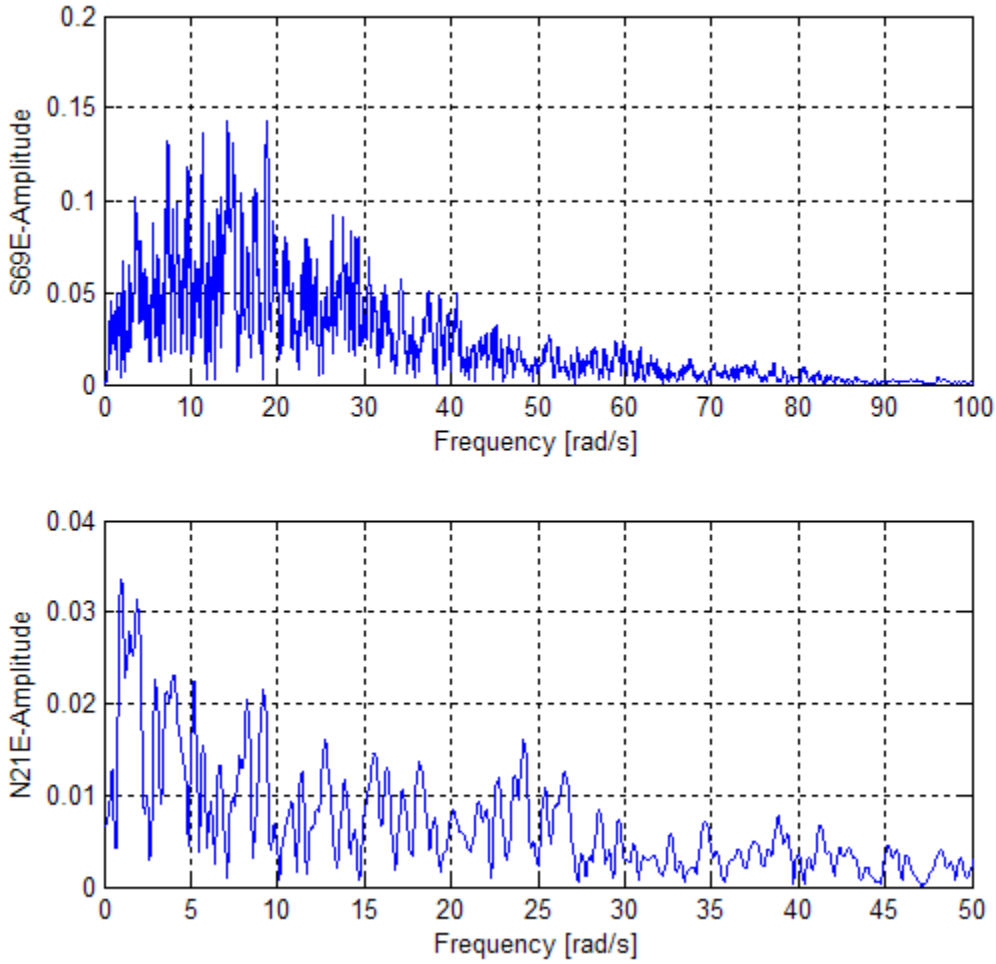

Fig. 4-2: Kern County earthquake frequency spectrum (S69E and N21E Taft components)

For many years the record of the El Centro earthquake has also been used to evaluate the performance of different structures in Puerto Rico. This earthquake occurred in Imperial Valley, California on May 19, 1940. The earthquake, with a magnitude of 7.1 in the Richter scale, was recorded in the El Centro station, which subsequently became the best well known name for the event. The accelerogram for the three components is shown in Fig. 4-3. The peak ground acceleration is 0.307g. The dominant frequency of this record is 7.54 rad/s as it can be observed

from the Fourier spectrum presented in Fig. 4-4. The peak ground acceleration for the E-W horizontal component is 0.215g and the maximum vertical acceleration is 0.205g. The data used herein was sampled at intervals of 0.01 seconds. The total duration of the earthquake was approximately 40 seconds.

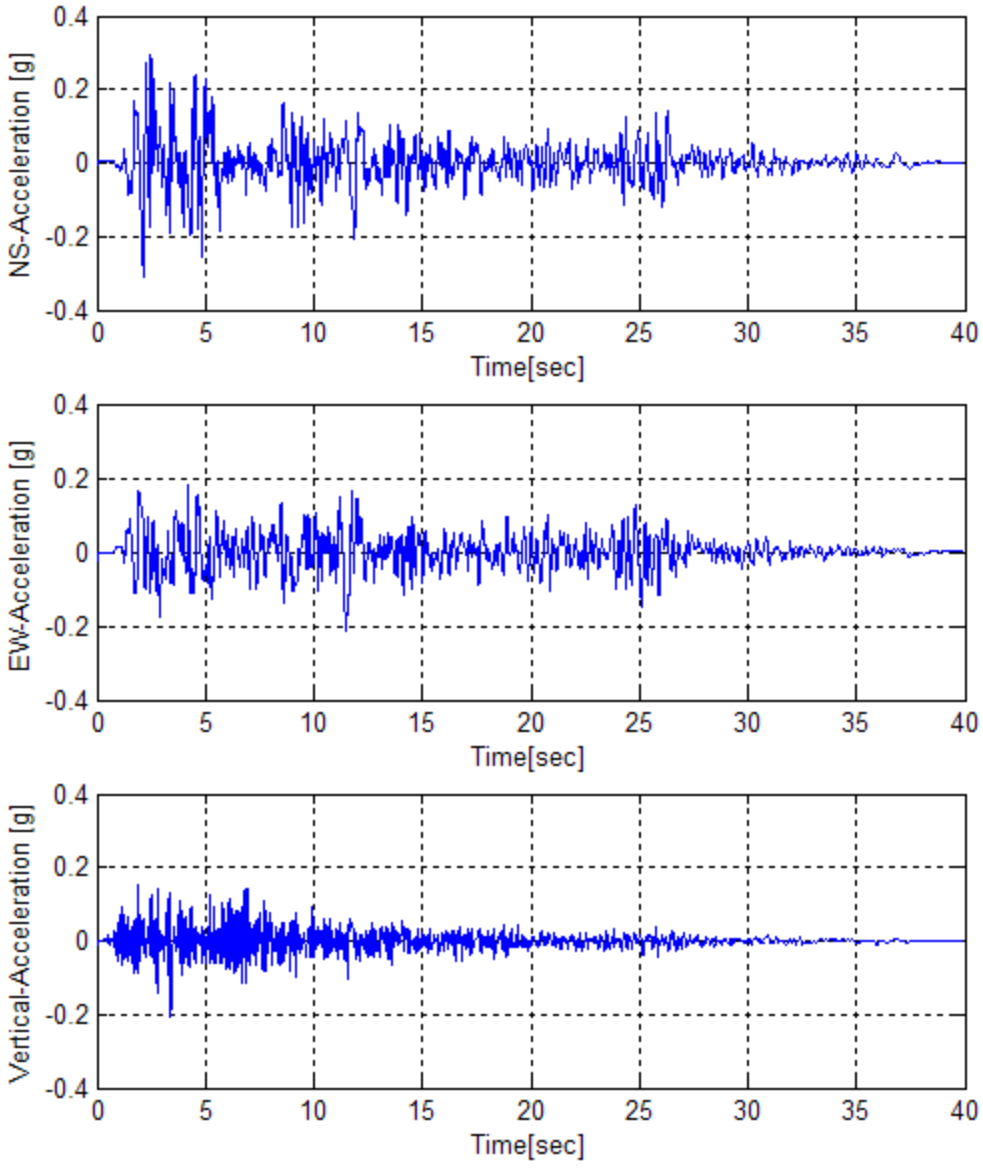

Fig. 4-3: El Centro earthquake acceleration time histories

In addition to the two previous historical earthquake records commonly used for seismic evaluation in Puerto Rico, two more earthquake records will be employed that exhibit rupture directivity and near-fault effects. In a study conducted by Martínez *et al*. (2001), they point out that the seismicity of the southwestern region of Puerto Rico has incremented since 1987 due to the motion of, until then, inactive in-land strike-slip faults found in the area. Since similar wind turbines than the one analyzed in this work will be installed about 20 km from these faults, it is relevant to consider how near-fault earthquake records, as well as records showing rupture directivity effects could affect wind turbine structures. Martínez *et al.* proposed that the records of the Northridge earthquake of 1994 registered at the Castaic-Old Ridge Route station and the San Salvador earthquake of 1986 recorded by the Geotechnical Investigation Center (GIC) station can be used as expected earthquakes for the southwestern region of Puerto Rico.

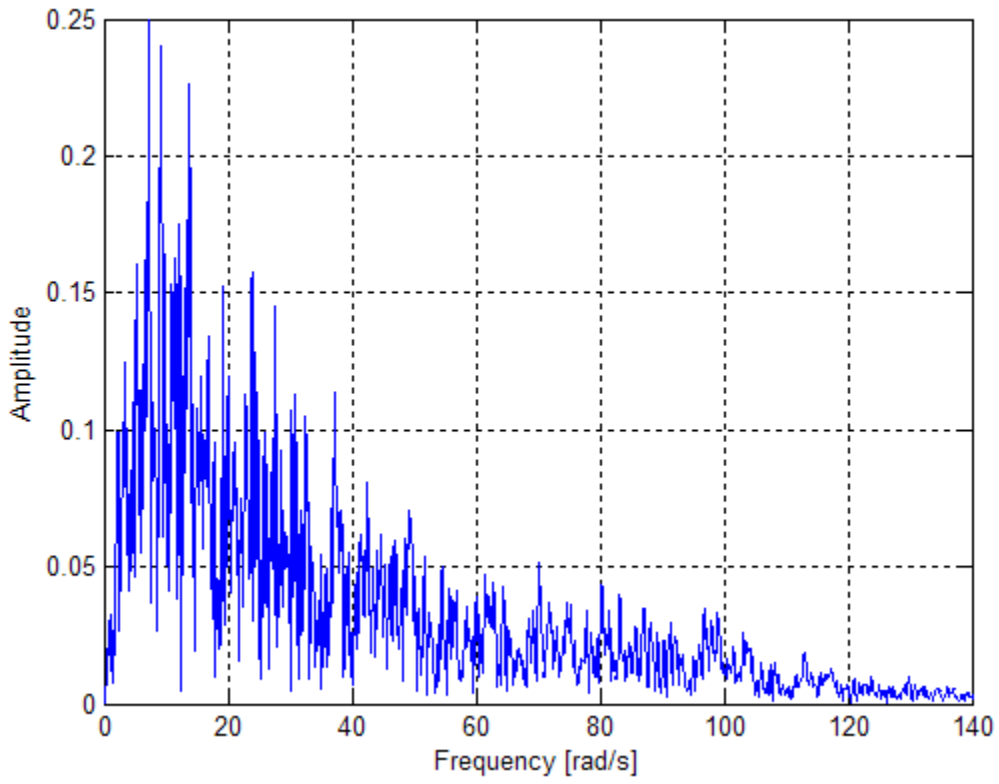

Fig. 4-4: El Centro earthquake frequency spectrum (N-S component)

The Northridge earthquake occurred on January 17, 1994 in Los Angeles, California with a moment magnitude of 6.7. The earthquake signal recorded by the Castaic station, shown in Fig. 4-5, is located at 23 km of the fault rupture; it shows a peak ground acceleration of 0.57g in the N-S component and a dominant frequency of 7.73 rad/s, shown in Fig. 4-6. The total duration of the record is approximately 40 seconds sampled at equal intervals of 0.02 seconds. This record provides a strong directivity component in the direction of the fault rupture. It is expected that an off-shore fault rupture at the west part of Puerto Rico will have similar characteristics to this earthquake (see Morales, 2006).

The San Salvador earthquake occurred on October 10, 1986 in San Salvador, El Salvador. The GIC station located at a distance of 4 km from the epicenter recorded the relatively small magnitude earthquake with a moment magnitude of 5.4 but with a high horizontal peak ground acceleration of 0.87g in the N-S component as shown in Fig 4-7. The Fourier spectrum in Fig. 4-8 shows a dominant frequency content of 9.05 rad/s. The total duration of the record is of only 9 seconds sampled at intervals of 0.005 seconds.

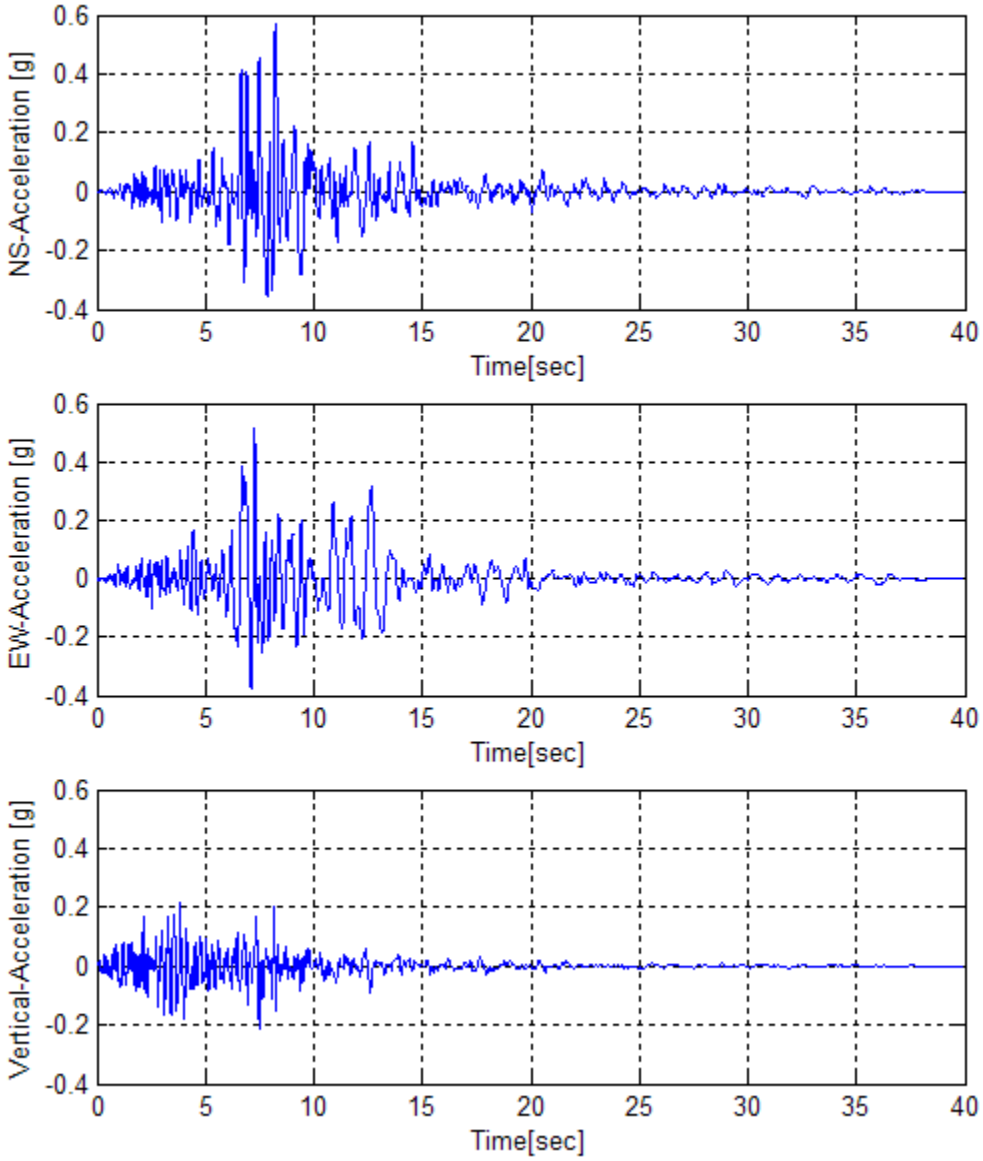

Fig. 4-5: Northridge earthquake acceleration time histories

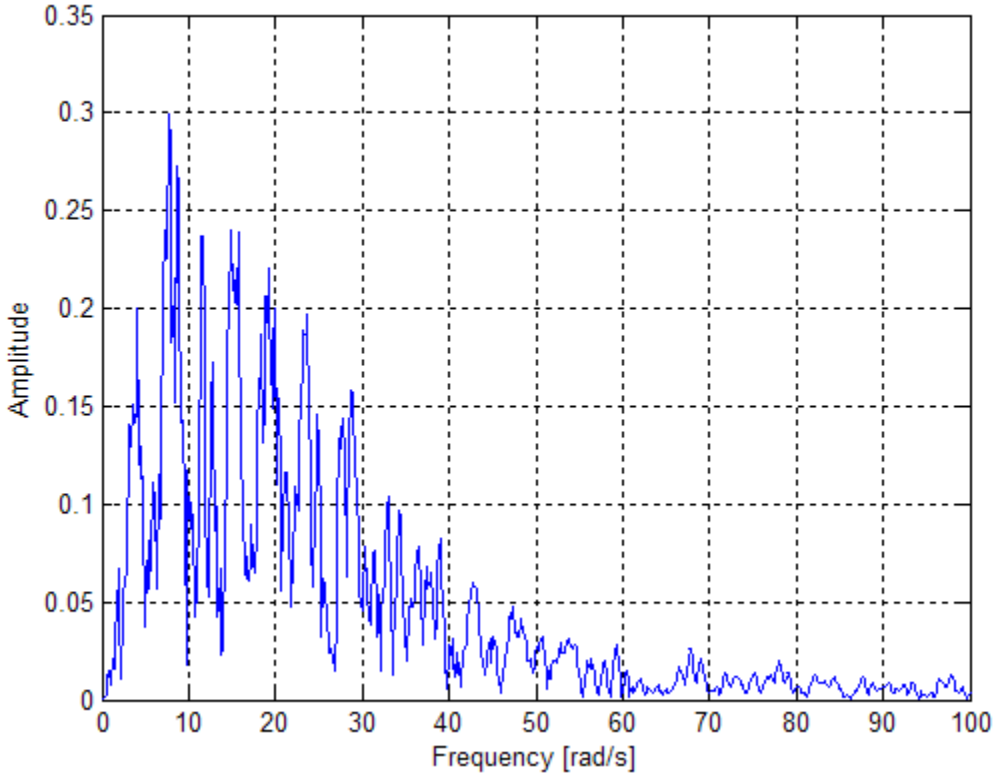

Fig. 4-6: Northridge earthquake frequency spectrum (N-S component)

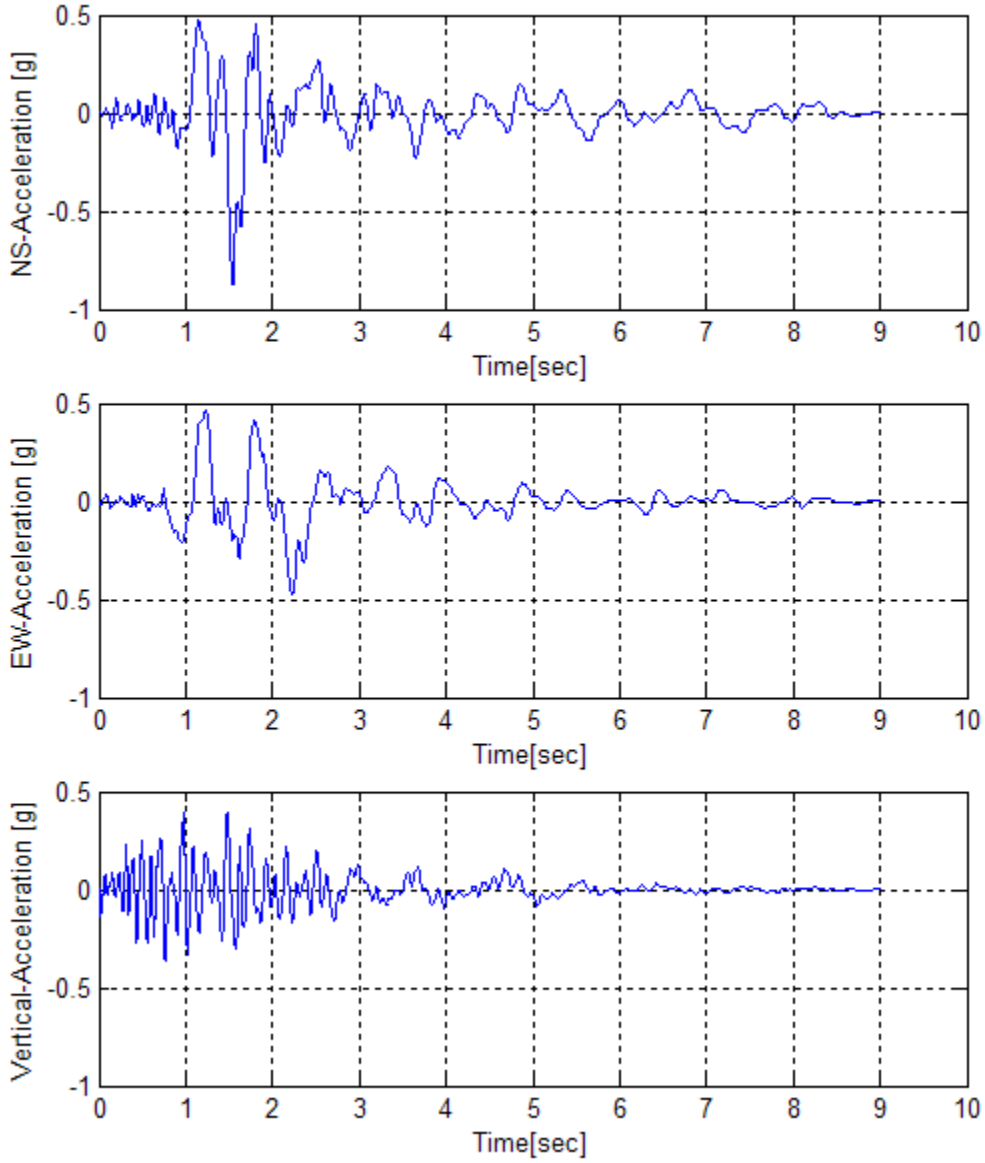

Fig. 4-7: San Salvador earthquake acceleration time histories

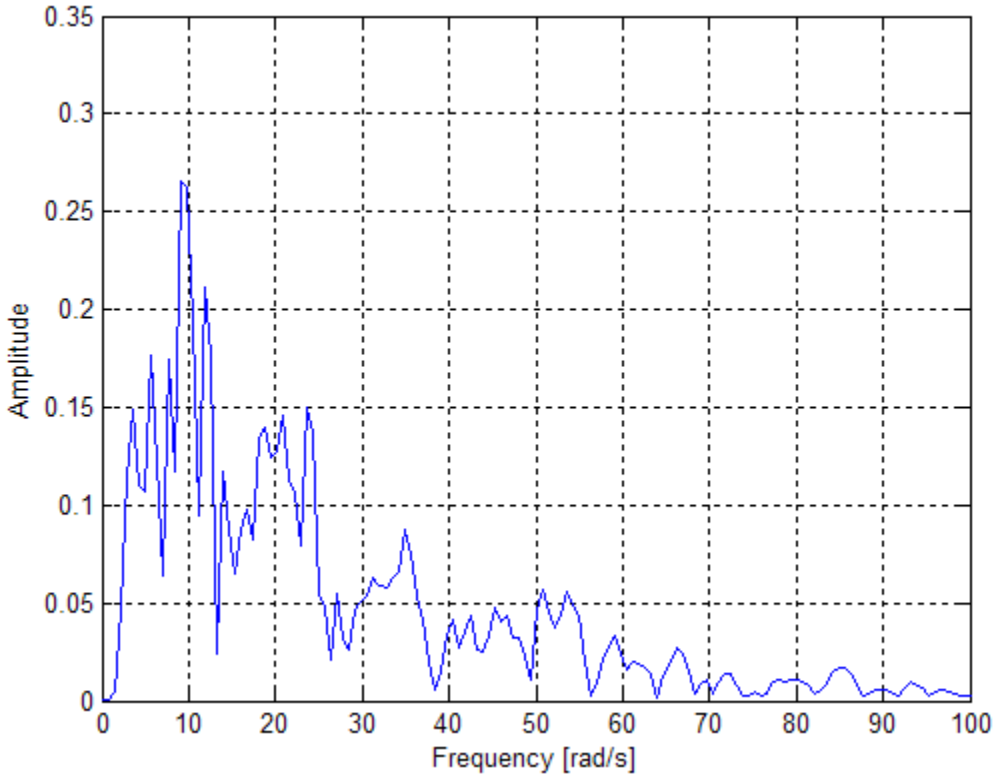

Fig. 4-8: San Salvador earthquake frequency spectrum (N-S component)

4.3 SEISMIC ANALYSIS SOLUTION USING MATLAB

In the previous chapter we have considered the free vibration of the operating wind turbine. It can be shown, in view of equations (2-30) to (2-54) and equations (2-61) and (2-62), that the equations of motion of the turbine subjected to three base linear accelerations $\ddot{X}_b$, $\ddot{Y}_b$ and $\ddot{Z}_b$ can be expressed in the following form:

$$[M(t)]\{\ddot{u}\}+[C(t)]\{\dot{u}\}+[K]\{u\}=-[M_e]\{r_x\}\ddot{X}_b-[M_e]\{r_y\}\ddot{Y}_b-[M_e]\{r_z\}\ddot{Z}_b \qquad (4\text{-}1)$$

The mass matrix [M_e] is a diagonal matrix defined as

$$[M_e]=\begin{bmatrix}
m_{ag} & 0 & 0 & 0 & 0 & 0 & 0 & 0 & 0 & 0 & 0 & 0 & 0 & 0 & 0 & 0\\
0 & m_{bg} & 0 & 0 & 0 & 0 & 0 & 0 & 0 & 0 & 0 & 0 & 0 & 0 & 0 & 0\\
0 & 0 & m_{cg} & 0 & 0 & 0 & 0 & 0 & 0 & 0 & 0 & 0 & 0 & 0 & 0 & 0\\
0 & 0 & 0 & m_{de} & 0 & 0 & 0 & 0 & 0 & 0 & 0 & 0 & 0 & 0 & 0 & 0\\
0 & 0 & 0 & 0 & m_{ee} & 0 & 0 & 0 & 0 & 0 & 0 & 0 & 0 & 0 & 0 & 0\\
0 & 0 & 0 & 0 & 0 & 0 & 0 & 0 & 0 & 0 & 0 & 0 & 0 & 0 & 0 & 0\\
0 & 0 & 0 & 0 & 0 & 0 & m_{gg} & 0 & 0 & 0 & 0 & 0 & 0 & 0 & 0 & 0\\
0 & 0 & 0 & 0 & 0 & 0 & 0 & m_{de} & 0 & 0 & 0 & 0 & 0 & 0 & 0 & 0\\
0 & 0 & 0 & 0 & 0 & 0 & 0 & 0 & m_{ii} & 0 & 0 & 0 & 0 & 0 & 0 & 0\\
0 & 0 & 0 & 0 & 0 & 0 & 0 & 0 & 0 & 0 & 0 & 0 & 0 & 0 & 0 & 0\\
0 & 0 & 0 & 0 & 0 & 0 & 0 & 0 & 0 & 0 & m_{kk} & 0 & 0 & 0 & 0 & 0\\
0 & 0 & 0 & 0 & 0 & 0 & 0 & 0 & 0 & 0 & 0 & 0 & 0 & 0 & 0 & 0\\
0 & 0 & 0 & 0 & 0 & 0 & 0 & 0 & 0 & 0 & 0 & 0 & m_{mm} & 0 & 0 & 0\\
0 & 0 & 0 & 0 & 0 & 0 & 0 & 0 & 0 & 0 & 0 & 0 & 0 & 0 & 0 & 0\\
0 & 0 & 0 & 0 & 0 & 0 & 0 & 0 & 0 & 0 & 0 & 0 & 0 & 0 & m_{oo} & 0\\
0 & 0 & 0 & 0 & 0 & 0 & 0 & 0 & 0 & 0 & 0 & 0 & 0 & 0 & 0 & 0
\end{bmatrix} \tag{4-2}$$

where the entries were defined previously in equation (2-96). The vectors of influence coefficients are defined as:

$$\begin{aligned}
\{r_x\} &= [0\ 0\ 0\ 1\ 1\ 0\ 0\ 0\ 1\ 0\ 0\ 0\ 1\ 0\ 0\ 0]^T\\
\{r_y\} &= [0\ 0\ 0\ 0\ 0\ 0\ 0\ -1\ 0\ 0\ 0\ 0\ 0\ 0\ 0\ 0]^T\\
\{r_z\} &= [1\ 1\ 1\ 0\ 0\ 0\ 1\ 0\ 0\ 0\ 1\ 0\ 0\ 0\ 1\ 0]^T
\end{aligned} \tag{4-3}$$

To solve the problem using the MATLAB *ode* functions, the system must be transformed into the first order equations in the state space as follows:

$$\{\dot{q}\} = [A(t)]\{q\} + [B(t)]\{r_x\}\ddot{X}_b + [B(t)]\{r_y\}\ddot{Y}_b + [B(t)]\{r_z\}\ddot{Z}_b \tag{4-4}$$

where the state vector is $\{q\} = \left[\{u\}^T\ \{\dot{u}\}^T\right]^T$ with $\{u\}$ as defined in equation (2-95) and the matrices [$A(t)$] and [$B(t)$] are defined as:

$$[A(t)] = \begin{bmatrix} 0 & I \\ -M^{-1}K & -M^{-1}C \end{bmatrix} \qquad [B(t)] = \begin{bmatrix} 0 \\ -M^{-1}M_e \end{bmatrix} \tag{4-5}$$

The general form of the MATLAB *ode* suite solvers applied to a system of differential equations was described in Section 3.4. As it has been shown in the previous chapter, the solution of a system of homogeneous equations, such as the case of a free vibration system, is a quite straightforward task. For the case of forced vibration, the application of the *ode* solvers is simple if the forcing function can be described by a mathematical expression. A more complicated situation occurs when the forcing function consists of discrete input data such as the case described by equation (4-4), in which the earthquake ground accelerations appear in the equations of motion of the turbine. Now, in terms of MATLAB programming, the main problem consists on how to incorporate each ground acceleration record inside the *function* file defined earlier. The problem can be conveniently solved by including an interpolation solver called `interp1` into the original *function* file that contained the differential equations. The `interp1` solver is essentially a function to interpolate one-dimensional data at intermediate points, but for our application its main advantage is that it also provides a way to convert the discrete data into a sort of time-dependent function. Also, the possibility of interpolating the earthquake record at time intervals smaller than the original sampling time can be useful if a more precise solution is required.

The basic structure of the command `interp1` can be written as `Xb = interp1(tx,Xg,t)`, where `Xb` is the desired result, i.e. the function `Xg` interpolated at the time `t`. The vector `tx` specifies the points (instants of time) at which the data `Xg` is given. In the problem considered here, `Xg` will be one of the components of the original earthquake record

and `tx` the vector of instants of time associated with the record, usually spaced at time intervals of 0.01 seconds. The scalar `t` is the specific time at which the new acceleration `Xb` is computed. When the earthquake data is loaded into the main program and stored in the vector `Xg`, this vector must be transferred to the *function* M-file that contains the differential equations by means of the `global` command. This command allows the main program and the *function* file to share the variables assigned in `global`, for instance `Xg`. As mentioned before, the *function* file contains the interpolation command in which `Xg` is given as input, so the exact base acceleration at the specific required time is then calculated inside the *function* M-file step by step as needed by the *ode* solver. Since for the present application the three base acceleration time histories are acting simultaneously, this procedure is repeated for each component.

4.4 SEISMIC ANALYSIS WITH HISTORICAL EARTHQUAKES

The seismic analysis of the wind turbine will be performed using first the linearized set of equations of motion and the traditionally recommended earthquake records used in Puerto Rico such as the Taft and El Centro records. The seismic analysis considering the near-fault earthquake records will be considered later on. It is important to mention that for the seismic analysis of the wind turbine the horizontal component with the greatest peak ground acceleration for both earthquakes was assigned to the *z*-axis of the wind turbine (i.e., the frontal turbine direction). This direction was selected to study the occurrence of a potentially critical situation, namely the blade tip colliding with the tower.

4.4.1 Response to the Taft record

The three components of the Taft record were considered as the input to the equations of motion (4-4). The response in terms of some important generalized coordinates is plotted in the figures shown in the next pages. Fig. 4-9 shows the blade flap angle response of each of the three blades of the system for the duration of the event. The maximum flap angle obtained was 0.00464 radians or 0.27^{o} which produces a blade tip displacement of 0.19 m and thus precluding any possibility of a blade hitting the tower. In conformity with the specifications of the turbine, a clearance of approximately 1.9 m exists between the tower and the blade tip at their closest position. Note that the behavior of the three blades is very similar in both phase and amplitude suggesting that a symmetrical rotor mode is excited.

The tower motion in the fore-aft direction, shown in Fig. 4-11, is out of phase with respect to the blade flap motion, meaning that probably the mode associated to the characteristic exponent s_4 is governing the response (see Section 3.5). To confirm this hypothesis a frequency analysis of the motion of the blades was performed. Fig. 4-10 shows the frequency (or Fourier) spectrum of the blade 1, which is representative of the other two blades. The graph reveals a clear dominant frequency at 2.32 rad/s that is very close to the frequency obtained for s_4, the first fore-aft tower mode of the turbine (the fourth mode overall shown in Fig. 3-4). There is a slight difference between the frequency obtained from the Fourier spectrum (2.32 rad/s) and the corresponding modal frequency (2.18 rad/s) found by the Floquet analysis. The reason for this small variation is that this last frequency was adjusted so the constant k in equation (3-14) was an integer number as required by the Floquet theory. In this case and henceforth, the seismic response of the system will be characterized in terms of the modal frequencies obtained by the Floquet theory and summarized in Table 3-4.

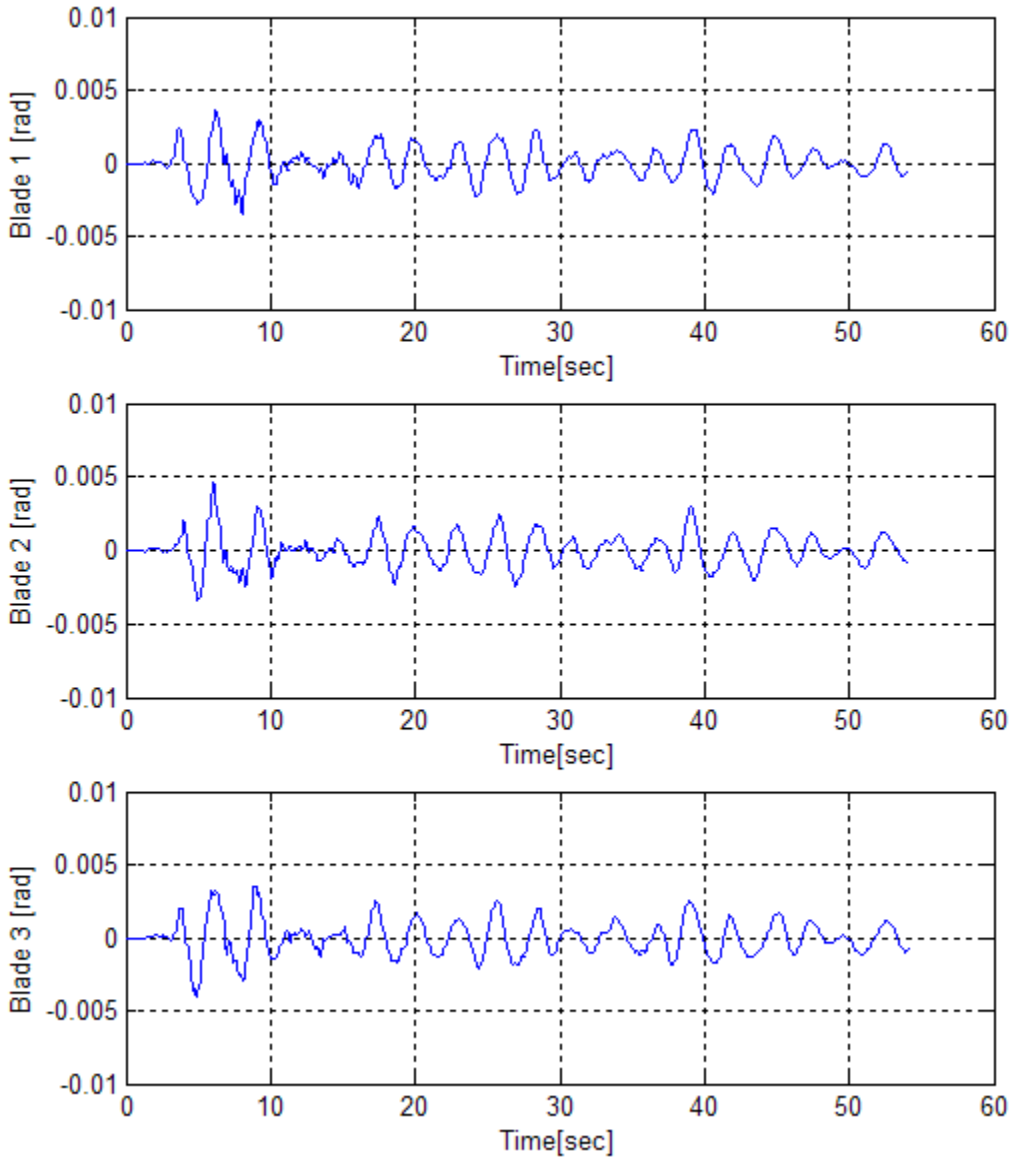

Fig. 4-9: Blade flap angle response, Taft record

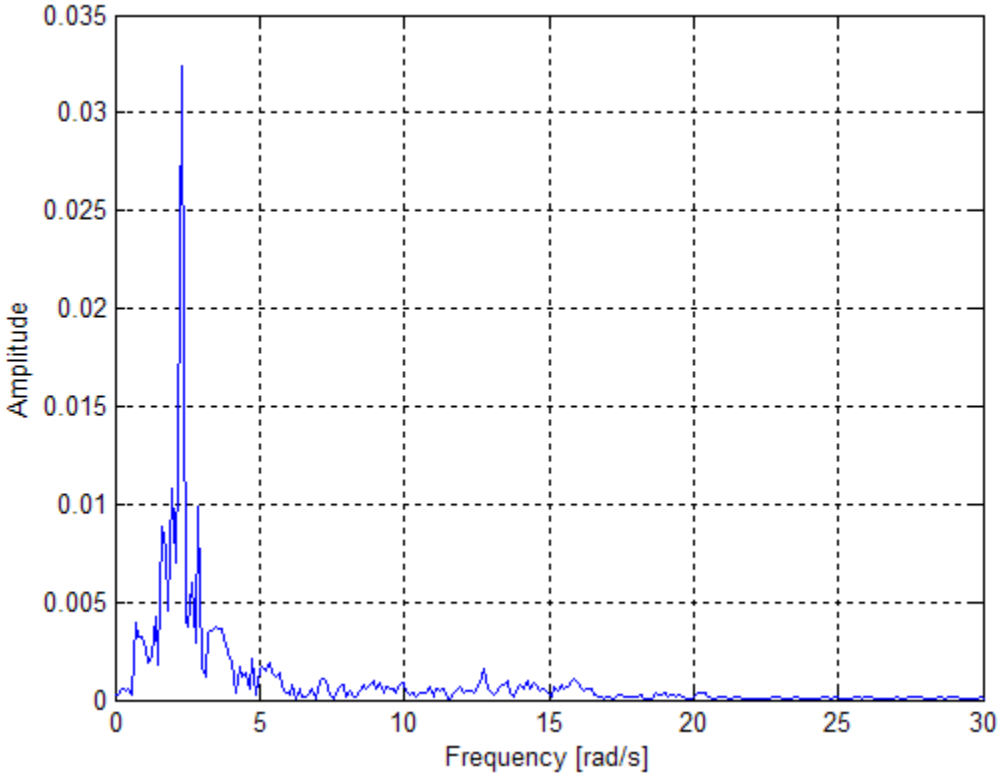

Fig. 4-10: Frequency spectrum of flap angle blade 1, Taft record

The fore-aft motion of the tower during the total duration of the earthquake is shown in Fig. 4-11. The figure illustrates mostly an in-phase motion of the coordinates z_1, z_2 and z_3. The response clearly presents a dominant frequency, but the signals also have higher frequency content, albeit of lesser importance. These frequencies can be identified from the frequency spectrum of the coordinate z_2 shown in Fig. 4-12. The dominant frequency is at 2.18 rad/s which correspond to the first fore-aft mode. There is a small contribution of the second fore-aft tower mode with a frequency of 14.07 rad/s. The maximum displacement of the tower occurred at its top end with a value of 0.095 m.

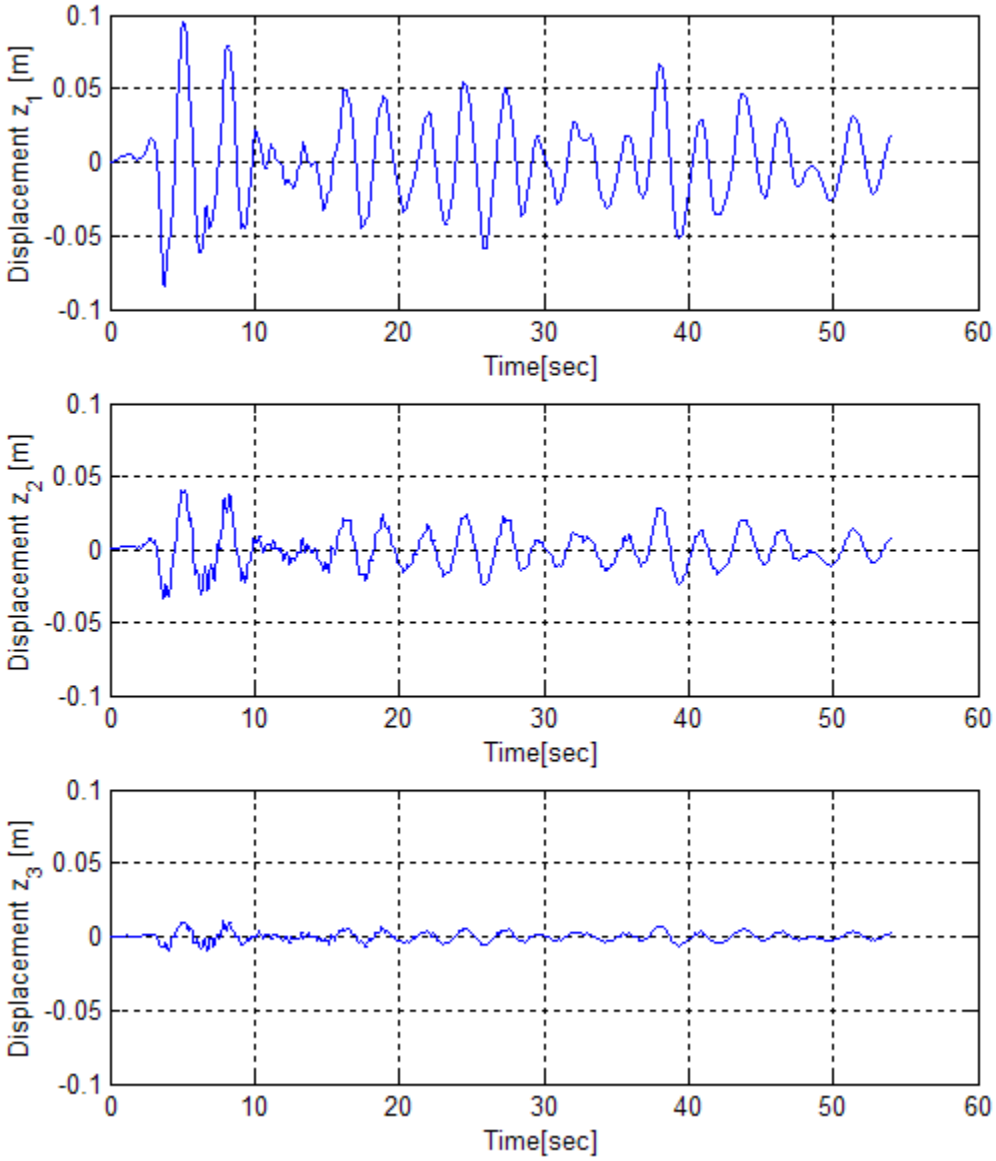

Fig. 4-11: Tower fore-aft response, Taft record

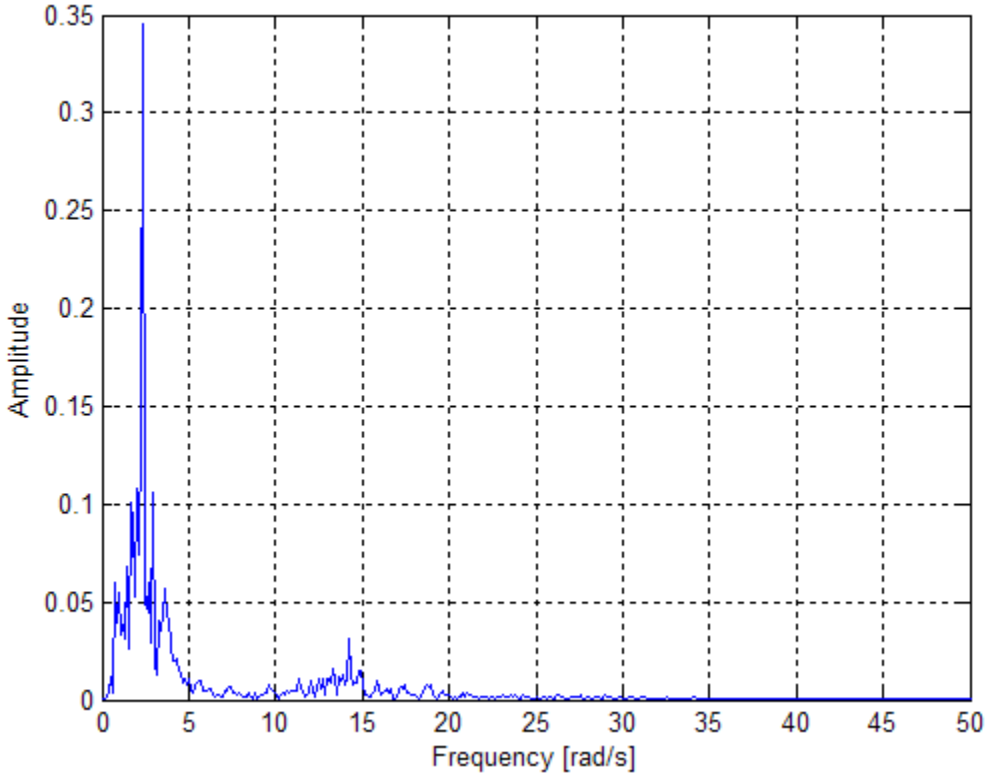

Fig. 4-12: Frequency spectrum of coordinate z_2, Taft record

We investigate next the lateral motion response of the wind turbine. Fig. 4-13 presents the displacements of the nodal coordinates for the lateral motion of the tower. At first glance, the three displacement traces display signs of instability at the end of the record. This type of behavior can also indicate the onset of a resonant condition. To investigate the potential occurrence of resonance or instability, an examination of the frequency content of the last part of the N21E Taft record was performed using a Fourier analysis. This is shown in the second plot of Fig. 4-2. The figure revealed that the dominant frequencies in that interval were in the range of 0.98 to 1.95 rad/s. The latter value is tuned to the frequency of the first lateral tower mode, namely 1.96 rad/s. This means that during the last part of the earthquake, the system

experienced temporarily some resonance situations. Because this occurs near the end of the excitation, it does not pose a problem to the structure: the response after the end of the earthquake record corresponds to a decaying free vibration.

Returning to the lateral response of the tower, the maximum displacement occurs at the top end (coordinate x_1) with a value of 0.23 m. As can be observed, the maximum displacement in the lateral direction is larger (138% larger) than in the fore-aft direction, even when the strongest record is applied in the last direction. This happens mainly because the system is undamped in the lateral direction, as it was anticipated by the Floquet analysis previously performed. It is recalled that thus far no structural damping was introduced in the model and that only the damping associated to aerodynamic effects was considered. The aerodynamic damping is present in the system if there is a change in the relative wind speed with respect to the blades. This change in the apparent wind speed can be originated by the fore-aft motion of the tower, the twisting motion of the tower, as well as the flapping motion of the blades; however, all of these motions are missing in this lateral mode.

There are two dominant frequencies of the system in the lateral direction and they can be observed in the Fourier spectrum presented in Fig. 4-14. They correspond to the first lateral tower mode and the second lateral tower mode with frequencies of 1.96 rad/s and 14.27 rad/s, respectively; the first mode being the most significant.

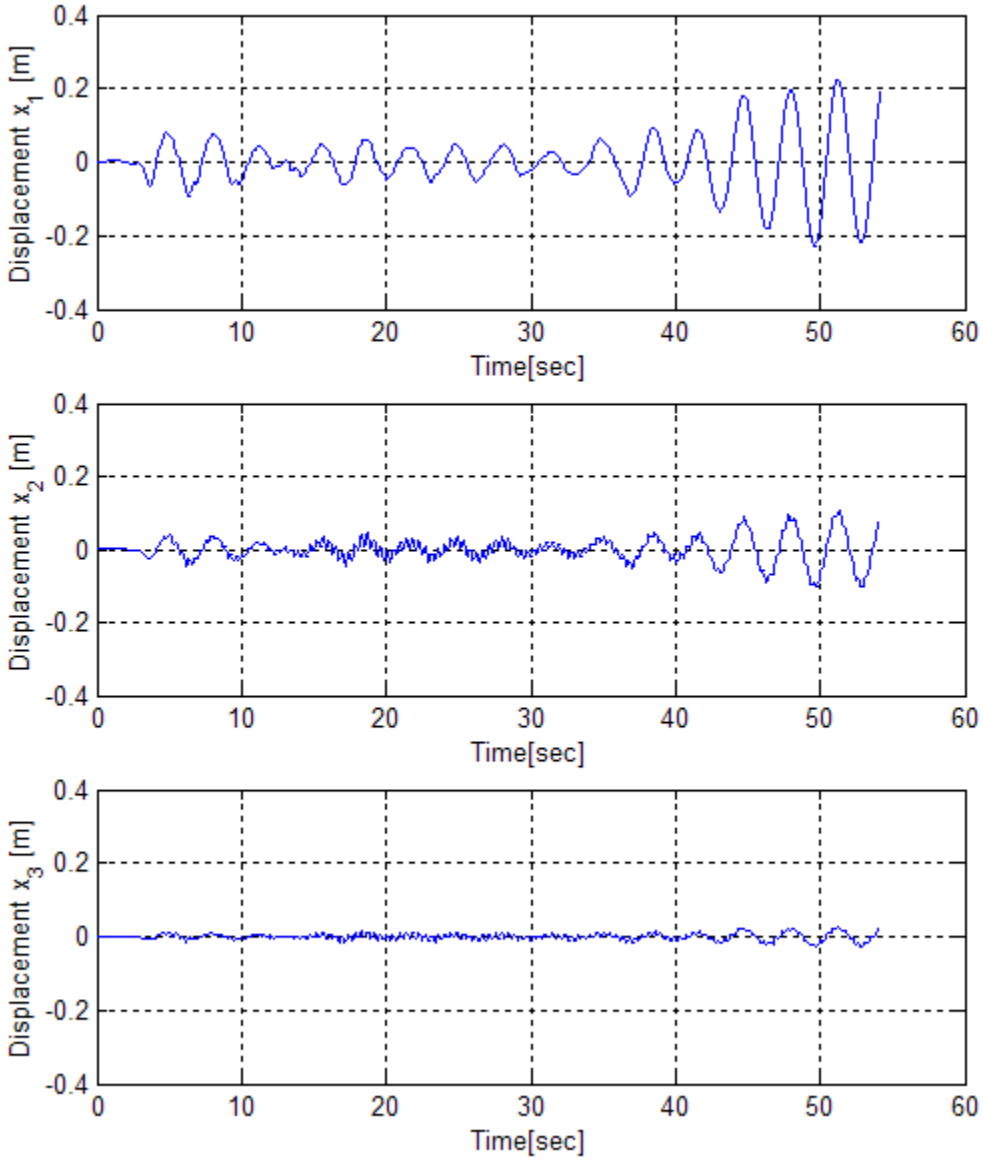

Fig. 4-13: Lateral tower response, Taft record

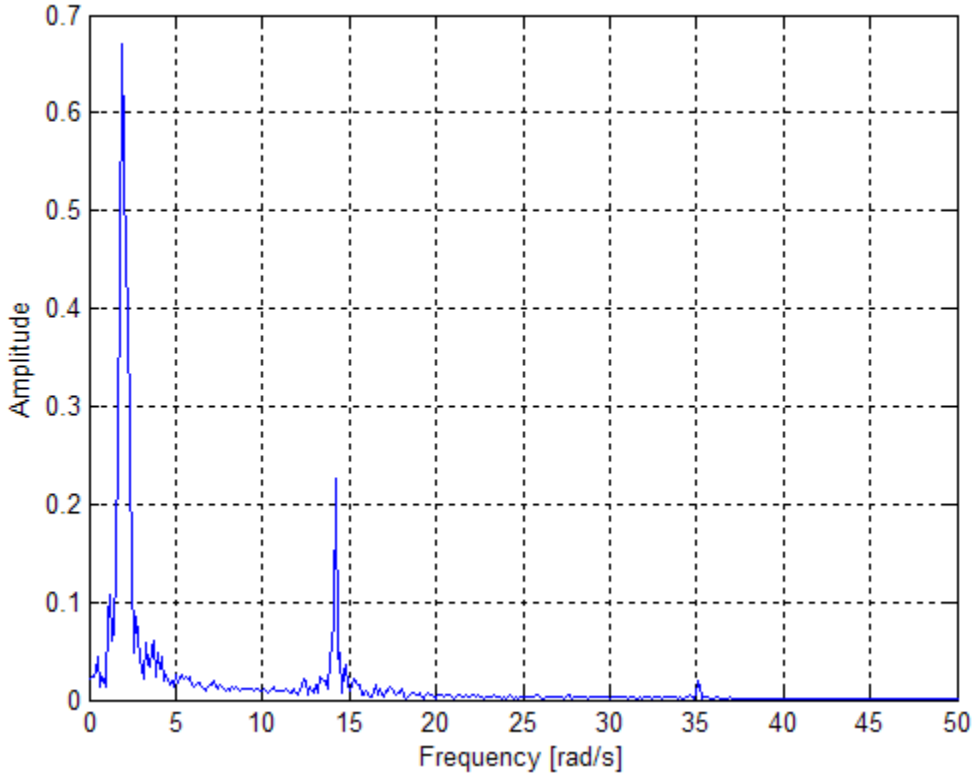

4-14: Frequency spectrum of coordinate x_2, Taft record

4.4.2 Response to the El Centro record

The response of the wind turbine using the El Centro record as input will be evaluated next. This record has a greater PGA than the Taft record, thus larger displacements are expected in this case. Fig. 4-15 shows the time variation of the flap angle of the blades for the total duration of the record. Similar to the previous case, the motion of the blades is governed by the fore-aft motion of the tower at a frequency of 2.18 rad/s. The maximum rotation of the blade is of 0.011 radians (0.61^o), roughly twice the value obtained with the Taft record. However, this rotation produced a tip displacement of 0.44 m which is still within a safety zone in terms of blade-tower collision.

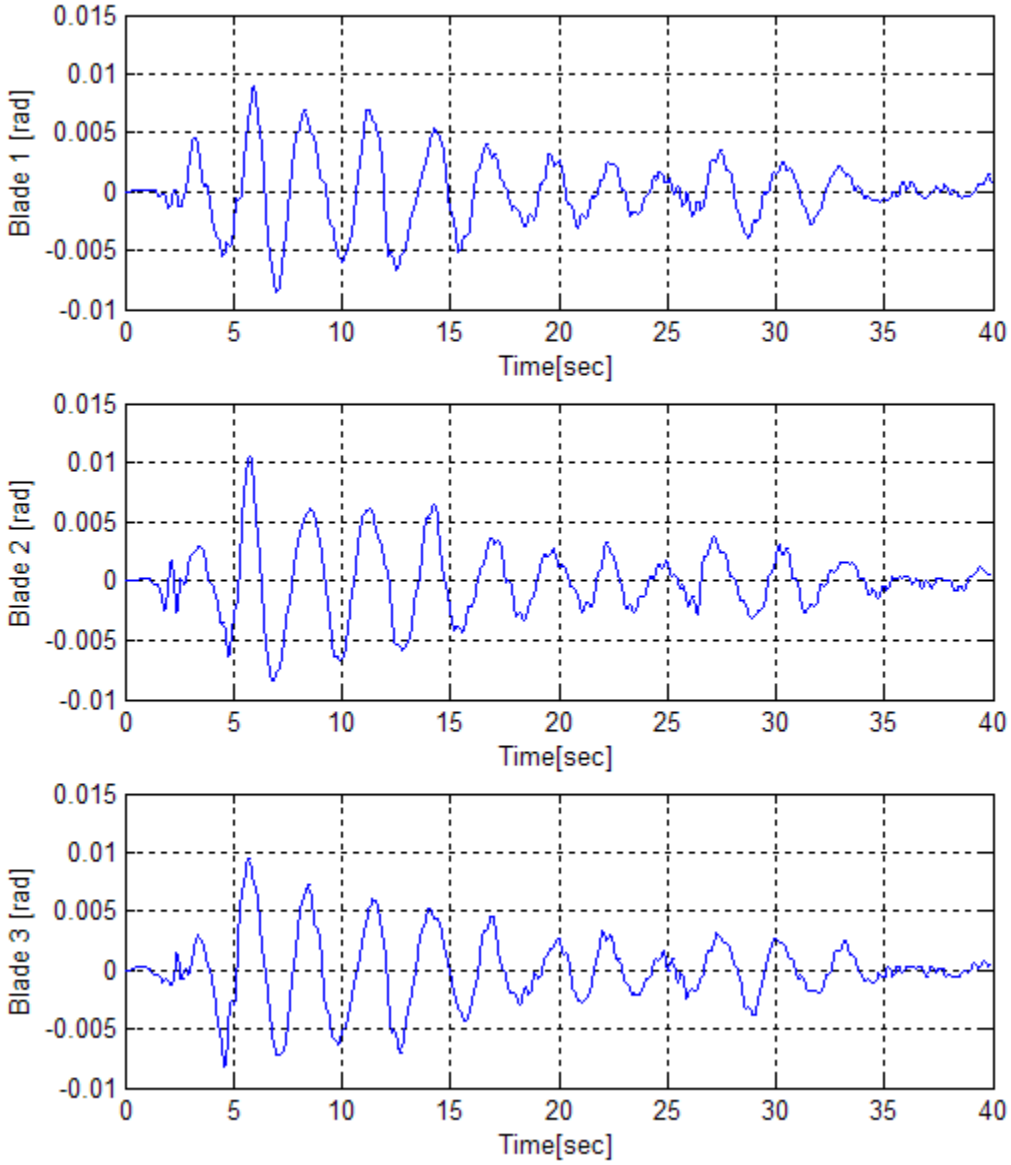

Fig. 4-15: Blade flap angle response, El Centro record

The seismic response of the tower fore-aft motion is shown in Fig. 4-16. The figure shows clearly a dominant motion of the first fore-aft mode and a small contribution of a higher mode associated to the second fore-aft tower mode. As it can be observed, the larger displacement occurred at the tower top end with a value of 0.21 m. The frequency spectrum of the coordinate z_2 at the middle of the tower is shown in Fig. 4-17. It reveals that there are mainly two frequencies present in the response, the dominant frequency at 1.96 rad/s and a second less important frequency at 14.07 rad/s.

The lateral motion of the tower displayed in Fig. 4-18 shows larger displacements (about 0.48 m at the tower top end) than for the frontal motion. As expected, they are greater because the there are no means to dissipate energy in this direction. The motion along the height of the tower is in-phase showing a clear dominant frequency corresponding to the first lateral tower mode, but it can be observed that higher frequencies are also present, especially in the motion of the middle and bottom coordinates of the tower (see Fig. 4-18). The frequency spectrum of the coordinate x_2 at the middle of the tower is shown in Fig. 4-19. The spectrum indicates that the dominant frequency is 1.96 rad/s and there is another important frequency at 14.27 rad/s. This frequency corresponds to the second lateral tower mode.

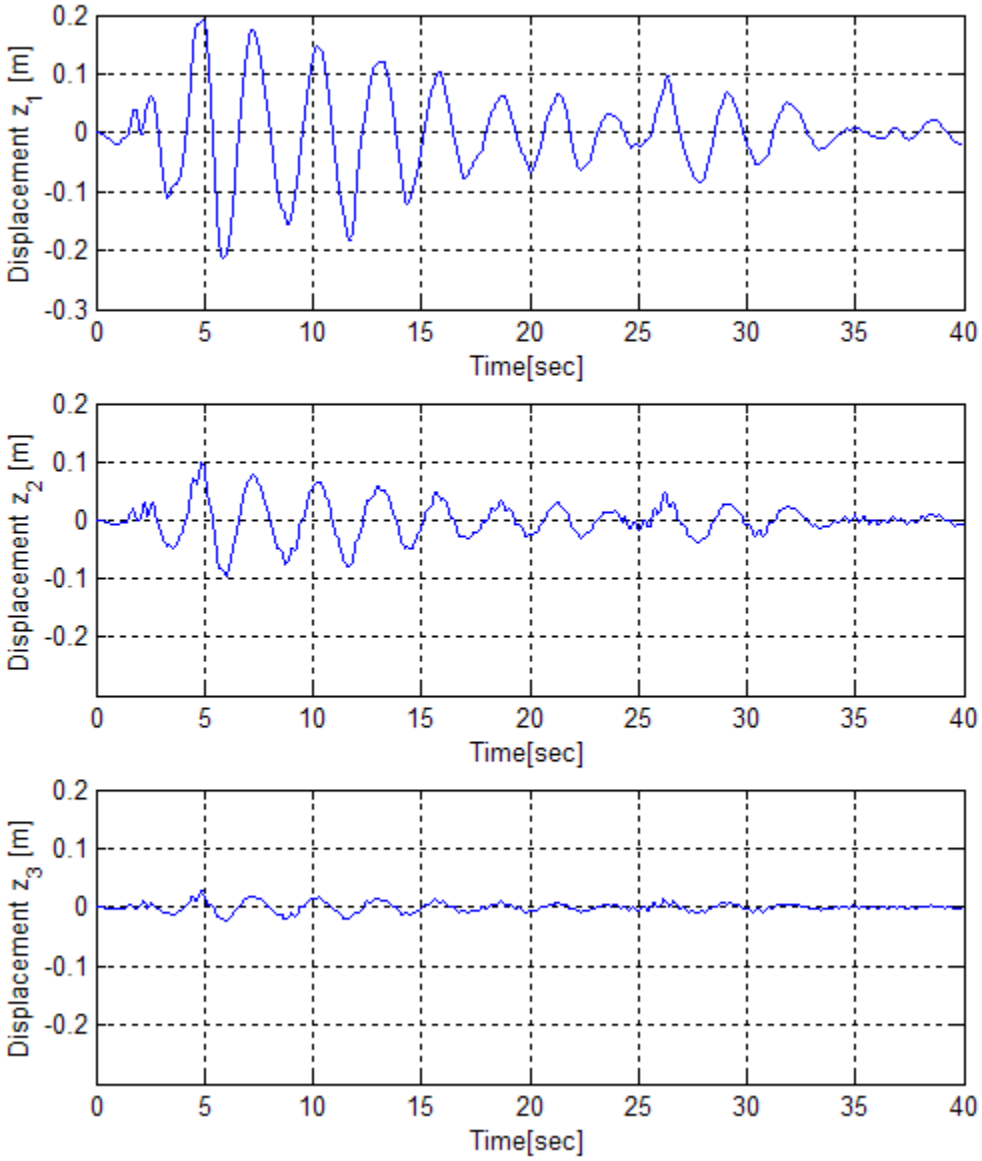

Fig. 4-16: Tower fore-aft response, El Centro record

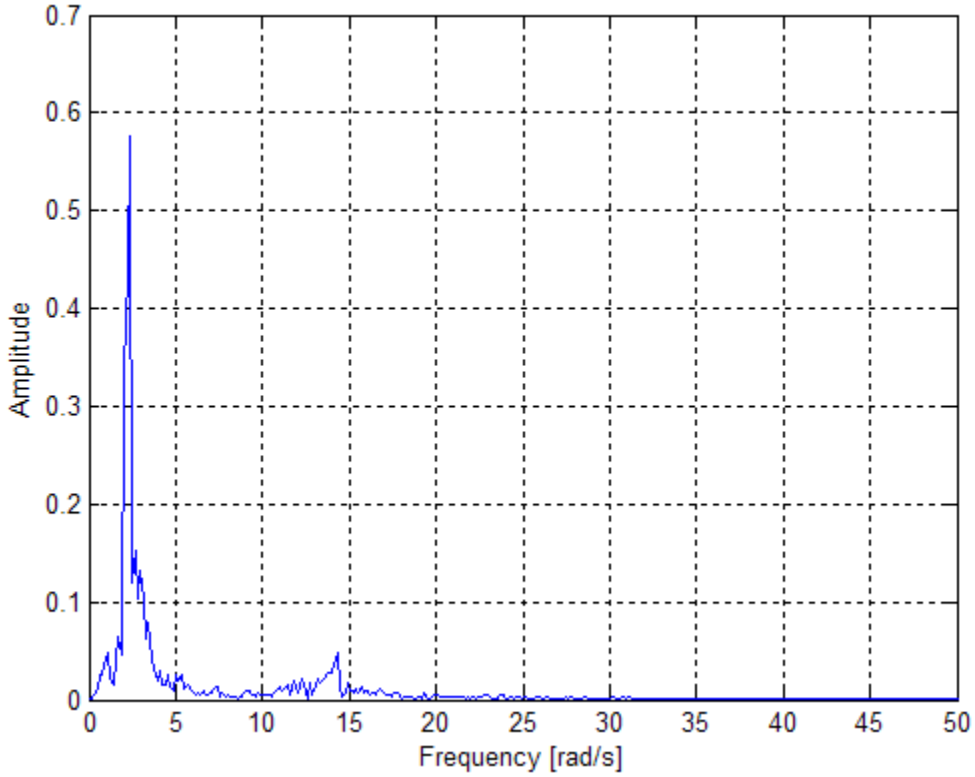

Fig. 4-17: Frequency spectrum of coordinate z_2, El Centro record

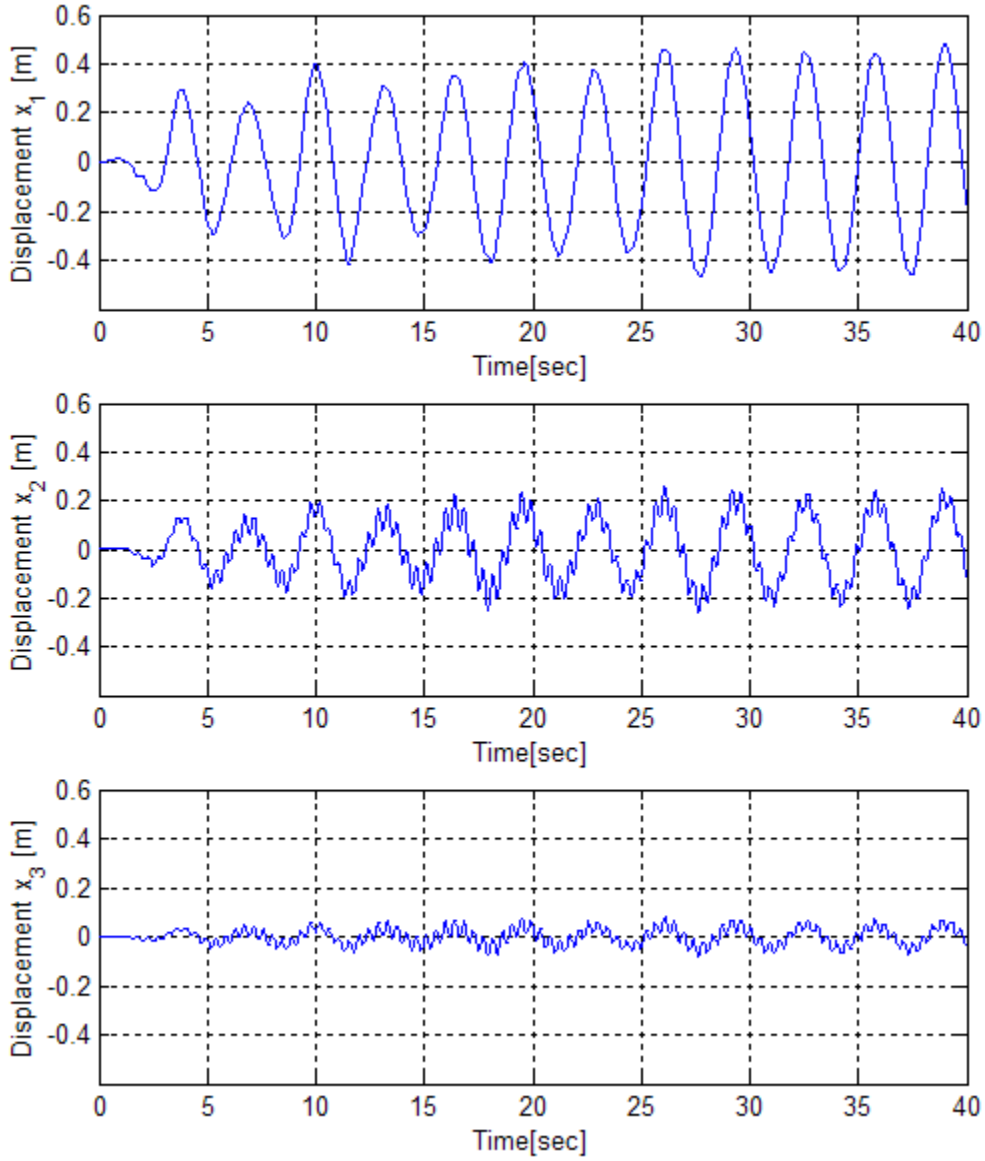

Fig. 4-18: Lateral tower response, El Centro record

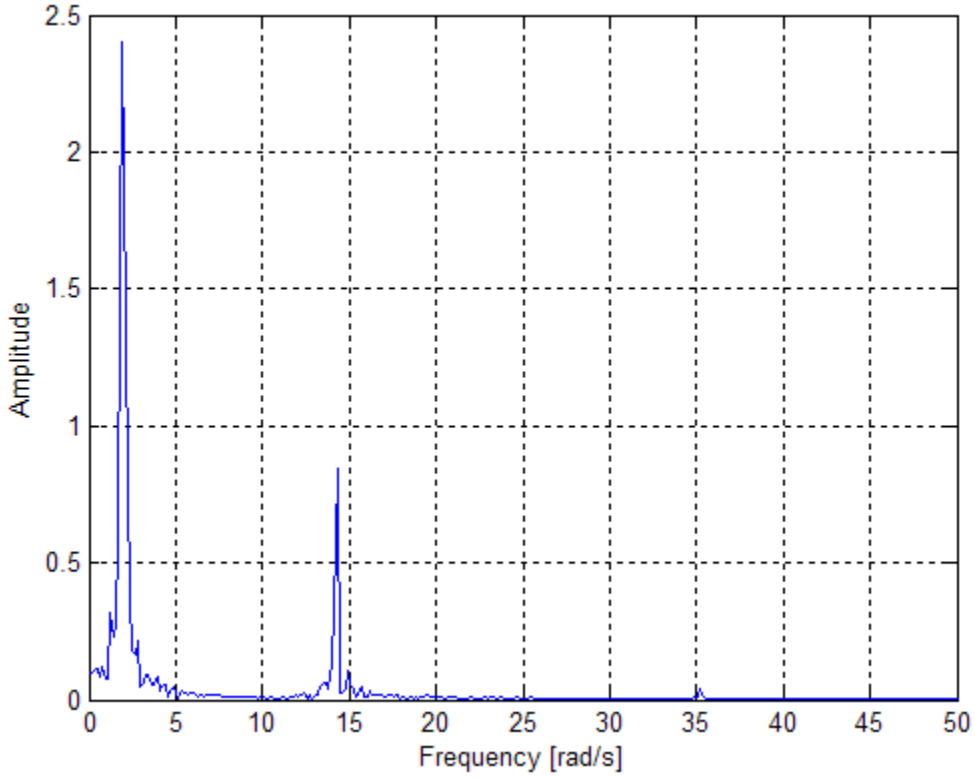

Fig. 4-19: Frequency spectrum of coordinate x_2, El Centro record

4.5 STRUCTURAL DAMPING IN THE SYSTEM

Since the lateral motion of the wind turbine is practically undamped and it seems to display signs of resonance, one may argue about the validity of the results when structural damping is not included. To address this issue a more realistic scenario will be considered here by introducing means to dissipate energy into the model. This can be accomplished by assigning modal damping ratios to all the vibration modes of the structure. To obtain the structural damping matrix we begin solving the eigenvalue problem for the linear model of the wind turbine with the rotor in the parked position (i.e., $\Omega = 0$) and ignoring the aerodynamic damping

effects by assuming the air density ρ_a = 0. Since the rotor of the turbine is stationary, all the periodic terms in the mass matrix and the gyroscopic matrix vanish. Note that both the resultant mass matrix in equation (2-96) and the stiffness matrix in equation (2-98) have elements outside their main diagonals maintaining the system statically and dynamically coupled. Hence, since periodicity is not present, a conventional eigenanalysis of the system can be performed. The modal analysis is a convenient method to define a diagonal damping matrix with modal damping ratios and then obtain the physical structural damping matrix [C_s]. It can be shown that this process can be achieved by employing the following equation which comes directly from the application of the modal analysis method:

$$[C_s] = [M][\Phi][C_d][\Phi]^T[M] \tag{4-6}$$

where [Φ] is the matrix of eigenvectors normalized with respect to the mass matrix and [C_d] is a diagonal matrix known as the modal damping matrix with the diagonal entries equal to $2\xi_i\omega_i$. A modal damping ratio ξ_i = 0.01 to all the modes, can be used which is a common value recommended for bolted-steel structures such as those found in the tower (see Burton *et al*., 2001, Prowell *et al*., 2008b).

Table 4-1 shows the natural frequencies obtained for the Vestas V82 turbine with the rotor stopped in the initial configuration (i.e., blade 1 in the horizontal position), as well as their related corresponding operational modal frequency. We can notice that the values for the majority of the natural frequencies ω_i obtained from the non-operating turbine do not differ significantly from those obtained previously from the Floquet analysis. Inspecting the eigenvectors one conclude that also the mode shapes of the parked turbine, especially those related to the tower modes, are very similar to the optimum mode shapes of the operating

turbine, suggesting that the operating rotor in this case does not change noticeably the response of the non-operating turbine. However, there are some differences in the shape and order of appearance of some modes, especially those associated to the rotor modes. The first mode obtained still corresponds to a front-aft mode comparable to the first mode of the operating turbine. The second mode is a lateral mode similar to the third mode in the operating turbine. The third and fourth modes correspond essentially to rotor modes, but none of them resemble the rotor modes obtained previously for the operating turbine. This is reasonable because the operating rotor is affected by damping and dynamic loads not present in the stationary rotor, such as gyroscopic moments and aerodynamic damping. Also in the operational wind turbine we obtained two overdamped modes that obviously do not appear here. The rest of the higher modes (from ϕ_9 to ϕ_{16}) can be described as tower modes oscillating at relatively high frequencies. At these frequencies the contribution of the rotor dynamics is insignificant, so there are no apparent differences between having a parked rotor or an operating one. All these mode shapes and frequencies match one by one with those obtained for the operating turbine. For comparison purposes, the eigenvectors of all modes were normalized such as the maximum entries were 1 and the results are given in Table 4-2.

To complete the process of incorporating structural damping to the system, the total damping matrix must be computed by adding the matrix $[C_s]$ to the previous damping matrix of the operating turbine $[C]$. Although the modal damping matrix $[C_d]$ is diagonal, the damping matrix $[C_s]$ is full, i.e., it contained values in all its elements. For the sake of compactness the numerical results are omitted here.

Table 4-1: Natural frequencies in [rad/s] of the wind turbine with a parked rotor

Natural Frequency (Stationary Rotor)		*Associated Frequency (Operational Rotor)*
ω_1	1.73	s_{12}
ω_2	1.96	s_2
ω_3	2.27	--
ω_4	2.36	--
ω_5	2.94	s_4
ω_6	14.14	s_{13}
ω_7	14.24	s_1
ω_8	33.56	--
ω_9	35.00	s_3
ω_{10}	37.12	--
ω_{11}	56.94	--
ω_{12}	68.07	s_7
ω_{13}	77.70	s_9
ω_{14}	80.67	s_8
ω_{15}	96.59	s_6
ω_{16}	96.71	s_5

Table 4-2: Mode shapes of the wind turbine model with a parked rotor

	ϕ_1	ϕ_2	ϕ_3	ϕ_4	ϕ_5	ϕ_6
θ_{b1}	0.04	0	1	0.28	−0.11	0.01
θ_{b2}	0.02	0	−0.50	1	−0.05	−0.06
θ_{b3}	0.07	0	−0.50	−0.45	−0.17	0.08
$\theta_{y'}$	0	0	−0.10	0	0	0
x_1	0	1	0.52	0	0	0
θ_{z1}	0	−0.02	−0.01	0	0	0
z_1	1	0	0	0.21	1	−0.18
θ_{x1}	−0.03	0	0	0.02	−0.02	0.08
x_2	0	0.44	0.23	0	0	0
θ_{z2}	0	−0.02	−0.01	0	0	0
z_2	0.43	0	0	0.33	0.47	1
θ_{x2}	−0.02	0	0	−0.01	−0.02	0
x_3	0	0.11	0.06	0	0	0
θ_{z3}	0	−0.01	0	0	0	0
z_3	0.10	0	0	0.11	0.12	0.51
θ_{x3}	−0.01	0	0	−0.01	−0.01	−0.03

Table 4-2: (Cont.) Mode shapes of the wind turbine model with a parked rotor

	ϕ_7	ϕ_8	ϕ_9	ϕ_{10}	ϕ_{11}
θ_{b1}	−0.01	0	0.17	−0.75	0.01
θ_{b2}	0.01	0.13	−0.09	0.38	0.24
θ_{b3}	0.01	−0.13	−0.09	0.38	−0.22
$\theta_{y'}$	−0.01	0	0.17	−0.72	0
x_1	−0.14	0	−0.19	1	0
θ_{z1}	0.07	0	−0.12	−0.13	0
z_1	0	0	0	0	−0.22
θ_{x1}	0	−0.15	0	0	−0.25
x_2	1	0	−0.65	−0.20	0
θ_{z2}	0	0	0.11	0.03	0
z_2	0	−0.47	0	0	1
θ_{x2}	0	0.11	0	0	−0.01
x_3	0.51	0	1	0.34	0
θ_{z3}	−0.03	0	−0.03	−0.01	0
z_3	0	1	0	0	−0.56
θ_{x3}	0	−0.03	0	0	−0.01

	ϕ_{12}	ϕ_{13}	ϕ_{14}	ϕ_{15}	ϕ_{16}
θ_{b1}	0.09	0.01	0.14	0	−0.03
θ_{b2}	−0.05	0.10	−0.07	−0.03	0.02
θ_{b3}	−0.05	−0.09	−0.07	0.03	0.02
$\theta_{y'}$	0.09	0	0.13	0	−0.03
x_1	−0.25	0	−0.40	0	0.11
θ_{z1}	−0.39	0	−0.47	0	0.10
z_1	0	−0.13	0	0.05	0
θ_{x1}	0	−0.11	0	0.03	0
x_2	1	0	0.23	0	1
θ_{z2}	0.11	0	−0.37	0	0.33
z_2	0	−0.22	0	1	0
θ_{x2}	0	−0.32	0	0.30	0
x_3	−0.79	0	1	0	0.11
θ_{z3}	−0.05	0	0.18	0	0.47
z_3	0	1	0	0.12	0
θ_{x3}	0	0.14	0	0.46	0

4.6 SEISMIC RESPONSE OF THE WIND TURBINE WITH STRUCTURAL DAMPING

The structural damping matrix obtained from equation (4-6) was incorporated in the global damping matrix. The equations of motion in state form expressed in equation (4-4) were evaluated again for the same two earthquake records to assess the reduction of the lateral displacements and inspect the situation of resonance or instability in the lateral direction. Figs. 4-20 to 4-22 show the displacement and rotation response of the damped turbine using the Taft record as input. Notice that in this scenario trailing zeros were added at the end of the Taft record to observe the behavior of the wind turbine after the earthquake ended.

The corresponding response for the El Centro record is shown in Figs. 4-23 to 4-25. As it can be observed in all the figures, the amplitude of the response slightly decreased when structural damping was present, except for the lateral response. The maximum displacements of the system with and without structural damping are summarized in Table 4-3. The use of 1% of modal damping ratio produced displacement reductions of up to 41% in the lateral direction.

In the case of the Taft record, the lateral response still showed an increment in amplitude between the 35 to 50 seconds time interval followed by a small decay after the end of the earthquake. A log decrement analysis of the free vibration part revealed a damping ratio of 0.01, the same value used as modal ratios. A similar analysis but for the free vibration motion in the fore-aft direction revealed a higher damping ratio of 0.11 which is mainly a consequence of the aerodynamic damping. As we mentioned before, the turbine was in resonance during the last seconds of the Taft record because the first lateral modal frequency of the wind turbine coincided

with one of the dominant frequencies at the end part of the record. The amplitude did not increase more because it was restricted by the upper bound obtained by the structural damping and because the excitation vanished. Nevertheless, even with the inclusion of structural damping, the tower lateral displacements are two times greater than the frontal tower displacements and the duration of the free vibration of the tower is considerable. A possible corrective measure to increase the lateral damping is to cover the interior and/or the exterior walls of the tower with a damping material (i.e., an engineered elastomeric material). Another possible solution is to place tuned mass dampers inside the tower.

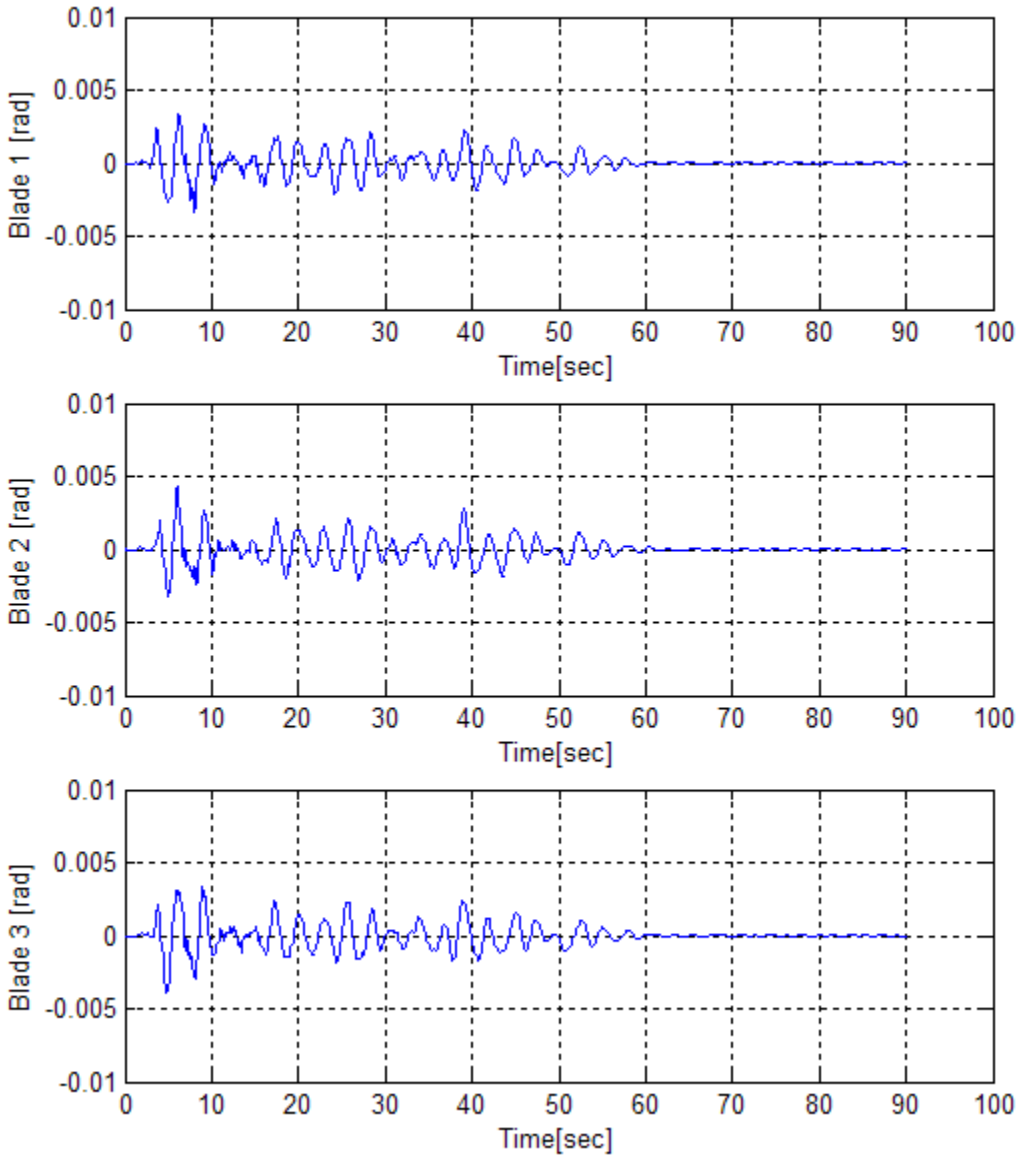

Fig. 4-20: Blade flap angle damped response, Taft record

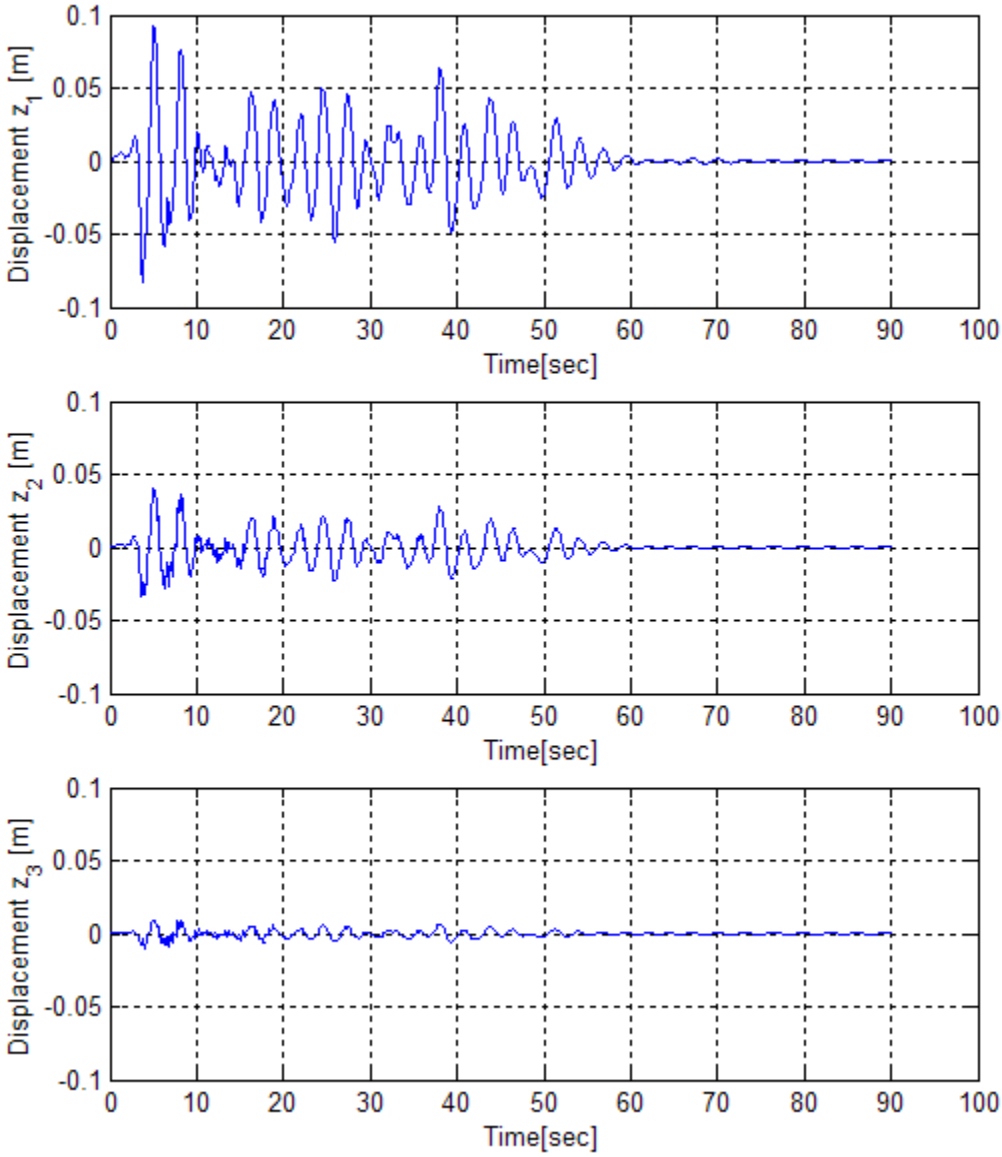

Fig. 4-21: Tower fore-aft damped response, Taft record

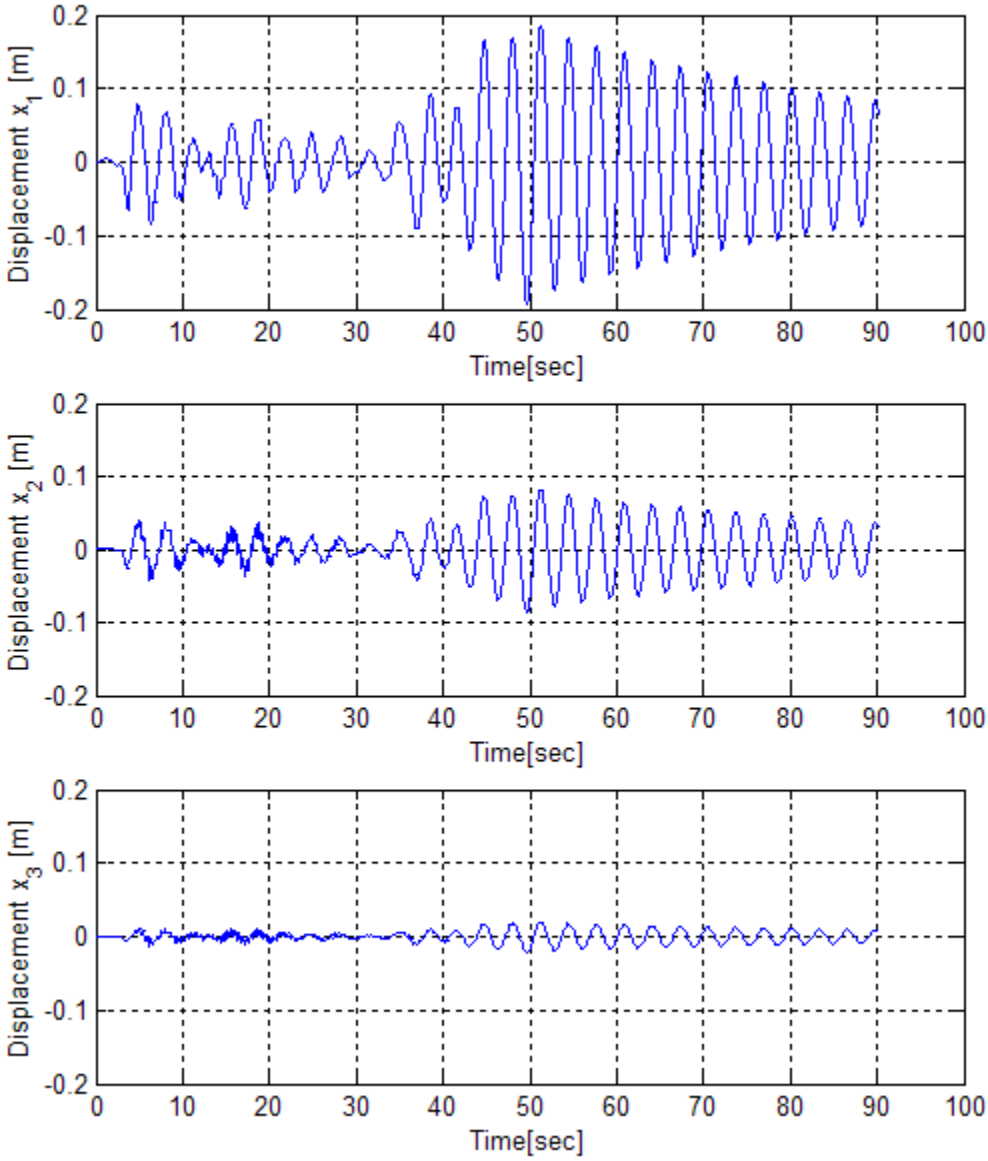

Fig. 4-22: Lateral tower damped response, Taft record

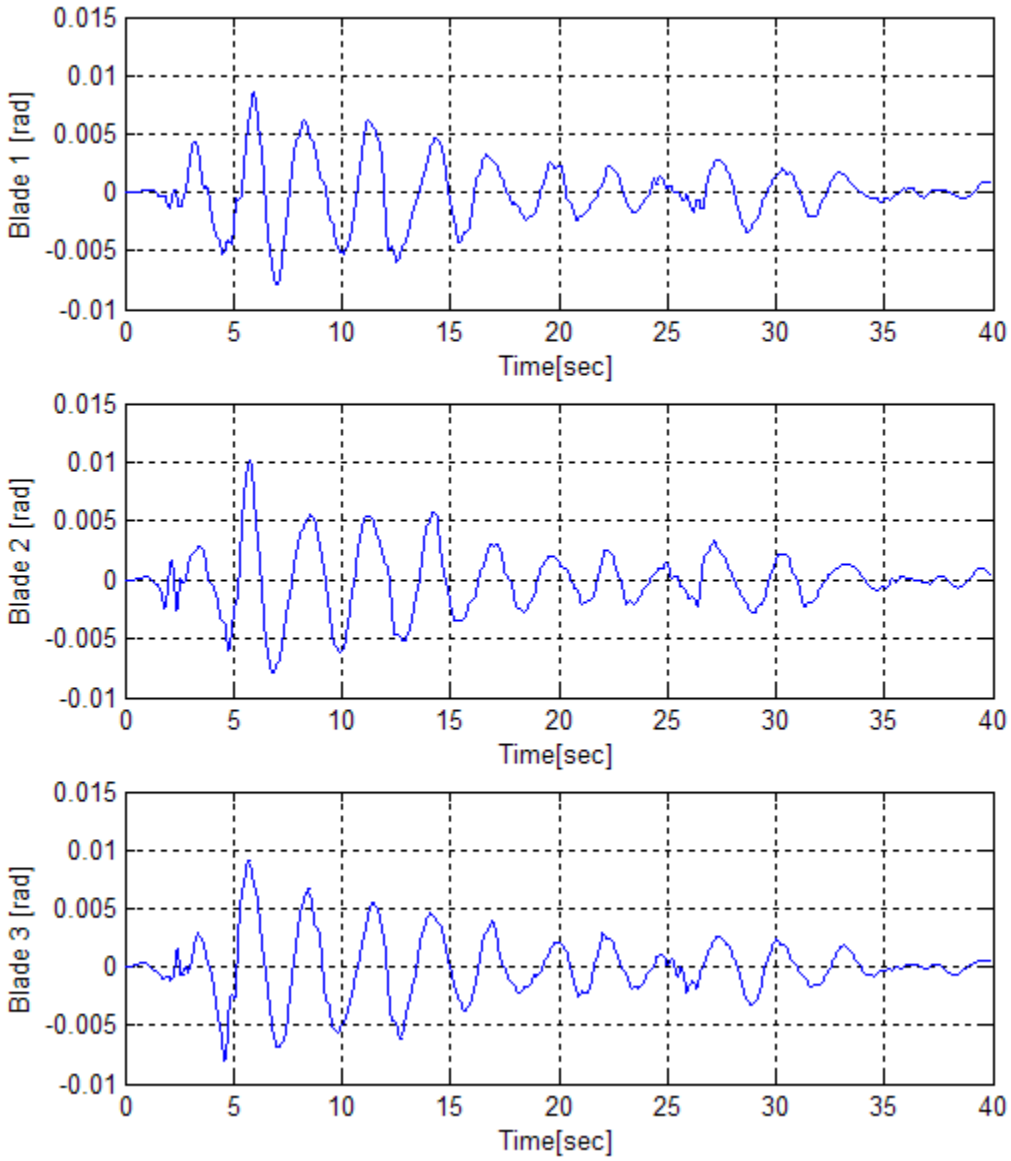

Fig. 4-23: Blade flap angle damped response, El Centro record

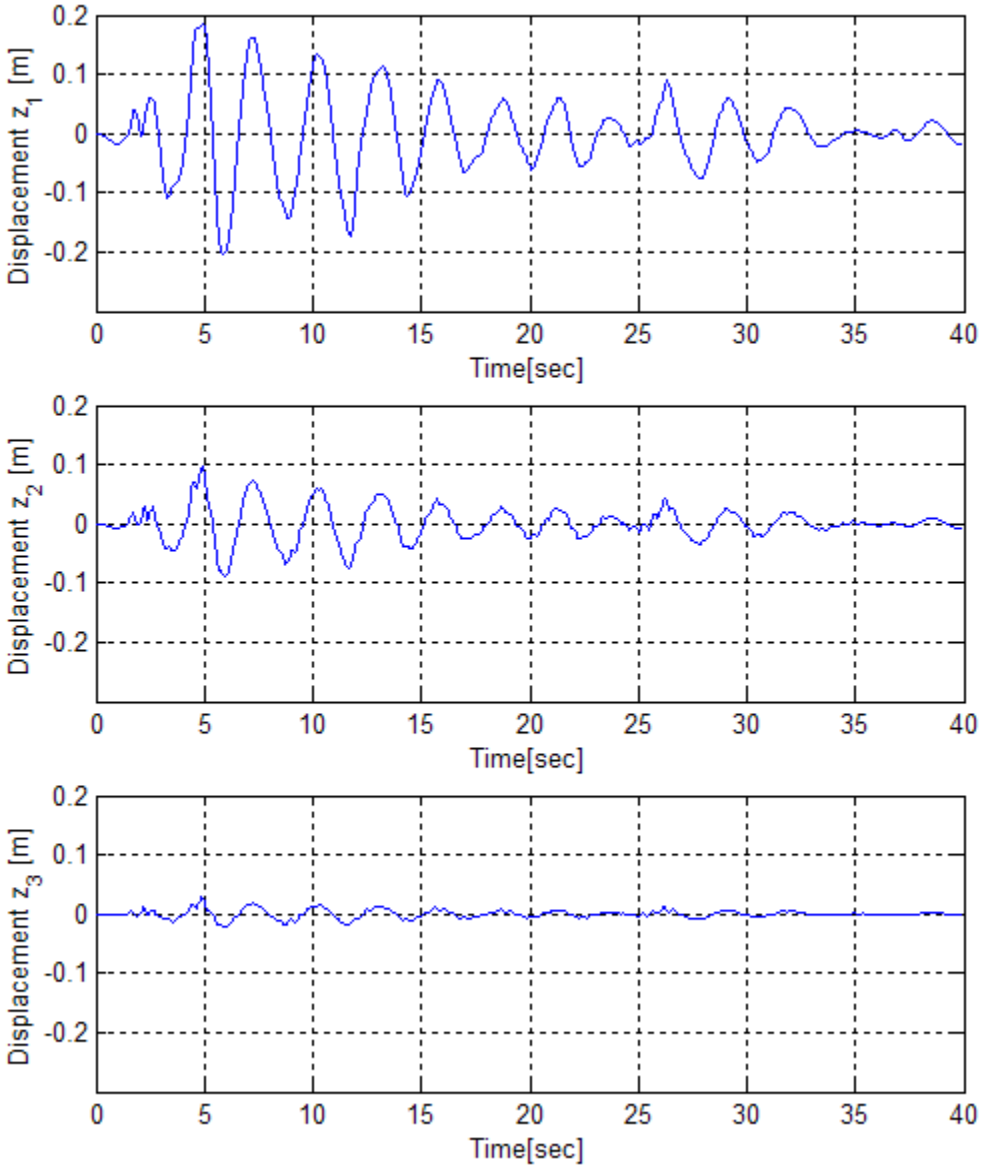

Fig. 4-24: Tower fore-aft damped response, El Centro record

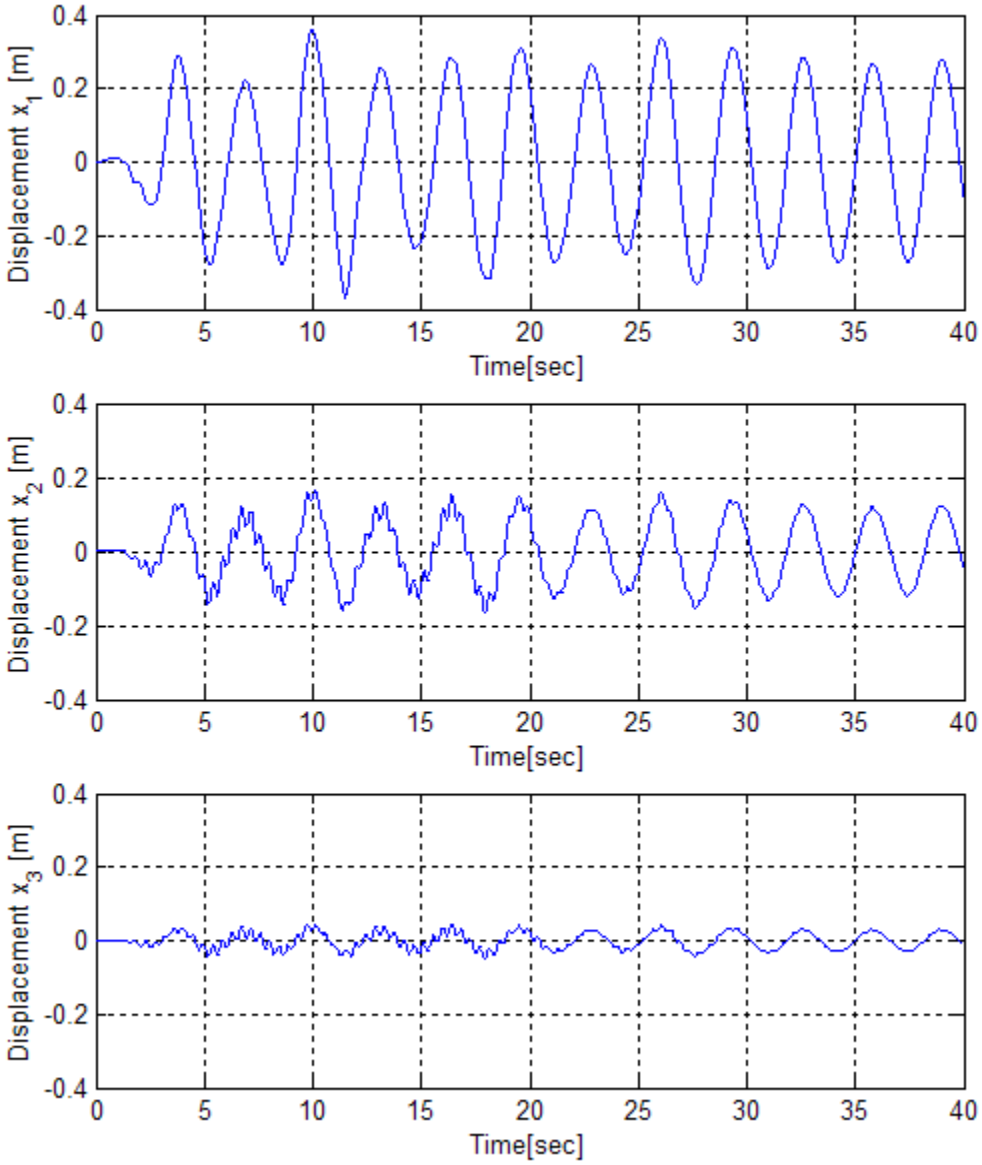

Fig. 4-25: Lateral tower damped response, El Centro record

Table 4-3: Maximum displacements of the wind turbine with and w/o structural damping

Coordinate		***Taft Record***			***El Centro Record***		
		w/o damping	*with damping*	*% diff.*	*w/o damping*	*with damping*	*% diff.*
Blades Flap Angle	θ_{b1} [rad]	0.004	0.003	25.0	0.009	0.009	0
	θ_{b2} [rad]	0.005	0.004	20.0	0.011	0.010	9.1
	θ_{b3} [rad]	0.004	0.004	0	0.010	0.009	10.0
Tower Twist	θ_y' [rad]	0.001	0.001	0	0.002	0.002	0
Tower Flexure Angle	θ_{x1} [rad]	0.003	0.003	0	0.006	0.006	0
	θ_{z1} [rad]	0.006	0.005	16.7	0.016	0.011	31.3
Tower Fore-aft Displacement	z_1 [m]	0.095	0.092	3.2	0.214	0.205	4.2
	z_2 [m]	0.041	0.040	2.4	0.100	0.097	3.0
	z_3 [m]	0.010	0.010	0	0.029	0.028	3.4
Tower Lateral Displacement	x_1 [m]	0.227	0.194	14.5	0.481	0.368	23.5
	x_2 [m]	0.105	0.086	18.1	0.261	0.167	36.0
	x_3 [m]	0.029	0.021	27.6	0.083	0.049	41.0

4.7 SEISMIC RESPONSE USING EARTHQUAKE RECORDS WITH DIRECTIVITY AND NEAR-FAULT EFFECTS

Now that the structural damping in the system has been included, we will consider the seismic response of the wind turbine using the remaining two records that show directivity and near-fault effects. Figs. 4-26 to 4-28 show the response of the principal degrees of freedom of the turbine using as input the Northridge earthquake record. The maximum blade rotation is 0.010 radians causing a blade tip displacement of 0.4 m. As mentioned before, there is a clearance of 1.9 m between the blade tip and the tower, and thus blade-tower collision is not occurring. The maximum displacement at the upper end of the tower in the fore-aft direction is 0.22 m. The maximum lateral displacement at the top end of the tower is 0.26 m. The lateral

motion of the tower still exhibits larger displacements due to the small structural damping in this direction, but they are much closer than the displacement obtained with the previous two records (El Centro and Taft). This is a direct consequence of the strong directivity component that exhibits the Castaic record. As it can be observed from the figures, there are two dominant modes of vibration in each direction. In the response of the tower in the fore-aft direction there is a dominant motion that corresponds to the first frontal tower mode, as well as the second frontal tower mode. The same situation is repeated in the lateral direction but the higher mode is more perceptible now.

Figs. 4-29 to 4-31 show the response of the wind turbine under the action of the San Salvador earthquake. The maximum blade flap rotation is of 0.0119 radians (there is no blade tip and tower collision). The maximum fore-aft displacement of the top end of the tower is 0.25 m and the maximum lateral displacement is also 0.25 m. Even though this is a small magnitude earthquake and some of the maximum displacements produced in the wind turbine are smaller than those for the previous records we found greater stresses in the wind turbine due to the high PGA. These results will be shown later in Section 4.9. It is pertinent to observe the instant when the turbine felt the PGA of the record at 1.5 seconds. As can be observed, this is not the instant of the greatest displacement in the structure but the relative displacements or drift of the tower top end z_1 with respect to the subsequent lower tower node z_2 are the largest. Due to the fact that the wind turbine is essentially a flexible structure with a relatively long first natural period, the strong acceleration of the earthquake is not transmitted instantaneously to the nacelle. Instead, it produces a small frontal relative displacement of the lower and middle tower section and a backward relative motion of the nacelle. This means that, in terms of absolute motion, the nacelle tends to stay stationary while the two lower sections of the tower are moving with the ground. Certainly this situation will adversely stress the tower especially in the top section.

The dominant excitation mode in the fore-aft tower direction is once again the first frontal mode whereas the dominant mode in the lateral direction is the first lateral mode with small traces of the second lateral mode.

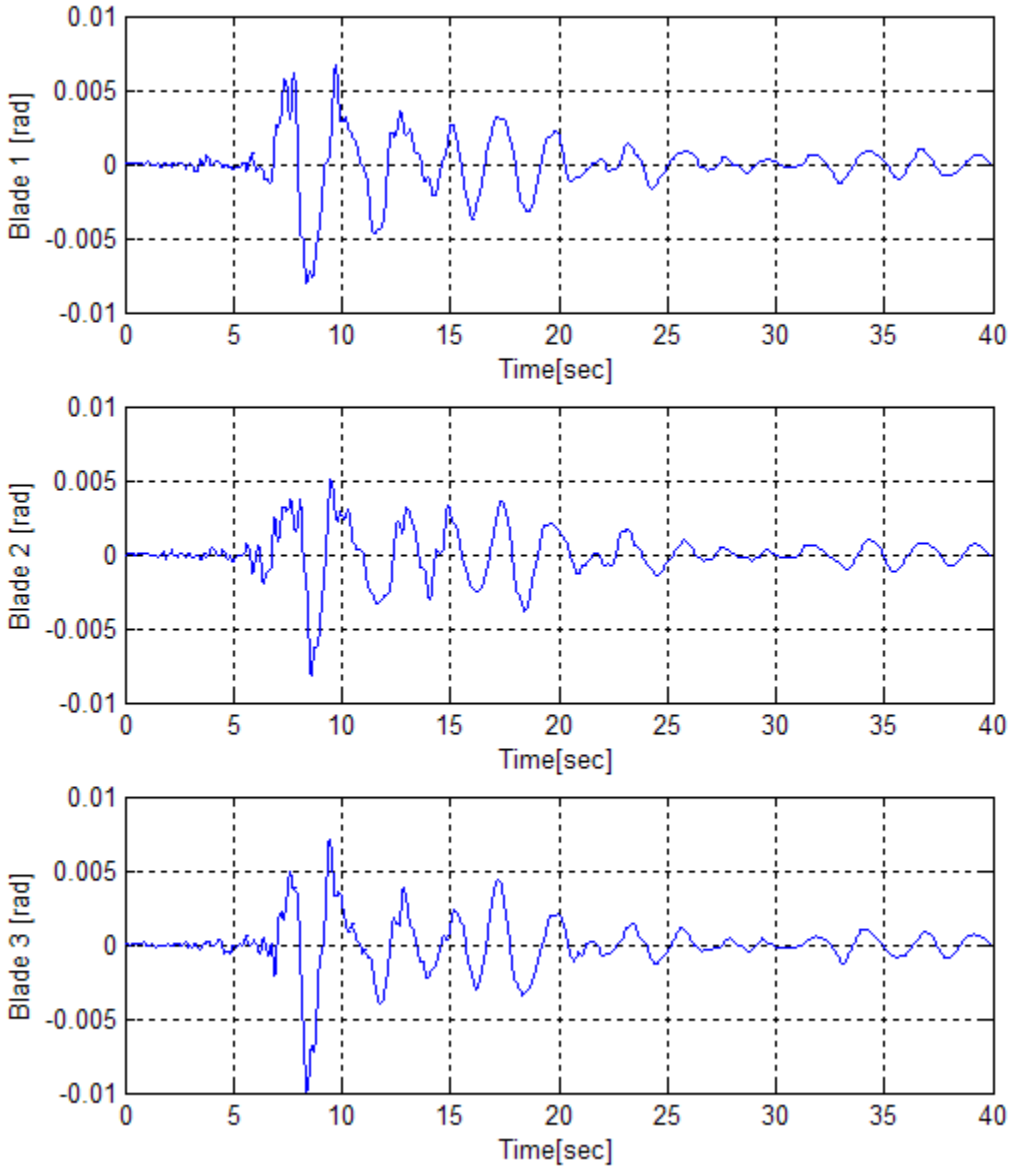

Fig. 4-26: Blade flap angle damped response, Northridge earthquake

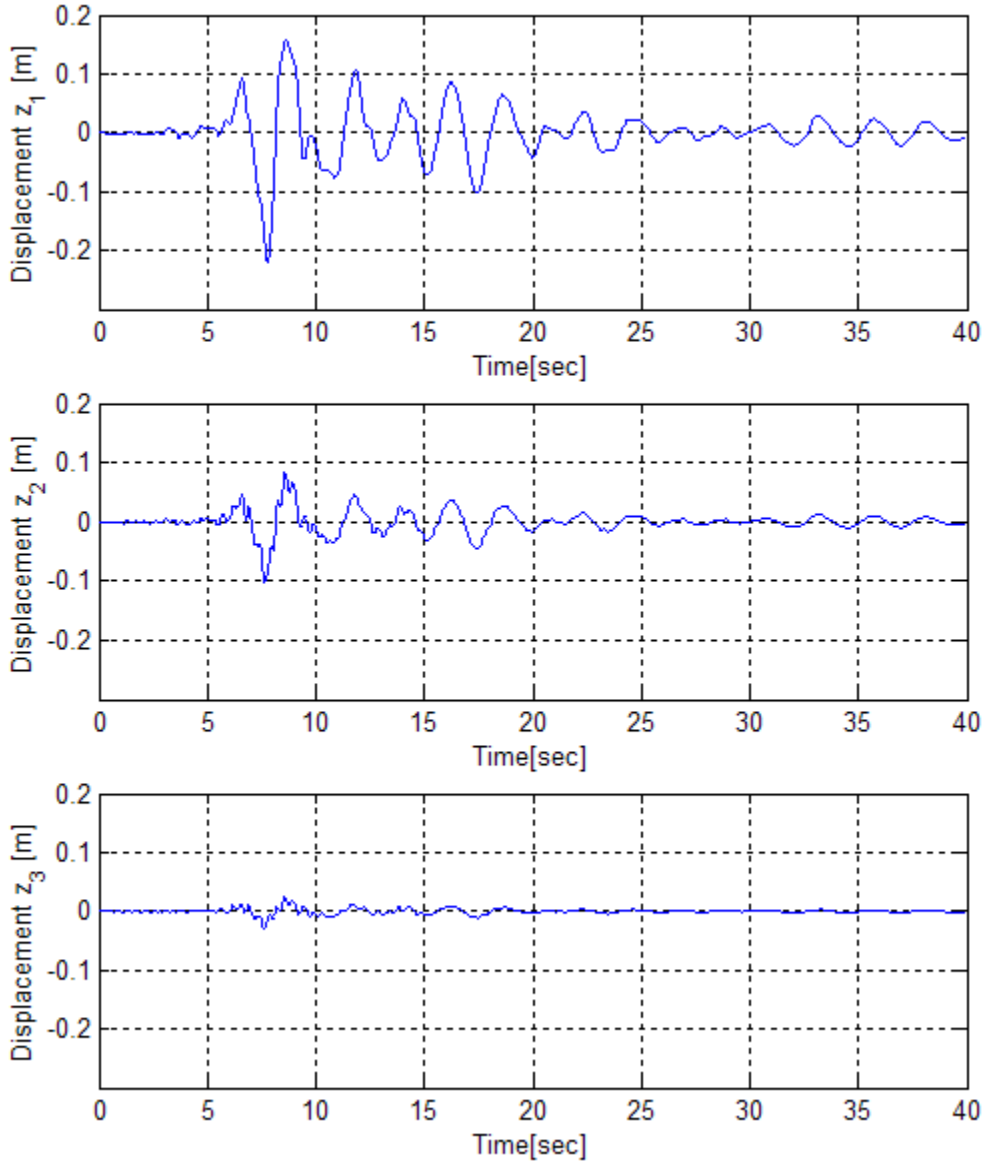

Fig. 4-27: Tower fore-aft damped response, Northridge earthquake

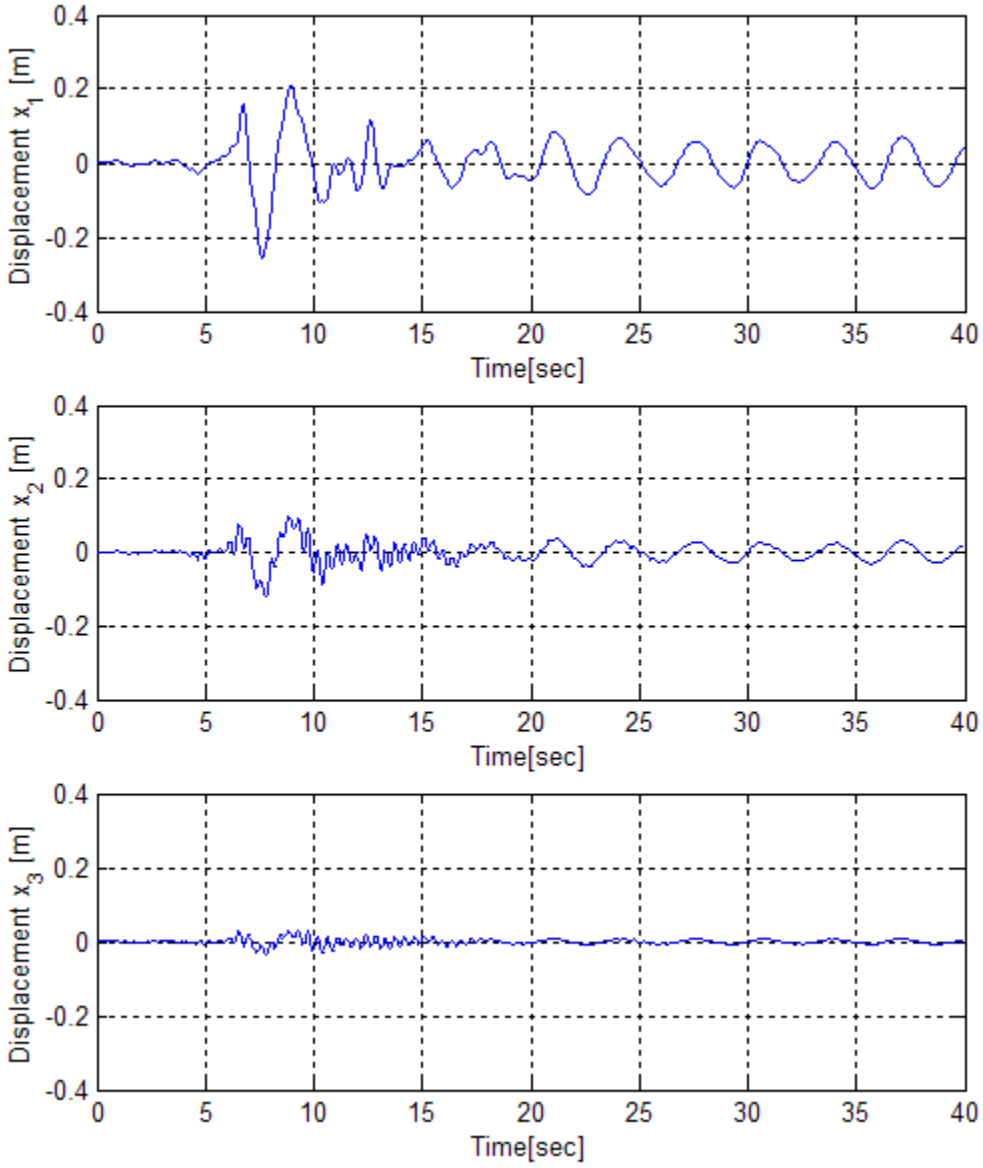

Fig. 4-28: Lateral tower damped response, Northridge earthquake

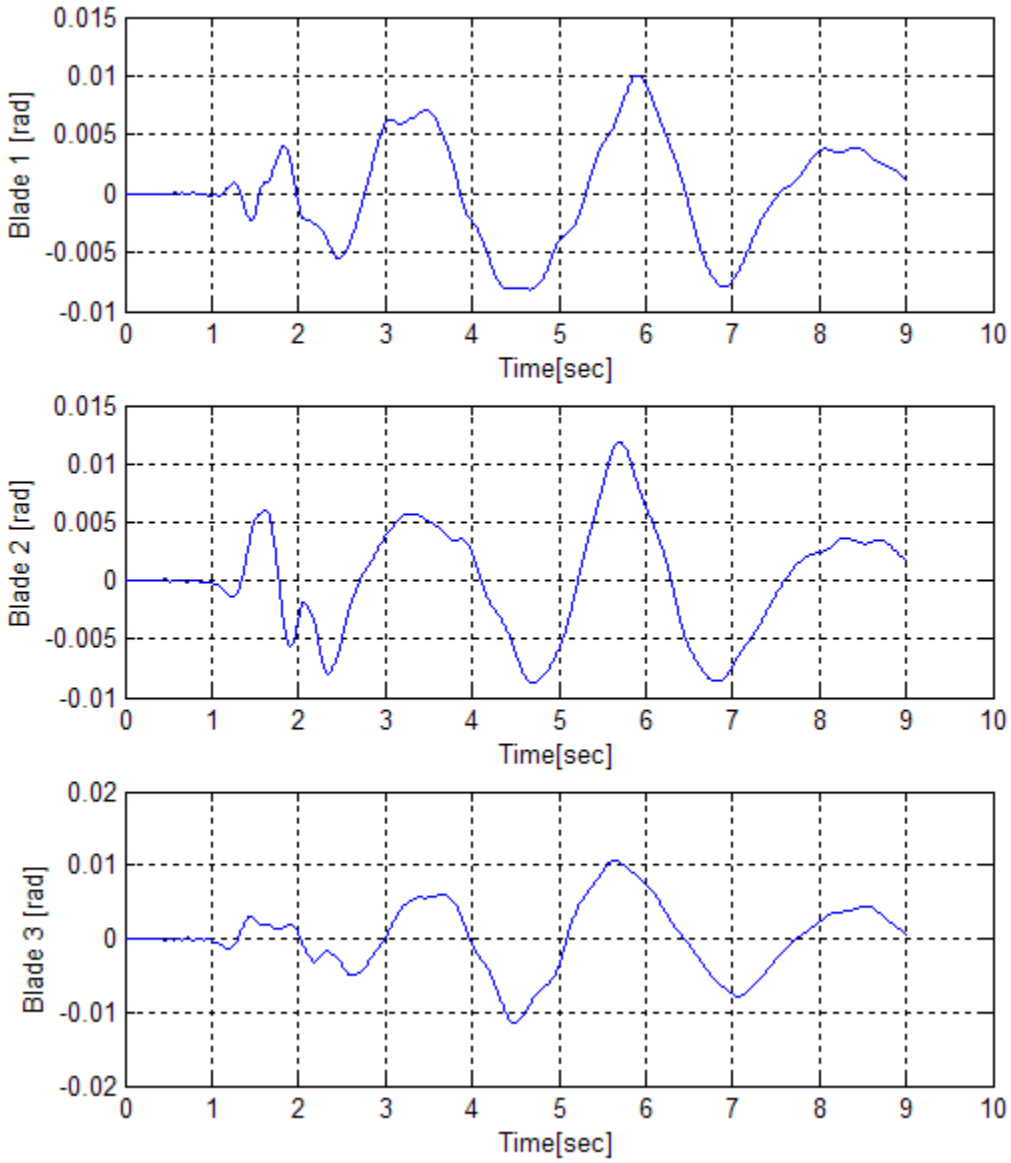

Fig. 4-29: Blade flap angle damped response, San Salvador earthquake

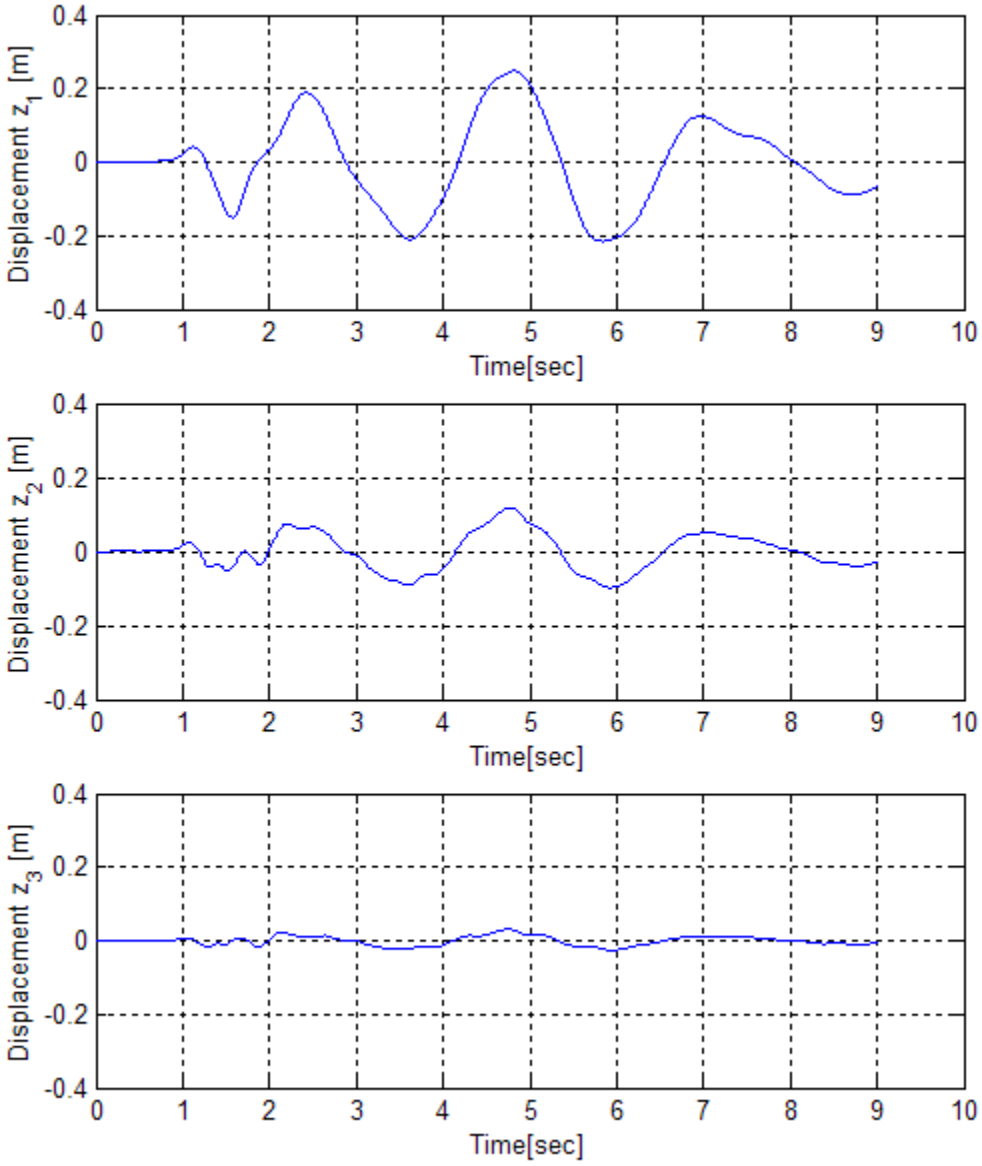

Fig. 4-30: Tower fore-aft damped response, San Salvador earthquake

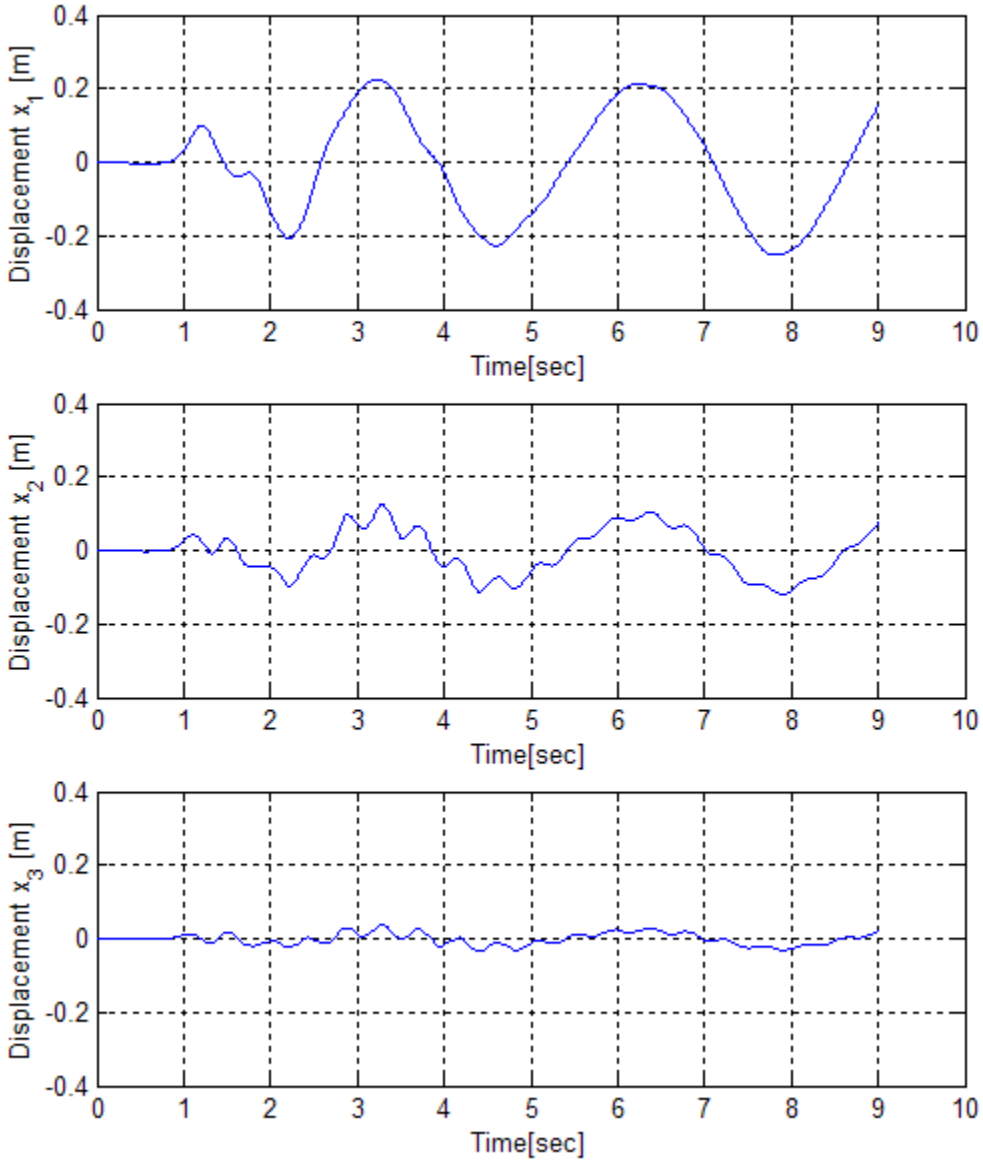

Fig. 4-31: Lateral tower damped response, San Salvador earthquake

4.8 SEISMIC RESPONSE OF THE NON-LINEAR WIND TURBINE MODEL

One of the objectives of this dissertation is to evaluate the importance of the non-linear terms in the equations of motion of the wind turbine and determine if they can be neglected without affecting the accuracy of the dynamic response. As it was demonstrated in a previous chapter, all the non-linear terms arise from the dynamics of the rotor. The non-linear terms can be observed in equations (2-32) to (2-48) and represent gyroscopic terms than cross-couple the angular velocity $\dot{\theta}_{x1}$ and $\dot{\theta}_{y'}$ with the angular velocity of a blade Ω or between them. An exception to this is the appearance of two non-linear terms multiplying moments of inertia quantities. After some mathematical manipulation, the non-linear equations of motion can be arranged in matrix form as:

$$\left[M\left(t,\theta_{y'}\right)\right]\{\ddot{u}\}+\left[\left[C(t)\right]+\left[D\left(t,\dot{\theta}_{x1},\dot{\theta}_{y'},\theta_{y'}\right)\right]\right]\{\dot{u}\}+[K]\{u\}= -[M_e]\{r_x\}\ddot{X}_b-[M_e]\{r_y\}\ddot{Y}_b-[M_e]\{r_z\}\ddot{Z}_b \tag{4-7}$$

Almost all the matrices in equation (4-7) were previously defined; however the periodic mass matrix $\left[M\left(t,\theta_{y'}\right)\right]$ changed sligtly. Basically this matrix is the same than that in equation (2-96) with the exception of the term m_{hh} that is now replaced by the non-linear term:

$$m_{hh}=m_r d_h^{\,2}+I_t+\frac{3}{2}I_b+\frac{1}{24}\rho A_1 l_e^{\,3}-3m_b\left(r_h+\tfrac{L_b}{2}\right)d_h\theta_{y'}-\left[I_a+3I_b\right]\theta_{y'}^2 \tag{4-8}$$

The new non-linear gyroscopic matrix $\left[D\left(t,\dot{\theta}_{x1},\dot{\theta}_{y'},\theta_{y'}\right)\right]$ is defined as:

$$\left[D\left(t,\dot{\theta}_{x1},\dot{\theta}_{y'},\theta_{y'}\right)\right]=\left[\begin{array}{cccccccccccccccc}
0 & 0 & 0 & -D_{ad} & 0 & 0 & 0 & 0 & 0 & 0 & 0 & 0 & 0 & 0 & 0 & 0\\
0 & 0 & 0 & -D_{db} & 0 & 0 & 0 & 0 & 0 & 0 & 0 & 0 & 0 & 0 & 0 & 0\\
0 & 0 & 0 & -D_{cd} & 0 & 0 & 0 & 0 & 0 & 0 & 0 & 0 & 0 & 0 & 0 & 0\\
D_{ad} & D_{bd} & D_{cd} & 0 & 0 & 0 & 0 & D_{dh} & 0 & 0 & 0 & 0 & 0 & 0 & 0 & 0\\
0 & 0 & 0 & 0 & 0 & 0 & 0 & 0 & 0 & 0 & 0 & 0 & 0 & 0 & 0 & 0\\
0 & 0 & 0 & 0 & 0 & 0 & 0 & 0 & 0 & 0 & 0 & 0 & 0 & 0 & 0 & 0\\
0 & 0 & 0 & 0 & 0 & 0 & 0 & 0 & 0 & 0 & 0 & 0 & 0 & 0 & 0 & 0\\
D_{ha} & D_{hb} & D_{hc} & D_{hd} & 0 & 0 & 0 & 0 & 0 & 0 & 0 & 0 & 0 & 0 & 0 & 0\\
0 & 0 & 0 & 0 & 0 & 0 & 0 & 0 & 0 & 0 & 0 & 0 & 0 & 0 & 0 & 0\\
0 & 0 & 0 & 0 & 0 & 0 & 0 & 0 & 0 & 0 & 0 & 0 & 0 & 0 & 0 & 0\\
0 & 0 & 0 & 0 & 0 & 0 & 0 & 0 & 0 & 0 & 0 & 0 & 0 & 0 & 0 & 0\\
0 & 0 & 0 & 0 & 0 & 0 & 0 & 0 & 0 & 0 & 0 & 0 & 0 & 0 & 0 & 0\\
0 & 0 & 0 & 0 & 0 & 0 & 0 & 0 & 0 & 0 & 0 & 0 & 0 & 0 & 0 & 0\\
0 & 0 & 0 & 0 & 0 & 0 & 0 & 0 & 0 & 0 & 0 & 0 & 0 & 0 & 0 & 0\\
0 & 0 & 0 & 0 & 0 & 0 & 0 & 0 & 0 & 0 & 0 & 0 & 0 & 0 & 0 & 0\\
0 & 0 & 0 & 0 & 0 & 0 & 0 & 0 & 0 & 0 & 0 & 0 & 0 & 0 & 0 & 0
\end{array}\right] \tag{4-9}$$

$$\begin{aligned}
D_{ad} &= \left[\tfrac{1}{2}m_b\left(r_h+\tfrac{L_b}{2}\right)L_b+I_b\right]\dot{\theta}_{x1}\theta_{y'}\sin\Omega t\\
D_{bd} &= \left[\tfrac{1}{2}m_b\left(r_h+\tfrac{L_b}{2}\right)L_b+I_b\right]\dot{\theta}_{x1}\theta_{y'}\sin\left(\Omega t+\tfrac{2\pi}{3}\right)\\
D_{cd} &= \left[\tfrac{1}{2}m_b\left(r_h+\tfrac{L_b}{2}\right)L_b+I_b\right]\dot{\theta}_{x1}\theta_{y'}\sin\left(\Omega t+\tfrac{4\pi}{3}\right)\\
D_{dh} &= \left[\tfrac{3}{2}m_b\left(r_h+\tfrac{L_b}{2}\right)^2-I_a+I_t-\tfrac{3}{2}I_b\right]\dot{\theta}_{x1}\theta_{y'}-\left[3m_b\left(r_h+\tfrac{L_b}{2}\right)d_h\right]\dot{\theta}_{x1}\\
D_{ha} &= -\left[\tfrac{1}{2}m_b\left(r_h+\tfrac{L_b}{2}\right)L_b+I_b\right]\dot{\theta}_{y'}\theta_{y'}\sin\Omega t\\
D_{hb} &= -\left[\tfrac{1}{2}m_b\left(r_h+\tfrac{L_b}{2}\right)L_b+I_b\right]\dot{\theta}_{y'}\theta_{y'}\sin\left(\Omega t+\tfrac{2\pi}{3}\right)\\
D_{hc} &= -\left[\tfrac{1}{2}m_b\left(r_h+\tfrac{L_b}{2}\right)L_b+I_b\right]\dot{\theta}_{y'}\theta_{y'}\sin\left(\Omega t+\tfrac{4\pi}{3}\right)\\
D_{hd} &= \left(I_a-2I_t\right)\dot{\theta}_{x1}\theta_{y'}-\left[6m_b\left(r_h+\tfrac{L_b}{2}\right)d_h\right]\dot{\theta}_{x1}
\end{aligned}$$

To solve the problem using the MATLAB *ode* functions, the equations of motion must be transformed in a set of first order equations in the state space:

$$\{\dot{q}\}=[A(t)]\{q\}+[B(t)]\{r_x\}\ddot{X}_b+[B(t)]\{r_y\}\ddot{Y}_b+[B(t)]\{r_z\}\ddot{Z}_b \tag{4-10}$$

The matrices $[A(t)]$ and $[B(t)]$ are now defined as:

$$[A(t)] = \begin{bmatrix} [0] & [I] \\ -[M(t,\theta_{y'})]^{-1}[K] & -[M(\theta_{y'})]^{-1}[[C(t)]+[D(t,\dot{\theta}_{x1},\dot{\theta}_{y'},\theta_{y'})]] \end{bmatrix}$$
$$[B(t)] = \begin{bmatrix} [0] \\ -[M(t,\theta_{y'})]^{-1}[M_e] \end{bmatrix} \quad (4\text{-}11)$$

The results obtained from the seismic analysis of the Vestas V82 wind turbine considering the non-linear terms showed that the response of the structure was the same as in the linear case up to an order of 10^{-5}. Therefore, for a structural analysis these terms can be neglected without affecting the accuracy of the results. This result was expected since the nominal speed of the rotor used here was very small (14.4 rpm = 1.51 rad/s), which is the standard on wind turbines of this size. Also the angular deformations at the top of the tower when the system was subjected to all the earthquake motions were very small, as well as the twisting angle, thus reducing even more the contribution of the non-linear gyroscopic terms to the dynamic behavior of the structure. Nevertheless, for faster rotors such as those found in smaller wind turbines, the non-linear terms might have a more important contribution to the response and thus they should be studied.

4.9 STRUCTURAL ANALYSIS OF THE WIND TURBINE MODEL

Until now we examined the dynamic behavior of the wind turbine during earthquake events, but we still need to assess if the structure can resist the demand imposed by the ground motions without suffering structural damages. There are several reasons why the wind turbines must be in operational condition after an earthquake. One reason is that after the earthquake there is a need to maintain the supply of electrical power. Moreover, the economic investment in

their construction and installation is very high. In Section 2.7 we derived formulas to calculate the maximum stresses on critical locations of the turbine where different components are connected together, such as the blade roots with the hub, the nacelle with the tower, and the tower with the foundation. These equations were developed for an elastic analysis in the cross-sectional area of the structural element and do not consider the particular characteristics of the connection between the two components. Thus, the evaluation of the stresses in flanges, holes, bolts or welds, as well as the stress concentrations factors was not considered here.

In Sections 4.4, 4.6, and 4.7, during the application of the acceleration records, we found that the earthquakes excited predominantly two vibration modes in each direction. The second mode has a shape that could help to increase the internal loads in the connections between the middle and the two remaining tower sections. Although not derived previously, it is necessary to carry out an analysis of the stresses in the connections of these sections. To obtain the forces and moments in the connections, the rows of the stiffness matrix [K] associated to them must be multiplied by the vector of generalized coordinates. Additionally the static moment and shear force induced by the wind pressure acting on the rotor must be included. Finally, the sum of these forces and moments are used to obtain the stresses in those regions.

Table 4-4 summarizes the maximum stresses in each blade root and in the tower obtained for the four earthquake records. The first two columns on each record correspond to maximum tension and maximum compressive normal stresses in the structure. The third column shows the maximum shear stresses. Table 4-5 contains the estimated strength properties for the typical fiberglass used in the construction of the blades and the steel S355 used in the tower. Also, the critical stress for local buckling in the tower based on Fig. 2-7 is presented for different ratios between the tower radius and the wall thickness encountered at different heights of the tower.

In terms of strength capacity, the relatively small stresses in the blade roots revealed that their structural integrity was not at risk during the strong ground motion events. Actually, the design of the blades is usually controlled by fatigue loads in which the allowable stresses must be kept below the endurance limit to have a lifetime of 20 years. It is relevant to mention that other areas of the blade could be susceptible to damage but the simplified model of a prismatic beam used here and the unavailability of the specific dimensions of the actual blade profile did not allow us for a more detailed assessment of its structural integrity.

On the other hand, the induced stresses in the tower were larger than the blades, since the actual tower design is usually controlled by yielding or local buckling instead of fatigue. The local buckling of the tower is a very dangerous condition because if the tower buckles, in addition to the tower damage, probably a collision between the blades and the tower may occur. As it can be observed in Table 4-5, the critical buckling capacity for the tower varies from 263 MPa at the top to 279 MPa at the base and the yield strength of the steel S355 is 355 MPa. In terms of tension and shear stresses the tower performed well for all the records employed. Also, none of the records considered produced compressive stresses that exceeded the local buckling strength at any place of the tower. It can be observed from Table 4-4 that the base and top sections of the tower were the places where larger compressive stresses were found. Since the tower radius to wall-thickness ratio was larger at the top end, the factor of safety (FS) against local buckling was smaller there. The worst condition occurred with the San Salvador record, which still reflects a satisfactory margin of safety with a FS = 2.77. In Section 4-7 we mentioned that although the San Salvador record had the lower magnitude among the earthquakes considered it contained a very high PGA of 0.87g, which was a sign of a near-fault effect. The strong impulsive signal in the tower base in combination with the large concentrated mass at the top end and the flexibility of the tower, especially at the tower top section, produced a large drift

or relative displacement between the tower nodes z_1 and z_2. Therefore, as can be observed in Table 4-4, the stresses at the tower top section were larger than the stressed produced by the other records.

Table 4-4: Maximum stresses in the wind turbine in [MPa]

	Taft Record			***El Centro Record***			***Castaic Record***			***S. Salvador GIC Rec.***		
	σ_t	σ_c	τ	σ_t	σ_c	τ	σ_t	σ_c	τ	σ_t	σ_c	τ
Blade #1	8.61	7.47	0.36	8.71	7.58	0.37	8.67	7.54	0.37	8.63	7.50	0.37
Blade #2	8.67	7.52	0.37	8.81	7.68	0.37	8.77	7.66	0.37	8.93	7.81	0.38
Blade #3	8.60	7.46	0.36	8.67	7.55	0.37	8.72	7.58	0.37	8.59	7.48	0.36
Tower-top	29.01	52.46	9.35	43.47	66.92	12.09	53.36	76.81	16.37	71.51	94.96	18.01
Tower-51 m	41.82	58.42	5.21	47.79	64.39	8.19	47.66	64.26	10.14	46.75	63.35	11.24
Tower-25 m	52.47	66.82	3.47	56.41	70.75	4.85	56.68	71.03	5.20	55.51	69.85	7.58
Tower-base	59.98	73.79	2.32	79.33	93.14	3.54	80.91	94.72	4.08	81.90	95.71	4.24

Table 4-5: Strength properties of the materials in [MPa]

Material			σ_{cr} ***(buckling)***	σ_y	σ_u ***(tens.)***	σ_u ***(comp.)***	τ_y	τ_u
Blades (Fiber glass)			-	-	860 - 900	720	-	-
Tower (Steel S355)	*Top*	*r/t =104.5*	263	355	510	510	~ 206	~ 408
	51 m	*r/t = 91.1*	271	355	510	510	~ 206	~ 408
	25 m	*r/t = 84.2*	276	355	510	510	~ 206	~ 408
	Base	*r/t = 79.6*	279	355	510	510	~ 206	~ 408

Finally, it is interesting to check if the stresses induced in the operating wind turbine by a strong earthquake are greater that those obtained when only the extreme wind speed is reached. According to the manufacturer, the extreme wind speed for which the wind turbine is designed is of 42.5 m/s applied during 10 minutes (General Specification, 2004). Normally this situation is avoided since the turbine has control means to stop the rotor before reaching the extreme wind speed. The actual cut-off wind speed is of 20 m/s. However, let us examine here the worse case in where a wind gust reaches the extreme speed and the rotor is still in operation. Table 4-6 contains the results of the stresses induced in the blade roots and the tower sections considering a constant extreme wind load. In addition, the stresses from the steady wind condition are also included for comparative purposes. As expected, the turbine could withstand the extreme wind without suffering structural damage. The larger stresses took place at the middle section of the tower at 25.33 m height. The security factor against local buckling in this zone was FS = 1.1 which, although safe, it was quite low. The zero value in the tension stress obtained at the tower top end implies that the whole cross-sectional area undergoes only compressive stresses. Comparing the extreme wind scenario with the operational wind turbine under the action of the studied earthquakes in Table 4-4 we see that almost the entire tower design was governed by the extreme wind loads. However, the tower top end was subjected to larger stresses from the selected earthquakes than the obtained from the extreme wind. In view of this, we can conclude that in seismic zone regions some aspects of the wind turbine design, in particular the design of the tower top end section, can be controlled by the combination of earthquake loads plus steady wind loads instead of extreme wind loads alone.

Table 4-6: Stresses induced in the wind turbine in [MPa] during extreme and steady wind speeds

	Extreme wind speed			***Steady wind speed***		
	σ_t	σ_c	τ	σ_t	σ_c	τ
Blade root #1	24.38	23.25	0.90	8.52	7.38	0.36
Blade root #2	24.38	23.25	0.90	8.52	7.38	0.36
Blade root #3	24.38	23.25	0.90	8.52	7.38	0.36
Tower top end	0	23.37	23.23	14.88	38.33	6.02
Tower @ 50.66 m	218.28	234.88	13.09	39.78	56.38	3.39
Tower @ 25.33 m	240.78	255.13	8.46	51.36	65.71	2.20
Tower bottom end	216.95	230.76	5.91	47.69	61.50	1.53

CHAPTER 5: CONCLUSIONS AND RECOMMENDATIONS

5.1 CONCLUSIONS

This dissertation presented the development of a dynamical model of a three-bladed horizontal axis wind turbine subjected to three base acceleration components due to an earthquake while it is in operation at a constant rotor speed. The equations of the rotor were developed by the Lagrange equations and they were coupled with the tower equations described by beam finite elements. The system was modeled using 16 degrees of freedom (i.e., 3 for the blade flap angles, 1 for the tower twist angle, and 12 for the tower lateral deflection). The flexibility of the blades was accounted by means of torsion springs placed at the blade root in the flapwise direction while it was assumed infinitely rigid in the edgewise direction. The rotor main shaft was also assumed infinitely rigid. Aerodynamic effects were included for a steady wind speed in accordance to the manufacturer wind speed and air density design conditions. The aerodynamic loads on the blades were considered by using the actual blade parameters obtained from the manufacturer. However, the equations were also derived for blades dimensioned according to Betz theory. The aerodynamic damping constants were obtained by assuming the blades are dimensioned just following the Betz theory.

The equations of motion contained periodic and non-linear terms as consequence of the rotational nature of the blades and the induced gyroscopic effects. The importance of the non-linear gyroscopic terms that appeared in the equations of motion was evaluated. Due to their negligible contribution to the response they were subsequently eliminated, which allowed for the linearization of the system.

As an example, the seismic response of the Vestas V82 wind turbine was studied using a specially developed MATLAB code that makes use of the numerical *ode* solvers. This turbine was selected among others because it is expected to be the first type of large wind turbine erected in Puerto Rico. To evaluate the dynamic stability of the operational turbine, the Floquet theory was applied since the traditional eigenanalysis is not applicable to periodic systems. Ignoring structural damping, the Floquet analysis revealed that the system was stable. Also the Floquet theory, in conjunction with the Fourier transform, permitted us to identify the modal frequencies, as well as the vibration modes of the system in operation. It was observed that the modes associated with large blade flap motions were highly damped and, in some instances, overdamped due to the large aerodynamic damping. On the other hand, the modes associated with the lateral motion of the turbine were more susceptible to larger displacements since the aerodynamic damping was negligible in this direction. In general, the contribution of the gyroscopic terms was small to a large extent to the slow rotational speed of the rotor and the small tower yaw and flexure rotations generated at the top end of the tower.

The three components of selected historical earthquake records were used to evaluate the seismic response of the wind turbine. The component with the largest peak ground acceleration was always applied in the direction of the rotor axis. These records were selected among those traditionally used for seismic evaluation in Puerto Rico for many years, such as the El Centro

and Taft records, due to the lack of strong motion accelerograms recorded in the island. Other records containing directivity and near-fault effects such as the 1994 Northridge-Castaic and the 1986 San Salvador-GIC records were also considered.

In general, the earthquake records considered excited the first tower mode in both directions but there are small traces of excitation of the second tower mode, especially in the lateral direction. With all ground motion records the response of the flap angles of the blades was very small, thus precluding a collision between the tip of the blades and the tower.

On the other hand, as consequence of the undamped situation of the lateral motion of the tower, signs of resonant conditions appeared at the end of the application of the Taft record. The addition of structural damping to the system was required to examine a more realistic scenario. Using the modal analysis technique for the same turbine but with a stationary rotor in the initial configuration, a damping matrix was generated using a 1% damping ratios for all the modes. The use of structural damping to the system diminished somewhat the response, up to 27.6 % of the original values for the lateral motion. Therefore the addition of artificial sources of damping such as the covering of the tower wall with elastomeric materials or placing tuned mass dampers in the structure can be useful to attenuate possible resonance problems.

One of the important goals of this research was to evaluate the structural capacity of the wind turbine to sustain a strong earthquake. Some critical locations, as allowed by the model, were evaluated such as the blade roots, the top end of the tower, and the base of the tower, as well as the connection between tower sections. With all the earthquake records, the blade roots demonstrated to be safe because the actual stresses in the roots were very small in comparison to their ultimate strength. The tower sections were considerably more stressed than the blades, particularly the top and bottom ends of the tower. Based on the present study we can conclude

that the tower was safe against local buckling and yielding during all the strong ground motions considered.

It also was confirmed that the stresses induced in the tower by the extreme wind loads were in general larger than those produced by the earthquake loads in combination with the steady average wind loads, with the exception of the tower top end, which resulted to be more stressed by the seismic loads. In view of this, we can conclude that in seismic regions some aspects of the wind turbine design, in particular the tower sections, can be controlled by the earthquake loads in combination with steady wind loads instead of the extreme wind loads alone. Therefore, it is justified that seismic analyses must be performed in those wind turbines that will be designed for and installed in high seismic prone regions.

It is important to mention that the present conclusions in this chapter were based on the analysis of a particular wind turbine subjected to specific earthquakes. Moreover, some important characteristics and properties of the physical wind turbine model used here were estimated from the small information available to the public. Therefore, they cannot be considered of general applicability to other wind turbines. To establish more general conclusions a parametric study with several turbines under a large variety of seismic records must be performed. Nevertheless the analytical and numerical tools required to execute such kind of studies were developed here.

5.2 RECOMMENDATIONS

Some recommendations to consider for future research works are presented here. There are many modifications that can be done to the wind turbine model to enhance the accuracy of the response, but all of them increase noticeably the difficulty of the derivation of the equations of motion, as well as the computational effort to obtain their solution. An important modification is to utilize beam elements to model the blades. In the model developed, the blade was assumed to be rigid with a spring hinge at the root. Also the blade flap stiffness was evaluated using a prismatic wing profile based on the average cord of the actual blade. Certainly this is a rough approximation of the actual situation. Simultaneously to the development of the beam element for the blade, more realistic aerodynamic damping constants can be calculated for each element making unnecessary the use of the idealized Betz theory. The implementation of these enhancements will convert the actual approximate model in a more versatile finite element model in which the user can select the number of degrees of freedoms and vary the sections of the blades the way they want.

In the meantime, maintaining the actual quantity of degrees of freedoms, a better approximation of the torsion spring of the blade can be made by analyzing the actual blade with variable section and including the twisting of the profile in any commercial finite element software. This can be done applying a uniform distributed load and increasing its intensity to the point of find out a relation between the moment at the root and the equivalent angle to reach the displaced tip.

Another recommendation is to provide rotational degrees of freedom and a lumped mass at the base of the tower. This will enable us to analyze rotational phenomena in soil-structure interaction, as well as the more recent conception of off-shore wind turbines with floating foundations.

To reduce the lateral displacements of the wind turbine and the possibility of damage in the structure due to a resonant condition it will be interesting to study the benefits of placing tuned mass dampers or elastomeric materials in the tower.

Finally, to further validate the model and the results of the present dissertation, an experimental physical model subjected to controlled base motions will be extremely useful.

REFERENCES

1. Alcalde, R. (2004), "Producción de Energía Mediante Molinos de Viento – Energía Eólica", Personal interview during seminar by General Electric International in the CIAPR on February 17, 2004.
2. Bauchau, O. A. and Nikishkov, Y. G. (2001), "An Implicit Floquet Analysis for Rotorcraft Stability Evaluation", *Journal of the American Helicopter Society*, Vol. 46, pp. 200-209.
3. Bhaskar, A. (1999), "Mode Shapes During Asynchronous Motion and Non-Proportionality Indices", *Journal of Sound and Vibration*. Vol. 224(1), pp. 1-16.
4. Billings Gazette (n.d.), from: http://www.billingsgazette.com/topic/?q=wind%20 turbines&t=&l= 25&d= &d1=&d2=&f=html&s=&sd=asc.
5. Bir, G. S. and Stol, K. (1999), "Operating Modes of a Teetered-Rotor Wind Turbine", National Renewable Energy Laboratory, NREL/CP-500-25983, Golden, Colorado.
6. Borg, J. P. and Kirchhoff, R. H. (1997), "The Effects of Static and Dynamic Imbalance on a Horizontal Axis Wind Turbine", *Journal of Solar Energy Engineering*, ASME, Vol. 119, pp. 261-262.
7. Borg, J. P. and Kirchhoff, R. H. (1998), "Mass and Aerodynamic Imbalance of a Horizontal Axis Wind Turbine", *Journal of Solar Energy Engineering*, ASME, Vol. 120, pp. 66-74.
8. Bourke, J. W., Sánchez, M., Martínez, L., Fabré, C., and Rodríguez, T. (2004), "Gyroscopic Effect in Windmill Generators", Technical Report, Department of Applied Mechanics, ISPJAE, Cuba.

9. Brazier, L. G. (1927), "Of the Flexure of Thin Cylindrical Shells and Other Thin Sections", *Proceedings of the Royal Society of London,* Ser. A, Vol. 116, p. 104.

10. Burton, T., Sharpe, D., Jenkins, N., and Bossanyi, E. (2001), "Wind Energy Handbook", John Wiley & Son, LTD, England.

11. Carne, T. G., Lobitz, D. W., Nord, A. R., and Watson, R. A. (1982), "Finite Element Analysis and Modal Testing of a Rotating Wind Turbine", Sandia National Laboratories, SAND82-0345, Albuquerque, Nuevo Mexico.

12. Chandrupatla, T. R. and Belegundu, A. D. (1997), "Introduction to Finite Elements in Engineering", Second Edition, Prentice Hall, New Jersey.

13. Danish Standards (1992), "DS 472: Loads and Safety of Wind Turbine Construction", Denmark.

14. DIA-F WindMar, (2007), "Parque de Energía Eólica WindMar Renewable Energy", http://www.gobierno.pr/JCA/DocumentosAmbientales/2007/Final/Default.htm?Page=4

15. DOE (2008), "20% Wind Energy by 2030: Increasing Wind Energy's Contribution to U.S. Electrical Supply", Report of the U.S. Department of Energy, DOE/GO-102008-2567, July.

16. Donnell, L. H. (1934), "A New Theory for Buckling of Thin Cylinder Under Axial Compressive and Bending", *Transactions,* ASME, Vol. 56, p. 795.

17. Dutch Standard (1988), "Safety Regulations for Wind Generators". NEN 6096, The Netherlands.

18. Eggers, A. J., Ashley, H., Rock, S. M., Chaney, K., and Digumarthi, R. (1996), "Effects of the Blade Bending on Aerodynamic Control of Fluctuating Loads on

Teetered HAWT Rotors", *Journal of Solar Energy Engineering,* ASME, Vol. 118, pp. 239-245.

19. Energy Systeme Nord (n.d.), from: http://ec.europa.eu/research/energy/nn/nn_rt/nn_rt_wind/images/wind_en_1370.gif
20. Fabricating & Metalworking Magazine (n.d.), from: http://www.fandmmag.com/web/online/Metal-Cutting/BLOWING-IN-THE-WIND—MACHININGOPORTUNITIES/4$3707
21. Fuglsang, P., Antoniou, I., Dahl, K. S., and Madsen, H. A. (1998), "Wind Tunnel Tests of the FFA-W3-241, FFA-W3-301 and NACA 63-430 Airfoils" Report Riso-R-1041(EN), Riso National Laboratory, Roskilde.
22. Gasch, R. and Twele, J. (2004), "Wind Power Plants, Fundamentals, Design, Construction and Operation" James & James, London, UK.
23. GE (2005), "1.5 MW Wind Turbine – Reference Material", GE Wind Energy Internal Training Course, Rev. L.
24. General Specification from the Vestas Wind Systems A/S (2004), "General Specification V82-1.65 MW MK II, NM82/1650 Vers. 2", Technical Sales Document TDS 4000258-01 EN. http://www.energymaine.com/brwind/brdocs/Appendix2_V82%20%20General%20 Specification.pdf
25. Germanischer Lloyd (2003), "Guideline for the Certification of Wind Turbines", Hamburg, Germany.
26. GH Bladed (2010), "Wind Turbine Design Software" from http://www.gl-garradhassan.com/en/software/GHBladed.php.

27. Greenwood, D. T. (1988), “Principles of Dynamics”, Second Edition, Prentice Hall, New Jersey.

28. Hansen, A. C. (1995), “Aerodynamic Damping of Blade Flap Motions at High Angles of Attack”, *Journal of Solar Energy Engineering*, ASME, Vol. 117, pp. 194-199.

29. Hermann, T. M., Mamarthupatti, D., and Locke, J. E. (2005), “Postbuckling Analysis of a Wind Turbine Blade Substructure”, *Journal of Solar Energy Engineering*, ASME, Vol. 127, pp. 544-552, and Erratum Vol. 128, p. 262.

30. Hibbeler, R. C. (2004), “Mechanics of Materials”, Sixth Edition, Prentice Hall, New Jersey.

31. Hong, R. C. (1984), “Response of a Wind Turbine Blade to Seismic and Turbulent Wind Excitations” Ph.D. Dissertation, University of Illinois at Urbana-Champaign, 179 pages.

32. Horn, R. A. and Johnson, C. R. (1991), “Topics in Matrix Analysis”, Cambridge University Press.

33. International Electrotechnical Commission (2005), “IEC 61400-1: Wind Turbines-Part 1: Design Requirements”, Geneva, Switzerland.

34. Johnson, W. (1994), “Helicopter Theory”, Dover Publications, Inc., New York.

35. Jordan, D. W. and Smith, P. (1983), “Nonlinear Ordinary Differential Equations”, Oxford University Press, New York.

36. Lobitz, D. W. (1984), “A NASTRAN-Based Computer Program For Structural Dynamic Analysis of Horizontal Axis Wind Turbines”, Proceedings of the Horizontal Axis Wind Turbine Technology Workshop, Department of Energy and NASA-Lewis, Cleveland.

37. Malcolm, D. J. (2002), "Modal Response of 3-Bladed Wind Turbines", *Journal of Solar Energy Engineering,* ASME, Vol. 124, pp. 372-377.

38. Malcolm, D. J. and Laird, D. L. (2003), "Modeling of Blades as Equivalent Beams for Aeroelastic Analysis", Proceedings of the AIAA Wind Energy Symposium, Paper Nr. 0870, Reno, Nevada.

39. Martínez, J. A., Irizarry, J., and Portela, G. (2001), "Espectros de Diseño para las Ciudades Principales de Puerto Rico Basado en Registros de Aceleración Mundiales" *Revista Internacional de Desastres Naturales, Accidentes e Infraestructura Civil*, Vol. 1, No. 1, pp. 21-31.

40. Meirovitch, L. (1988), "Methods of Analytical Dynamics", Reissued Series, McGraw-Hill.

41. Morales, J. C. (2006), "Dynamic Properties and Seismic Response of the Cable Structures and Towers of the Arecibo Observatory", PhD dissertation, University of Puerto Rico, Mayagüez Campus.

42. Moretti, G. (1964), "Function of a Complex Variable", Prentice Hall.

43. Narayana, M. (1999), "Catastrophic Failure due to Gyroscopic Effect of Small Scale Tilt up Horizontal Axis Wind Turbines", *DEWI Magazine,* Nr. 15, pp. 80-85.

44. NEi (2010), NASTRAN, from: http://www.nenastran.com/nei-nastran.php.

45. Oscar, D. S. and Paez, T. L. (1988), "Analysis of Wind Turbines on Offshore Support Structures Excited by Random Wind and Random Waves", Sandia National Laboratories, SAND87-1689, Albuquerque, New Mexico.

46. Prowell, I. and Veers, P. (2009), "Assessment of Wind Turbine Seismic Risk: Existing Literature and Simple Study of Tower Moment Demand" Sandia National Laboratories, SAND2009-1100, Albuquerque, New Mexico.

47. Prowell, I., Veletzos, M., and Elgamal, A. (2008a), "Full Scale Testing for Investigation of Wind Turbine Seismic Response", Unpublished.

48. Prowell, I., Veletzos, M., and Elgamal, A. (2008b), "Shake Table Test of a 65kW Wind Turbine and Computational Simulation", 14th World Conference on Earthquake Engineering, Beijing, China.

49. Saad, Y. (1981), "Krylov Subspace Methods for Solving Large Unsymmetric Linear Systems", *Mathematics of Computation*, Vol. 37, pp. 105-126.

50. Sinha, S. C. (2005), "Analysis and Control of Nonlinear Dynamical Systems with Periodic Coefficients", *Proceedings of the Workshop on Nonlinear Phenomena Modeling and Their Applications*, 2-4 May, 2005, Sao Paulo, Brazil.

51. Sorensen, P., Larsen, G. C., and Christensen, C. J. (1995), "A Complex Domain Model of Wind Turbine Structures", *Journal of Solar Energy Engineering,* ASME, Vol. 117, pp. 311-317.

52. Stol, K. and Balas, M. (2001), "Full-State Feedback Control of a Variable-Speed Wind Turbine: A Comparison of Periodic and Constant Gains", *Journal of Solar Energy Engineering,* ASME, Vol. 123, pp. 319-326.

53. Stol, K., Balas, M., and Bir, G. (2002), "Floquet Modal Analysis of a Teetered-Rotor Wind Turbine", *Journal of Solar Energy Engineering,* ASME, Vol. 124, pp. 364-371.

54. Suárez, L. E., Singh, M. P., and Rohanimanesh, M. S. (1992), "Seismic Response of Rotating Machines", *Earthquake Engineering and Structural Dynamics*, Vol. 21, pp. 21-36.

55. Sutherland, H. J. (1999), "On the Fatigue Analysis of Wind Turbines", Sandia National Laboratories, SAND99-0089, Albuquerque, Nuevo Mexico.

56. Tangler, J. L. (1987), "A Horizontal Axis Wind Turbine Performance Prediction Code for Personal Computers", Solar Energy Research Institute, Golden, Colorado.

57. Witcher, D. (2005), "Seismic Analysis of Wind Turbines in the Time Domain", *Wind Energy*, Vol. 8, pp. 81-91.

58. Zhao, X. and Maisser, P. (2006), "Seismic Response Analysis of Wind Turbine Towers Including Soil-structure Interaction", *Proceedings of the Institution of Mechanical Engineers, Part K: Journal of Multi-body Dynamics*, Vol. 220, pp. 53-61.

59. Zhao, X., Maisser, P., and Wu, J. (2006), "A New Multibody Modelling Methodology for Wind Turbine Structures Using a Cardanic Joint Beam Element", *Renewable Energy*, Vol. 32, pp. 532-546.

APPENDIX: NUMERICAL PROGRAMS

```
%-----------------------------HAWTSeismicAnalysis.m--------------------------
% Is the main program to evaluate the seismic response of the operating wind
% turbine model in combination with the function program SeismicHAWT.m. It
% calculates the structural damping matrix from the non-operational turbine.
% Also it calculate the forces and stresses at the blade roots, tower top
% end, tower union sections, tower base.
%--------------------------------------------------------------------------
clc
clear all
close all

global Xg Yg Zg N tf Cs

%----------------------Physical & Mechanical Properties--------------------

mr = 43000;                          % Rotor mass [kg]
mb = 8600;                           % Blade mass [kg]
mn = 52000;                          % Nacelle mass [kg]
mt = 125000;                         % Tower mass [kg]
At = 5281;                           % Rotor swept area [m^2]
dh = 3.45;                           % Tower to hub distance [m]
Lb = 40;                             % Blade length [m]
rh = 1;                              % Hub radius [m]
rb = 0.96;                           % Blade root radius [m]
tb = 0.12;                           % Blade root wall thickness [m]
Ib = 1.15e6;                         % Blade moment of inertia [kg.m^2]
Ia = 8600;                           % Hub axial moment of inertia [kg.m^2]
It = 4300;                           % Hub transverse moment of inertia
[kg.m^2]
I = 5.96e-3;                         % Blade sectional moment of inertia [m^4]
Eb = 4.4e10;                         % Blade modulus of elasticity [N/m^2]
ht = 76;                             % Tower height [m]
hh = 77;                             % Hub height [m]
rbe = 1.99;                          % Tower base end radius [m]
tbe = 2.5e-2;                        % Tower base end wall thickness [m]
rte = 1.15;                          % Tower top end radius [m]
tte = 1.1e-2;                        % Tower top end wall thickness [m]
rm = 1.43;                           % Tower upper middle section radius [m]
tm = 1.57e-2;                        % Tower upper middle wall thickness [m]
rl = 1.71;                           % Tower lower middle section radius [m]
tl = 2.03e-2;                        % Tower upper middle wall thickness [m]
rho = 8900;                          % Steel density [kg/m^3]
```

```
E = 2.07e11;                          % Steel modulus of elasticity [N/m^2]
G = 7.9e10;                           % Steel shear modulus [N/m^2]
v = 0.3;                              % Steel Poisson's ratio
rhoa = 0.0;                           % Vaccum density [kg/m^3]
Rhoa = 1.225;                         % Air density [kg/m^3]
%ct = 0.438;                           % Thrust coefficient
ct = 0.158;
%va = 13;                              % Average wind speed [m/s]
va = 42.5;
W = 1.65e6;                           % Output power [W]
eta = 0.92;                           % Overall efficiency
Omega = 0.0;                          % Rotor stationary angular velocity
[rad/s]
omega = 1.51;                         % Rotor operating angular velocity
[rad/s]
kb = 2.62e7;                          % Blade stiffness coefficient [N.m/rad]
kt = 3.90e8;                          % Tower torsional stiffness coefficient
[N.m/rad]
c1 = 6.80e5;                          % Aerodyamic damping constant [N.s/rad]
c2 = 2.49e4;                          % Aerodyamic damping constant [N.s/m]
c3 = 1.79e7;                          % Aerodyamic damping constant [N.m.s/rad]
c4 = 6.56e5;                          % Aerodyamic damping constant [N.m.s/m]
le = 25.33;                           % Tower element length [m]
A1 = 0.108;                           % Tower element area [m^2]
A2 = 0.178;                           % Tower element area [m^2]
A3 = 0.264;                           % Tower element area [m^2]
I1 = 8.83e-2;                         % Tower sectional moment of inertia [m^4]
I2 = 0.215;                           % Tower sectional moment of inertia [m^4]
I3 = 0.443;                           % Tower sectional moment of inertia [m^4]
g = 9.81;                             % Acceleration of gravity [m/s^2]
t = 0.0;                              % Original Parked rotor
zi = 0.01;                            % Modal damping ratio
delta = 0.07;                         % Precone angle [rad]

%---------------------------------Mass Matrix--------------------------------

M = zeros(16,16);
M(1,1) = 1/4*mb*Lb^2+Ib;
M(1,4) = -(1/2*mb*(rh+Lb/2)*Lb+Ib)*cos(Omega*t);
M(1,7) = 1/2*mb*Lb;
M(1,8) = (1/2*mb*(rh+Lb/2)*Lb+Ib)*sin(Omega*t);
M(2,4) = -(1/2*mb*(rh+Lb/2)*Lb+Ib)*cos(Omega*t+2*pi/3);
M(2,7) = 1/2*mb*Lb;
M(2,8) = (1/2*mb*(rh+Lb/2)*Lb+Ib)*sin(Omega*t+2*pi/3);
M(3,4) = -(1/2*mb*(rh+Lb/2)*Lb+Ib)*cos(Omega*t+4*pi/3);
M(3,7) = 1/2*mb*Lb;
M(3,8) = (1/2*mb*(rh+Lb/2)*Lb+Ib)*sin(Omega*t+4*pi/3);
M(4,4) = mr*dh^2+3/2*mb*(rh+Lb/2)^2+It+3/2*Ib;
M(4,5) = mr*dh;
M(5,5) = mr+mn+1/2*rho*A1*le;
M(6,6) = 1/24*rho*A1*le^3;
M(8,8) = mr*dh^2+3/2*mb*(rh+Lb/2)^2+It+3/2*Ib+1/24*rho*A1*le^3;
M(9,9) = 1/2*rho*(A1+A2)*le;
M(10,10) = 1/24*rho*(A1+A2)*le^3;
M(13,13) = 1/2*rho*(A2+A3)*le;
```

```
M(14,14) = 1/24*rho*(A2+A3)*le^3;
M(2,2) = M(1,1);
M(3,3) = M(1,1);
M(4,1) = M(1,4);
M(4,2) = M(2,4);
M(4,3) = M(3,4);
M(5,4) = M(4,5);
M(8,1) = M(1,8);
M(8,2) = M(2,8);
M(8,3) = M(3,8);
M(7,1) = M(1,7);
M(7,2) = M(2,7);
M(7,3) = M(3,7);
M(7,7) = M(5,5);
M(11,11) = M(9,9);
M(12,12) = M(10,10);
M(15,15) = M(13,13);
M(16,16) = M(14,14);

%------------------------------Stiffness Matrix-----------------------------

K = zeros(16,16);
K(1,1) = kb;
K(2,2) = K(1,1);
K(3,3) = K(1,1);
K(4,4) = kt;
K(5,5) = 12*E*I1/le^3;
K(5,6) = 6*E*I1/le^2;
K(5,9) = -12*E*I1/le^3;
K(5,10) = 6*E*I1/le^2;
K(6,6) = 4*E*I1/le;
K(6,9) = -6*E*I1/le^2;
K(6,10) = 2*E*I1/le;
K(7,7) = 12*E*I1/le^3;
K(7,8) = 6*E*I1/le^2;
K(7,11) = -12*E*I1/le^3;
K(7,12) = 6*E*I1/le^2;
K(8,8) = 4*E*I1/le;
K(8,11) = -6*E*I1/le^2;
K(8,12) = 2*E*I1/le;
K(9,9) = 12*E*(I1+I2)/le^3;
K(9,10) = 6*E*(I2-I1)/le^2;
K(9,13) = -12*E*I2/le^3;
K(9,14) = 6*E*I2/le^2;
K(10,10) = 4*E*(I1+I2)/le;
K(10,13) = -6*E*I2/le^2;
K(10,14) = 2*E*I2/le;
K(11,11) = 12*E*(I1+I2)/le^3;
K(11,12) = 6*E*(I2-I1)/le^2;
K(11,15) = -12*E*I2/le^3;
K(11,16) = 6*E*I2/le^2;
K(12,12) = 4*E*(I1+I2)/le;
K(12,15) = -6*E*I2/le^2;
K(12,16) = 2*E*I2/le;
K(13,13) = 12*E*(I2+I3)/le^3;
```

```
K(13,14) = 6*E*(I3-I2)/le^2;
K(14,14) = 4*E*(I2+I3)/le;
K(15,15) = 12*E*(I2+I3)/le^3;
K(15,16) = 6*E*(I3-I2)/le^2;
K(16,16) = 4*E*(I2+I3)/le;
K(6,5) = K(5,6);
K(8,7) = K(7,8);
K(9,5) = K(5,9);
K(9,6) = K(6,9);
K(10,5) = K(5,10);
K(10,6) = K(6,10);
K(10,9) = K(9,10);
K(11,7) = K(7,11);
K(11,8) = K(8,11);
K(12,7) = K(7,12);
K(12,8) = K(8,12);
K(12,11) = K(11,12);
K(13,9) = K(9,13);
K(13,10) = K(10,13);
K(14,9) = K(9,14);
K(14,10) = K(10,14);
K(14,13) = K(13,14);
K(15,11) = K(11,15);
K(15,12) = K(12,15);
K(16,11) = K(11,16);
K(16,12) = K(12,16);
K(16,15) = K(15,16);

%-------------------Calculate the eigenvalues and eigenvectors---------------

[Phi, lambda] = eig(K,M);
alf = 1./sqrt(diag(Phi'*M*Phi));
Phi = Phi*diag(alf);
omegan = sqrt(diag(lambda));
[omegan,id] = sort(omegan);
Phi = Phi(:,id);

disp('***The natural frequencies [rad/s] are:'); omegan;
disp('***The normalized vibration modes are:'); Phi;

%------------------------Calculate modal damping matrix----------------------

Cd = diag(2*zi*omegan);
Cs = M*Phi*Cd*Phi'*M;

%----------------------------Load earthquake data----------------------------

load(['ElCentroNS.dat'])
load(['ElCentroUp.dat'])
load(['ElCentroEW.dat'])
load(['TaftS69E.dat'])
load(['TaftN21E.dat'])
load(['TaftUp.dat'])
load(['NorthridgeNS.dat'])
load(['NorthridgeEW.dat'])
```

```
load(['NorthridgeUP.dat'])
load(['SanSalvadorNS.dat'])
load(['SanSalvadorEW.dat'])
load(['SanSalvadorUP.dat'])
%[nr,nc] = size(ElCentroNS);
%[nr,nc] = size(TaftS69E);
%[nr,nc] = size(NorthridgeNS);
%[nr,nc] = size(SanSalvadorNS);
%N = nr*nc;
N = 4000;
Xg(1:N) = zeros(1,N)';
Yg(1:N) = zeros(1,N)';
Zg(1:N) = zeros(1,N)';

%Xg(1:N) = g*ElCentroEW';
%Yg(1:N) = g*ElCentroUp';
%Zg(1:N) = g*ElCentroNS';

%Xg(1:N) = g*TaftN21E';
%Yg(1:N) = g*TaftUp';
%Zg(1:N) = g*TaftS69E';

%Xg(1:N) = g*NorthridgeEW';
%Yg(1:N) = g*NorthridgeUP';
%Zg(1:N) = g*NorthridgeNS';

%Xg(1:N) = g*SanSalvadorEW';
%Yg(1:N) = g*SanSalvadorUP';
%Zg(1:N) = g*SanSalvadorNS';
%------------------------------State equation solver-------------------------

dt = 0.01; % actual record time increment
tf = (N-1)*dt;
n = 32;% Number of state equations
ti = 0.01; % solver time increment
tspan = (0:ti:tf);
xo = diag(zeros(n));% Initial conditions
options = odeset('RelTol',1e-6,'AbsTol',1e-6);
[t,x] = ode45('SeismicHAWT',tspan,xo,options);

%---------------------------------Response plots-------------------------------

figure;
subplot(3,1,1);
plot(t,x(:,1)); grid on;
xlabel('Time[sec]'); ylabel('Blade 1 [rad]')
subplot(3,1,2);
plot(t,x(:,2)); grid on;
xlabel('Time[sec]'); ylabel('Blade 2 [rad]')
subplot(3,1,3);
plot(t,x(:,3)); grid on;
xlabel('Time[sec]'); ylabel('Blade 3 [rad]')

figure;
subplot(3,1,1);
```

```
plot(t,x(:,7)); grid on;
xlabel('Time[sec]'); ylabel('Displacement z_{1} [m]')
subplot(3,1,2);
plot(t,x(:,11)); grid on;
xlabel('Time[sec]'); ylabel('Displacement z_{2} [m]')
subplot(3,1,3)
plot(t,x(:,15)); grid on;
xlabel('Time[sec]'); ylabel('Displacement z_{3} [m]')

figure;
subplot(3,1,1);
plot(t,x(:,5)); grid on;
xlabel('Time[sec]'); ylabel('Displacement x_{1} [m]')
subplot(3,1,2);
plot(t,x(:,9)); grid on;
xlabel('Time[sec]'); ylabel('Displacement x_{2} [m]')
subplot(3,1,3)
plot(t,x(:,13)); grid on;
xlabel('Time[sec]'); ylabel('Displacement x_{3} [m]')

%figure; plot(t,x(:,4)); grid on;
%xlabel('Time[sec]'); ylabel('Tower Twist Angle [rad]')

%figure; plot(t,x(:,8)); grid on;
%xlabel('Time[sec]'); ylabel('Tower Top End Angle [rad]')

%--------------------Calculate the discrete Fourier transform----------------

%T = N*dt;
%dw = 2*3.14159/T;
%w = 0:dw:(N*dt/ti-1)*dw;

%FB1 = dt*fft(x(:,1));
%FFT = dt*fft(x(:,11));
%FLT = dt*fft(x(:,9));
%FTT = dt*fft(x(:,4));

%figure; plot(w,abs(FB1));grid on;
%xlabel('Frequency [rad/s]'); ylabel('Amplitude')

%figure; plot(w,abs(FFT));grid on;
%xlabel('Frequency [rad/s]'); ylabel('Amplitude')

%figure; plot(w,abs(FLT));grid on;
%xlabel('Frequency [rad/s]'); ylabel('Amplitude')

%figure; plot(w,abs(FTT));grid on;
%xlabel('Frequency [rad/s]'); ylabel('Amplitude')

%A = [w',abs(FFT)];

%---------------------------Calculate the Stresses--------------------------

F = K*(x(:,1:16))';
```

```
%---------------------------------Blade Roots-------------------------------

%Ft = 1/3*(8/9*Rhoa/2*va^2)*pi*(2*rh*Lb+Lb^2);  %Betz blade
Ft = 1/3*(1/2*Rhoa*ct*va^2*At);                 %Actual blade
alfa = rh/Lb;
xc = 1/3*(2*alfa+2)/(2*alfa+1)*Lb;

%Mb1f = kb*delta-F(1,:);
%Mb2f = kb*delta-F(2,:);
%Mb3f = kb*delta-F(3,:);
Mb1f = Ft*xc-F(1,:);
Mb2f = Ft*xc-F(2,:);
Mb3f = Ft*xc-F(3,:);

T = W/omega/eta;

Mmb1 = mb*g*Lb/2*cos(omega*t);
Mmb2 = mb*g*Lb/2*cos(omega*t+2*pi/3);
Mmb3 = mb*g*Lb/2*cos(omega*t+4*pi/3);

Mb1e = Mmb1'-T/3/(2*rh/Lb+1);
Mb2e = Mmb2'-T/3/(2*rh/Lb+1);
Mb3e = Mmb3'-T/3/(2*rh/Lb+1);

Mb1 = sqrt(Mb1f.^2+Mb1e.^2);
Mb2 = sqrt(Mb2f.^2+Mb2e.^2);
Mb3 = sqrt(Mb3f.^2+Mb3e.^2);

sb1 = Mb1*rb/pi/rb^3/tb;
sb2 = Mb2*rb/pi/rb^3/tb;
sb3 = Mb3*rb/pi/rb^3/tb;
%----------------------------------------
Fc = mb*(rh+Lb/2)*omega^2;

Fg1 = mb*g*sin(omega*t);
Fg2 = mb*g*sin(omega*t+2*pi/3);
Fg3 = mb*g*sin(omega*t+4*pi/3);

Fb1 = Fc-Fg1';
Fb2 = Fc-Fg2';
Fb3 = Fc-Fg3';

sa1 = Fb1/2/pi/rb/tb;
sa2 = Fb2/2/pi/rb/tb;
sa3 = Fb3/2/pi/rb/tb;
%----------------------------------------
Sb1T = sb1+sa1;
Sb2T = sb2+sa2;
Sb3T = sb3+sa3;
Sb1C = -sb1+sa1;
Sb2C = -sb2+sa2;
Sb3C = -sb3+sa3;
disp('***The max tension stress in blade 1 [Mpa] is:'); max(Sb1T)/10^6
disp('***The max tension stress in blade 2 [Mpa] is:'); max(Sb2T)/10^6
disp('***The max tension stress in blade 3 [Mpa] is:'); max(Sb3T)/10^6
```

```
disp('***The max compressive stress in blade 1 [Mpa] is:'); min(Sb1C)/10^6
disp('***The max compressive stress in blade 2 [Mpa] is:'); min(Sb2C)/10^6
disp('***The max compressive stress in blade 3 [Mpa] is:'); min(Sb3C)/10^6
%----------------------------------------
Vc = T/3/(rh+Lb/2);

Vmb1 = mb*g*cos(omega*t);
Vmb2 = mb*g*cos(omega*t+2*pi/3);
Vmb3 = mb*g*cos(omega*t+4*pi/3);

Ve1 = Vc-Vmb1';
Ve2 = Vc-Vmb2';
Ve3 = Vc-Vmb3';

Vi1 = 2*kb/Lb*(x(:,1))';
Vi2 = 2*kb/Lb*(x(:,2))';
Vi3 = 2*kb/Lb*(x(:,3))';

Vt1 = Vi1-Ft;
Vt2 = Vi2-Ft;
Vt3 = Vi3-Ft;

Vb1 = sqrt(Ve1.^2+Vt1.^2);
Vb2 = sqrt(Ve2.^2+Vt2.^2);
Vb3 = sqrt(Ve3.^2+Vt3.^2);
%----------------------------------------
tau1 = 2*Vb1/2/pi/rb/tb;
tau2 = 2*Vb2/2/pi/rb/tb;
tau3 = 2*Vb3/2/pi/rb/tb;
disp('***The max shear stress in blade 1 [Mpa] is:'); max(abs(tau1))/10^6
disp('***The max shear stress in blade 2 [Mpa] is:'); max(abs(tau2))/10^6
disp('***The max shear stress in blade 3 [Mpa] is:'); max(abs(tau3))/10^6

%-------------------------------Tower Top End-------------------------------

Fxte = F(5,:);
Fzte = F(7,:)-3*Ft;
Mzte = F(6,:);
Mxte = F(8,:)-3*Ft*(hh-ht);
Tte = F(4,:);

Mrte = sqrt((Mxte+mr*g*dh).^2+Mzte.^2);
Sbte = Mrte*rte/pi/rte^3/tte;
SbtemaxT = Sbte-(mr+mn)*g/2/pi/rte/tte;
SbtemaxC = -Sbte-(mr+mn)*g/2/pi/rte/tte;
disp('***The max tension stress in tower top end section in [Mpa] is:');
max(SbtemaxT)/10^6
disp('***The max compressive stress in tower top end section in [Mpa] is:');
min(SbtemaxC)/10^6

Frte = sqrt(Fxte.^2+Fzte.^2);
taute = 2*Frte/2/pi/rte/tte;
tautemax = taute+abs(Tte)*rte/2/pi/rte^3/tte;
disp('***The max shear stress in tower top end section in [Mpa] is:');
max(tautemax)/10^6
```

```
%--------------------------Tower Upper Middle Section----------------------

Fxm = F(9,:);
Fzm = F(11,:)-3*Ft;
Mzm = F(10,:);
Mxm = F(12,:)-3*Ft*(hh-2*ht/3);

Mrm = sqrt((Mxm+mr*g*dh).^2+Mzm.^2);
Sbm = Mrm*rm/pi/rm^3/tm;
SbmmaxT = Sbm-(mr+mn+rho*A1*le)*g/2/pi/rm/tm;
SbmmaxC = -Sbm-(mr+mn+rho*A1*le)*g/2/pi/rm/tm;
disp('***The max tension stress in tower middle section in [Mpa] is:');
max(SbmmaxT)/10^6
disp('***The max compressive stress in tower middle section in [Mpa] is:');
min(SbmmaxC)/10^6

Frm = sqrt(Fxm.^2+Fzm.^2);
taum = 2*Frm/2/pi/rm/tm;
taummax = taum+abs(Tte)*rm/2/pi/rm^3/tm;
disp('***The max shear stress in tower middle section in [Mpa] is:');
max(taummax)/10^6

%--------------------------Tower Lower Middle Section----------------------

Fxl = F(13,:);
Fzl = F(15,:)-3*Ft;
Mzl = F(14,:);
Mxl = F(16,:)-3*Ft*(hh-ht/3);

Mrl = sqrt((Mxl+mr*g*dh).^2+Mzl.^2);
Sbl = Mrl*rl/pi/rl^3/tl;
SblmaxT = Sbl-(mr+mn+rho*(A1+A2)*le)*g/2/pi/rl/tl;
SblmaxC = -Sbl-(mr+mn+rho*(A1+A2)*le)*g/2/pi/rl/tl;
disp('***The max tension stress in tower lower middle section in [Mpa] is:');
max(SblmaxT)/10^6
disp('***The max compressive stress in tower lower middle section in [Mpa]
is:'); min(SblmaxC)/10^6

Frl = sqrt(Fxl.^2+Fzl.^2);
taul = 2*Frl/2/pi/rl/tl;
taulmax = taul+abs(Tte)*rl/2/pi/rl^3/tl;
disp('***The max shear stress in tower lower middle section in [Mpa] is:');
max(taulmax)/10^6

%-----------------------------Tower Bottom End-----------------------------

k13 = -12*E*I3/le^3;
k23 = -6*E*I3/le^2;
k14 = -k23;
k24 = 2*E*I3/le;
k57 = k13;
k67 = k23;
k58 = -k23;
k68 = k24;
```

```
Fxbe = (k13*x(:,13)+k23*x(:,14))';
Mzbe = (k14*x(:,13)+k24*x(:,14))';
Fzbe = (k57*x(:,15)+k67*x(:,16))'-3*Ft;
Mxbe = (k58*x(:,15)+k68*x(:,16))'-3*Ft*hh;

Mrbe = sqrt((Mxbe+mr*g*dh).^2+Mzbe.^2);
Sbbe = Mrbe*rbe/pi/rbe^3/tbe;
SbbemaxT = Sbbe-(mr+mn+mt)*g/2/pi/rbe/tbe;
SbbemaxC = -Sbbe-(mr+mn+mt)*g/2/pi/rbe/tbe;
disp('***The max tension stress in tower bottom end in [Mpa] is:');
max(SbbemaxT)/10^6
disp('***The max compressive stress in tower bottom end in [Mpa] is:');
min(SbbemaxC)/10^6

Frbe = sqrt(Fxbe.^2+Fzbe.^2);
taube = 2*Frbe/2/pi/rbe/tbe;
taubemax = taube+abs(Tte)*rbe/2/pi/rbe^3/tbe;
disp('***The max shear stress in tower bottom end in [Mpa] is:');
max(taubemax)/10^6
```

```
%---------------------------------SeismicHAWT.m-----------------------------
% This code is a function subprogram required by HAWTSeismicAnalysis.m to
% evaluate the seismic response of the wind turbine. It contains the
% equations of motion in first order state form. Also permits the
% interpolation of the acceleration records of the earthquakes if needed.
%---------------------------------------------------------------------------


function xdot=SeismicHAWT(t,x)
global Xg Yg Zg N tf Cs
%-------------------------Physical & Mechanical Properties------------------

mr = 43000;                          % Rotor mass [kg]
mb = 8600;                           % Blade mass [kg]
mn = 52000;                          % Nacelle mass [kg]
dh = 3.45;                           % Tower to hub distance [m]
Lb = 40;                             % Blade length [m]
rh = 1;                              % Hub radius [m]
rb = 0.96;                           % Blade root radius [m]
tb = 0.12;                           % Blade root wall thickness [m]
Ib = 1.15e6;                         % Blade moment of inertia [kg.m^2]
Ia = 8600;                           % Hub axial moment of inertia [kg.m^2]
It = 4300;                           % Hub transverse moment of inertia
[kg.m^2]
I = 5.96e-3;                         % Blade sectional moment of inertia [m^4]
Eb = 4.4e10;                         % Blade modulus of elasticity [N/m^2]
ht = 76;                             % Tower height [m]
rbe = 1.99;                          % Tower base end radius [m]
tbe = 2.5e-2;                        % Tower base end wall thickness [m]
rte = 1.15;                          % Tower top end radius [m]
tte = 1.1e-2;                        % Tower top end wall thickness [m]
rho = 8900;                          % Steel density [kg/m^3]
E = 2.07e11;                         % Steel modulus of elasticity [N/m^2]
G = 7.9e10;                          % Steel shear modulus [N/m^2]
v = 0.3;                             % Steel Poisson's ratio
rhoa = 1.225;                        % Air density [kg/m^3]
%va = 13;                             % Average wind speed [m/s]
va = 42.5;
W = 1.65e6;                          % Output power [W]
eta = 0.92;                          % Overall efficiency
Omega = 1.51;                        % Rotor operating angular velocity
[rad/s]
kb = 2.62e7;                         % Blade stiffness coefficient [N.m/rad]
kt = 3.90e8;                         % Tower torsional stiffness coefficient
[N.m/rad]
c1 = 6.80e5;                         % Aerodyamic damping constant [N.s/rad]
c2 = 2.49e4;                         % Aerodyamic damping constant [N.s/m]
c3 = 1.79e7;                         % Aerodyamic damping constant [N.m.s/rad]
c4 = 6.56e5;                         % Aerodyamic damping constant [N.m.s/m]
le = 25.33;                          % Tower element length [m]
A1 = 0.108;                          % Tower element area [m^2]
A2 = 0.178;                          % Tower element area [m^2]
A3 = 0.264;                          % Tower element area [m^2]
I1 = 8.83e-2;                        % Tower sectional moment of inertia [m^4]
I2 = 0.215;                          % Tower sectional moment of inertia [m^4]
```

```
I3 = 0.443;                          % Tower sectional moment of inertia [m^4]
g = 9.81;                            % Acceleration of gravity [m/s^2]


%----------------------------------Mass Matrix---------------------------------

M = zeros(16,16);
M(1,1) = 1/4*mb*Lb^2+Ib;
M(1,4) = -(1/2*mb*(rh+Lb/2)*Lb+Ib)*cos(Omega*t);
M(1,7) = 1/2*mb*Lb;
M(1,8) = (1/2*mb*(rh+Lb/2)*Lb+Ib)*sin(Omega*t);
M(2,4) = -(1/2*mb*(rh+Lb/2)*Lb+Ib)*cos(Omega*t+2*pi/3);
M(2,7) = 1/2*mb*Lb;
M(2,8) = (1/2*mb*(rh+Lb/2)*Lb+Ib)*sin(Omega*t+2*pi/3);
M(3,4) = -(1/2*mb*(rh+Lb/2)*Lb+Ib)*cos(Omega*t+4*pi/3);
M(3,7) = 1/2*mb*Lb;
M(3,8) = (1/2*mb*(rh+Lb/2)*Lb+Ib)*sin(Omega*t+4*pi/3);
M(4,4) = mr*dh^2+3/2*mb*(rh+Lb/2)^2+It+3/2*Ib;
M(4,5) = mr*dh;
M(5,5) = mr+mn+1/2*rho*A1*le;
M(6,6) = 1/24*rho*A1*le^3;
M(8,8) = mr*dh^2+3/2*mb*(rh+Lb/2)^2+It+3/2*Ib+1/24*rho*A1*le^3;
M(9,9) = 1/2*rho*(A1+A2)*le;
M(10,10) = 1/24*rho*(A1+A2)*le^3;
M(13,13) = 1/2*rho*(A2+A3)*le;
M(14,14) = 1/24*rho*(A2+A3)*le^3;
M(2,2) = M(1,1);
M(3,3) = M(1,1);
M(4,1) = M(1,4);
M(4,2) = M(2,4);
M(4,3) = M(3,4);
M(5,4) = M(4,5);
M(8,1) = M(1,8);
M(8,2) = M(2,8);
M(8,3) = M(3,8);
M(7,1) = M(1,7);
M(7,2) = M(2,7);
M(7,3) = M(3,7);
M(7,7) = M(5,5);
M(11,11) = M(9,9);
M(12,12) = M(10,10);
M(15,15) = M(13,13);
M(16,16) = M(14,14);

Me = zeros(16,16);
Me(1,1) = M(1,7);
Me(2,2) = M(2,7);
Me(3,3) = M(3,7);
Me(4,4) = M(4,5);
Me(5,5) = M(5,5);
Me(7,7) = M(7,7);
Me(8,8) = M(4,5);
Me(9,9) = M(9,9);
Me(11,11) = M(11,11);
Me(13,13) = M(13,13);
```

```
Me(15,15) = M(15,15);

%----------------------------------Damping Matrix-----------------------------

C = zeros(16,16);
C(1,1) = c3;
C(1,4) = (1/2*mb*(rh+Lb/2)*Lb+Ib)*Omega*sin(Omega*t);
C(1,7) = c4;
C(1,8) = (1/2*mb*(rh+Lb/2)*Lb+Ib)*Omega*cos(Omega*t);
C(2,2) = c3;
C(2,4) = (1/2*mb*(rh+Lb/2)*Lb+Ib)*Omega*sin(Omega*t+2*pi/3);
C(2,7) = c4;
C(2,8) = (1/2*mb*(rh+Lb/2)*Lb+Ib)*Omega*cos(Omega*t+2*pi/3);
C(3,3) = c3;
C(3,4) = (1/2*mb*(rh+Lb/2)*Lb+Ib)*Omega*sin(Omega*t+4*pi/3);
C(3,7) = c4;
C(3,8) = (1/2*mb*(rh+Lb/2)*Lb+Ib)*Omega*cos(Omega*t+4*pi/3);
C(4,8) = -(3*mb*(rh+Lb/2)^2+Ia+3*Ib)*Omega;
C(7,1) = c1;
C(7,2) = c1;
C(7,3) = c1;
C(7,7) = 3*c2;
C(4,1) = C(1,4);
C(4,2) = C(2,4);
C(4,3) = C(3,4);
C(8,1) = C(1,8);
C(8,2) = C(2,8);
C(8,3) = C(3,8);
C(8,4) = -C(4,8);
C = C+Cs;

%---------------------------------Stiffness Matrix----------------------------

K = zeros(16,16);
K(1,1) = kb;
K(2,2) = K(1,1);
K(3,3) = K(1,1);
K(4,4) = kt;
K(5,5) = 12*E*I1/le^3;
K(5,6) = 6*E*I1/le^2;
K(5,9) = -12*E*I1/le^3;
K(5,10) = 6*E*I1/le^2;
K(6,6) = 4*E*I1/le;
K(6,9) = -6*E*I1/le^2;
K(6,10) = 2*E*I1/le;
K(7,7) = 12*E*I1/le^3;
K(7,8) = 6*E*I1/le^2;
K(7,11) = -12*E*I1/le^3;
K(7,12) = 6*E*I1/le^2;
K(8,8) = 4*E*I1/le;
K(8,11) = -6*E*I1/le^2;
K(8,12) = 2*E*I1/le;
K(9,9) = 12*E*(I1+I2)/le^3;
K(9,10) = 6*E*(I2-I1)/le^2;
K(9,13) = -12*E*I2/le^3;
```

```
K(9,14) = 6*E*I2/le^2;
K(10,10) = 4*E*(I1+I2)/le;
K(10,13) = -6*E*I2/le^2;
K(10,14) = 2*E*I2/le;
K(11,11) = 12*E*(I1+I2)/le^3;
K(11,12) = 6*E*(I2-I1)/le^2;
K(11,15) = -12*E*I2/le^3;
K(11,16) = 6*E*I2/le^2;
K(12,12) = 4*E*(I1+I2)/le;
K(12,15) = -6*E*I2/le^2;
K(12,16) = 2*E*I2/le;
K(13,13) = 12*E*(I2+I3)/le^3;
K(13,14) = 6*E*(I3-I2)/le^2;
K(14,14) = 4*E*(I2+I3)/le;
K(15,15) = 12*E*(I2+I3)/le^3;
K(15,16) = 6*E*(I3-I2)/le^2;
K(16,16) = 4*E*(I2+I3)/le;
K(6,5) = K(5,6);
K(8,7) = K(7,8);
K(9,5) = K(5,9);
K(9,6) = K(6,9);
K(10,5) = K(5,10);
K(10,6) = K(6,10);
K(10,9) = K(9,10);
K(11,7) = K(7,11);
K(11,8) = K(8,11);
K(12,7) = K(7,12);
K(12,8) = K(8,12);
K(12,11) = K(11,12);
K(13,9) = K(9,13);
K(13,10) = K(10,13);
K(14,9) = K(9,14);
K(14,10) = K(10,14);
K(14,13) = K(13,14);
K(15,11) = K(11,15);
K(15,12) = K(12,15);
K(16,11) = K(11,16);
K(16,12) = K(12,16);
K(16,15) = K(15,16);


rx = [0;0;0;1;1;0;0;0;1;0;0;0;1;0;0;0];
ry = [0;0;0;0;0;0;0;-1;0;0;0;0;0;0;0;0];
rz = [1;1;1;0;0;0;1;0;0;0;1;0;0;0;1;0];

A = [zeros(16) eye(16);-(inv(M))*K -(inv(M))*C];
B = [zeros(16);-(inv(M))*Me];


%-----------------------Interpolation of earthquake data--------------------

Dt = 0.01; % Actual record time increment
tx = (0:Dt:tf);
ty = tx;
tz = tx;
```

```
Xb = interp1(tx,Xg,t);
Yb = interp1(ty,Yg,t);
Zb = interp1(tz,Zg,t);

%---------------------------------State Equation-------------------------------

xdot =
A*[x(1);x(2);x(3);x(4);x(5);x(6);x(7);x(8);x(9);x(10);x(11);x(12);x(13);x(14)
;x(15);x(16);x(17);x(18);x(19);x(20)...

;x(21);x(22);x(23);x(24);x(25);x(26);x(27);x(28);x(29);x(30);x(31);x(32)]+(B*
rx*Xb)+(B*ry*Yb)+(B*rz*Zb);
```

```
%---------------------------------Floquet.m---------------------------------
% Main program to calculate the Floquet matrix and obtain the eigenvalues and
% eigenvectors of the free vibration operating wind turbine. It needs the
% function program HAWT.m to run.  Also evaluates for each eigenvector the
% optimum modal shape and normalizes it so the maximum entry will be 1.
%---------------------------------------------------------------------------

clc
clear all
close all

n = 32                                % Number of state equations
Omega = 1.51;
T = 2*pi/Omega;                       % Period [sec]
dt = 0.01;
%tspan = (0:dt:T);
tspan = [0 T];
xo = eye(n);                          % Initial conditions
options = odeset('RelTol',1e-6,'AbsTol',1e-6);

for i = 1:n
[t,x] = ode45('HAWT',tspan,xo(:,i),options);
%[t,x] = ode45('HAWT',tspan,xo(:,i));
[nr,nc] = size(t);
    for j = 1:n
    Phi(j,i)= x(nr,j);
    end
end

[V, lambda] = eig(Phi);
S = 1/T*log(diag(lambda));
Vabs = abs(V(1:n/2,:));
Vangle = angle(V(1:n/2,:));
%disp ('*** The Floquet transition matrix is:'); Phi
%disp ('*** The characteristic multipliers are:'); lambda
%disp ('*** The eigenvectors are:'); V
disp ('*** The characteristic exponent are:'); S
disp ('*** The module of V are:'); Vabs
disp ('*** The phase angle of V are:'); Vangle*180/pi

aa = abs(V(1:n/2,:));
bb = angle(V(1:n/2,:));
SS = sum(aa.^2.*sin(2*bb));
CC = sum(aa.^2.*cos(2*bb));
theta = 1/2*atan(SS./CC);
thetan = pi/180*[-0.0395,0.0395,-0.0010,0.0010,0.0128,-0.0128,4.2968,-
4.2968,0.0992,-0.0992,-1.1527,1.1527,...
        -0.3453,0.3453,1.3917,-1.3917,-0.5040,0.5040,-28.8368,28.8368,-
13.9532,13.9532,1.5969,-1.5969,7.4711,-7.4711,0,...
         40.9089,-40.9089,-19.0323,19.0323,0];
for i = 1:n
    maxp(i) = sum(aa(:,i).^2.*cos(2*(bb(:,i)-theta(:,i))));
    P(:,i) = Vabs(:,i).*cos(Vangle(:,i)-thetan(:,i));
    Pnorm(:,i) = P(:,i)./max(abs(P(:,i)));
end
```

```
disp ('*** The optimal mode shape phase angle'); theta*180/pi
disp ('*** Condition for maximum synchronous motion'); maxp
```

```
%-------------------------------------HAWT.m---------------------------------
% This is a function subprogram required by the frogram Floquet.m to run.  It
% contains the equations of motion of the wind turbine to perform an
% operating free vibration analysis ignoring structural damping and including
% aerodynamic damping.
%------------------------------------------------------------------------------

function xdot=HAWT(t,x)

%-----------------------Physical & Mechanical Properties--------------------

mr = 43000;                             % Rotor mass [kg]
mb = 8600;                              % Blade mass [kg]
mn = 52000;                             % Nacelle mass [kg]
dh = 3.45;                              % Tower to hub distance [m]
Lb = 40;                                % Blade length [m]
rh = 1;                                 % Hub radius [m]
rb = 0.96;                              % Blade root radius [m]
tb = 0.12;                              % Blade root wall thickness [m]
Ib = 1.15e6;                            % Blade moment of inertia [kg.m^2]
Ia = 8600;                              % Hub axial moment of inertia [kg.m^2]
It = 4300;                              % Hub transverse moment of inertia
[kg.m^2]
I = 5.96e-3;                            % Blade sectional moment of inertia [m^4]
Eb = 4.4e10;                            % Blade modulus of elasticity [N/m^2]
ht = 76;                                % Tower height [m]
rbe = 1.99;                             % Tower base end radius [m]
tbe = 2.5e-2;                           % Tower base end wall thickness [m]
rte = 1.15;                             % Tower top end radius [m]
tte = 1.1e-2;                           % Tower top end wall thickness [m]
rho = 8900;                             % Steel density [kg/m^3]
E = 2.07e11;                            % Steel modulus of elasticity [N/m^2]
G = 7.9e10;                             % Steel shear modulus [N/m^2]
v = 0.3;                                % Steel Poisson's ratio
rhoa = 1.225;                           % Air density [kg/m^3]
va = 13;                                % Average wind speed [m/s]
W = 1.65e6;                             % Output power [W]
eta = 0.92;                             % Overall efficiency
Omega = 1.51;                           % Rotor operating angular velocity
[rad/s]
kb = 2.62e7;                            % Blade stiffness coefficient [N.m/rad]
kt = 3.90e8;                            % Tower torsional stiffness coefficient
[N.m/rad]
c1 = 6.80e5;                            % Aerodyamic damping constant [N.s/rad]
c2 = 2.49e4;                            % Aerodyamic damping constant [N.s/m]
c3 = 1.79e7;                            % Aerodyamic damping constant [N.m.s/rad]
c4 = 6.56e5;                            % Aerodyamic damping constant [N.m.s/m]
le = 25.33;                             % Tower element length [m]
A1 = 0.108;                             % Tower element area [m^2]
A2 = 0.178;                             % Tower element area [m^2]
A3 = 0.264;                             % Tower element area [m^2]
I1 = 8.83e-2;                           % Tower sectional moment of inertia [m^4]
I2 = 0.215;                             % Tower sectional moment of inertia [m^4]
I3 = 0.443;                             % Tower sectional moment of inertia [m^4]
```

```
%---------------------------------Mass Matrix-------------------------------

M = zeros(16,16);
M(1,1) = 1/4*mb*Lb^2+Ib;
M(1,4) = -(1/2*mb*(rh+Lb/2)*Lb+Ib)*cos(Omega*t);
M(1,7) = 1/2*mb*Lb;
M(1,8) = (1/2*mb*(rh+Lb/2)*Lb+Ib)*sin(Omega*t);
M(2,4) = -(1/2*mb*(rh+Lb/2)*Lb+Ib)*cos(Omega*t+2*pi/3);
M(2,7) = 1/2*mb*Lb;
M(2,8) = (1/2*mb*(rh+Lb/2)*Lb+Ib)*sin(Omega*t+2*pi/3);
M(3,4) = -(1/2*mb*(rh+Lb/2)*Lb+Ib)*cos(Omega*t+4*pi/3);
M(3,7) = 1/2*mb*Lb;
M(3,8) = (1/2*mb*(rh+Lb/2)*Lb+Ib)*sin(Omega*t+4*pi/3);
M(4,4) = mr*dh^2+3/2*mb*(rh+Lb/2)^2+It+3/2*Ib;
M(4,5) = mr*dh;
M(5,5) = mr+mn+1/2*rho*A1*le;
M(6,6) = 1/24*rho*A1*le^3;
M(8,8) = mr*dh^2+3/2*mb*(rh+Lb/2)^2+It+3/2*Ib+1/24*rho*A1*le^3;
M(9,9) = 1/2*rho*(A1+A2)*le;
M(10,10) = 1/24*rho*(A1+A2)*le^3;
M(13,13) = 1/2*rho*(A2+A3)*le;
M(14,14) = 1/24*rho*(A2+A3)*le^3;
M(2,2) = M(1,1);
M(3,3) = M(1,1);
M(4,1) = M(1,4);
M(4,2) = M(2,4);
M(4,3) = M(3,4);
M(5,4) = M(4,5);
M(8,1) = M(1,8);
M(8,2) = M(2,8);
M(8,3) = M(3,8);
M(7,1) = M(1,7);
M(7,2) = M(2,7);
M(7,3) = M(3,7);
M(7,7) = M(5,5);
M(11,11) = M(9,9);
M(12,12) = M(10,10);
M(15,15) = M(13,13);
M(16,16) = M(14,14);

%---------------------------------Damping Matrix-----------------------------

C = zeros(16,16);
C(1,1) = c3;
C(1,4) = (1/2*mb*(rh+Lb/2)*Lb+Ib)*Omega*sin(Omega*t);
C(1,7) = c4;
C(1,8) = (1/2*mb*(rh+Lb/2)*Lb+Ib)*Omega*cos(Omega*t);
C(2,2) = c3;
C(2,4) = (1/2*mb*(rh+Lb/2)*Lb+Ib)*Omega*sin(Omega*t+2*pi/3);
C(2,7) = c4;
C(2,8) = (1/2*mb*(rh+Lb/2)*Lb+Ib)*Omega*cos(Omega*t+2*pi/3);
C(3,3) = c3;
C(3,4) = (1/2*mb*(rh+Lb/2)*Lb+Ib)*Omega*sin(Omega*t+4*pi/3);
C(3,7) = c4;
```

```
C(3,8) = (1/2*mb*(rh+Lb/2)*Lb+Ib)*Omega*cos(Omega*t+4*pi/3);
C(4,8) = -(3*mb*(rh+Lb/2)^2+Ia+3*Ib)*Omega;
C(7,1) = c1;
C(7,2) = c1;
C(7,3) = c1;
C(7,7) = 3*c2;
C(4,1) = C(1,4);
C(4,2) = C(2,4);
C(4,3) = C(3,4);
C(8,1) = C(1,8);
C(8,2) = C(2,8);
C(8,3) = C(3,8);
C(8,4) = -C(4,8);

%-------------------------------Stiffness Matrix-----------------------------

K = zeros(16,16);
K(1,1) = kb;
K(2,2) = K(1,1);
K(3,3) = K(1,1);
K(4,4) = kt;
K(5,5) = 12*E*I1/le^3;
K(5,6) = 6*E*I1/le^2;
K(5,9) = -12*E*I1/le^3;
K(5,10) = 6*E*I1/le^2;
K(6,6) = 4*E*I1/le;
K(6,9) = -6*E*I1/le^2;
K(6,10) = 2*E*I1/le;
K(7,7) = 12*E*I1/le^3;
K(7,8) = 6*E*I1/le^2;
K(7,11) = -12*E*I1/le^3;
K(7,12) = 6*E*I1/le^2;
K(8,8) = 4*E*I1/le;
K(8,11) = -6*E*I1/le^2;
K(8,12) = 2*E*I1/le;
K(9,9) = 12*E*(I1+I2)/le^3;
K(9,10) = 6*E*(I2-I1)/le^2;
K(9,13) = -12*E*I2/le^3;
K(9,14) = 6*E*I2/le^2;
K(10,10) = 4*E*(I1+I2)/le;
K(10,13) = -6*E*I2/le^2;
K(10,14) = 2*E*I2/le;
K(11,11) = 12*E*(I1+I2)/le^3;
K(11,12) = 6*E*(I2-I1)/le^2;
K(11,15) = -12*E*I2/le^3;
K(11,16) = 6*E*I2/le^2;
K(12,12) = 4*E*(I1+I2)/le;
K(12,15) = -6*E*I2/le^2;
K(12,16) = 2*E*I2/le;
K(13,13) = 12*E*(I2+I3)/le^3;
K(13,14) = 6*E*(I3-I2)/le^2;
K(14,14) = 4*E*(I2+I3)/le;
K(15,15) = 12*E*(I2+I3)/le^3;
K(15,16) = 6*E*(I3-I2)/le^2;
K(16,16) = 4*E*(I2+I3)/le;
```

```
K(6,5) = K(5,6);
K(8,7) = K(7,8);
K(9,5) = K(5,9);
K(9,6) = K(6,9);
K(10,5) = K(5,10);
K(10,6) = K(6,10);
K(10,9) = K(9,10);
K(11,7) = K(7,11);
K(11,8) = K(8,11);
K(12,7) = K(7,12);
K(12,8) = K(8,12);
K(12,11) = K(11,12);
K(13,9) = K(9,13);
K(13,10) = K(10,13);
K(14,9) = K(9,14);
K(14,10) = K(10,14);
K(14,13) = K(13,14);
K(15,11) = K(11,15);
K(15,12) = K(12,15);
K(16,11) = K(11,16);
K(16,12) = K(12,16);
K(16,15) = K(15,16);

%----------------------------------State Equation-----------------------------


A = [zeros(16) eye(16);-(inv(M))*K -(inv(M))*C];

xdot =
A*[x(1);x(2);x(3);x(4);x(5);x(6);x(7);x(8);x(9);x(10);x(11);x(12);x(13);x(14)
;x(15);x(16);x(17);x(18);x(19);x(20)...
  ;x(21);x(22);x(23);x(24);x(25);x(26);x(27);x(28);x(29);x(30);x(31);x(32)];
```